Preclinical molecular imaging in oncology – From chemical synthesis to clinical translatable applications

Elvira García de Jalón Viñegra

Thesis for the degree of Philosophiae Doctor (PhD)
University of Bergen, Norway
2021

UNIVERSITY OF BERGEN

Preclinical molecular imaging in oncology – From chemical synthesis to clinical translatable applications

Elvira García de Jalón Viñegra

Thesis for the degree of Philosophiae Doctor (PhD)
at the University of Bergen

Date of defense: 25.06.2021

Year: 2021

Title: Preclinical molecular imaging in oncology – From chemical synthesis to clinical translatable applications

Name: Elvira García de Jalón Viñegra

Print: Skipnes Kommunikasjon / University of Bergen

Experiment is the interpreter of nature. Experiments never deceive. It is our judgment which sometimes deceives itself because it expects results which experiment refuses.

Leonardo Da Vinci, 15th century

La lumière joue dans notre vie un rôle essentiel: elle intervient dans la plupart de nos activités. Les Grecs de l'Antiquité le savaient déjà, eux qui pour dire «mourir» disaient «perdre la lumière».

Louis de Broglie, 1941

Contents

Scientific environment **7**

Acknowledgements **8**

Abbreviations and terms **10**

Abstract **13**

List of Publications **16**

1. Introduction **17**

1.1 Cancer *17*

1.2 Molecular imaging of cancer *19*

1.2.1 Optical imaging 23

1.2.2 Positron Emission Tomography (PET) 25

1.3 Reporter genes *26*

1.3.1 Luciferase and bioluminescence imaging (BLI) 27

1.3.2 Green fluorescence protein (GFP) 28

1.3.3 Nitroreductase (NTR) 29

1.3.4 Fluorescence imaging (FLI) of GFP or NTR substrates 31

1.4 Organic fluorophores for Fluorescence imaging *33*

1.4.1 Near-infrared Fluorescent (NIRF) probes 35

1.4.2 Cyanine derived probes 37

1.5 Targeted fluorescent imaging approaches *40*

1.6 Applications and clinical translatability of reporter genes and/or fluorescence imaging *41*

1.6.1 Gene-directed enzyme prodrug therapy 41

1.6.2 Fluorescence image-guided surgery (FIGS) 43

2. Aims of the study **45**

2.1 Background and general aims *45*

2.2 Specific aims *45*

3. Methodological considerations **47**

3.1 General synthetic overview *47*

3.1.1 Synthesis of Fischer bases 47

3.1.2 Condensation final compounds 48

3.1.3 Condensation with squaric acid esters of Substrate 1 (Stepwise strategy) 49
3.1.4 Solid support synthetic approach for Substrate 1 49
3.1.5 Synthesis of targeting ligand 50
3.1.6 Conjugation to targeting ligands 51
3.2 Purification methods *52*
3.3 Characterisation techniques *52*
3.4 In vitro experiments *53*
3.4.1 Enzymatic assay 53
3.4.2 Cell culture 53
3.4.3 Viral transduction and gene expression assessment 54
3.4.4 Flow cytometry 55
3.4.5 Fluorescence confocal microscopy 55
3.5 In vivo experiments *56*
3.5.1 Ethical approval 56
3.5.2 Optical imaging 56
3.5.3 Nuclear imaging 57
3.6 Ex vivo analysis *58*
4. Summary of results 59
4.1 Paper I *59*
4.2 Paper II *60*
4.3 Paper III *60*
5. General discussion 62
5.1 Fluorescent probes and their physicochemical properties, a double edged sword *63*
5.2 NTR-activatable cyanine-based fluorophores *66*
5.3 Stability, sensitivity and specificity: considerations in the design of fluorescent conjugates towards the clinic *69*
5.4 NTR beyond preclinical research *72*
6. Conclusions 75
7. Future perspectives 76
References 78
8. Appendix I 97

Scientific environment

This multidisciplinary project was conducted in between the Department of Clinical Science and the Department of Chemistry and Centre for Pharmacy at the University of Bergen, Norway. The progress of the scientific activities related to *in vitro* and *in vivo* experiments was supervised by Professor Emmet Mc Cormack. The synthetic approaches were supervised by Professor Bengt Erik Haug. Dr. Gorka Ruiz de Garibay supervised my progress during the experimental and writing phases of this thesis. During the research time I was affiliated with The Norwegian PhD School of Pharmacy and with the Centre for Cancer Biomarkers (CCBIO).

The project was carried out in collaboration with the Center for Nuclear Medicine/PET, Haukeland University Hospital and with the Department of Pathology from the Oslo University Hospital. This project has received funding from the University of Bergen, Helse Vest, The Research Council of Norway, the Norwegian Cancer Society and the Trond Mohn Foundation. I was the recipient of a MedIm bridging grant from the Norwegian Research School in Medical Imaging.

Acknowledgements

First of all, I would like to thank my main supervisor, Professor Emmet Mc Cormack, for giving me the opportunity to do this project in his group and for his just-in-time motivational kicks. My co-supervisor, Professor Bengt Erik Haug, deserves a big thank for always having 5 minutes to discuss and for his much appreciated moral support in these last months. And to you, Dr. Gorka Ruiz de Garibay, arriving here would not have been possible without you. Thanks for your patience, for your admirable capacity to listen, for teaching me so many new things. It has been a pleasure working with you and discussing science with you.

As this is a multidisciplinary thesis, many people have been involved in teaching me new methodologies and helping me to understand the "strange" phenomena observed in some cases. First of all, Bjarte Holmelid, thank you very much for all the time you have spent with me reviewing data and giving me good tips and tricks. Thanks to Brith Bergum, for her incredible energy, her Advent calendars and her experienced assistance when needed. Thanks to the members of the NNP platform, especially to Jarl Underhaug, for his assistance with the NMR. Thanks to the members of MIC, in particular Heidi Espedal, for her assistance with the PET/CT. Thanks to Hege, Endy and Linda, for their assistance with the microscopes and tissue sectioning. Thanks to all my co-authors for their contributions. To the various people who proof read this document, thank you very much.

Thanks to the members of the Mc Cormack lab, current and former, for making the lab a good place to work. The same goes to the Haug lab members, current and former, it was fun to do chemistry around you. Thank you all for the experiences and science shared.

I am indebted to many friends who accompanied me through happy and tough times. Thanks to Markus Baumann, for being there from the beginning through thick and thin. Thanks to Katrin Kleinmanns, for keeping me afloat when I was sinking. Thanks to Matteo Luzzi for dealing with me all these years. Thanks to Yehia Mokhtar, for the

warm meals and hugs. Thanks to Jasmine Pani, for being a constant even when far apart. Thanks to my travel partner, Etienne López, for teaching me backgammon. Thanks to my dive buddy, Endre Stigen, for the Sundays that felt like family. Thanks to my friends back home, Alba, María Jose, Marta and Georgina, for all the trips and moments shared over the years. To my school friends, thank you for making every Christmas more special. Thanks to everyone who in some way made the time away from the lab very enjoyable. Thank you for the hikes, the dinners, the beers, the movies, the calls, the work-outs, the camping-weekends, the trips… Thanks to Anika, Mireia, Sam, Christiane, Benjamin, Rob, Ángel, Pablo, Abdul, Mahla, Sophie, Kjetil, María and Anna.

Y por último, mi más sincero agradecimiento a mi familia. A mis abuelos, a mi tía y sobre todo a mis padres. Por su amor incondicional y todo su apoyo a lo largo de los años. Y por creer siempre en mí, incluso ni cuando yo misma creía.

Abbreviations and terms

^{18}F-FDG	2-Deoxy-2-[^{18}F]fluoroglucose
^{18}F-FHBG	9-(4-[^{18}F]Fluoro-3-hydroxymethylbutyl) guanine
^{18}F-FIAU	1-(2´-deoxy-2´-[^{18}F]fluoro-β-D-arabinofuranosyl)-5-iodouracil
^{18}F-FMISO	^{18}F-Fluoromisonidazole
^{18}F-HX4	^{18}F-Flortanidazole
ATP	Adenosine triphosphate
BLI	Bioluminescence imaging
CAR T-cell	Chimeric antigen receptor T-cell
Cas9	CRISPR-associated protein 9
CB1954	(5-(Aziridin-1-yl)-2,4-dinitrobenzamide)
CCD	Charged-coupled device
CD	Cytosine deaminase
CE	Carboxylesterase
CRISPR	Clustered regularly interspaced short palindromic repeats
CT	Computed tomography
D2R	Dopamine receptor D2
DMSO	Dimethyl sulfoxide
DNA	Deoxyribonucleic acid
EBFP	Enhanced blue fluorescent protein
ECFP	Enhanced cyan fluorescent protein
EGFP	Enhanced green fluorescent protein
EPR	Enhanced permeability and retention
EYFP	Enhanced yellow fluorescent protein
FDA	Food and drug administration

FIGS	Fluorescence image-guided surgery
FLI	Fluorescence imaging
FLuc	Firefly luciferase
FMN	Flavin mononucleotide
$FMNH_2$	Dihydroflavin mononucleotide
FRα	Folate receptor alpha
GCV	Ganciclovir
GDEPT	Gene-directed enzyme prodrug therapy
GFP	Green fluorescent protein
HER-2	Human epidermal growth factor receptor 2
hERL	Human estrogen receptor ligand
HPLC	High-performance liquid chromatography
hRLuc	Renilla reniformis
HSV1-TK	Herpes simplex virus type 1 thymidine kinase
IC	Internal conversion
ICG	Indocyanine green
iPSCs	Induced pluripotent stem cells
ISC	Intersystem crossing
KRAS	KRAS proto-oncogene
LUMO	Lowest unoccupied molecular orbital
MB	Methylene blue
MI	Molecular imaging
MRI	Magnetic resonance imaging
MS	Mass spectrometry
NADH	Nicotinamide adenine dinucleotide

NADPH	Nicotinamide adenine dinucleotide phosphate
NCL	NTR caged luciferin
NHS	*N*-Hydroxysuccinimide
NIRF	Near-infrared fluorescence
NIS	Sodium iodide symporter
NTR	Nitroreductase
OCT	Optical coherence tomography
OR	Operating room
PEG	Polyethylene glycol
PET	Positron emission tomography
PeT	Photoinduced electron transfer
PMT	Photomultiplier tube
PNP	Purine nucleoside phosphorylase
PSMA	Prostate-specific membrane antigen
SBR	Signal-to-background ratio
SLN	Sentinel lymph node
SN23862	5-(Bis(2-chloroethyl)amino)-2,4-dinitrobenzamide
SPECT	Single photon emission computed tomography
SUV_{bw}	Standardised uptake value based on body weight
SWNT	Single walled carbon nanotubes
TBR	Tumour-to-background ratio
TME	Tumour microenvironment
US	Ultrasound
UV	Ultraviolet
WHO	World Health Organisation

Abstract

Background: Molecular imaging (MI) is fundamental in clinical settings for diagnosis, treatment selection, intraoperative guidance and treatment efficacy evaluation. This field has progressed rapidly in recent years, driven by the need for diagnostic tools and as a tool to monitor the efficacy of new cancer treatments, including gene-based therapies. MI in combination with reporter genes allows *in vivo* monitoring of enzyme expression and follow-up of the success of gene-directed enzyme prodrug therapies (GDEPT), where the suicide gene also acts as reporter gene. In this thesis, nitroreductase NfsB (NTR) from *E. coli* has been concurrently employed as a reporter gene (**Papers I** and **III**) and suicide gene (**Paper III**). The work of this thesis has also focused on the contrast agents of two main MI methodologies, namely optical imaging (mainly fluorescence imaging (FLI) for longitudinal imaging (**Papers I – III**) and fluorescence image-guided surgery (FIGS) (**Paper II**)) and nuclear-based PET/CT imaging (**Paper III**).

Aims: To highlight and resolve the discrepancies present in the literature in regard to the near-infrared (NIR) dye CytoCy5S. For this purpose, four NIR dyes were synthesised and analysed. Based on their physicochemical and optical properties and their *in vivo* behaviour, we aimed to define the best candidate for preclinical optical imaging of NTR (**Paper I**). To compare how common NIR dyes affect the *in vivo* behaviour of conjugates and to identify the optimal dye that could be used to improve the further development of fluorescent conjugates for FIGS (**Paper II**). To repurpose the hypoxia radiopharmaceutical ^{18}F-FMISO for PET/CT imaging of NTR expression in an *in vivo* GDEPT setting (**Paper III**).

Materials and methods: We synthesised, purified and characterised four NTR substrates (**1** – **4**), including alternately described structures currently referred by the name CytoCy5S. A comparative NTR enzymatic assay was performed to assess the spectroscopic characteristics of the different reductively activated dyes. The NTR expressing triple-negative breast carcinoma cell line, MDA-MB-231 NTR^{+}, was

employed to compare, both *in vitro* and *in vivo*, the suitability of these fluorophores as reporters of NTR activity. Comparison of the reporting properties was achieved by flow cytometry, fluorescence microscopy and optical imaging, both *in vivo* and *ex vivo* (**Paper I**). The NHS esters of ZW800-1, ZW800-1 Forte, IRDye® 800CW, ICG, and Cy7 derivative were conjugated to folate through an ethylenediamine linker to give conjugates **1** – **5**, respectively. The optical properties of conjugates **1** – **5** were determined by spectroscopy, their specificity assessed *in vitro* by flow cytometry and FLI, and their biodistribution studied *in vivo* and *ex vivo* using FLI in a subcutaneous Skov-3 ovarian cancer model (**Paper II**). The efficacy of ^{18}F-FMISO to report NfsB NTR activity *in vivo* was investigated using the MDA-MB-231 model. For validation, subcutaneous xenografts of cells constitutively expressing NTR were imaged using ^{18}F-FMISO PET/CT and FLI with CytoCy5S. Further, examination of the non-invasive functionality of ^{18}F-FMISO PET/CT in reporting NfsB NTR activity *in vivo* was assessed in metastatic orthotopic NfsB NTR expressing xenografts and metastasis confirmed by bioluminescence imaging. ^{18}F-FMISO biodistribution was acquired *ex vivo* by an automatic gamma counter measuring radiotracer retention to confirm *in vivo* results. To assess the functional imaging of NTR-based GDEPT with ^{18}F-FMISO, PET/CT was performed to assess both gene transduction and cytotoxicity effects of prodrug therapy (CB1954) in subcutaneous models (**Paper III**).

Results: The introduction of the methoxy group in **3** and the sulfonate and cyanine scaffold in **4** resulted in a modest bathochromic shift compared to **1** and **2**. All compounds were confirmed as NTR substrates with delayed kinetics observed for **2** and low emission intensities for **3** and **4**. *In vitro,* **3** was found to display the highest NTR^+/NTR^- ratio, followed by **1**. **4** performed poorly *in vitro* and *in vivo*. **1** and **2** provided similar suitability for NTR interrogation, being **1** slightly more sensitive at smaller tumour volumes and presenting faster kinetics and a functional group for conjugation to biomolecules. We determined that substrate **1** is the ideal candidate for further studies (**Paper I**). We demonstrated time- and receptor-dependent binding of folate conjugates *in vitro* and *in vivo*. Healthy tissue clearance characteristics and

tumour-specific signal varied between conjugates **1** - **5**. **2** revealed the highest contrast in folate receptor alpha (FRα) positive xenografts and was the only conjugate that reported significant differences between Skov-3 and A549 ($p < 0.05$). Whilst conjugates **1**, **2** and **3** are renally cleared, hepatobiliary excretion and no or very low accumulation in tumours was observed for **4** and **5** (**Paper II**). ^{18}F-FMISO retention was detected in NTR^{+} subcutaneous xenografts, displaying significantly higher PET contrast than NTR^{-} xenografts ($p < 0.0001$). Substantial ^{18}F-FMISO retention was evident in metastases of orthotopic xenografts ($p < 0.05$). Accordingly, higher ^{18}F-FMISO biodistribution was prevalent *ex vivo* in NTR^{+} xenografts. ^{18}F-FMISO NfsB NTR PET/CT imaging proved useful for monitoring *in vivo* NTR transduction and the cytotoxic effect of prodrug therapy (**Paper III**).

Conclusions: We have fully characterised the chemical and biological properties of four NIR dyes and clearly defined which is the best for imaging of NTR (**Paper I**). Our work highlights the high impact the physicochemical properties of the dye have on the tumour accumulation and biodistribution of the conjugate and demonstrates the potential of alternative fluorophores to IRDye® 800CW for targeted approaches in FIGS (**Paper II**). We have demonstrated that ^{18}F-FMISO is a readily implementable PET probe to be employed as companion diagnostic test for NTR-based GDEPT systems (**Paper III**).

List of Publications

I. **Elvira García de Jalón**, Gorka Ruiz de Garibay, Bengt Erik Haug and Emmet McCormack (2021): "CytoCy5S™, a compound of many structures. *In vitro* and *in vivo* evaluation of four near-infrared fluorescent substrates of nitroreductase (NTR)" *Manuscript under peer review*

II. **Elvira García de Jalón***, Katrin Kleinmanns*, Vibeke Fosse, Ben Davidson, Line Bjørge, Bengt Erik Haug, Emmet Mc Cormack: "Comparison of five near-infrared fluorescent folate conjugates in an ovarian cancer model" *Manuscript*

III. Gorka Ruiz de Garibay*, **Elvira García de Jalón***, Endre Stigen, Kjetil B Lund, Mihaela Popa, Ben Davidson, Mireia Mayoral Safont, Cecilie B. Rygh, Heidi Espedal, Torill M Barrett, Bengt Erik Haug and Emmet McCormack (2021): "Repurposing ^{18}F-FMISO as a PET tracer for translational imaging of nitroreductase-based gene directed enzyme prodrug therapy" *Theranostics* 2021; 11(12):6044-6057. doi: 10.7150/thno.55092.

*Authors contributed equally to the work

1. Introduction

1.1 Cancer

Cancer is characterised by the rapid increase of abnormal cells that grow uncontrolled, followed by invasion of adjacent tissues, entry into the blood stream migrating to other organs, and infiltration in a process known as metastasis [1]. It defines a range of diseases with high heterogeneity and challenging prognosis based on its molecular phenotype, location or stage of disease. Cancer requires accumulation of several mutations in different genes to pass from a normal cell to a malignant one and this occurs in a multistep process (tumour progression) (Figure 1) [2]. Mutations in two main types of genes are believed responsible in the early stages of cancer initiation in healthy cells, i.e. activation of oncogenes or loss of tumour suppressor genes.

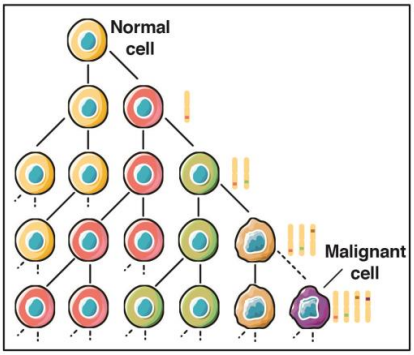

Figure 1: Schematic representation of tumour progression and clonal evolution of tumours. [2]

The different biological capabilities acquired by the cells during clonal evolution allow them to become malignant and conform the hallmarks of cancer [3] (Figure 2). They include biological capabilities such as sustained proliferative signalling, replicative immortality or induced angiogenesis; and enabling characteristics such as genomic instability or inflammation. The exploitation of these cellular traits can be applied to select appropriate treatment strategies (examples included in Figure 2), as well as to develop novel molecular probes for imaging modalities suitable for disease monitoring [4, 5].

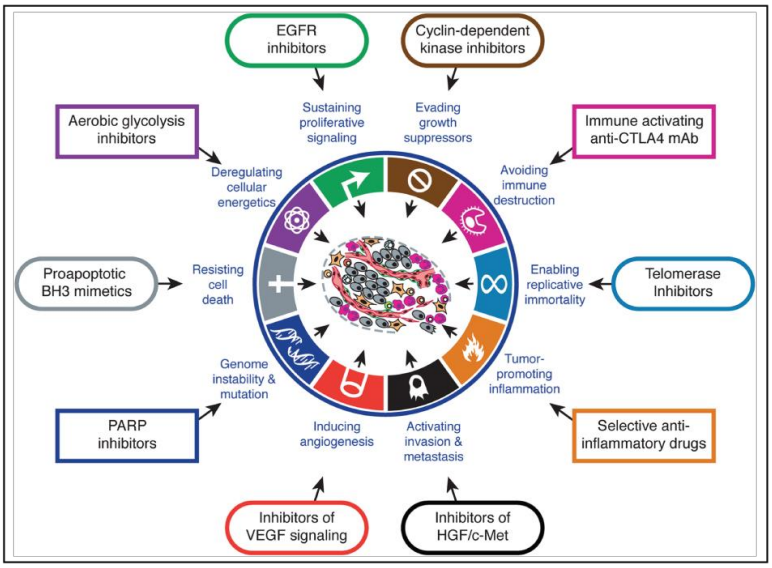

Figure 2: Therapeutic targeting of the hallmarks of cancer. Reproduced from [3] with permission from Elsevier.

According to the WHO, more than 70% of the deaths caused by cancer are reported in low- to middle-income countries, where the resources in place for prevention, diagnosis or treatment are limited [6]. Early detection, either by early diagnosis of symptomatic patients at early stages of the disease or by mass screening of an asymptomatic population (for breast, cervical and colorectal cancers), plays a key role in disease control [7]. One of the most successful examples of screening methods, and one of the few imaging-based, has been the use of mammography for breast cancer [8]. This X-ray picture of the breast permits the detection of cancerous lesions in asymptomatic women prior to the development of metastatic disease. Accordingly, breast cancer is more often successfully treated in early stages resulting in a pronounced decrease in mortality in the last decades (Figure 3) [9].

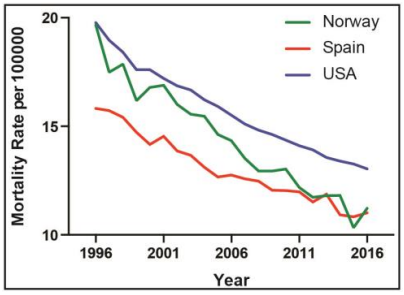

Figure 3: Breast cancer mortality statistics over 20 years from Norway, Spain and USA. [9]

In general, conventional imaging, including mammography screening [10], has limitations, such as false-positive or false-negative results due to insufficient

specificity and sensitivity, respectively, which molecular imaging (MI) aims to overcome [11]. A recently published multicenter study investigated the use of a novel imaging strategy. This method combined prostate specific membrane antigen (PSMA) and positron emission tomography/computed tomography (PET/CT) and has been shown to be superior to CT and bone scanning, supporting the claim of being “a suitable replacement for conventional imaging” [12]. This supports a paradigm shift from conventional imaging (structure) towards MI (function).

1.2 Molecular imaging of cancer

Cancer therapies have progressed rapidly in recent decades [13], moving from chemotherapies to personalised therapies using cancer-specific targeted approaches [14] (e.g. with prognosis (HER-2) and prediction (KRAS) biomarkers). In addition, immune cell therapies are used to boost the patient's tumour-supressing immune responses [15] (e.g. with CAR T-cells or immune checkpoint inhibitors). These personalised strategies targeting specific molecular traits have led to reduced toxicity and increased efficacy, and their development requires the employment of MI to clinically monitor efficacy. Moreover, the emergence of drug resistance requires continuous therapeutic development in relevant preclinical models, where MI is a prerequisite. This remains key to advancing the most promising therapies into clinical trials, while reducing the bench-to-bed time required [16, 17].

MI allows the study of gene and protein function, as well as molecular processes preclinically in small animals or clinically in humans [18]. Therefore, MI in cancer has gained traction in the last 25 years, with more than 6000 works published on the subject in the last five years [19]. This highly multidisciplinary strategy begins with the identification of a molecular target. Once the relevant target has been validated, the proof-of-principle testing phase follows, which includes synthetic chemistry, cell biology and imaging technology. If the preclinical results obtained are favourable, further translational phases with clear endpoints will be implemented to ultimately develop the imaging strategy for clinical use (Figure 4). This lengthy research process

is a challenge that must be addressed by an interdisciplinary team of chemists, biologists, physicists, physicians, pharmacists and imaging specialists [20].

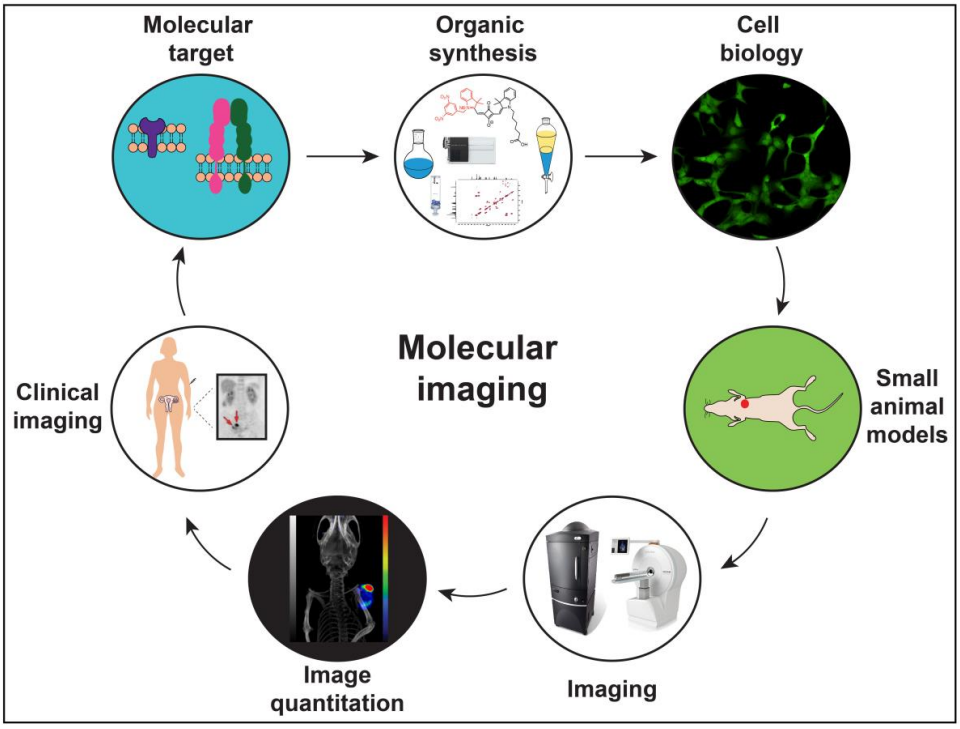

Figure 4: Schematic overview of the main steps of a molecular imaging study. From conceptualisation identifying a molecular target to the clinical evaluation of the imaging methodology. Adapted from [18, 21]

MI can be divided in two main groups: nuclear imaging (pink in Table 1) and non-radionuclide-based imaging (blue in Table 1). Nuclear imaging requires the use of radionuclides that decay via the emission of two collinear gamma rays (positron emission tomography, PET) or of a single gamma ray (single-photon emission computed tomography, SPECT). These rays are captured by detector rings (PET) or by a gamma camera that rotates around the imaged subject (SPECT) creating a tomographic reconstruction. Optical imaging comprises a variety of techniques including fluorescence imaging (FLI) and bioluminescence imaging (BLI). They allow non-invasive monitoring of biological processes by detection of light and will be described in detail below. Magnetic resonance imaging (MRI) is an anatomical/morphological methodology that employs an external magnetic field to

obtain images based on the different relaxation times of magnetic particles from certain atomic nuclei like ^{1}H in different tissues. Computed tomography (CT) is a tomographic technique that relies on the attenuation of X-rays when travelling through tissues providing 3D anatomic images. CT is often combined with functional techniques such as PET or SPECT. Ultrasound (US) relies on the propagation of sound waves from a transducer through tissue. Interaction of these waves with the tissues, that present different elastic properties, reflect the waves (echo) non-uniformly and energy is detected by the transmitting transducer, reporting structural or functional information.

All the aforementioned imaging modalities differ in key features such as depth penetration, spatial and time resolution and type of probes employed. Other factors such as the target organ or cells, its use in either human or animal models, together with the availability of the necessary probes, determine which technique is best for a specific purpose [22]. Each of these techniques shows weaknesses, such as use of radiation or low penetration, and strengths such as being non-invasive or high spatial resolution. The synergistic integration of several techniques is a favourable strategy to overcome drawbacks of the individual techniques [23]. The different characteristics of the methodologies comprised within each group are briefly described in Table 1 [18, 21, 22]. In clinical practice, molecular imaging techniques that provide information about function are combined with anatomical modalities that provide structure information. Some common examples are PET/CT and PET/MRI, which improve the image visualisation and thereby aid surgeons in locating diseased tissue and vital structures preoperatively.

Table 1: Overview of the characteristics of different imaging modalities employed in preclinical and clinical settings.

	Radionuclide-based		Non-radionuclide-based				
	PET§	SPECT	FLI§	BLI§	MRI	CT§	US
Spatial resolution	Low	Low	High	High	High	High	High
Depth	Unlimited	Unlimited	≤ 1 cm	≤ 1 cm	Unlimited	Unlimited	ν dependent
Sensitivity	High	High	Limited	High	Limited	ND	Limited
Time	Long	Long	Short	Short	Long	Short	Short
Constrast agents†	β^+- emitters	γ - emitters	Fluoro-chromes	Luciferins	Magnetic particles	Radio-contrasts	Micro-bubbles
Multiplexing	No	Yes	Yes	Yes	No	Possible	Possible
Cost	Expensive	Expensive	Cheap	Cheap	Expensive	Moderate	Cheap
Application	Pre- and clinical		Preclinical*		Preclinical and clinical		

PET = **P**ositron **E**mission **T**omography; SPECT = **S**ingle **P**hoton **E**mission **C**omputed **T**omography; FLI = **F**luorescence **I**maging; BLI = **B**ioluminescence **I**maging; MRI = **M**agnetic **R**esonance **I**maging; CT = **C**omputed **T**omography; US = **U**ltrasound. The modalities indicated with § have been used during the research of this thesis and will be further described. ND: not determined. † Not always required * Fluorescence imaging employed clinically in intraoperative settings e.g. fluorescence image-guided surgery (FIGS) [18, 21, 22]

1.2.1 Optical imaging

The use of light to visualise cells and tissues is a simple method that has been widely employed in preclinical and clinical settings since the invention of the microscope in 1674 [21]. The introduction of live cell fluorescence microscopy has permitted the evaluation of molecular events in real time using fluorophores. Further development of macroscopic imaging techniques allowed whole-body interrogation of molecular events in living small animals and patients. A number of different macroscopic optical imaging techniques [24] are available, including endoscopy [25, 26], optical coherence tomography (OCT) [27, 28], super-resolution intravital microscopy [28, 29], photoacoustic imaging [30, 31] or Raman spectroscopy [32, 33]. All these techniques present distinct advantages and are at different stages of technology readiness and clinical acceptance and they are further discussed elsewhere [21]. The main focus of this thesis is in reflectance FLI and to a minor extent BLI, techniques that are described in detail below.

FLI requires an external energy source, i.e. light, to obtain information from cells and tissues. Light with an appropriate wavelength excites either an endogenous or an exogenous fluorophore that upon relaxation will emit light with lower energy than that absorbed. In the case of bioluminescence imaging, an enzymatic reaction causes the spontaneous emission of photons and therefore the presence of an external excitation source is not needed.

FLI systems, including fluorescence image-guided surgery (FIGS) systems, are composed of an excitation light source, a detection system, excitation and emission filters and imaging software. Based on the position of the light source and the detector, epi-illumination or trans-illumination techniques are distinguished. In epi-illumination, the light source and the detector are placed on the same side and the light is reflected (Figure 5). For trans-illumination, the light source and detector are on opposite sides and the light is transmitted through the imaged subject (Figure 5A). This distinct configuration of the FLI system confers different advantages, such as rapid imaging times in the case of epi-illumination or increased sensitivity due to the attenuation of tissue autofluorescence in the case of trans-illumination [34]. For BLI,

the same instruments are employed, but only the detection system and the imaging software come into play (Figure 5B).

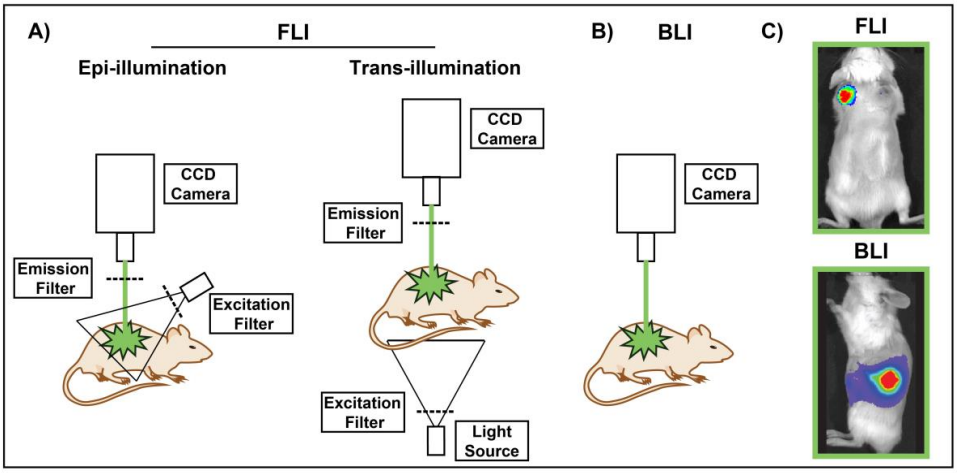

Figure 5: Schematic overview of the instrumentation employed in fluorescence imaging (FLI), depicting the differences between A) epi-illumination and trans-illumination, and B) in bioluminescence imaging (BLI). C) Fluorescence planar image of a subcutaneous xenograft obtained with epi-illumination and bioluminescence planar image of an orthotopic xenograft (Image courtesy of Katrin Kleinmanns).

The excitation source can be a laser at a given wavelength or a white-light source with low-pass filters. Excitation and emission filters maximise the detected signal by blocking the photons at undesired wavelengths. This maximised signal is detected by a photomultiplier tube detector (PMT) or by a charged-coupled device (CCD) camera. CCD cameras, particularly cooled back-tinned and back-illuminated CCD, are preferred over PMTs since they are more sensitive and provide better resolution. For BLI, the use of emission filters is not required and all the photons emitted by the sample under study are collected. The acquired photons are then converted into electric charges proportional to the light intensity that are further amplified and digitised by means of the imaging software. This results in a planar (Figure 5C) image that allows localisation of the fluorophore under study and hence evaluation of the physiological process of interest [35-37]. This final image shows the number of photons per region in the animal under study and this fluorescent/bioluminescent signal is often reported as average radiance ($p/s/cm^2/sr$).

1.2.2 Positron Emission Tomography (PET)

PET is a functional imaging modality that allows preclinical and clinical evaluation of metabolic or biologic function by radiotracer uptake. It is commonly combined with X-ray CT for structural localisation. Clinically, it is a very relevant modality that allows investigation of cancer during the different stages of the disease from diagnosis to treatment efficacy assessment [38].

Radiotracers are composed of a radionuclide, an organic targeting ligand and, in many cases, a linker between these. Radionuclides are the unstable isotopes of a given atom and they emit radiation while decaying towards more stable nuclear configurations. One of the most widely employed radionuclides is ^{18}F, which is present in the glucose analogue ^{18}F-fluorodeoxyglucose (^{18}F-FDG). Different synthetic methods are known to obtain ^{18}F [39], but the most commonly employed method is the proton bombardment of ^{18}O-enriched water in a cyclotron, $^{18}O(p,n)^{18}F$ [40]. ^{18}F exhibits an excess of protons, and neutron deficiency, and its decay results in positron (β^+) emission accompanied by a neutrino (Figure 6) [41]. One of the advantages of ^{18}F over other positron emitters, such as ^{15}O, ^{13}N or ^{11}C, is its low positron energy (0.635 MeV), which translates into shorter diffusion ranges within tissues and hence higher resolution [42].

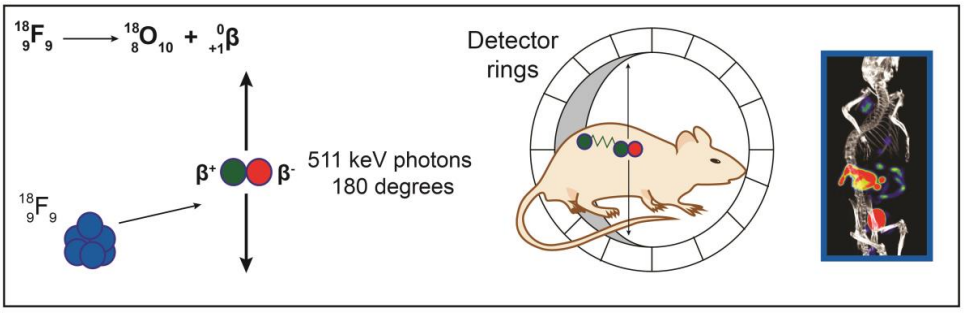

Figure 6: The principles of PET. The positron (β^+) is emitted and it travels a short distance before interacting with an electron (β^-) and undergoing annihilation. The two gamma photons (511 keV and 180°) are simultaneously detected by detector rings (coincidence). Reconstruction of registered events gives a PET/CT 3D image that can be overlaid with a CT image (image from a subcutaneous xenograft).

As illustrated in Figure 6, the emitted positron travels briefly through tissue until it loses its kinetic energy. It then reacts with an electron (β^-) in an annihilation process

that produces two 511 keV gamma photons with opposed directions of around 180°. These photon pairs, when detected simultaneously in a coincidence event by the detector rings that are formed of scintillation crystals coupled to PMTs, provide the localisation of the annihilation process. The many annihilation processes registered by the detectors are reconstructed to give accurate 3D images of the radiotracer biodistribution in the tissue under study [41, 42]. The radiotracer activity (disintegrations per second) is most commonly reported as Standard Uptake Value per body weight (SUV_{bw}) and it comprises the activity concentration of the radionuclide (kBq/mL), the total dosage of injected radiotracer (MBq) and the body weight of the study subject [43].

1.3 Reporter genes

MI techniques based on indirect imaging strategies require the genetic insertion of a reporter gene that encodes for a certain protein that can be visualised employing MI. This genetic insertion, or cell transduction, is commonly performed, both *in vitro* and *in vivo*, using viral vectors. Non-replicating adenoviruses are widely employed, but dilution of the expressed gene through division and proliferation limits their potential. Retroviruses target only actively dividing cells and DNA methylation leads to undesired gene silencing. Thus, lentiviruses, a class of retroviruses, which target replicating cells and cells in the stationary phase, integrating the exogenous gene in the host cells with low cytotoxicity and exhibiting no gene silencing are preferred [44].

When the reporter gene is a fluorescent protein, FLI can be employed for visualisation. In other instances, exogenous reporter probes (e.g fluorophore or radiotracer) are necessary to image the reporter gene [45, 46]. In these cases, reporter genes allow retention and accumulation of the reporter probe thereby permitting detection of the signal by different imaging techniques (e.g. FLI or PET) [45]. The reporter genes used in imaging express a wide variety of proteins, such as membrane

transporters (e.g. sodium iodide symporter, NIS [47]), intra- and extra-cellular receptors (e.g. human estrogen receptor ligand, hERL [48] and dopamine 2 receptor, D2R [49]) or enzymes (e.g. thymidine kinase, HSV1-TK [50] and β-lactamase [51]). Some of the most commonly used reporter genes are luciferase and green fluorescent protein (GFP), which have been used together with the nitroreductase (NTR) in this project, and are further described (see section 1.7).

1.3.1 Luciferase and bioluminescence imaging (BLI)

Luciferase proteins have been isolated from different terrestrial organisms, such as the firefly *Photinus pyralis* (FLuc) and from marine species, such as the sea pansy *Renilla reniformis* (hRLuc). These enzymes can be divided into two main groups based on the substrate preference, benzothiazoyl-thiazole luciferin (FLuc) or benzylimidazo-pyrazinone coelenterazine (hRLuc) (Figure 7) [52].

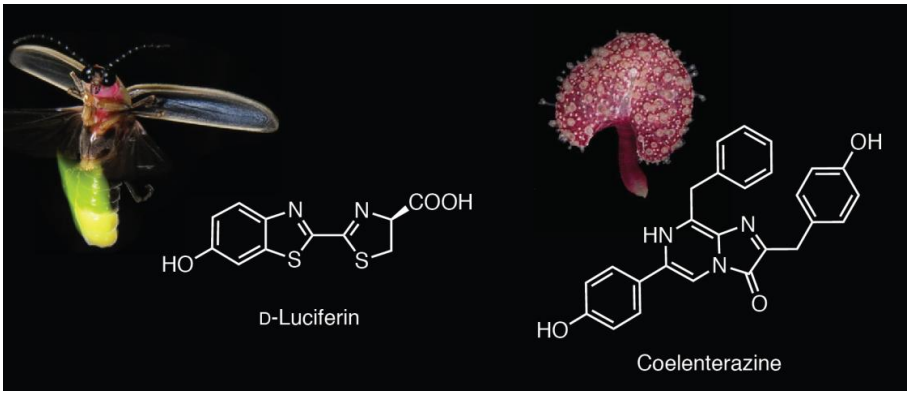

Figure 7: Substrates of luciferase and organisms from which the enzymes were isolated. D-Luciferin is the substrate of Fluc from *Photinus pyralis* (left) and Coelenterazine is the substrate of hRLuc from *Renilla reniformis* (right).

BLI of molecular and cellular processes is routinely employed in different biomedical fields [53] and is a reporter-based technique that requires the combination of an enzyme, luciferase, and its corresponding substrate, luciferin. FLuc catalyzes the oxidation of D-luciferin to oxyluciferin in the presence of O_2, Mg^{2+} and ATP (Figure 8). Unlike FLuc, coelenterazine-oxidasing enzymes (hRLuc) do not require ATP to convert coelenterazine into its corresponding coelenteramide, CO_2 and light.

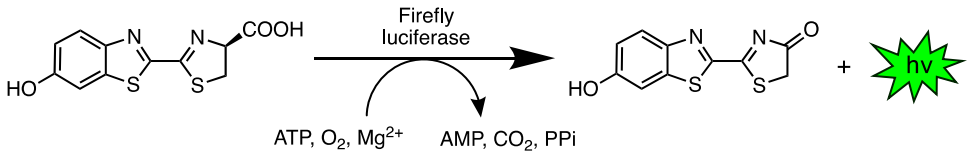

Figure 8: The enzymatic oxidation of luciferin to produce light in the presence of different cofactors.

This biochemical reaction produces spontaneous emission of visible light when the electrons of the oxidised molecule, which are in an electronically excited state, return to the ground state ($S_1 \rightarrow S_0$). The emitted photons are captured by the CCD camera and converted into electronic signals that are processed to provide planar real-time images within short data acquisition times [18, 52].

BLI does not require an excitation source, thus avoiding photon attenuation, scatter and diffusion of light when passing through the different tissues. It is a very sensitive technique due to the lack of enzyme expression in animal tissues, and hence signal, from healthy surrounding tissues, providing high signal to background ratios (SBR). One of the major limitations is the requirement of cell engineering by means of viral transduction to achieve luciferase expression. This has hampered its clinical translation but it remains a key tool in preclinical oncological models for visualisation of cancer cells.

1.3.2 Green fluorescence protein (GFP)

GFP, a visible light-emitting fluorophore isolated from the bioluminescent jellyfish *Aequorea victoria* (Figure 9), is one of the most widely employed reporter genes. Its discovery and development awarded three scientists with the Nobel Prize in Chemistry in 2008.

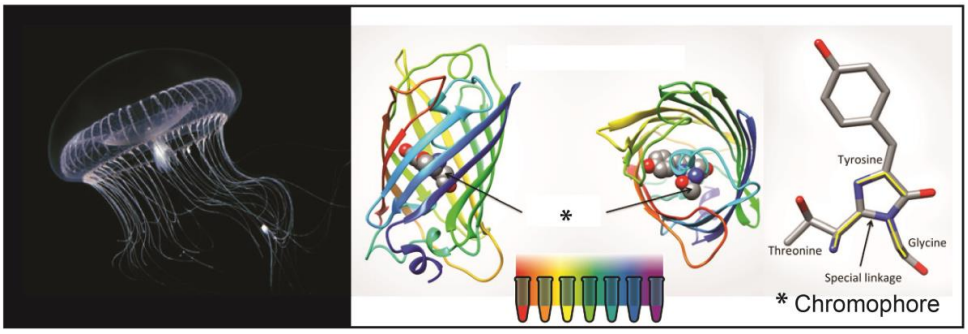

Figure 9: *Aequorea victoria* and schematic representation of the β-barrel structure of EGFP and its covalently bound chromophore. Representation of the alternative colours obtained by modification of the chromophore. [54-57]

The chromophore of this protein is located inside a β-barrel structure in the protein and it is formed by three amino acid residues (Ser 65, Tyr 66 and Gly 67) that spontaneously cyclise to form a highly conjugated imidazolidinone ring (Figure 9) [54, 55]. Genetic modifications of this chromophore, e.g. substitution of Ser 65 by Thr 65, have provided fluorescent proteins with higher photostability, longer emission and absorption wavelengths, generating a whole palette of alternative colours, e.g. enhanced green fluorescent protein (EGFP; λ_{exc} = 490 nm λ_{em} = 510 nm), blue-shifted (EBFP; λ_{exc} = 382 nm λ_{em} = 448 nm), cyan-shifted (ECFP; λ_{exc} = 439 nm λ_{em} = 476 nm) or yellow-shifted variants (EYFP; λ_{exc} = 514 nm λ_{em} = 527 nm) [54-57]. Moreover, problems such as low fluorescence or slow maturation (fluorophore formation) have been overcome [18]. These fluorescent proteins have allowed monitoring of gene expression or tumour growth *in vivo* [58, 59].

1.3.3 Nitroreductase (NTR)

The nitroreductase superfamily, with its diverse enzymatic functionalities that contains over 20,000 different sequences [60], receives its name from the discovery of the killing potency of some nitroaromatic compounds towards bacteria. This observation, which led to the development of nitrofurazone [61], was followed by the discovery of nitrofurazone sensitivity genes (*NfsA* and *NfsB*) in *Escherichia coli* [62].

The *NfsB* gene encodes for the NTR enzyme that is formed by two identical subunits (homodimeric, 48 kDa) that catalyses the reduction of nitro-containing compounds in the presence of bound flavin mononucleotide (FMN) cofactor and NADH or NADPH

as electron donors [63-65]. This catalytic reaction, in which a nitro group (R-NO_2) is reduced to the hydroxylamine group (R-NHOH) via the nitroso form (R-NO), requires two electron (e^-) transfers (Figure 10) [66].

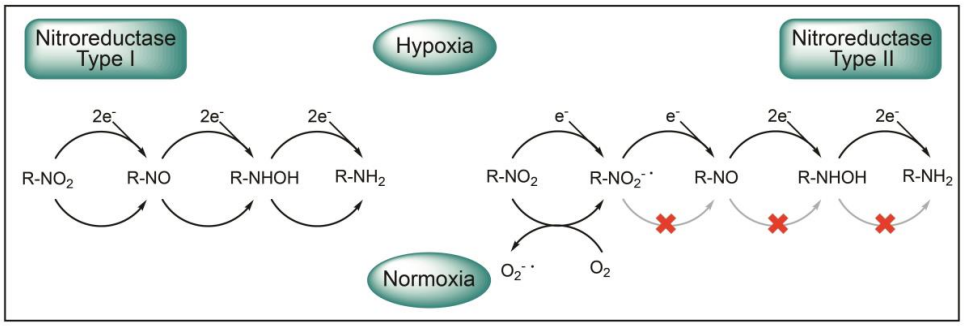

Figure 10: The catalytic mechanisms of type I and II nitroreductases under different oxygenation conditions.

The reduction of the substrate follows a ping-pong Bi-Bi mechanism and in this type of non-sequential mechanism, the enzyme, like a ping-pong ball, bounces from the initial state to an intermediate state and back to the initial state. In the intermediate state, reduction by NADPH of FMN in a two e^- transfer to $FMNH_2$ leads to a small conformational change in the pyrazine ring. The oxidised species, $NADP^+$, leaves the binding pocket and the second substrate, in this case a nitro-containing compound, binds close to $FMNH_2$. The R-NO_2 group is reduced to R-NHOH thereby oxidising reduced $FMNH_2$ to its initial state (FMN) in a two e^- transfer [63].

NTR belongs to the Type I or oxygen-insensitive nitroreductases (Figure 10) that are able to reduce their substrates in both the presence and absence of oxygen due to the simultaneous transfer of the two electrons. Type II or oxygen-sensitive nitroreductases, on the other hand, are only able to reduce their substrates in the absence of oxygen. The reduction occurs by two consecutive transfers of one e^-, producing an unstable radical intermediate that oxidises in the presence of oxygen (Figure 10) [66, 67]. This type of nitroreductases are found in hypoxia, and are the basis of PET/CT or FLI imaging of this condition both pre- and clinically [68, 69].

NfsB NTR has been widely used as suicide gene for gene enzyme prodrug therapy

(GDEPT) by exploiting the capacity of this enzyme to reductively activate nitro-containing prodrugs to their cytotoxic metabolites in the presence of oxygen [70, 71]. Some examples of commonly employed prodrugs in the setting of NTR-based GDEPT are the azidirinyldinitrobenzamide CB1954 and the dinitrobenzamide mustard SN23862, whose hydroxylamine products get acetylated causing DNA cross-linking and hence cell death [72, 73]. In addition, the imaging possibilities offered by NTR as reporter gene have been explored in a wide variety of studies. Our group demonstrated the promising potential of CytoCy5S, a near-infrared quenched fluorophore substrate of NTR, for non-invasive *in vivo* near-infrared (NIR) reporter gene imaging in preclinical metastatic cancers [71].

1.3.4 Fluorescence imaging (FLI) of GFP or NTR substrates

The first written evidence of the phenomenon of fluorescence corresponds to a Spanish physician in 1565. Nicolás Monardes reported (in *Joyful News out of the New Found World*) the peculiar blue colour of an infusion of a wood called *Lignum nephriticum* used by the Aztecs to treat kidney and urine diseases [74]. The molecule responsible for this case of luminescence, the product of a chain of spontaneous oxidations of a flavonoid, was recently identified [75] (Figure 11).

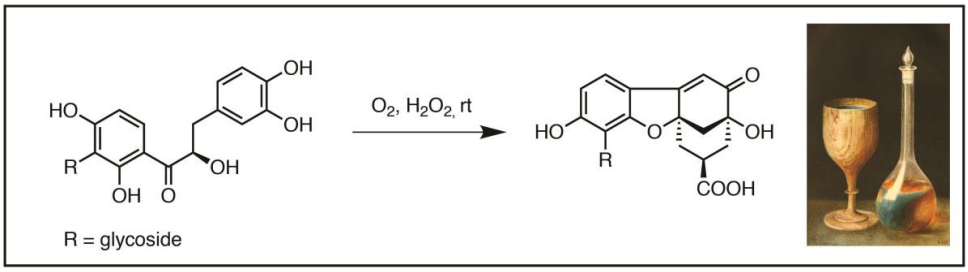

Figure 11: Schematic of the sequential reaction from Coatline B to Matlaline, the fluorophore responsible for the blue tinge of *Lignum nephriticum* [75]

FLI of biological molecular processes is also broadly employed in different biomedical fields, both preclinically and clinically [76]. It requires a fluorophore (e.g. a fluorescent protein or an exogenous fluorescent contrast agent) and an external excitation source. The fluorophore absorbs photons that bring the molecule to a higher singlet electronic state (S_1). There it resides for a certain time (ps – ns) before

it returns to the fundamental electronic state (S_0) with the release of photons and the retention of the state multiplicity (Figure 12). This spontaneous emission of radiation (fluorescence) occurs at lower energies and higher wavelengths than the absorption, and the difference in wavelength between absorption and emission is known as the Stokes shift of the probe (Figure 12). The energy loss is caused by vibrational relaxation during the residency of the molecule in the excited state. High Stokes shifts are desirable to avoid excitation photons contributing to the fluorescent image. Non-radiative decays from excited electronic states such as $S_2 \rightarrow S_1$ or $S_1 \rightarrow S_0$ with the same spin multiplicity are also possible and are known as internal conversion (IC). Additionally, forbidden transitions to the T_1 triplet state by inter-system crossing (ISC), followed by relaxation to the electronic ground state, result in emission of photons in a process known as phosphorescence. Compared to fluorescence, phosphorescence is a very slow process due to the fact that the transition $T_1 \rightarrow S_0$ is forbidden [74].

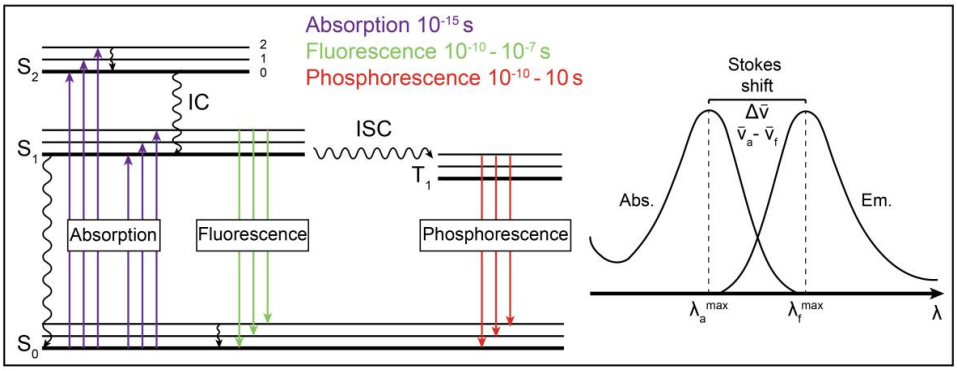

Figure 12: Perrin-Jablonski diagram depicting absorption, fluorescence and phosphorescence processes and their corresponding characteristic times. Straight arrows represent radiative processes while wavy arrows correspond to non-radiative processes, such as internal conversion (IC) or intersystem crossing (ISC). Graphical illustration of the Stokes shift, gap between the maximum of the first absorption band and the maximum of the fluorescence spectrum expressed in wavenumbers. [74]

FLI is an inexpensive imaging modality that allows non-invasive and repetitive imaging of different pathologies in small animals. Due to its low cost it is a key tool in the preclinical development of new drugs, since it allows full evaluation of drug efficacy in biological systems before moving them into lengthy and more expensive

clinical phases. Another advantage is that FLI allows multiplexed imaging [71, 77, 78]. However, the limited depth of penetration of light (< 1 cm) has hampered its use in humans. In addition, autofluorescence, scattering and tissue absorption of light diminish the sensitivity of this technique. By taking advantage of fluorophores with spectral properties in the NIR region, some of these issues can be circumvented.

1.4 Organic fluorophores for Fluorescence imaging

To date, the different fluorophores available for *in vivo* imaging can be divided into two groups based on their chemical nature: organic compounds or inorganic nanomaterials. The first group (see Figure 13) includes heterocyclic compounds like coumarins (D), xanthene dyes (E&F), pyrromethene derivatives (G), cyanines (H&I), quinone-imine dyes (J) and fluorescent proteins. The second group is formed by nanoparticles (NPs) including semiconductor nanocrystals like quantum dots (QDs) [79, 80] or lanthanide-based NPs [81, 82] and by carbon nanostructures like single-walled carbon nanotubes (SWNTs) [83, 84]. This last group exhibits desirable properties such as strong absorption, stability and tunable optical properties, but due to their inherent inorganic properties and their safety profile, fluorescent proteins and organic dyes are preferred for biomedical imaging applications.

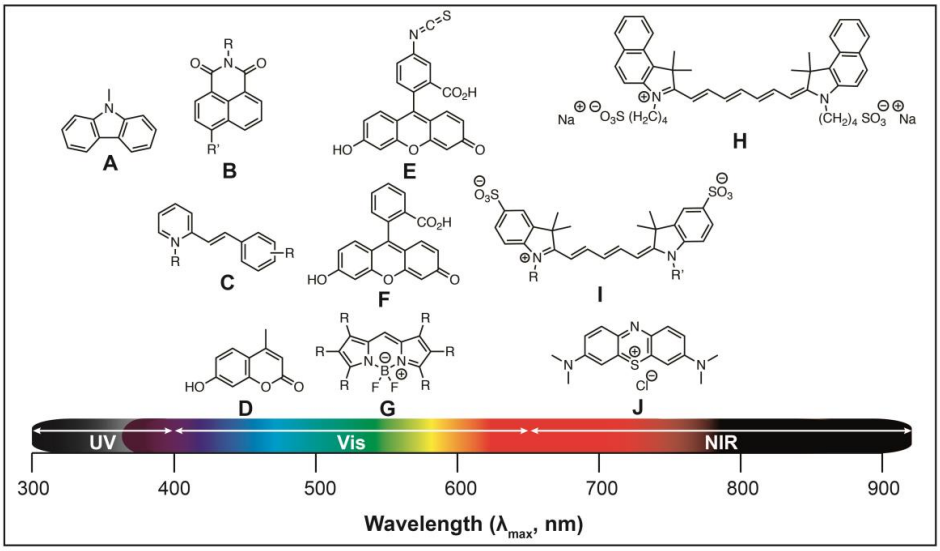

Figure 13: General structures of common fluorophores and fluorescent scaffolds with emission in the UV, visible and NIR regions. A: *N*-Carbazole; B: Naphthalimide; C: Styryl; D: Coumarin; E: FITC; F: Fluorescein; G: BODIPY; H: ICG; I: Cy5; J: MB. [74, 85]

The chemical structure and the nature of the different organic fluorophores dictate the fluorescence properties of these compounds. In figure 13, the chemical structures of some representative organic fluorophores and fluorescent scaffolds are shown. As observed for the cyanine derivatives (H and I), an increase in the length of the π-system (conjugation) is translated into a red-shifted emission wavelength, bathochromic shift [86]. In addition, introduction of substituents onto the core scaffolds of fluorescent probes, such as coumarin or BODIPY (D and G, respectively), with either electron-donating or electron-withdrawing groups, will have an effect on their physicochemical and optical properties. These derivatisations can also be exploited to enhance the affinity of the fluorophores towards a given molecular target [87].

The ideal fluorophore for biomedical imaging must meet certain minimum requirements, such as high brightness, photochemical stability, long Stokes shift, aqueous solubility and low toxicity [87, 88]. The brightness of the fluorophore is determined by the molar absorption coefficient (**ε**, or extinction coefficient) and by

the quantum yield (ϕ_F) of the compound [74]. The ε indicates the ability of a molecule to absorb light of a given wavelength (λ_E), with high values indicating probable electronic transitions. The ϕ_F expresses the ratio between the number of emitted photons during relaxation and the number of absorbed photons, and the larger the value the easier it is to observe the fluorophore. Hence, the product of these two terms, $\varepsilon(\lambda_E)$ x ϕ_F, determines the brightness of a given fluorophore. Excitation and emission spectra are also characteristic properties of each fluorophore. The excitation spectrum represents the fluorescence intensity at different wavelengths and the emission spectrum represents the distribution of the probability of $S_1 \rightarrow S_0$ electronic transitions during relaxation [74]. Fluorophores with spectral properties (λ_{ex} and λ_{em}) in the NIR region (650 – 900 nm) are of great interest due to their promising properties for biomedical imaging [89, 90] (see section 1.4.1).

1.4.1 Near-infrared Fluorescent (NIRF) probes

Electromagnetic radiation ranging from the ultraviolet (UV) to the near-infrared region (NIR) is widely exploited for imaging in the biomedical field, as illustrated in Figure 13. The UV region comprises wavelengths below 400 nm while the visible window ranges from 400 to 650 nm. The NIR region is divided further into NIR I (650 to 900 nm) and NIR II (1000 to 1700 nm). Between 900 and 1000 nm there is an increase in the absorption by water and lipids, limiting the applicability of this small region [91]. Compared to UV or visible light, NIR light exhibits favourable properties for bioimaging applications, such as reduced scattering and attenuation by tissues, as well as reduced absorption by cytochromes, haemoglobin or melanin in living organisms (Figure 14) [52, 92]. Thus, the use of fluorescent probes emitting in this privileged region of the electromagnetic spectrum allows for deeper tissue penetration and increased sensitivity due to reduced tissue autofluorescence [21].

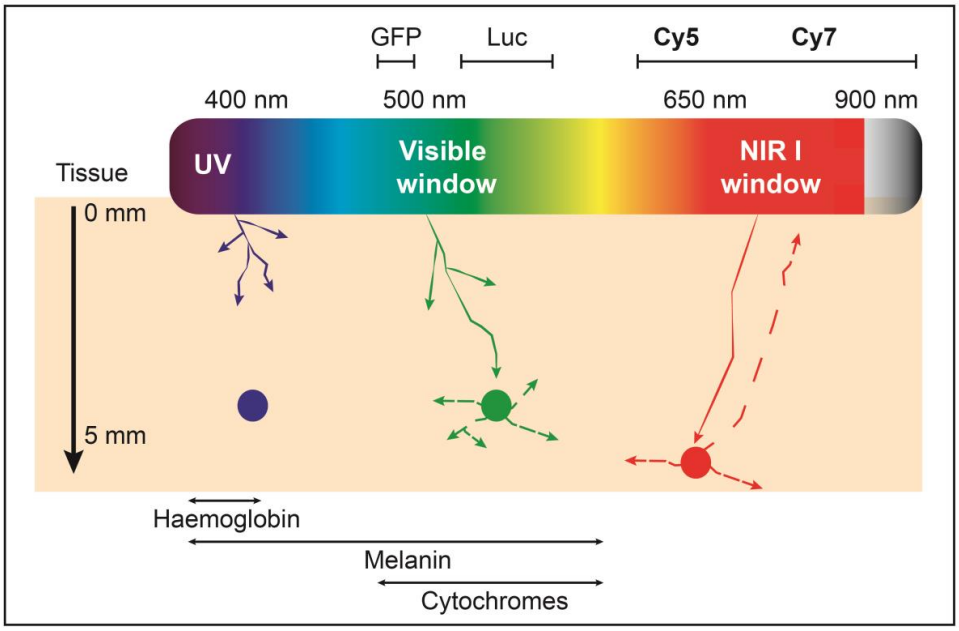

Figure 14: Schematic overview of the behaviour of light in the different regions of the electromagnetic spectrum. UV suffers from complete absorption by tissue, the visible suffers absorption and scattering of light, and NIR allows deep tissue imaging [90].

Ever since the 1980s, extensive research has been undertaken in order to exploit the NIR region of the spectrum for biological imaging applications, with particular interest in fluorescence image-guided surgery (FIGS). Two representative examples are indocyanine green (ICG; λ_{ex} = 807 nm and λ_{em}= 822 nm) and methylene blue (MB; λ_{ex} = 665 nm and λ_{em} = 688 nm), the only two NIR fluorophores clinically approved as contrast agents (structures H and J in Figure 13, respectively). They have been used to identify sentinel lymph nodes (SLN) [93, 94] and certain tumours [95-98]. However, the poor optical properties and the high chemical instability of MB have hampered its use [88]. ICG exhibits better optical properties than MB, and its tumour accumulation by the enhanced permeability and retention (EPR) effect has been exploited in intraoperative settings. Despite good malignancy detection rates, it was not able to specifically distinguish between healthy and diseased tissue, resulting in high background signals and thus high false-positive rates [95]. In addition, its poor aqueous stability, poor photostability, tendency to form aggregates and lack of

functional groups for conjugation to targeting moieties have limited its adoption as the standard contrast agent [4, 88, 99]. Formulations based on the encapsulation of ICG have overcome some of these limitations [100-102], however, much effort is being dedicated to the development of improved cyanine-derived probes with clinical translational potential for disease investigation [103, 104].

1.4.2 Cyanine derived probes

Cyanine (derived from the Greek κυανος [*kyanos*] = dark blue) dyes are a class of polymethine functional dyes with applications that range from electrophotography to photovoltaics. Cyanines are cationic compounds with two *N*-heteroaromatic electron-donating groups connected through a polymethine bridge of varying length with an odd number of carbon atoms. Two examples of natural occurring cyanine dyes, betanin and musca aurin (Figure 15), were accidentally discovered and their structures elucidated in the 1960s by Dreiding and in the 1970s by Musso, respectively [105]. Both dyes, responsible for the colour of beetroot and *Amanita muscaria* respectively, were found to share a common pentamethinium scaffold and an L-amino acid-derived chiral group.

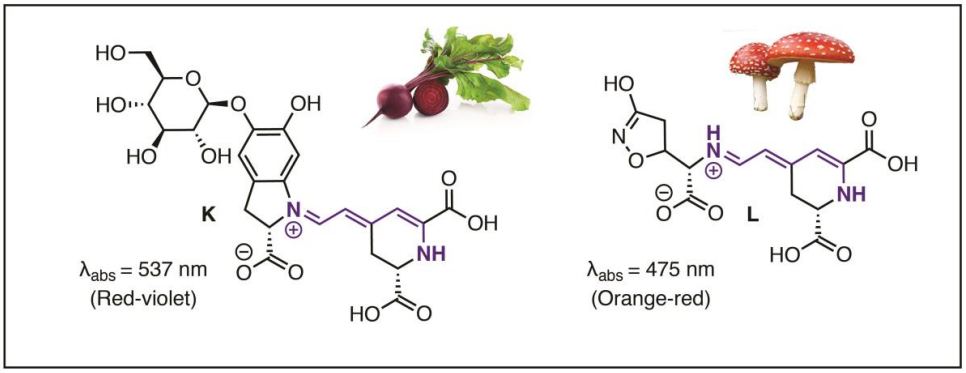

Figure 15: Structures of betanin (K) and musca aurin (L) with their corresponding absorption wavelengths and their distinct colouration.

Based on the number of methine groups present in the bridge they are classified as monomethine (n = 0; Cy1), trimethine (n = 1, Cy3), pentamethine (n = 2, Cy5) or heptamethine (n = 3, Cy7) cyanines (Figure 16) [86]. While Cy1 and Cy3 exhibit spectral properties in the visible region of the spectrum (400 - 650 nm), Cy5 and Cy7

show absorption and emission in the NIR-I region (650 – 900 nm). The increase in the number of methine groups and increased conjugation entails an advantageous bathochromic shift of around 100 nm for each extra methine group, albeit with reduced fluorescence quantum yield [86, 106]. It has also been observed that elongation of the polymethine chain alters the pharmacokinetic properties of conjugates composed of the same $\alpha_v\beta3$–recognising peptide bound to either Cy3, Cy5 or Cy7 derived fluorophores [107]. Introduction of a squaryl moiety (M, Figure 16) or a cyclohexenyl (N, Figure 16) groups in the conjugating system increases the planarity and rigidity of the structure and has given compounds with improved photochemical stability compared to the corresponding cyanines [89, 106, 108].

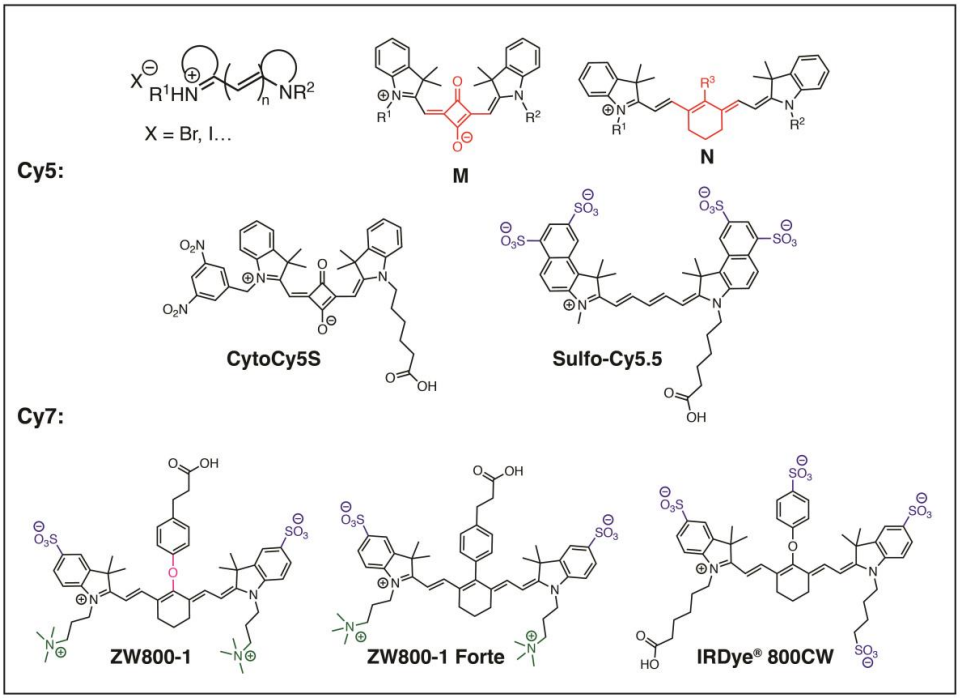

Figure 16: Schematic overview of the general structure of cyanines. M and N represent two common modifications of the polymethine chain to improve the stability of Cy5 and Cy7 derivatives. Some common examples of Cy5 and Cy7 compounds employed in preclinical and clinical settings for fluorescence imaging are shown.

In addition to modifications of the polymethine chain, variations in the nitrogen substituents R^1 and R^2 and/or in the heterocycles can tune the physicochemical and

optical properties of these compounds. Cyanines are quite lipophilic and this limits their applicability for *in vivo* FLI. Introduction of charged groups such as sulfonates on the heterocycles or aliphatic chains with terminal sulfonate groups as nitrogen substituents has rendered these compounds more hydrophilic [109]. In addition, a balanced surface net charge of zero (zwitterionic) is desirable to avoid off-target accumulation, thus reducing background signal [110]. ZW800-1 is an example of a zwitterionic fluorophore with reduced binding to proteins compared to ICG, however the labile ether linkage on the meso carbon renders this compound unstable, which results in decreasing fluorescence signal over time [88]. To overcome this, a stable derivative with a carbon-carbon bond in the meso position, ZW800-1 Forte, was synthesised [111]. This derivative exhibits long-term stability, but it displays H-aggregation due to the distinct polarity and the rigidity of the meso carbon substituent [111]. IRDye® 800CW is the most widely employed cyanine derivative and it has been conjugated to a variety of targeting ligands in preclinical FLI and clinical FIGS [112-115]. The highly hydrophobic core is decorated with four negatively charged groups that confer a highly anionic surface charge [116]. Therefore, excretion is expected to occur via the renal route, but when targeting ligands are conjugated to this fluorophore, increased liver uptake and off-target accumulation has been observed, likely due to the interaction of this fluorophore with serum proteins [116]. It is evident that the physicochemical properties of the fluorophores play a key role in their *in vivo* behaviour, even when conjugated to large molecules such as antibodies, and should be balanced to obtain optimal results [87].

These are just a few examples of cyanine dyes under development for optical imaging, but the list of potential candidates is long (AF680 [117], BM104 [118, 119], AF750 [120, 121], S0456 [122, 123] or LS288 [124, 125]). Hence, part of the work of this thesis has focused on derivatives of the polymethines Cy5 and Cy7 and their potential as conjugatable fluorophores for targeted approaches.

1.5 Targeted fluorescent imaging approaches

The dyes described in the previous section have proven useful for imaging a wide variety of biological processes. However, their utility is often restricted by their lack of specificity, rendering them inefficient for FLI [95]. In this context, many different targeted approaches have been implemented to reduce undesired background signal and thus obtain better contrast [126-128].

Targeted approaches employ fluorophores, often referred to as "always-on" probes, covalently bound through a linker to a targeting ligand against a specific overexpressed target in the tumoral tissue or the tumour microenvironment (TME) [129]. The number of molecular targets (biomarkers) that can be exploited for disease interrogation has increased in the last decades [114, 130, 131]. And with this, the number of different targeting ligands has also risen including small molecules, peptides, antibodies (intact or fragments), functionalised nanoparticles, *etc*. [114, 122, 132, 133]. Fluorophores for stable labelling and long-term monitoring of these molecular ligands are also well developed, as explained earlier [76, 134]. The ideal conjugate needs to exhibit low toxicity, high photochemical stability and fast clearance. Hence, the design of targeted molecular contrast agents requires special attention not only with regard to the choice of targeting ligand, but also to the linker and to the fluorescent contrast agent selection. Several cases have been previously reported in which the choice of linker or fluorescent contrast agent affected the affinity of the targeting ligand for the molecular target of interest [123, 135].

Folate receptor alpha (FRα) is an example of a widely studied molecular target with both diagnostic [136] and therapeutic applications [137, 138]. FRα is overexpressed in several different types of tumours, including ovarian and lung adenocarcinomas, but has limited expression in healthy epithelial tissues [139, 140]. Folate is a vital vitamin for DNA synthesis and repair, thus playing an important role in rapid cell division and growth. The internalisation of folate after binding to the membrane-bound FRα has been exploited for drug delivery [141-143], as well as for contrast agents with imaging purposes [122, 144, 145].

However, most of these targeted approaches employ “always-on” contrast agents that contribute to background signal by off-target accumulation of unbound fluorescent contrast agent, which degrades the quality of the images and requires longer washout periods. To further increase the specificity of the signal, targeted strategies employing activatable fluorescent probes [146] could be implemented to provide increased tumour-to-background ratios (TBR) by reducing off-target fluorescence signals. The fluorescence of such probes is quenched until activation by tumour-specific enzymes [147] or by chemical reactions that occur once specifically internalised in the cells [148, 149]. CytoCy5S is an example of a quenched fluorescent contrast agent activated by NTR enzymatic reduction. NTR reduces the nitro groups of this cyanine derivative to hydroxylamine groups, thereby restoring its fluorescence and allowing sensitive investigation of NTR expression by fluorescence imaging [150].

These activatable probes represent a good choice for applications where high contrast is imperative, such as FIGS. Additionally, they offer potential applicability in intraoperative settings where washing procedures are not possible, i.e. probes topically applied for residual disease identification after tumour debulking or probes employed during endoscopic examinations [88, 151, 152].

1.6 Applications and clinical translatability of reporter genes and/or fluorescence imaging

1.6.1 Gene-directed enzyme prodrug therapy

GDEPT is a promising anti-tumour strategy that aims to reduce off-target toxicity and limit severe side effects by the combination of a prodrug and its activating enzyme [153]. In a first step, tumours are transduced to express a gene encoding the prodrug-activating enzyme. In a second step, a non-toxic prodrug, delivered systemically, is converted *in situ* into a cytotoxic metabolite by the expressed enzyme [154] (Figure 17). In some cases, the activated metabolites are able to diffuse to neighbouring cells (bystander effect) exerting their cytotoxic effect and thus increasing the killing potential of this approach [155, 156]. In this way, GDEPT achieves high

concentration of cytotoxic compounds locally, minimising systemic side effects associated with conventional cancer chemotherapy [157].

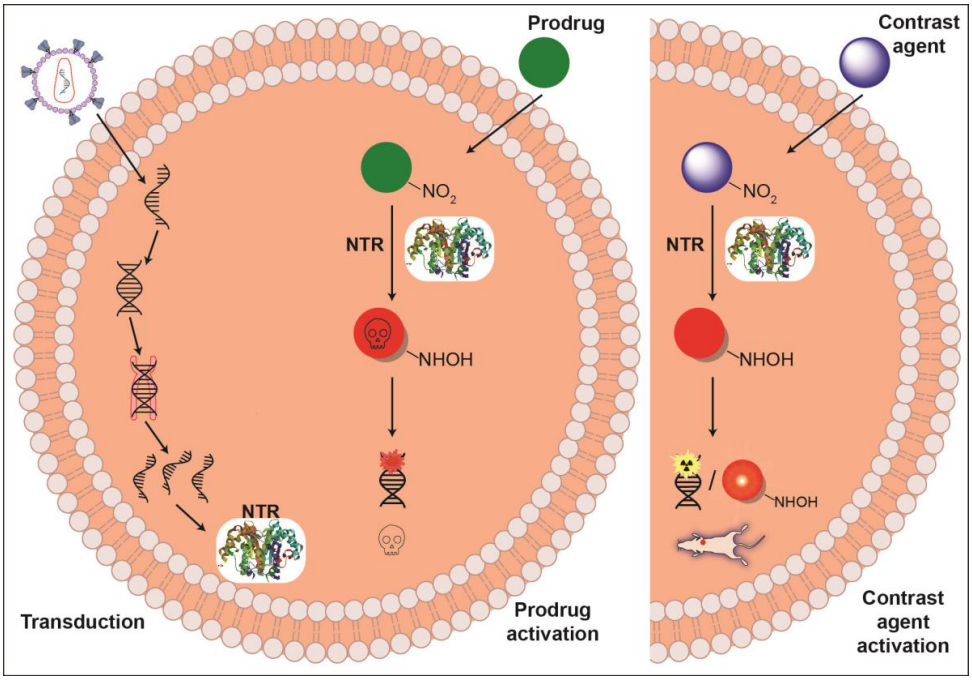

Figure 17: Schematic overview of the key steps in GDEPT. From left to right: Transduction of cells to express protein of interest, in this case NTR. Bioreductive activation of prodrug CB1954 by NTR. Reduction of contrast agents, radiotracers or fluorescent contrast agents, by NTR allows PET or FLI imaging.

The most extensively studied prodrug/enzyme pairs for GDEPT are ganciclovir (GCV)/herpes simplex virus-thymidine kinase (HSV-TK) [158] and 5-(aziridin-1-yl)-2,4-dinitrobenzamide (CB1954)/*E. coli* nitroreductase NfsB (NTR) [159]. HSV-TK phosphorylates GCV, allowing its incorporation into DNA and resulting in toxicity due to interference with the DNA synthesis. NTR reduces the nitroaromatic groups ($R\text{-}NO_2$), present in CB1954, into hydroxylamines (R-NHOH), converting it into an alkylating agent with cytotoxic activity [160, 161]. In addition, the activity of these enzymes can also be exploited with imaging purposes, i.e. to identify promising responder candidates before therapy and to monitor the drug efficacy post-treatment.

Radiolabeled probes, such as ^{18}F-FIAU (1-(2- deoxy-2-[^{18}F]-fluoro-1-D-arabinofuranoside)-5-iodouracil), ^{18}F-FHBG (9-[4-[^{18}F]-fluoro-3-

(hydroxymethyl)butyl]guanine) and GCV analogues are available for the assessment of HSV-TK activity. Thus, PET/CT imaging has been successfully applied preclinically to monitor transduction efficiency, tissue specificity and therapeutic effect [162, 163] and it was subsequently incorporated into phase I clinical trials to monitor transduction efficiency in healthy individuals and in cancer patients [164, 165].

NTR exhibits promising therapeutic potential by generating alkylating agents that target both dividing and quiescent cells indistinctly, a clear advantage compared to HSV-TK, which is only able to kill rapidly dividing cells. NTR activity has been successfully evaluated in preclinical settings using a NIR fluorescent dye, CytoCy5S [150] and a caged bioluminescent substrate, "NTR caged luciferin" (NCL) [166]. However, the lack of probes for NTR activity investigation by employing well-established clinical imaging modalities, such as PET/CT, has hampered the further progress of NTR-based GDEPT clinical trials [159]. But the last word is not yet spoken as Mowday and co-workers have recently demonstrated effective NTR PET imaging employing NfsA from *E. coli* in combination with the PET tracer ^{18}F-HX4 [167].

1.6.2 Fluorescence image-guided surgery (FIGS)

FLI has proven useful in a variety of preclinical studies, but translation to the clinic is hampered outside the intraoperative settings. This is due to different factors, mainly to the low depth of penetration of the light but also to the lack of FDA-approved NIR probes hindered by the lack of standardisation protocols, or the lack of adequate instrumentation [24]. However, promising examples on the clinical use of fluorescence imaging to aid surgeons delineate the surgical area of interest in real-time are available [114, 168-170].

FIGS aims for complete diseased tissue resection, while avoiding morbidity by preserving vital structures like nerves or blood vessels [90]. It relies on the fluorescence emitted by an exogenous fluorescent probe, either untargeted or targeted, after excitation by an appropriate light source [171]. This fluorescence-

based imaging technique provides real-time illumination of tumour burden allowing surgeons to resect margins [172] and small metastases that are difficult to identify with the naked eye. Other advantages are its safety, because light is non-destructive and non-ionising probes are employed to provide contrast, and its low cost compared to other techniques employed in the operating room (OR) such as CT or MRI. Moreover, this technique can easily be implemented in the OR, without compromising sterility or workflow, and allowing increased sensitivity compared to preoperative imaging modalities [21].

One critical aspect for the success of this technique is a high SBR. Targeting highly expressed molecular biomarkers with despisable expression in surrounding tissues can help to attain the desired high contrast. The use of targeted-activatable fluorophores is another promising approach that is being actively researched [88]. In addition, the last years have witnessed an increased interest in exploiting the NIR II window, were the spectral characteristics of tissues play no role in scattering, allowing even better contrast and deeper tissue penetration. Some promising examples include the localisation of minute tumour metastases in a murine model of ovarian cancer employing SWNT in the NIR II window [84] or the first-in-human multispectral approach exploiting simultaneously the NIR I and II windows with ICG, suggesting the potential of the latter to improve FIGS outcomes [173].

Despite the promising results obtained using FIGS in different clinical trials, unmet needs have hampered its extensive use in the clinic and most surgeries are still performed without real-time image-based assistance [174]. Vast efforts in chemistry and in preclinical imaging research are ongoing [121] to resolve these issues and to develop improved targeted contrast agents, with particular emphasis in NIR II agents, for optimal performance during intraoperative procedures [149]. Development of improved contrast agents and multispectral surgical image-based systems exploiting simultaneously the NIR I and II windows will facilitate progress of molecular characterisation of disease by means of imaging [175].

2. Aims of the study

2.1 Background and general aims

Nitroreductases are enzymes of bacterial origin capable of reducing nitro groups. This nitroreduction potential has been widely exploited in different biotechnology applications. Nitroreductase NfsB (NTR) from *E. coli* is an example of an oxygen-insensitive nitroreductase that has been relevant in biomedical research. The presence of nitro groups on some aromatic compounds, such as CytoCy5S, quenches the fluorescence of these compounds. NTR-catalysed reduction of the nitro groups to hydroxylamines or amines restores the fluorescence of these compounds allowing detection of the signal in optical imaging settings. In addition, non-toxic nitro-containing compounds (prodrugs), such as CB1954, can be converted to highly toxic compounds by NTR reduction, that restores the reactivity capacity of these compounds.

In this thesis, we aimed to develop fluorescent NTR substrates with improved physicochemical and optical properties for NTR fluorescence imaging in oncology settings. Furthermore, to improve the tumour contrast provided by ”always-on” fluorophores, we employed a targeted approach against an overexpressed biomarker such as folate receptor alpha (FRα) and studied and compared the impact of the physicochemical properties of five fluorophores on the *in vivo* behaviour of the same ligand. In addition, we assessed whether NTR nitroreduction of a hypoxia radionuclide (^{18}F-FMISO) could be exploited in more clinically amenable settings employing PET/CT imaging of NTR expression. The suitability of ^{18}F-FMISO for imaging transgene expression and prodrug treatment efficacy in an *in vivo* GDEPT setting was evaluated.

2.2 Specific aims

1. To define the physicochemical and optical properties of CytoCy5S **(Paper I)**

2. To identify the substrate with the best *in vitro* and *in vivo* characteristics for NTR interrogation in preclinical oncology animal models (**Paper I**)
3. To compare the imaging performance of five different fluorophores conjugated to a ligand targeting folate receptor alpha in an ovarian cancer model (**Paper II**)
4. To repurpose ^{18}F-FMISO for PET/CT imaging of NTR expression (**Paper III**)
5. To use the validated NTR PET/CT tracer to monitor the two main steps of an NTR gene-directed enzyme prodrug therapy (GDEPT) (**Paper III**)
6. To analyse the potential of CytoCy5S in a "two-hit strategy" exploiting NTR for activation and folate receptor alpha for targeting (**Appendix I**)

3. Methodological considerations

3.1 General synthetic overview

3.1.1 Synthesis of Fischer bases

The different Fischer bases employed in the synthesis of the four NTR substrates (**1** – **4** in **paper I**) and the NIR dyes **3**, **5** and **6** in **appendix I** were obtained through *N*-alkylation of 2,3,3-trimethyl-3*H*-indole, its 5-methoxy analogue or 1,1,2-trimethyl-1*H*-benzo[*e*]indole (Scheme 1).

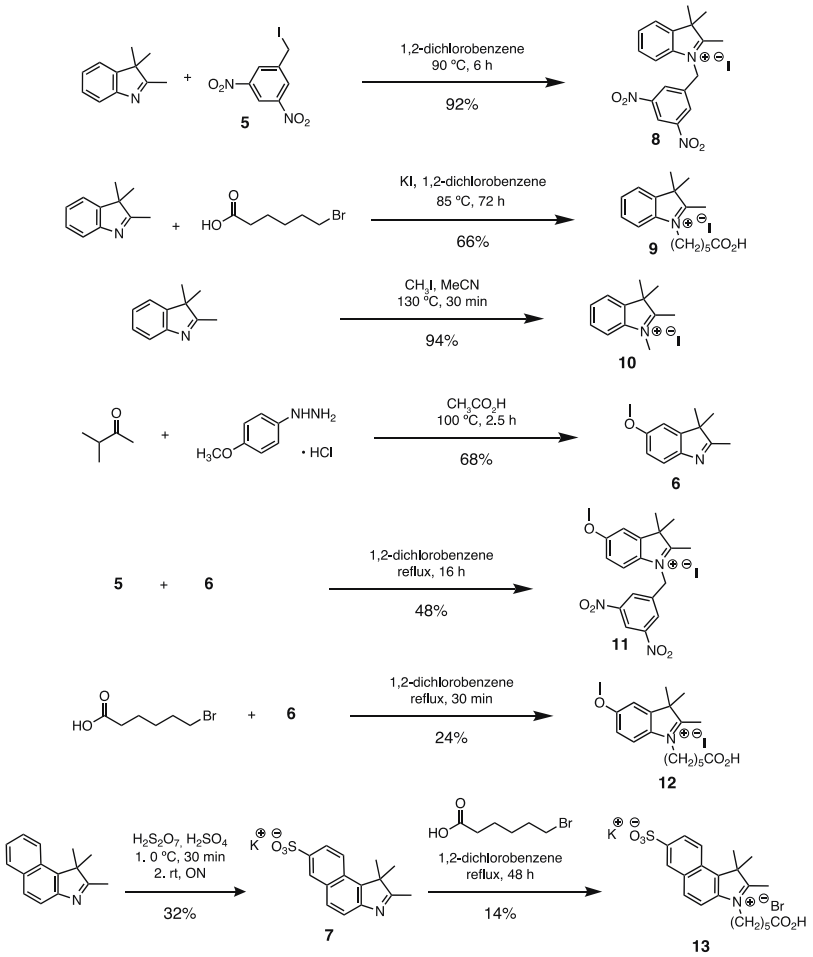

Scheme 1: Synthesis of Fischer bases **8** - **13** that have been employed in the synthesis of NTR substrates **1** – **4** and NIR dyes **3**, **5** and **6**.

Their reaction with the different halogenated starting materials (3,5-dinitrobenzyl iodide, 6-bromohexanoic acid or iodomethane) under the conditions described in Scheme 1 yielded the intermediates **8** – **13** (**paper I**) in yields that ranged from 14% to 94%

3.1.2 Condensation final compounds

Substrates **1** (**4** in **appendix I**), **3** and **4** in **paper I** and NIR dyes **16** in **paper II** and **3** in **appendix I** were successfully synthesised through a one-pot condensation of the various Fischer bases with either squaric acid, malonaldehyde bis(phenylimine) or the Vilsmeier-Haack reagent shown in Scheme 2.

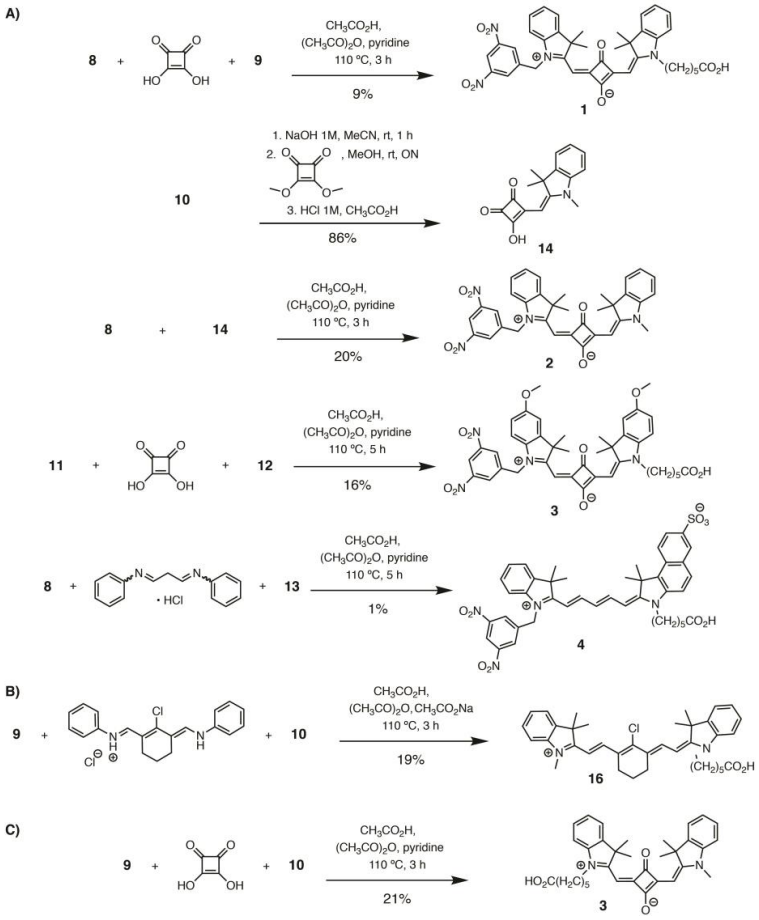

Scheme 2: Synthesis of A) NTR substrates **1** – **4** (**paper I**) and NIR dyes B) **16** (**paper II**) and C) **3** (**appendix I**).

Substrate **2** was obtained in a stepwise manner through synthesis of the mono-substituted methyl squaraine intermediate. Deprotection of the methyl ester under acidic conditions to give **14** and subsequent condensation of **14** and **8** gave **2**.

3.1.3 Condensation with squaric acid esters of Substrate 1 (Stepwise strategy)

Substrate **1** in **paper I** (**4** in **appendix I**) was also synthesised employing an alternative strategy that required the stepwise introduction of methylene bases (as previously described for substrate **2**). Methyl and ethyl squarate were employed as starting materials and they were reacted with the Fischer bases **8** and **9** under the different conditions depicted in Scheme 3.

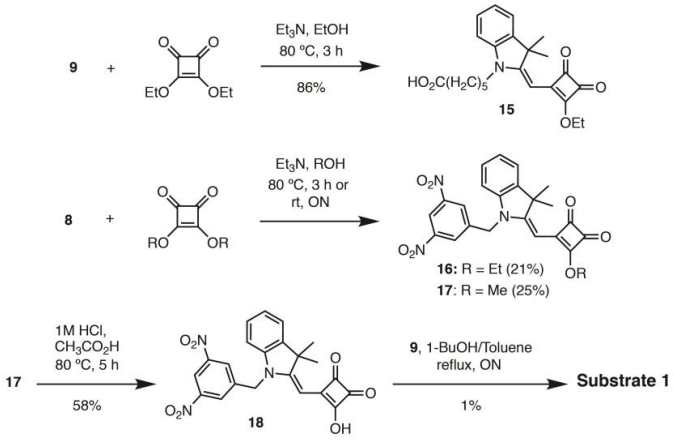

Scheme 3: Stepwise introduction of methylene bases [176-178]

3.1.4 Solid support synthetic approach for Substrate 1

A third synthetic approach was attempted to improve the yield of substrate **1** in **paper I** (**4** in **appendix I**). Fischer base **9** was immobilised on a 2-chlorotrytil chloride resin and reaction with **18** (Scheme 3) in the presence of carbodiimide (DIC) gave substrate **1** (Scheme 4).

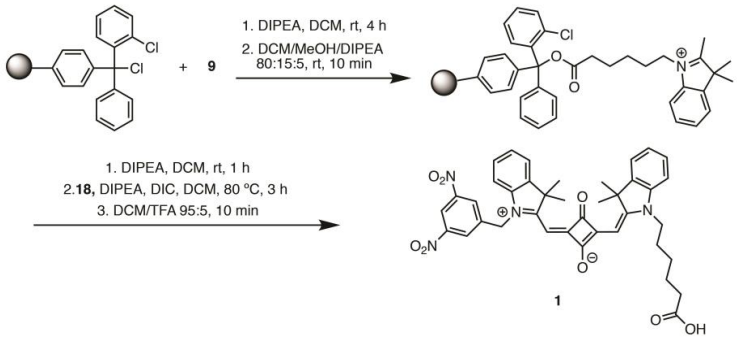

Scheme 4: Synthesis of substrate **1** using a solid supported approach.

3.1.5 Synthesis of targeting ligand

To obtain γ-ethylenediamine folate (EDAF, **7**), folic acid was converted to pteroic acid (**12**) in two steps. Ethylenediamine was protected with di-*tert*-butyl dicarbonate (Boc) to give *tert*-butyl (2-aminoethyl)carbamate (**6**) that was further reacted with Fmoc-Glu-OtBu followed by basic deprotection to yield **11**. **12** and **11** were reacted to give γ-ethylenediamine folate (**7**) after acidic deprotection and RP-HPLC purification.

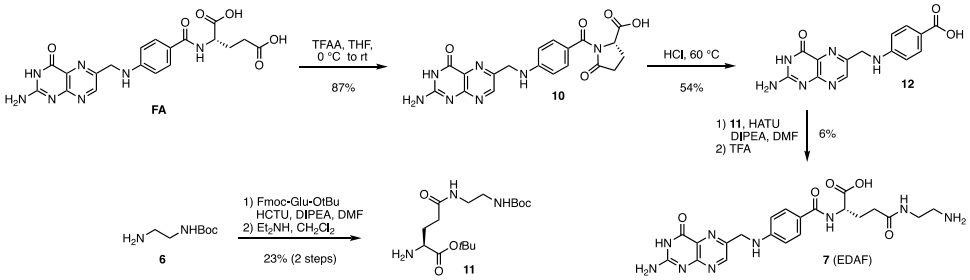

Scheme 5: Synthetic route through pteroic acid (**12**) and tert-butyl N^5-(2-((tert-butoxycarbonyl)amino)ethyl)-*L*-glutaminate (**11**) employed to obtain γ-ethylenediamine folate (EDAF, **7**). (Numbering from **paper II**)

3.1.6 Conjugation to targeting ligands

Conjugates **1** – **5** in **paper II** and **1** and **2** in **appendix I** were synthesised by common amide bond formation (Schemes 6 and 7, respectively). The NHS esters of the different fluorophores were reacted with the targeting ligand EDAF in dry DMSO at rt for 24 h (**1** – **5**) or for 6 h (**1** and **2**). All conjugates except **3** were formed in the presence of DIPEA as base. The synthesis of conjugate **3** required less sterically hindered bases and TEA was employed.

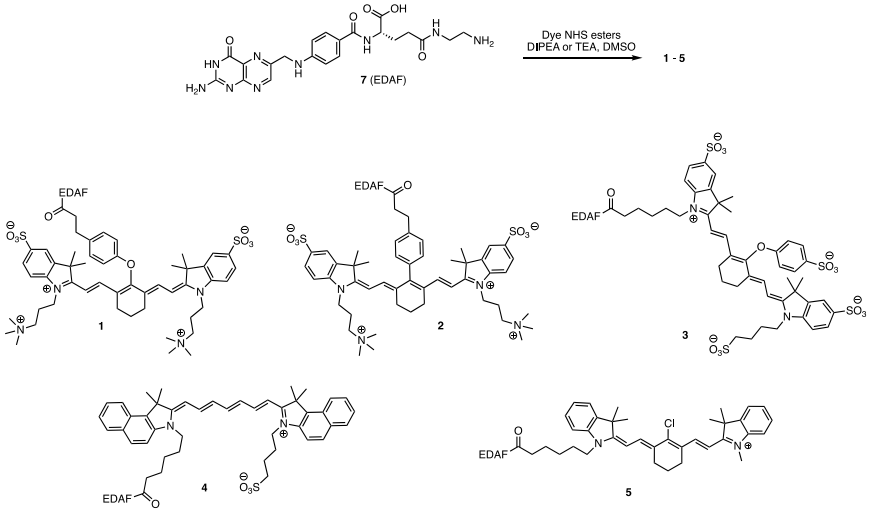

Scheme 6: Synthesis of EDAF-Cy7 conjugates **1** – **5** in **paper II**

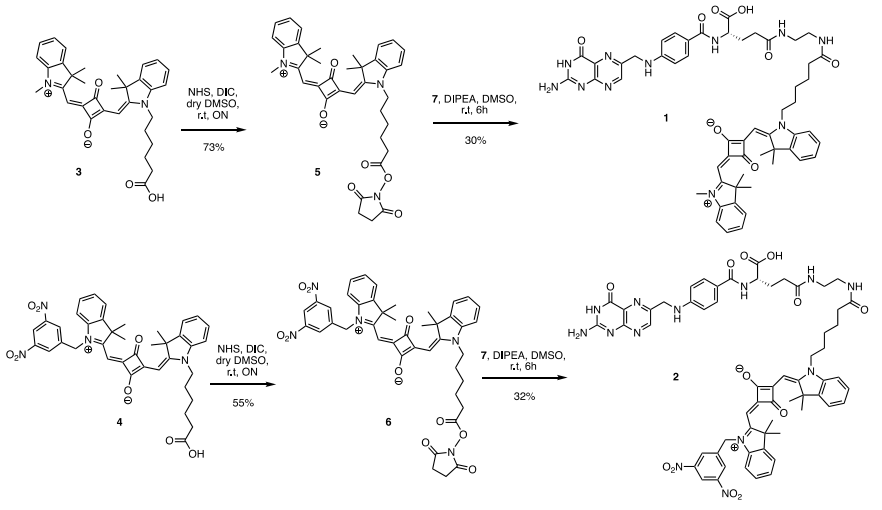

Scheme 7: Synthesis of EDAF-Cy5 conjugates **1** - **2** in **appendix I**

3.2 Purification methods

Most of the compounds synthesised required purification approaches prior to further reaction. Flash column chromatography with narrow particle range silica as stationary phase was employed for most of the intermediates. Mobile phase solvent composition and isocratic or gradient elutions were chosen based on the polarity properties of the different compounds.

Automated flash chromatography was employed for highly polar intermediates (sulfonate containing intermediates, **paper I**) whose elution required reversed-phase methods. 40 g octadecyl silane (C18) columns were employed in combination with water-based mobile phases in the presence of ion-pairing substances such as ammonium acetate ($CH_3CO_2NH_4$). This technique, which permits higher loading capacities than HPLC, was performed on a Puriflash XS 420 system (Interchim, Montlucon Cedex, France).

Final compounds aimed for biological testing were purified by high-performance liquid chromatography (HPLC) using C18 reversed-phase columns. The elution methods used mixtures of acetonitrile and water both containing 0.1% of either trifluoroacetic acid (TFA), formic acid (CH_3CO_2H) or 10 mM of ammonium acetate. The linear gradients employed are described in detail in the electronic supplementary materials for each compound (**Papers I** and **II**).

3.3 Characterisation techniques

Nuclear magnetic resonance (NMR) was employed to confirm the structure of the different compounds throughout the synthetic steps. 2D experiments including COSY, ROESY and NOESY were employed to unequivocally assign the protons in the final structures. This technique proved indispensable to discern the correct isomer of the sulfonate substrate (**paper I)** after purification based in the coupling constants *J* given in Hertz (Hz). Multiplicity of the signals reported as singlet (s), broad singlet

(bs), doublet (d), double doublet (dd), triplet (t) or multiplet (m). High-resolution mass spectra were recorded with an AccuTOF^{TM} mass spectrometer operated with an orthogonal electrospray ionization source (ESI), an orthogonal accelerated time of flight (TOF), single stage reflectron mass analyser and a dual micro channel plate (MCP) detector (**papers I, II and III**).

3.4 *In vitro* experiments

3.4.1 Enzymatic assay

The use of the nitroreductase NfsB (NTR) from *Escherichia coli* in the presence of β-NADH and β-NADPH allowed us to evaluate the suitability of four different compounds as substrates of this oxydoreductase (**paper I**). Once we proved that **1 - 4** were substrates of NTR, their kinetic profiles were studied by evaluation of the fluorescence emission intensity over time. Fluorescence intensity of the different substrates was analysed using a Tecan Spark® multimode microplate reader and it was plotted as the average of the triplicates ± standard deviation.

3.4.2 Cell culture

The human embryonic kidney HEK-293T cell line is one of the most commonly used cell lines for lentiviral vector production. This cell line stably expresses the large T-antigen (TAg) of simian virus 40 (SV40) that promotes plasmid-mediated gene expression during transient transfections [179]. These cells were used for lentiviral production for NTR-based gene therapy in **papers I** and **III**.

The human mammary carcinoma MDA-MB-231 cell line was employed for *in vitro* and *in vivo* studies in **papers I** and **III**. Two different variants, MDA-MB-231^{Luc+} referred to as NTR^{-} and MDA-MB-231$^{Luc+/GFP+NTR+}$ stably expressing NTR (NTR^{+}) were used.

Many non-small cell lung carcinoma (NSCLC) cell lines, including NCI-H460, present increased DT-diaphorase (oxidoreductase) activity, which is involved in the

bioreduction of nitro-containing compounds [180, 181] and it is known to present higher levels of hypoxia. The two variants of this cell line, NCI-H460 $^{Luc+}$ (NTR^{-}) and NCI-H460 $^{Luc+/GFP+NTR+}$ (NTR^{+}), were employed *in vitro* and *in vivo* in **paper III** to study the effect of higher levels of hypoxia in the retention of ^{18}F-FMISO.

The human ovarian adenocarcinoma Skov-3 cell line is commonly used in ovarian cancer models. Skov-3 was employed in **paper II** for comparative studies of five different folate conjugates due to its known folate receptor alpha (FRα) expression [182, 183]. Another human NSCLC cell line, A549, was employed as the negative control for FRα [184] and the human cervical carcinoma HeLa cell line was used as the positive control for FRα in the same study. OV-90, stably expressing GFP, was employed in **appendix I** to study the *in vivo* fate over time of **1** using confocal fluorescence microscopy.

Cell lines were maintained in DMEM (HEK293T, MDA-MB-231, Skov-3, A549 and HeLa) or in RPMI-1640 (NCI-H460, OV-90) media supplemented with 10% fetal bovine serum (FBS) and 1% L-glutamine. Cells were incubated in a humidified atmosphere at 37 °C and 5% CO_2. Media were supplemented with 1% penicillin/streptomycin after cells were sorted or virally transduced.

3.4.3 Viral transduction and gene expression assessment

For *in vitro* NTR transduction, retroviruses and lentiviruses have been used. Retroviral transductions of the cell lines employed in **paper III** have been described elsewhere [150].

For *in vivo* NTR transduction of subcutaneous tumours (**paper III**), lentiviruses were employed. Compared to retroviruses, lentiviruses are able to transduce cells in any step of their cycle offering higher transduction efficiencies. A more detailed description of the process can be found in the methods section of the corresponding **paper III**.

3.4.4 Flow cytometry

Flow cytometry allows simultaneous characterisation of cell size, granularity (optical properties) and protein expression (fluorescence emission) in a single cell basis [185]. In addition, the use of several fluorophores with distinct spectral properties can be exploited for simultaneous interrogation of different proteins of interest.

This technique was employed to assess the suitability of four in-house synthesised fluorophores to interrogate the levels of NTR expression in MDA-MB-231$^{Luc+/GFP+NTR+}$ cells (**Paper I**) and compared to MDA-MB-231^{Luc+}.

CytoCy5S was employed as the standard fluorophore for cytometric analysis of NTR expression in different cell lines after viral NTR transduction (**Papers I**, **II** and **III)**. Enrichment of NTR expressing cells before tumour implantation was performed based on the 5% brightest population by incubation with CytoCy5S (**Paper I**).

In **paper II** we investigated the expression of FRα in the ovarian carcinoma Skov-3. Pre-labelled antibodies and self-conjugated EDAF to commercial fluorophores were employed. HeLa was used as positive control showing the highest expression and A549 was employed as negative control to set the threshold of no expression. The FRα expression level of the different cell lines was quantified using calibration beads to measure the antibody-binding capacity (ABC) of each cell line.

3.4.5 Fluorescence confocal microscopy

Fluorescence microscopy allows the visualisation of general cell physiology traits and biological processes in living cells with the use of fluorophores. Better image resolution is achieved with confocal microscopy by acquiring only the light that comes from an equivalent point in the cell (confocal) [186].

Fluorescence confocal microscopy of live cells allowed us to study the uptake, fluorescence release and the intracellular fate of the four different substrates studied in **paper I** as well as the conjugates **1** and **2** from **appendix I**. Cells were kept at 37 °C and 5% CO_2 while images were acquired using a confocal Andor Dragonfly microscope (Oxford instruments).

3.5 *In vivo* experiments

3.5.1 Ethical approval

All applicable institutional and/or national guidelines for the care and use of animals were followed. Animal experiments were conducted according to The European Convention for the Protection of Vertebrates Used for Scientific Purposes and were approved by the Norwegian Food Safety Authority (FOTS ID no: 9059 and 14128).

3.5.2 Optical imaging

Bioluminescence

BLI was performed (**paper III**) to monitor metastatic progression in mice orthotopically xenografted with the mammary carcinoma cell line MDA-MB-231$^{Luc+/GFP+NTR+}$. Animals were intraperitoneally injected with D-Luciferin (Biosynth, Switzerland) at a dose of 150 mg/kg 10 minutes before imaging. BLI images were acquired weekly using an In-Vivo FX Pro molecular imaging system (Carestream Health Inc., NY, USA). During acquisition, mice were anesthetised with 1.5% isoflurane. Regions of interest (ROI) were manually drawn in the primary tumour location and in the axillary region were metastasis was observed and BLI signal was measured.

Fluorescence imaging

FLI is the main *in vivo* technique used in this thesis. It has been used in all three papers with distinct purposes. In **paper I**, FLI allowed us to evaluate the biological behaviour of four different NTR substrates in a subcutaneous MDA-MB-231 model, while in **paper II**, FLI was employed to compare the biological behaviour of five different NIR fluorescent probes (Cy7 range) conjugated through the same linker to a FRα targeting ligand. In both papers, the fluorophores or fluorescent conjugates in solution were intravenously injected and biodistribution studies at different time points and longitudinal FLI of xenografted tumours were performed. In **paper III**, CytoCy5S-FLI was used for monitoring disease progression, transgene expression and therapeutic response.

When working with the Cy5 fluorophores, animals were fed with low-autofluorescence rodent imaging food (Rodent imaging diet D1001; Research diets Inc., Brunswick, USA) from, at least, two weeks prior to experiments in an attempt to reduce fluorescence signal from the gastrointestinal tract. The fur was shaved to avoid autofluorescence. Animals anaesthetised and maintained with 1.5% isoflurane were imaged using an IVIS Spectrum imaging system (PerkinElmer Inc.) with the appropriate filter pairs ($\lambda_{ex}/\lambda_{em}$) for each investigated fluorophore. Analysis of the collected data was performed with the Living Imaging® software v4.5 (PerkinElmer Inc.).

Ex vivo FLI imaging was performed to further assess biodistribution of the different fluorophores and fluorescent conjugates with special attention to tumours and main organs involved in excretion.

In addition, in **paper II** FLI was exploited using an intraoperative image-guided system (FLARE^{TM}) to visualise the resected tumours and organs after intravenous injection of the five different studied conjugates. A comparative analysis of the fluorescent signals in the tumours and the main excretion organs was performed by manually drawn ROIs. The purpose was to identify the best conjugate candidates and the best imaging conditions to proceed further with more relevant orthotopic models.

3.5.3 Nuclear imaging

In **paper III** nuclear-based imaging was employed to monitor tumour progression, metastatic spreading, transgene expression and prodrug therapy response. ^{18}F-FMISO, a widely used hypoxia radiotracer, was repurposed for interrogation of *E. coli* nitroreductase (NfsB) expression. Mice were intravenously injected with ^{18}F-FMISO with activities ranging from 8 to 12 MBq. After 90 minutes of washout, mice were scanned using a dual mouse bed with integrated heating (37 °C) and anaesthesia (3 – 4% sevoflurane) over 30 minutes. PET scans were performed in an integrated nanoScan PC PET/CT (Mediso Ltd, Hungary) with whole-body CT scan prior to PET acquisition for anatomical information. Spatial resolution of 800 μm and

300 μm of the PET and CT detector systems, respectively. Further PET/CT imaging and reconstruction details can be found in the methodology section of **Paper III**.

3.6 *Ex vivo* analysis

Histopathology allows microscopic assessment of changes in tissue associated with pathologies like cancer, with e.g. haematoxylin and eosin (H&E) staining. In addition, immunohistochemistry allows the identification of different proteins (antibody-antigen interaction) expressed in the tissues that can be associated with distinct molecular processes in tumours.

For **papers II** and **III** tumours and organs of interest were cryopreserved (OCT at -80 °C) or/and fixed in a 4% paraformaldehyde solution at rt for 24 h. The tissues were later kept in PBS and protected from the light at 4 °C before paraffin embedding. Formalin fixed paraffin embedded (FFPE) tissue blocks were sectioned (5 μm) and stained with H&E for verification of malignancy (**Paper III**). To evaluate the expression of FRα (**Paper II**) and Hypoxia-inducible factor-1 (HIF-1; **Paper III**) sections were prepared for immunohistochemical staining of rabbit anti-human antibodies. Sections were incubated overnight with FRα (Cat# PA5-24186, clone SA170417DD, 1:2000, Invitrogen) and HIF-1 (Cat# ab51608, 1:300, Abcam) antibodies. Histopathology examinations and scoring of the samples was performed by experienced pathologists from the Department of Pathology, Haukeland University Hospital (Bergen) and the Department of Pathology, The Norwegian Radium Hospital, Oslo University Hospital.

4. Summary of results

4.1 Paper I

In this study, we set out to clarify an ongoing discrepancy regarding the structure and physicochemical properties of CytoCy5S, a NIR fluorescent NTR substrate, in order to establish which of the structures denoted as CytoCy5S in the literature is best suited for preclinical studies in oncology models. Four substrates (**1** – **4**) containing a 3,5-dinitrobenzyl moiety, which renders them non-fluorescent, were synthesised and analysed *in vitro* and *in vivo*. The introduction of the methoxy group in **3** and the sulfonate and cyanine scaffold in **4** resulted in a modest bathochromic shift in the spectral properties of these substrates compared to **1** and **2**. The kinetic assessment of NTR bioreduction of the four different substrates, revealed the delayed kinetics of substrate **2** and the low emission efficiency of substrates **3** and **4**. The suitability of the four substrates for intracellular interrogation of NTR expression was assessed by incubation of NTR^- and NTR^+ MDA-MB-231 cells under different conditions. The results evidenced the high contrast between cell lines obtained when using substrate **3** as well as the high dependence of this substrate on the concentration. Substrates **1** and **2** exhibited comparable performances and substrate **4** performed poorly. The biological behaviour of these substrates was further investigated in murine subcutaneous xenograft models. Despite the promising *in vitro* performance of substrate **3**, it did not prove as useful for discerning between NTR^- and NTR^+ tumours as substrates **1** or **2** did. Substrate **1** was found to be best suited for imaging of NTR, both *in vitro* and *in vivo*, with superior kinetics and lower background fluorescence from immediate surrounding tissues allowing a better delineation of tumours. In addition, this substrate presents a carboxylic functionality that can be further derivatised for biomarker interrogation.

4.2 Paper II

In this study, we aimed to compare the impact of five different NIR fluorophores on the biodistribution, specificity and contrast of conjugates targeting folate receptor alpha (FRα) using an ovarian cancer model. Skov-3 and A549 cell lines with intermediate and low FRα expression, respectively, were employed. Four commercially available and one in-house synthesised fluorophores, namely ZW800-1, ZW800-1 Forte, IRDye® 800CW, ICG and Cy7 derivative were conjugated to the folate ligand through an ethylenediamine linker to give conjugates **1** - **5**, respectively. The biodistribution of conjugates **1** – **5** was assessed *in vivo* by FLI, indicating preferential renal clearance for **1**, **2** and **3** and hepatobiliary clearance for **4** and **5**. Tumour accumulation was observed for all conjugates except **4**. However, the high off-target fluorescence obtained for **3** and the low fluorescence intensity of **5**, together with its probable albumin-mediated accumulation in tumours by the EPR effect, limited their applicability. Conjugate **2** showed an intense fluorescence signal in tumours and it was the only conjugate that reported significant fluorescence differences between Skov-3 and A549 ($p < 0.05$). Our results confirmed the high impact of the fluorophore on the biodistribution of the conjugates to excretory organs and tumours and the potential of **2** as fluorophore for targeted strategies providing specific fluorescence signal.

4.3 Paper III

In this study, we have investigated the repurposing of ^{18}F-FMISO as a companion diagnostic tool for NTR-based gene-directed enzyme prodrug therapy (GDEPT). To validate the suitability of ^{18}F-FMISO PET/CT to image NTR expression, a subcutaneous mammary carcinoma (MDA-MB-231) xenograft model constitutively expressing NTR was studied. We demonstrated that ^{18}F-FMISO PET/CT imaging is sensitive for detection of NTR with significantly higher contrast between NTR^+ and NTR^- xenografts from week four after implantation ($p < 0.0001$). We next evaluated

the sensitivity of this technique to detect NTR^+ small metastatic lesions in an orthotopic model. We proved that ^{18}F-FMISO PET/CT imaging allows visualisation of nodal metastatic tumours, with significantly higher contrast between healthy tissue and metastatic nodes from week ten after implantation ($p < 0.05$). Additional metastatic lesions in distal organs such as liver and lungs were observed in the PET/CT images and confirmed *ex vivo* by histological examination. Lastly, the suitability of ^{18}F-FMISO PET/CT imaging was challenged in a GDEPT setting. Subcutaneous xenografts of MDA-MB-231 NTR^- were transduced by intratumoral injection of NTR lentiviral particles. We demonstrated that ^{18}F-FMISO PET/CT imaging allowed for detection of NTR expression with significantly higher contrast between *in vivo* NTR transduced xenografts and NTR^- xenografts from week four after *in vivo* NTR transduction ($p < 0.05$). NTR transduced xenografts, NTR^+ and NTR^- xenografts were treated with the prodrug CB1954 and response to treatment was monitored by ^{18}F-FMISO PET/CT imaging. We demonstrated that ^{18}F-FMISO PET/CT imaging allowed the monitoring of treatment efficacy even when the response was limited, as is the case in the *in vivo* NTR transduced xenografts. Post-treatment ^{18}F-FMISO PET/CT imaging of *in vivo* transduced xenografts demonstrated a significant decrease in contrast compared to pre-treatment ($p < 0.05$). This decrease in contrast was also confirmed for the NTR^+ xenografts with higher significance both at day 3 ($p < 0.001$) and 17 ($p < 0.0001$) after treatment. This was accompanied by a significant tumour volume decrease of NTR^+ compared to NTR^- xenografts ($p < 0.0001$). These preclinical studies confirm ^{18}F-FMISO NTR PET/CT as a readily available methodology for clinical application in NTR-based GEDPT.

5. General discussion

Molecular imaging (MI) is fundamental in clinical settings for diagnosis, treatment selection, intraoperative guidance and treatment efficacy evaluation. This field has progressed rapidly in recent years, driven by the need for sensitive diagnostic tools and as a tool to monitor the efficacy of new cancer treatments, including gene-based therapies [20]. MI provides fundamental information on the *in vivo* behaviour of new drugs and contrast agents, simultaneously allowing assessment and visualisation of target expression and plays a key role in the early stages of drug discovery and development [16, 17]. The work of this thesis has focused on the contrast agents of two main MI methodologies, namely optical imaging (mainly fluorescence imaging (FLI) for longitudinal imaging (**Papers I – III**) and fluorescence image-guided surgery (FIGS) (**Paper II**)) and nuclear-based PET/CT imaging (**Paper III**).

MI in combination with reporter genes allows *in vivo* monitoring of enzyme expression and follow-up of the success of gene-based therapies, where the suicide gene also acts as reporter gene (theranostic). In this thesis, nitroreductase NfsB (NTR) from *E. coli* has been concurrently employed as a reporter gene (**Papers I** and **III**) and suicide gene (**Paper III**). NTR is an oxygen-insensitive enzyme capable of reducing nitro groups to their corresponding hydroxylamines or amines, permitting the conversion of prodrugs into highly toxic metabolites (CB1954 in **paper III**) and the activation or retention of contrast agents (CytoCy5S and ^{18}F-FMISO, respectively, in **papers I** and **III**). Our group has previously demonstrated the applicability of NTR in combination with CytoCy5S, a quenched NIR dye substrate of NTR, for imaging of cancer cells dissemination in an orthotopic murine model [150]. In addition, exploiting the NTR/CytoCy5S imaging platform has allowed the non-invasive monitoring of the therapeutic efficacy of prodrugs such as metronidazole and CB1954 in gene enzyme directed prodrug therapy (GDEPT) settings [150, 187].

In the context of this thesis work, the use of MI and different contrast agents for tumour detection and evaluation of therapeutic efficacy will be discussed in detail and compared with relevant literature.

5.1 Fluorescent probes and their physicochemical properties, a double edged sword

It is well accepted that exploiting the NIR region of the spectrum (650 – 1700 nm), where light scattering and background fluorescence are reduced and the penetration depth of light increases, is advantageous for acquiring fluorescent images with higher contrast [90]. To achieve the most out of this privileged region of the electromagnetic spectrum, novel fluorophores with appropriate spectral properties, high molecular brightness (ε x ϕ), large Stokes shifts, hydrophilicity, photochemical stability which are also safe to use are required [89, 188, 189]. Although the desired properties are clear, achieving all of them in a single molecule is a challenge that has not yet been solved.

Cyanine-based fluorophores, with high molar absorption coefficients (ε) in the NIR, are the most widely employed dyes for NIR-I bioimaging in the medical field [88] and their use for imaging in the NIR-II region (1000 - 1700 nm) is being actively investigated [190]. Cyanine-based dyes have been the main focus of this thesis (**Papers I** – **III**) and will be used to illustrate the importance of finding common ground in terms of their physicochemical properties.

Fluorophores with large Stokes shifts and emission at longer wavelengths provide better resolution and brighter images. However, the shift from Cy5 to Cy7 will have a detrimental effect on quantum yields (ϕ) caused by the loss of energy through non-radiative relaxation processes, which are enhanced at lower energies (longer wavelengths) [191, 192]. To mitigate this trade-off, structural elements that impart rigidity to the heptamethine scaffold, such as the meso cyclohexyl (conjugates **1**, **2**, **3** and **5** in **paper II**, dashed bonds in figure 18A), have been incorporated, thereby improving photostability and quantum yield [193]. Alternative strategies include the

substitution of indoline by indolizine groups in Cy5 scaffolds (Figure 18B & C). Despite being based on pentamethine chains, these compounds exhibit bathochromic shifts with respect to Cy7 dyes such as ICG and enhanced molecular brightness compared to their indole counterparts [194]. However, these cyanine derivatives (C_5 and $PhIn_2SQ$) were poorly soluble in water, a major limitation for their use in biological systems. To circumvent this, two sulfonate groups were appended to these dyes in positions where the substituents did not have a strong impact on conjugation and, therefore, on the optical properties, achieving dyes (SO_3C_5 and SO_3SQ) with enhanced hydrophilicity and stability in water with comparable spectral properties to their lipophilic counterparts [195].

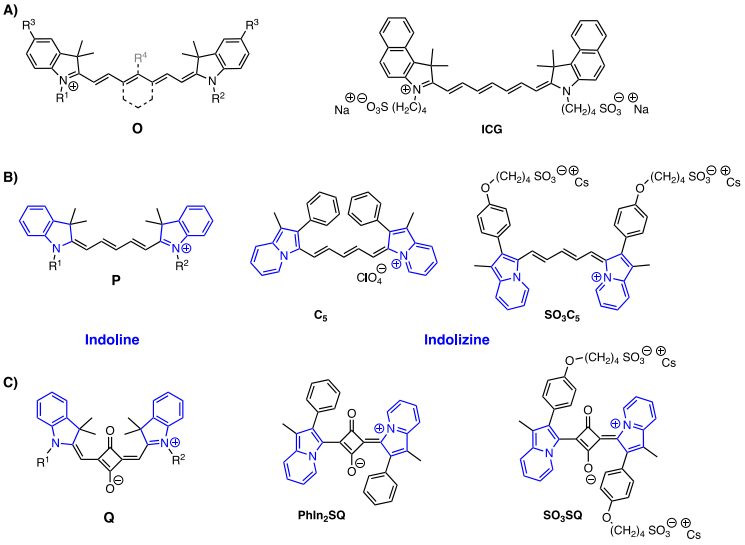

Figure 18: Overview of different cyanine/squaraine-based fluorophores with indoline and indolizine functionalities highlighted in blue. A) General structure of heptamethine dye with cyclohexyl functionality in dashed bonds (O) and ICG structure, λ_{em} = 835 nm; B) Cyanine-based dyes including indoline (P) and indolizine derivatives (C_5, λ_{em} = 852 nm and SO_3C_5); C) Squaraine-based dyes including indoline (Q) and indolizine derivatives ($PhIn_2SQ$ and SO_3SQ). Emission wavelengths reported in DMSO [194,195]

The use of sulfonate groups is a common approach to compensate for the high hydrophobicity of the cyanine scaffold [188]. However, the introduction of several negative charges has proved to be counterproductive, as was found to be the case with IRDye® 800CW (conjugate **3** in **paper II**), which displayed off-target fluorescence signals that reduced the contrast of the image in addition to suboptimal biodistribution [196]. Furthermore, the presence of a single sulfonate on substrate **4** (**paper I**) did not substantially improve water solubility but rather hampered cell penetration, limiting its usefulness.

To increase hydrophilicity while avoiding some of these constraints, different strategies have been evaluated including PEGylation of fluorophores and their corresponding conjugates [197-199] or encapsulation formulations using nanoparticles [200] or micelles [201]. These strategies have the trade-off of creating larger molecules with slower excretion rates, requiring delayed imaging time points. However, this feature is advantageous to obtain longer blood circulation times and enhanced tumour uptake by the EPR effect [202]. Another approach has been the synthesis of hydrophilic zwitterionic dyes (conjugates **1** and **2** in **paper II**). These compounds contain two sulfonates but are designed to have a balanced net charge of zero through the introduction of trimethylammonium substituents. Such zwitterionic dyes exhibit remarkable water solubility and reduced non-specific binding to proteins, resulting exclusively in renal clearance [110]. However, ZW800-1 (conjugate **1**) contains a labile ether linkage on the meso position (functionality also present in conjugate **3**) that renders this compound unstable towards nucleophilic attack with a decreasing fluorescence signal over time [203]. To overcome this, ZW800-1 Forte (conjugate **2**) was designed with a C-C bond substituting the ether group and long-term stability was achieved [111]. However, due to the increased rigidity of this substituent, self-aggregation (H-aggregates) was observed [111], a common problem for such structures [204, 205]. An alternative zwitterionic cyanine-based dye with improved stability and pharmacokinetic properties was later developed through shielding of the linear hydrophobic Cy7 scaffold by the introduction of two triethylenglycol chains [196]. These substituents increased the

photostability of the dye and prevented aggregation without limiting derivatisation with targeting ligands.

5.2 NTR-activatable cyanine-based fluorophores

Despite being at the limit of NIR spectral properties, Cy5-based dyes have found application in imaging of biological systems, including imaging of nitroreductases [206, 207]. In addition to the applications described above for the NTR/CytoCy5S imaging platform, it has also been employed in development studies to analyse differentiation and interaction of different cell types [208]. Moreover, it has proven useful for *in vivo* imaging of different bacterial strains and bacterial colonisation of tumours. The latter feature, has been suggested as a potential gene delivery method for gene therapy in cancer [209]. However, the structure or analytical characterisation of CytoCy5S is not included in any of the published papers and discrepancies were found regarding both the physicochemical and optical characteristics of this Cy5-based dye.

In an attempt to clarify these discrepancies and highlight the worryingly high number of biology papers reporting results of uncharacterised material, the unsymmetrical substrates **1** – **4** (**paper I** and depicted in Figure 19A) were synthesised, purified and chemically characterised, a key step for robust and reproducible inter- and intra-laboratory results. In general, indoline-containing Fischer bases were easily obtained in modest to good yields. However, the sulfonate group required for substrate **4** posed a challenge, as several isomers were formed in the sulfonation step and separation of these was unsuccessful using conventional purification methods.

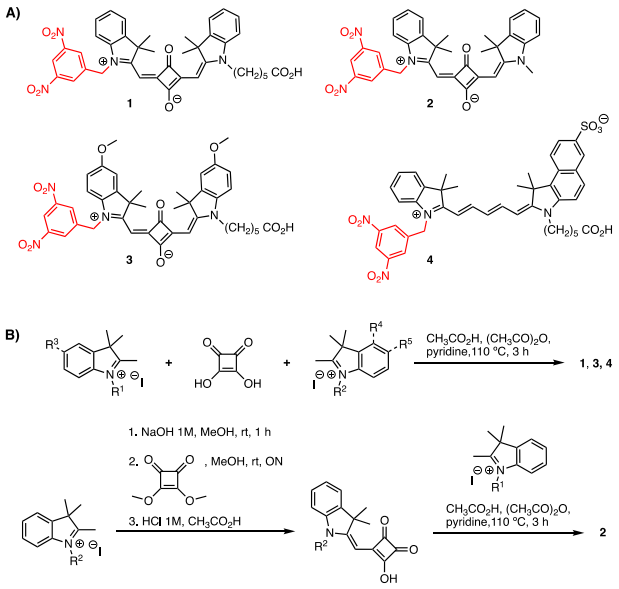

Figure 19: A) Chemical structures of substrates **1** to **4** employed in **paper I** with the 3,5-dinitrobenzyl moiety that quenches their fluorescence highlighted in red; B) One-pot synthetic route to obtain substrates **1**, **3** and **4** and stepwise route to **2** where R^1 corresponds to the N-methyl substituted Fischer base.

The final substrates **1** - **4** (Figure 19A) were prepared by condensation reactions via one-pot or stepwise approaches with yields that ranged from 1 - 16% due to the formation of symmetric by-products (Figure 19B). A stepwise strategy was required for substrate **2**, since the one-pot approach only produced the *N*-methylated by-product, probably due to the higher reactivity of this Fischer base. In addition, the synthetic reproducibility of substrate **4** proved to be limited. For the sake of proper comparison, substrate **4** from the same batch was used throughout the different experiments to avoid dye-based variability.

Substrates **1**, **2** and **3** are based on a squaraine scaffold, which in general imparts rigidity, increases polarity and photostability and reduces quantum yields [210, 211]. Substrate **4** is a cyanine-based dye and therefore longer absorption and emission wavelengths and better quantum yields are expected. However, it was not possible to directly compare the quantum yields of the different substrates, hereby limiting the

comparison of the brightness of the dyes. Despite this limitation, the data obtained from the emission spectra in comparison to the absorbance and excitation spectra suggest that substrates **3** and **4** exhibit limited brightness, possibly due to non-radiative decay. Most examples of NTR-activatable substrates in the literature [206, 212, 213] (only those with NIR spectral characteristics have been considered) correspond to fluorophores substituted with a *p*-nitrobenzyl moiety as a caging group (depicted in purple in figure 20), rendering the caged fluorophore silent. Upon NTR-mediated reduction, which results in a rearrangement-elimination reaction, the parent fluorophore is released and fluorescence is restored as illustrated in Figure 20.

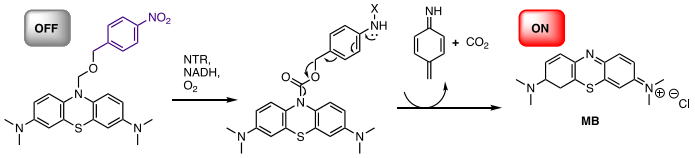

Figure 20: Example of the NTR-mediated uncaging mechanism of p-nitrobenzyl (depicted in purple) and release of the parent fluorophore, methylene blue (MB), with restoration of the fluorescence [212].

In our case, the quite unique 3,5-dinitrobenzyl moiety (depicted in red in Figure 19A) for NTR-mediated activation renders the substrates non-fluorescent due to a photoinduced electron transfer (PeT) process. Reduction of the nitro groups into hydroxylamines by NTR results in an increase in the energy of the lowest unoccupied molecular orbital (LUMO) of the acceptor, which hampers the quenching mechanism and results in fluorescent properties [214, 215].

Our results demonstrate the large impact that small modifications in dye structure have on the physicochemical and optical properties of the dyes and will help scientists to make an informed decision on the optimal fluorophore for their work. They also highlight the necessity for stricter reporting requirements of the chemical characterisation of compounds used in biomedical research, both for research groups and commercial suppliers.

5.3 Stability, sensitivity and specificity: considerations in the design of fluorescent conjugates towards the clinic

To avoid off-target fluorescence, which has a detrimental impact on contrast, in addition to activatable fluorophores, the use of fluorophores in targeted approaches is preferred. The properties of the fluorophores used should be optimised as described in section 5.1 for increased sensitivity [216]. To obtain highly specific signals, the conjugates should exhibit high receptor binding affinity leading to increased retention in the tumour and rapid clearance from off-target tissues [129]. Currently, a myriad of tumour-specific antibodies are approved for clinical use and their labelling with NIR cyanine-based fluorophores is a widely exploited approach for FIGS [88, 217]. However, the lack of control and consensus over labelling ratios makes it difficult to reproduce the results due to the different conjugates' composition after each conjugation [218, 219]. Therefore, small molecules with a single reactive site are preferred, as they also overcome the slow *in vivo* kinetics of antibodies, allowing faster imaging time points after conjugate administration. However, as for antibodies, the *in vivo* behaviour and physicochemical properties of these small molecules will be greatly influenced by the choice of fluorophore [107]. In **paper II** we aimed to compare how the physicochemical properties of five commonly used NIR fluorophores affected the *in vivo* performance of a folate receptor alpha (FRα) targeting ligand.

FRα is a well-known molecular target that has shown promising results when employed for MI as well as when used as a therapeutic target [136-138]. In fact, a phase III clinical trial of a folate-targeting small molecule labelled with a NIR fluorophore (OTL38, Figure 21A) for intra-operative imaging in ovarian cancer has recently been completed and results are awaited (NCT03180307). Hence, the folate ligand was conjugated though an ethylenediamine linker (Figure 21C) (same as for EC17, Figure 21B [220]) to five different NIR fluorophores and their *in vitro* and *in vivo* behaviour was compared (conjugates **1** – **5**, **paper II**).

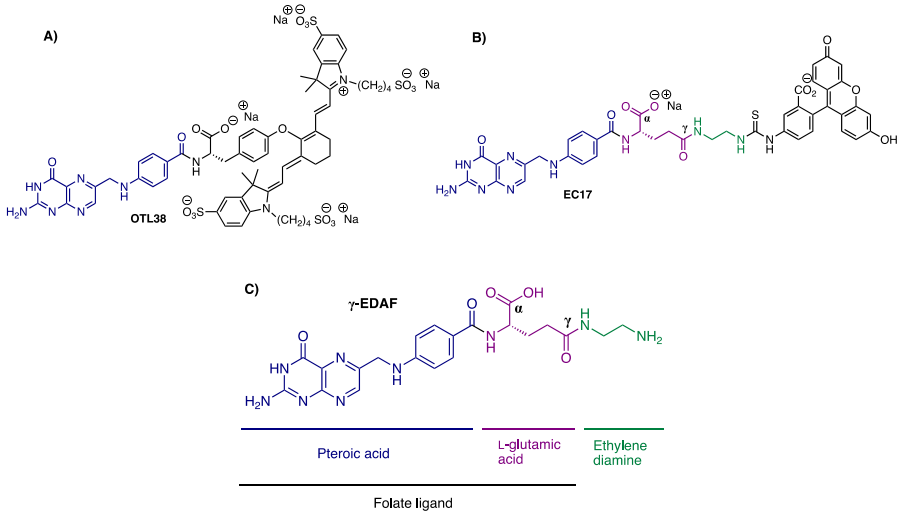

Figure 21: A) OTL38 is a folate analogue ligand conjugated to a heptamethine dye (S0456); B) EC17 is a γ-folate-fluorescein isothiocyanate (FITC) conjugate; C) Chemical structure of the folate ligand composed of pteroic acid (blue) and L-glutamic acid (purple) with the linker ethylenediamine (green) in the γ-carboxylic acid employed in **paper II**.

During the literature research for **paper II**, several references were found claiming attachment to folic acid via so-called γ-isomers (Figure 21A), while the chemistry described to obtain the conjugate proved to be inefficient for the synthesis of the desired regioisomer, resulting in mixtures of γ- and α- isomers [221-223]. This issue was also addressed by Figliola *et al.* [224]. The use of isomeric mixtures could pose a major problem for *in vivo* use, as the binding affinity to the target could be compromised, altering the reproducibility of the results, especially when the ratio of isomers is unknown. Although Bettio *et al.* reported that these isomers exhibited FRα-binding affinities in the same range [225], another study with a mixture of γ- and α- isomers of different conjugates showed differences in their biodistribution [226]. Therefore, to avoid variabilities caused by uncontrolled regioisomer ratios, the ideal approach is to synthesise isomerically pure compounds. To this end, different synthetic routes to obtain the pure γ-isomer were approached for **paper II** and the reaction of pteroic acid (blue in Figure 21C) with the protected glutamic acid (purple in Figure 21C) was found to be the most effective, as also described by Figliola *et al.* [224].

In the stepwise strategy, the carboxylic acid side chain of glutamic acid provides a convenient handle for conjugation of the probe via various linkers. In addition, it has been demonstrated that the glutamic part of the folate conjugate does not play a critical role in the FRα-binding affinity [227], as also demonstrated by the OTL38 structure (Figure 21A). This compound contains a tyrosine residue instead of the glutamic acid, in order to avoid by-product formation by R-NH_2 nucleophilic attack when the ligand is reacted with fluorophores containing an ether linkage in the meso position [228]. However, small variations in the structure of the folate conjugates have been shown to have a major impact on the optical properties and biological behaviour [123]. In our case, the use of the lipophilic fluorophores for conjugates **4** and **5** (Figure 22) compromised the targeting affinity of the conjugates, resulting in no tumour accumulation for **4** and the EPR effect-mediated accumulation for **5** after, most probably, fluorophore-mediated binding to albumin [229].

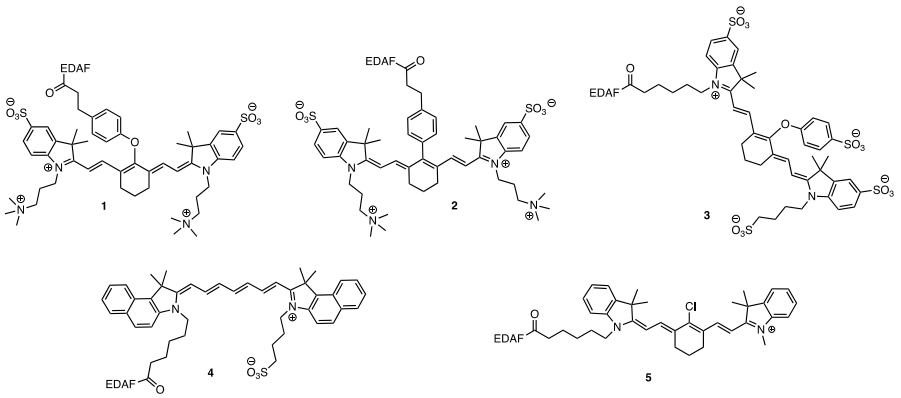

Figure 22: Chemical structures of conjugates **1** – **5** with the folate ligand and the linker part showed in Figure 21A abbreviated as EDAF. Conjugates **1** – **5** are based on ZW800-1, ZW800-1 Forte, IRDye® 800CW, ICG and an in house synthesised Cy7 derivative, respectively.

Due to the misplacement of one analytical HPLC trace, conjugates **1** – **5** were re-analysed six months after finalising the project. To our surprise, we found that conjugates formed by hydrophilic fluorophores (**1**, **2** and **3**) did not exhibit the same high purity as when they were analysed prior to use. An additional peak corresponding to a polar compound eluting at early retention times which absorbs both at 220 and at around 750 nm was observed for conjugates **1 - 3**. This finding led

us to initiate a study on the stability of the conjugates over time and this work is currently in progress. In addition, it was observed that one of the combined fractions for conjugate **1** exhibits a small shoulder in the HPLC trace, indicating the presence of free dye, as confirmed by the MS spectrum. Our study highlights the need for quality control and stability studies prior, during and after the imaging experiment to guarantee reproducible results from fluorophores and fluorescent conjugates.

5.4 NTR beyond preclinical research

Gene-based therapies, including *in vivo* delivery of viral vectors or genetically engineered T-cells and haemotopoietic stem cells, are applied to treat a myriad of inherited and acquired conditions and have become a promising therapeutic strategy [230]. In turn, the development of genome editing technologies, such as CRISPR-Cas9 [231], which awarded Charpentier and Doudna, two female biochemists the Nobel Prize in Chemistry in 2020, allows for precise genome modifications through the addition, ablation or correction of genes *ex vivo* or *in vivo*, and has revolutionised the field of gene therapy [232].

Suicide gene therapies, which aim to reduce the toxicity of cancer treatment by specifically activating prodrugs in cancer cells, have been investigated for several decades and there is resurgent interest in their use [167, 233-235]. Despite their promising potential and success in preclinical studies [155], their clinical application in cancer patients has not been fully realised [236]. There are several reasons for this, such as the choice of vector, suicide gene, prodrug or their combination thereof [237]. Despite this, I believe that the lack of appropriate molecular imaging methodologies to monitor transgene expression, particularly in the case of NTR, is a major limitation [238].

As stated earlier, our group has previously demonstrated the feasibility of using CytoCy5S as a fluorescent NTR reporter in a preclinical model of GDEPT [150]. Despite the promising results exhibited, its translatability to clinical gene therapies is hampered due to the main drawback of FLI, namely low tissue penetrance of light,

and clinically relevant methodologies such as PET/CT are preferred. Since there are no clinical radiopharmaceuticals currently available to image NTR, our aim in **paper III** was to demonstrate that, due to the similar mechanistic reduction characteristics between oxygen-sensitive (hypoxia) and oxygen-insensitive nitroreductases (NTR), the hypoxia radiopharmaceutical ^{18}F-FMISO could be repurposed to monitor the two steps of an NTR-based GDEPT.

To do so, we employed NfsB from *E. coli* (NTR) in combination with CB1954 as this is the most extensively investigated enzyme/prodrug combination in NTR-based GDEPT strategies. Despite some limitations, we have demonstrated in **paper III** that the hypoxia tracer ^{18}F-FMISO is useful to monitor NTR transgene expression after *in vivo* transduction and to evaluate prodrug treatment efficacy in an *in vivo* GDEPT setting. In parallel, Mowday *et al.* demonstrated the potential use of ^{18}F-HX4 to detect NfsA NTR expression in two cell models engineered for NfsA overexpression. However, I believe that the use of ^{18}F-FMISO, extensively used in clinical hypoxia imaging, compared to ^{18}F-HX4, which is in the early stages of clinical development [239], would accelerate the approval for repurposed applications, making it a valuable companion diagnostic for clinical NTR-based GDEPT.

In addition to NTR, other suicide genes have been investigated for their utility to treat different tumour types including HSV/TK [164], cytosine deaminase (CD) [240], purine nucleoside phosphorylase (PNP) [241] or carboxylesterases (CE) [242]. However, HSV/TK is the only one with a demonstrated clinically compatible imaging modality using either ^{18}F-FHBG or ^{124}I-FIAU. Furthermore, this imaging strategy has also been employed clinically for cell-based therapy imaging in glioma patients [243] emphasising the need for further development of MI to aid the improvement and rapid clinical translatability of these immunotherapies [244].

Cell therapies, in particular immune cell therapies, have flourished in recent decades and their clinical benefit has already been demonstrated in various diseases [15]. However, despite promising results, for example in the treatment of B-cell haematological diseases [245], side effects, such as cytokine release syndrome in

chimeric antigen receptor (CAR) T-cell therapies, and the lack of appropriate non-invasive clinical imaging techniques to follow the distribution of the engineered cells have hindered their wider application [246-248]. To avoid or modulate the side effects, safety strategies involving suicide genes have been envisaged. In a similar fashion to what has been proposed with the suicide genes HSV-TK [249] or caspase 9 [250], NTR could be inserted as a suicide gene switch in CAR T-cells. When required, dosing of the prodrug CB1954 would eliminate these NTR-expressing cells with remission of side effects. However, this approach is not a one-size-fits-all remedy and in a recent study, elevated cytotoxicity and gene expression silencing was reported when human induced pluripotent stem cells (iPSCs) expressing HSV/TK were employed as a safety switch [251]. This highlights the necessity for a plethora of suicide genes for distinct uses in cell therapies.

The advantage of NTR over other suicide genes is that its applicability would not be limited to its activity as a suicide gene, but could concurrently be exploited as a multimodal (FLI and PET/CT) imaging reporter gene. During the *in vitro* stages of CAR T-cell engineering, CytoCy5S activation by NTR could be leveraged for enrichment of fully functional cells by flow sorting or as a reporter of enzyme expression assessed by fluorescence microscopy, an advantage over other suicide genes that do not posses a specific NIR fluorescent substrate. In addition, the fate and expansion of NTR-engineered CAR T-cells after infusion could be tracked *in vivo* by PET/CT imaging using ^{18}F-FMISO, as has already been demonstrated for HSV/TK-engineered CAR T-cells using ^{18}F-FHBG in glioma patients [243]. This approach is particularly useful when CAR T-cells are used to treat solid tumours, since it would allow visualisation of T-cell trafficking, confirming the cells penetrance into the tumours and possible on-target off-tumour accumulation, the two main limitations of CAR T-cells applied to solid tumours [245, 252]. This methodology would also allow side effects to be pre-empted before they have a major impact on the patient, helping to overcome some of the challenges affecting these therapies and improving clinical outcome. However, due to the bacterial origin of the NTR suicide/reporter gene, immunogenicity effects should be carefully evaluated in clinical studies.

6. Conclusions

The work of this multidisciplinary thesis includes synthetic chemistry, basic molecular biology and molecular imaging. This work was based on the synthesis, purification and characterisation of small fluorescent molecules substrate of NTR and small molecules as biomarkers' targeting ligands and their combination thereof. Alternative synthetic strategies have been successfully pursued in an attempt to increase the reaction yields by lowering the formation of by-products. Subsequent biological studies of these compounds both *in vitro* and *in vivo* and the use of molecular imaging modalities such as FLI and PET/CT imaging allowed us to:

I) determine the best substrate for NTR expression interrogation in a preclinical oncology model using FLI

II) demonstrate the high impact of the fluorophores on the biodistribution of fluorescent molecular targeting conjugates

III) conclude that ^{18}F-FMISO NTR PET/CT imaging is readily available for clinical application in NTR-based GDEPT settings

7. Future perspectives

As discussed, the design of functional molecular dyes with optimal properties is a necessity for further development of the MI field and, at the same time, a challenge that requires careful chemical design to fine-tune the often in conflict physichochemical properties. To this end, the rational design of improved NIR dyes substrates of NTR aided by quantum chemistry calculations can improve our understanding of the structure-property relationships by using density functional theory (DFT). These calculations can also help us predict the optical properties of the different NIR dyes, reducing the need for lenghthy synthetic approaches to multiple compounds, leading to the synthesis and biological evaluation of a reduced number of candidates with the required characteristics.

We aim to complete the study on the identification of superior fluorophores for targeted approaches in FIGS. For this purpose, we plan to assess the role of protein binding in the biodistribution of the different conjugates used in **paper II** and to analyse their fate in cells over time by fluorescence microscopy. Moreover, our group is working on the incorporation of linkers that allow the release of the fluorophore into the cytoplasm to exploit NTR-activatable dyes for targeted approaches. As already demonstrated by our group [121], CD24 is a promising target for FIGS in ovarian cancer. A multiplexing approach combining fluorescent targeting ligands against CD24 and FRα could help to reduce the impact of the high inter- and intra-tumoral expression heterogeneity of FRα, improving the outcome of intraoperative procedures in ovarian cancer. To evaluate the full potential of this approach, representative animal models will be used to allow for complete cytoreductive surgery and survival studies.

For suicide gene therapies, PET/CT imaging provides relevant information that can help stratify patients into those who will benefit from prodrug treatment and those who require an additional transduction prior to treatment. Hence, to increase the potential of ^{18}F-FMISO PET/CT for imaging of NTR expression after *in vivo*

transduction we would like to investigate the correlation between the transduction efficiency and the SUV_{max} values. Since a commercial anti-NTR antibody is not available, we envision the generation of an NTR-specific nanobody to be able to confirm and quantify the *in vivo* transduction efficiency and correlate the heterogeneous levels of expression to distinct ^{18}F-FMISO SUV_{max} values.

References

[1] Kumar P, Clark M. (2017). Clinical medicine. Bailliere Tindall.
[2] Weinberg RA. (2014). The biology of cancer. Garland Science.
[3] Hanahan D, Weinberg RA. Hallmarks of cancer: the next generation. Cell. 2011;144(5):646.
[4] Martelli C, Lo Dico A, Diceglie C, Lucignani G, Ottobrini L. Optical imaging probes in oncology. Oncotarget. 2016;7(30):48753.
[5] Dhadve A, Deo A, Bishnu A, Mukherjee S, Ray P. Molecular Imaging in Cancer: How the hallmarks aid in hunting. Int J Drug Res Tech. 2017;7(1):1.
[6] World Health Organization. (2020, 20th April). Cancer. http://www.euro.who.int/en/health-topics/noncommunicable-diseases/cancer/cancer.
[7] World Health Organization. (2020, 20th April). Screening and early detection. http://www.euro.who.int/en/health-topics/noncommunicable-diseases/cancer/policy/screening-and-early-detection.
[8] (2005). Saving women's lives : strategies for improving breast cancer detection and diagnosis. Natl Academy Pr.
[9] International Agency for Research on Cancer. WHO. (2020, 20th April). ONLINE ANALYSIS > GRAPHS: TIME TRENDS. http://www-dep.iarc.fr/WHOdb/WHOdb.htm.
[10] Autier P, Boniol M. Mammography screening: A major issue in medicine. Eur J Cancer. 2018;90:34.
[11] American Cancer Society. (2020, 20th April). Newer and Experimental Breast Imaging Tests. https://www.cancer.org/cancer/breast-cancer/screening-tests-and-early-detection/experimental-breast-imaging.html.
[12] Hofman MS, Lawrentschuk N, Francis RJ, Tang C, Vela I, Thomas P, et al. Prostate-specific membrane antigen PET-CT in patients with high-risk prostate cancer before curative-intent surgery or radiotherapy (proPSMA): a prospective, randomised, multicentre study. The Lancet. 2020;395(10231):1208.
[13] Burotto M, Wilkerson J, Stein WD, Bates SE, Fojo T. Adjuvant and neoadjuvant cancer therapies: A historical review and a rational approach to understand outcomes. Semin Oncol. 2019;46(1):83.
[14] Jackson SE, Chester JD. Personalised cancer medicine. Int J Cancer. 2015;137(2):262.
[15] Weber EW, Maus MV, Mackall CL. The Emerging Landscape of Immune Cell Therapies. Cell. 2020;181(1):46.
[16] Mudd SR, Comley RA, Bergstrom M, Holen KD, Luo Y, Carme S, et al. Molecular imaging in oncology drug development. Drug Discov Today. 2017;22(1):140.
[17] Waaijer SJH, Kok IC, Eisses B, Schroder CP, Jalving M, Brouwers AH, et al. Molecular Imaging in Cancer Drug Development. Journal of nuclear medicine : official publication, Society of Nuclear Medicine. 2018;59(5):726.
[18] Weissleder R. (2010). Molecular imaging: Principles and practice. Shelton, Conn.: People's Med. Publ. House.

[19] Collection WoSC. (2021, 27th January). Molecular imaging AND/OR Cancer. https://apps.webofknowledge.com/Search.do?product=WOS&SID=E3eStRihUlF3ZXBTe7w&search_mode=GeneralSearch&prID=3d039258-5b02-4f11-ba8c-348ea07bf72c.
[20] Garland M, Yim Joshua J, Bogyo M. A Bright Future for Precision Medicine: Advances in Fluorescent Chemical Probe Design and Their Clinical Application. Cell Chem Biol. 2016;23(1):122.
[21] James ML, Gambhir SS. A Molecular Imaging Primer: Modalities, Imaging Agents, and Applications. Physiol Rev. 2012;92(2):897.
[22] Pysz MA, Gambhir SS, Willmann JK. Molecular imaging: current status and emerging strategies. Clin Radiol. 2010;65(7):500.
[23] McCarthy JR, Bhaumik J, Karver MR, Sibel Erdem S, Weissleder R. Targeted nanoagents for the detection of cancers. Mol Oncol. 2010;4(6):511.
[24] Wang C, Wang Z, Zhao T, Li Y, Huang G, Sumer BD, et al. Optical molecular imaging for tumor detection and image-guided surgery. Biomaterials. 2018;157:62.
[25] Waterhouse DJ, Joseph J, Neves AA, di Pietro M, Brindle KM, Fitzgerald RC, et al. Design and validation of a near-infrared fluorescence endoscope for detection of early esophageal malignancy. J Biomed Opt. 2016;21(8):84001.
[26] Luthman AS, Waterhouse DJ, Ansel-Bollepalli L, Yoon J, Gordon GSD, Joseph J, et al. Bimodal reflectance and fluorescence multispectral endoscopy based on spectrally resolving detector arrays. J Biomed Opt. 2018;24(3):1.
[27] van Manen L, Dijkstra J, Boccara C, Benoit E, Vahrmeijer AL, Gora MJ, et al. The clinical usefulness of optical coherence tomography during cancer interventions. J Cancer Res Clin Oncol. 2018;144(10):1967.
[28] Si P, Honkala A, de la Zerda A, Smith BR. Optical Microscopy and Coherence Tomography of Cancer in Living Subjects. Trends Cancer. 2020;6(3):205.
[29] Ilina O, Campanello L, Gritsenko PG, Vullings M, Wang C, Bult P, et al. Intravital microscopy of collective invasion plasticity in breast cancer. Dis Model Mech. 2018;11(9):dmm034330.
[30] Xu MH, Wang LHV. Photoacoustic imaging in biomedicine. Rev Sci Instrum. 2006;77(4):041101.
[31] Fu Q, Zhu R, Song J, Yang H, Chen X. Photoacoustic Imaging: Contrast Agents and Their Biomedical Applications. Adv Mater. 2019;31(6):e1805875.
[32] Garai E, Sensarn S, Zavaleta CL, Loewke NO, Rogalla S, Mandella MJ, et al. A real-time clinical endoscopic system for intraluminal, multiplexed imaging of surface-enhanced Raman scattering nanoparticles. Plos One. 2015;10(4):e0123185.
[33] Gao P, Han B, Du Y, Zhao G, Yu Z, Xu W, et al. The Clinical Application of Raman Spectroscopy for Breast Cancer Detection. J Spectrosc (Hindawi). 2017;2017:5383948.
[34] Kleshnin M, Shirmanova M, Fiks I, Orlova A, Plekhanov V, Zagainova E, et al. Trans-illumination fluorescence imaging of deep-seated tumors in small animals. Photonics Lasers Med. 2015;4(1):85.
[35] Rice BW, Cable MD, Nelson MB. In vivo imaging of light-emitting probes. J Biomed Opt. 2001;6(4):432.

[36] Choy G, Choyke P, Libutti SK. Current Advances in Molecular Imaging: Noninvasive in Vivo Bioluminescent and Fluorescent Optical Imaging in Cancer Research. Mol Imaging. 2003;2(4):303.
[37] Ntziachristos V, Bremer C, Weissleder R. Fluorescence imaging with near-infrared light: new technological advances that enable in vivo molecular imaging. Eur Radiol. 2003;13(1):195.
[38] Voigt W. Advanced PET imaging in oncology: status and developments with current and future relevance to lung cancer care. Curr Opin Oncol. 2018;30(2):77.
[39] Guillaume M, Luxen A, Nebeling B, Argentini M, Clark JC, Pike VW. Recommendations for fluorine-18 production. Int J Rad Appl Instrum A. 1991;42(8):749.
[40] Hjelstuen OK, Svadberg A, Olberg DE, Rosser M. Standardization of fluorine-18 manufacturing processes: new scientific challenges for PET. Eur J Pharm Biopharm. 2011;78(3):307.
[41] Mettler FA, Guiberteau MJ. (2018). Essentials of nuclear medicine and molecular imaging. Elsevier.
[42] Li Z, Conti PS. Radiopharmaceutical chemistry for positron emission tomography. Adv Drug Deliv Rev. 2010;62(11):1031.
[43] Zimmerman BE. Current status and future needs for standards of radionuclides used in positron emission tomography. Appl Radiat Isot. 2013;76:31.
[44] Lois C, Hong EJ, Pease S, Brown EJ, Baltimore D. Germline transmission and tissue-specific expression of transgenes delivered by lentiviral vectors. Science. 2002;295(5556):868.
[45] Li M, Wang Y, Liu M, Lan X. Multimodality reporter gene imaging: Construction strategies and application. Theranostics. 2018;8(11):2954.
[46] Shaikh FA, Kurtys E, Kubassova O, Roettger D. Reporter gene imaging and its role in imaging-based drug development. Drug Discov Today. 2020;25(3):582.
[47] Penheiter AR, Russell SJ, Carlson SK. The Sodium Iodide Symporter (NIS) as an Imaging Reporter for Gene, Viral, and Cell-based Therapies. Curr Gene Ther. 2012;12(1):33.
[48] Furukawa T, Lohith TG, Takamatsu S, Mori T, Tanaka T, Fujibayashi Y. Potential of the FES-hERL PET reporter gene system -- basic evaluation for gene therapy monitoring. Nucl Med Biol. 2006;33(1):145.
[49] Liang Q, Satyamurthy N, Barrio JR, Toyokuni T, Phelps MP, Gambhir SS, et al. Noninvasive, quantitative imaging in living animals of a mutant dopamine D2 receptor reporter gene in which ligand binding is uncoupled from signal transduction. Gene Ther. 2001;8(19):1490.
[50] Tjuvajev JG, Stockhammer G, Desai R, Uehara H, Watanabe K, Gansbacher B, et al. Imaging the expression of transfected genes in vivo. Cancer Res. 1995;55(24):6126.
[51] Yao H, So MK, Rao J. A bioluminogenic substrate for in vivo imaging of beta-lactamase activity. Angew Chem Int Ed Engl. 2007;46(37):7031.
[52] Zhao H, Doyle TC, Coquoz O, Kalish F, Rice BW, Contag CH. Emission spectra of bioluminescent reporters and interaction with mammalian tissue determine the sensitivity of detection in vivo. J Biomed Opt. 2005;10(4):41210.

[53] Mezzanotte L, van 't Root M, Karatas H, Goun EA, Lowik CWGM. In Vivo Molecular Bioluminescence Imaging: New Tools and Applications. Trends Biotechnol. 2017;35(7):640.
[54] Heim R, Cubitt AB, Tsien RY. Improved green fluorescence. Nature. 1995;373(6516):663.
[55] Reid BG, Flynn GC. Chromophore Formation in Green Fluorescent Protein. Biochemistry. 1997;36(22):6786.
[56] Heim R, Prasher DC, Tsien RY. Wavelength mutations and posttranslational autoxidation of green fluorescent protein. Proc Natl Acad Sci U S A. 1994;91(26):12501.
[57] Lakowicz JR. (2006). Principles of fluorescence spectroscopy. Springer.
[58] Cubitt AB, Heim R, Adams SR, Boyd AE, Gross LA, Tsien RY. Understanding, improving and using green fluorescent proteins. Trends Biochem Sci. 1995;20(11):448.
[59] Chishima T, Miyagi Y, Wang X, Yamaoka H, Shimada H, Moossa AR, et al. Cancer Invasion and Micrometastasis Visualized in Live Tissue by Green Fluorescent Protein Expression. Cancer Res. 1997;57(10):2042.
[60] Akiva E, Copp JN, Tokuriki N, Babbitt PC. Evolutionary and molecular foundations of multiple contemporary functions of the nitroreductase superfamily. Proc Natl Acad Sci U S A. 2017;114(45):E9549.
[61] Stillman WB, Scott AB. (1947). Therapeutically active substituted nitrofurans of the imino series. (United States) (Patent No. US2416234). https://patentimages.storage.googleapis.com/d8/dd/8c/9532dd53918723/US2416233.pdf
[62] McCalla DR, Kaiser C, Green MHL. Genetics of nitrofurazone resistance in Escherichia coli. J Bacteriol. 1978;133(1):10.
[63] Parkinson GN, Skelly JV, Neidle S. Crystal Structure of FMN-Dependent Nitroreductase from Escherichia coli B: A Prodrug-Activating Enzyme. J Med Chem. 2000;43(20):3624.
[64] Johansson E, Parkinson GN, Denny WA, Neidle S. Studies on the Nitroreductase Prodrug-Activating System. Crystal Structures of Complexes with the Inhibitor Dicoumarol and Dinitrobenzamide Prodrugs and of the Enzyme Active Form. J Med Chem. 2003;46(19):4009.
[65] Oliveira IAMd, Bonatto D, Antonio J, Henriques P, Vargas RFG. (2010). Current research, technology and education topics in applied microbiology and microbial biotechnology. Nitroreductases: Enzymes with Environmental, Biotechnological and Clinical Importance. Badajoz, Spain : Formatex Research Center.
[66] Peterson FJ, Mason RP, Hovsepian J, Holtzman JL. Oxygen-sensitive and -insensitive nitroreduction by Escherichia coli and rat hepatic microsomes. J Biol Chem. 1979;254(10):4009.
[67] Roldán MD, Pérez-Reinado E, Castillo F, Moreno-Vivián C. Reduction of polynitroaromatic compounds: the bacterial nitroreductases. FEMS Microbiol Rev. 2008;32(3):474.

[68] Watanabe S, Shiga T, Hirata K, Magota K, Okamoto S, Toyonaga T, et al. Biodistribution and radiation dosimetry of the novel hypoxia PET probe [18F]DiFA and comparison with [18F]FMISO. EJNMMI Res. 2019;9(1):60.
[69] Wei C, Shen Y, Xu Z, Peng S, Yuan Z, He Y, et al. A novel off-on fluorescent probe for imaging of hypoxia in tumor cell. J Photoch Photobio A. 2018;353:292.
[70] Denny WA. Nitroreductase-based GDEPT. Current pharmaceutical design. 2002;8(15):1349.
[71] McCormack E, Mujić M, Osdal T, Bruserud Ø, Gjertsen BT. Multiplexed mAbs: a new strategy in preclinical time-domain imaging of acute myeloid leukemia. Blood. 2013;121(7):e34.
[72] Christofferson A, Wilkie J. Mechanism of CB1954 reduction by Escherichia coli nitroreductase. Biochem Soc Trans. 2009;37(Pt 2):413.
[73] William RW, Kevin OH, Susan MP, Dianne MF, Nuala AH, Adam VP. Bystander Effects of Bioreductive Drugs: Potential for Exploiting Pathological Tumor Hypoxia with Dinitrobenzamide Mustards. Radiat Res. 2007;167(6):625.
[74] Valeur B, Berberan-Santos MrN. (2013). Molecular fluorescence : principles and applications. Wiley-VCH ; John Wiley distributor.
[75] Acuna AU, Amat-Guerri F, Morcillo P, Liras M, Rodriguez B. Structure and formation of the fluorescent compound of Lignum nephriticum. Org Lett. 2009;11(14):3020.
[76] Hong GS, Antaris AL, Dai HJ. Near-infrared fluorophores for biomedical imaging. Nat Biomed Eng. 2017;1(1).
[77] Kobayashi H, Longmire MR, Ogawa M, Choyke PL, Kawamoto S. Multiplexed imaging in cancer diagnosis: applications and future advances. Lancet Oncol. 2010;11(6):589.
[78] Stoletov K, Montel V, Lester RD, Gonias SL, Klemke R. High-resolution imaging of the dynamic tumor cell–vascular interface in transparent zebrafish. Proc Natl Acad Sci U S A. 2007;104(44):17406.
[79] Smith AM, Duan H, Mohs AM, Nie S. Bioconjugated quantum dots for in vivo molecular and cellular imaging. Adv Drug Deliv Rev. 2008;60(11):1226.
[80] McHugh KJ, Jing L, Behrens AM, Jayawardena S, Tang W, Gao M, et al. Biocompatible Semiconductor Quantum Dots as Cancer Imaging Agents. Adv Mater. 2018;30(18):1706356.
[81] Yi Z, Luo Z, Qin X, Chen Q, Liu X. Lanthanide-Activated Nanoparticles: A Toolbox for Bioimaging, Therapeutics, and Neuromodulation. Accounts Chem Res. 2020;53(11):2692.
[82] Li D, He S, Wu Y, Liu J, Liu Q, Chang B, et al. Excretable Lanthanide Nanoparticle for Biomedical Imaging and Surgical Navigation in the Second Near-Infrared Window. Adv Sci. 2019;6(23):1902042.
[83] Liu ZA, Yang K, Lee ST. Single-walled carbon nanotubes in biomedical imaging. J Mater Chem. 2011;21(3):586.
[84] Ceppi L, Bardhan NM, Na Y, Siegel A, Rajan N, Fruscio R, et al. Real-Time Single-Walled Carbon Nanotube-Based Fluorescence Imaging Improves Survival after Debulking Surgery in an Ovarian Cancer Model. Acs Nano. 2019;13(5):5356.
[85] Vendrell M, Zhai D, Er JC, Chang Y-T. Combinatorial Strategies in Fluorescent Probe Development. Chem Rev. 2012;112(8):4391.

[86] Mojzych M, Henary M. (2008). Synthesis of Cyanine Dyes. Springer Berlin Heidelberg.
[87] Kobayashi H, Ogawa M, Alford R, Choyke PL, Urano Y. New strategies for fluorescent probe design in medical diagnostic imaging. Chem Rev. 2010;110(5):2620.
[88] Debie P, Hernot S. Emerging Fluorescent Molecular Tracers to Guide Intra-Operative Surgical Decision-Making. Front Pharmacol. 2019;10:510.
[89] Luo S, Zhang E, Su Y, Cheng T, Shi C. A review of NIR dyes in cancer targeting and imaging. Biomaterials. 2011;32(29):7127.
[90] Owens EA, Lee S, Choi J, Henary M, Choi HS. NIR fluorescent small molecules for intraoperative imaging. Wiley Interdiscip Rev Nanomed Nanobiotechnol. 2015;7(6):828.
[91] Li L, Dong X, Li J, Wei J. A short review on NIR-II organic small molecule dyes. Dyes Pigm. 2020;183:108756.
[92] Jacques SL. Optical properties of biological tissues: a review (vol 58, pg R37, 2013). Phys Med Biol. 2013;58(14):5007.
[93] Zhu B, Sevick-Muraca EM. A review of performance of near-infrared fluorescence imaging devices used in clinical studies. Br J Radiol. 2014;88(1045):20140547.
[94] How J, Gotlieb WH, Press JZ, Abitbol J, Pelmus M, Ferenczy A, et al. Comparing indocyanine green, technetium, and blue dye for sentinel lymph node mapping in endometrial cancer. Gynecol Oncol. 2015;137(3):436.
[95] Tummers QRJG, Hoogstins CES, Peters AAW, de Kroon CD, Trimbos JBMZ, van de Velde CJH, et al. The Value of Intraoperative Near-Infrared Fluorescence Imaging Based on Enhanced Permeability and Retention of Indocyanine Green: Feasibility and False-Positives in Ovarian Cancer. Plos One. 2015;10(6):e0129766.
[96] Liberale G, Vankerckhove S, Caldon MG, Ahmed B, Moreau M, El Nakadi I, et al. Fluorescence Imaging After Indocyanine Green Injection for Detection of Peritoneal Metastases in Patients Undergoing Cytoreductive Surgery for Peritoneal Carcinomatosis From Colorectal Cancer A Pilot Study. Ann Surg. 2016;264(6):1110.
[97] Tummers QRJG, Boonstra MC, Frangioni JV, van de Velde CJH, Vahrmeijer AL, Bonsing BA. Intraoperative near-infrared fluorescence imaging of a paraganglioma using methylene blue: A case report. Int J Surg Case Rep. 2015;6:150.
[98] van der Vorst JR, Schaafsma BE, Verbeek FPR, Swijnenburg RJ, Tummers QRJG, Hutteman M, et al. Intraoperative near-infrared fluorescence imaging of parathyroid adenomas with use of low-dose methylene blue. Head Neck. 2014;36(6):853.
[99] Olson MT, Ly QP, Mohs AM. Fluorescence Guidance in Surgical Oncology: Challenges, Opportunities, and Translation. Mol Imaging Biol. 2019;21(2):200.
[100] Kraft JC, Ho RJY. Interactions of Indocyanine Green and Lipid in Enhancing Near-Infrared Fluorescence Properties: The Basis for Near-Infrared Imaging in Vivo. Biochemistry. 2014;53(8):1275.
[101] Wojtynek NE, Olson MT, Bielecki TA, An W, Bhat AM, Band H, et al. Nanoparticle Formulation of Indocyanine Green Improves Image-Guided Surgery in a Murine Model of Breast Cancer. Mol Imaging Biol. 2020;22(4):891.

[102] Yeroslavsky G, Umezawa M, Okubo K, Nigoghossian K, Thi Kim Dung D, Miyata K, et al. Stabilization of indocyanine green dye in polymeric micelles for NIR-II fluorescence imaging and cancer treatment. Biomater Sci. 2020;8(8):2245.
[103] Pandey RK, James N, Chen Y, Dobhal MP. (2008). Cyanine Dye-Based Compounds for Tumor Imaging With and Without Photodynamic Therapy. Springer Berlin Heidelberg.
[104] Laramie MD, Fouts BL, MacCuaig WM, Buabeng E, Jones MA, Mukherjee P, et al. Improved pentamethine cyanine nanosensors for optoacoustic imaging of pancreatic cancer. Sci Rep. 2021;11(1):4366.
[105] Reichardt C. Chiral polymethine dyes: A remarkable but forgotten conjugated π system. J Phys Org Chem. 1995;8(12):761.
[106] Matsuoka M. (1990). Infrared absorbing dyes. Springer-Verlag New York.
[107] Buckle T, van Willigen DM, Spa SJ, Hensbergen AW, van der Wal S, de Korne CM, et al. Tracers for Fluorescence-Guided Surgery: How Elongation of the Polymethine Chain in Cyanine Dyes Alters the Pharmacokinetics of a Dual-Modality c[RGDyK] Tracer. J Nucl Med. 2018;59(6):986.
[108] Tarazi L, George A, Patonay G, Strekowski L. Spectral characterization of a novel near-infrared cyanine dye: a study of its complexation with metal ions. Talanta. 1998;46(6):1413.
[109] Mujumdar RB, Ernst LA, Mujumdar SR, Lewis CJ, Waggoner AS. Cyanine dye labeling reagents: sulfoindocyanine succinimidyl esters. Bioconjug Chem. 1993;4(2):105.
[110] Choi HS, Nasr K, Alyabyev S, Feith D, Lee JH, Kim SH, et al. Synthesis and in vivo fate of zwitterionic near-infrared fluorophores. Angew Chem Int Ed Engl. 2011;50(28):6258.
[111] Hyun H, Owens EA, Narayana L, Wada H, Gravier J, Bao K, et al. Central C-C bonding increases optical and chemical stability of NIR fluorophores. Rsc Adv. 2014;4(102):58762.
[112] Huang R, Vider J, Kovar JL, Olive DM, Mellinghoff IK, Mayer-Kuckuk P, et al. Integrin αvβ3-Targeted IRDye 800CW Near-Infrared Imaging of Glioblastoma. Clin Can Res. 2012;18(20):5731.
[113] van Driel PBAA, Boonstra MC, Prevoo HAJM, van de Giessen M, Snoeks TJA, Tummers QRJG, et al. EpCAM as multi-tumour target for near-infrared fluorescence guided surgery. Bmc Cancer. 2016;16(1):884.
[114] Tummers WS, Miller SE, Teraphongphom NT, Gomez A, Steinberg I, Huland DM, et al. Intraoperative Pancreatic Cancer Detection using Tumor-Specific Multimodality Molecular Imaging. Ann Surg Oncol. 2018;25(7):1880.
[115] Marston JC, Kennedy GD, Lapi SE, Hartman YE, Richardson MT, Modi HM, et al. Panitumumab-IRDye800CW for Fluorescence-Guided Surgical Resection of Colorectal Cancer. J Surg Res. 2019;239:44.
[116] Choi HS, Gibbs SL, Lee JH, Kim SH, Ashitate Y, Liu F, et al. Targeted zwitterionic near-infrared fluorophores for improved optical imaging. Nat Biotechnol. 2013;31(2):148.
[117] Kleinmanns K, Bischof K, Anandan S, Popa M, Akslen LA, Fosse V, et al. CD24-targeted fluorescence imaging in patient-derived xenograft models of high-grade serous ovarian carcinoma. EBioMedicine. 2020;56:102782.

[118] Gutowski M, Framery B, Boonstra MC, Garambois V, Quenet F, Dumas K, et al. SGM-101: An innovative near-infrared dye-antibody conjugate that targets CEA for fluorescence-guided surgery. Surg Oncol. 2017;26(2):153.
[119] Hoogstins CES, Boogerd LSF, Sibinga Mulder BG, Mieog JSD, Swijnenburg RJ, van de Velde CJH, et al. Image-Guided Surgery in Patients with Pancreatic Cancer: First Results of a Clinical Trial Using SGM-101, a Novel Carcinoembryonic Antigen-Targeting, Near-Infrared Fluorescent Agent. Ann Surg Oncol. 2018;25(11):3350.
[120] Kuchimaru T, Kadonosono T, Corona C, Dwight SJ, McDougall M, Takahashi S, et al. Importance of the physicochemical properties of fluorescent dyes for obtaining target-specific in vivo images by membrane-permeable macromolecular imaging probes. J Pharm Technol Drug Res. 2013;2(1).
[121] Kleinmanns K, Fosse V, Davidson B, de Jalon EG, Tenstad O, Bjorge L, et al. CD24-targeted intraoperative fluorescence image-guided surgery leads to improved cytoreduction of ovarian cancer in a preclinical orthotopic surgical model. EBioMedicine. 2020;56:102783.
[122] Hoogstins CES, Tummers QRJG, Gaarenstroom KN, de Kroon CD, Trimbos JBMZ, Bosse T, et al. A Novel Tumor-Specific Agent for Intraoperative Near-Infrared Fluorescence Imaging: A Translational Study in Healthy Volunteers and Patients with Ovarian Cancer. Clin Can Res. 2016;22(12):2929.
[123] Corbett CJ, Frenzel Sulyok LG, Predina JD, Newton AD, Bryski MG, Xia L, et al. Comparison of a Short Versus Long Stokes Shift Near-Infrared Dye During Intraoperative Molecular Imaging. Mol Imaging Biol. 2020;22(1):144.
[124] Wayua C, Low PS. Evaluation of a Cholecystokinin 2 Receptor-Targeted Near-Infrared Dye for Fluorescence-Guided Surgery of Cancer. Mol Pharm. 2014;11(2):468.
[125] Miller J, Wang ST, Orukari I, Prior J, Sudlow G, Su X, et al. Perfusion-based fluorescence imaging method delineates diverse organs and identifies multifocal tumors using generic near-infrared molecular probes. J Biophotonics. 2018;11(4):e201700232.
[126] Sano K, Nakajima T, Ali T, Bartlett DW, Wu AM, Kim I, et al. Activatable fluorescent cys-diabody conjugated with indocyanine green derivative: consideration of fluorescent catabolite kinetics on molecular imaging. J Biomed Opt. 2013;18(10).
[127] Watanabe R, Sato K, Hanaoka H, Harada T, Nakajima T, Kim I, et al. Minibody-Indocyanine Green Based Activatable Optical Imaging Probes: The Role of Short Polyethylene Glycol Linkers. ACS Med Chem Lett. 2014;5(4):411.
[128] Cho SS, Jeon J, Buch L, Nag S, Nasrallah M, Low PS, et al. Intraoperative near-infrared imaging with receptor-specific versus passive delivery of fluorescent agents in pituitary adenomas. J Neurosurg. 2018;131(6):1974.
[129] Joshi BP, Wang TD. Targeted Optical Imaging Agents in Cancer: Focus on Clinical Applications. Contrast Media Mol Imaging. 2018;2018:2015237.
[130] Lamberts LE, Koch M, de Jong JS, Adams ALL, Glatz J, Kranendonk MEG, et al. Tumor-Specific Uptake of Fluorescent Bevacizumab-IRDye800CW Microdosing in Patients with Primary Breast Cancer: A Phase I Feasibility Study. Clin Cancer Res. 2017;23(11):2730.

[131] Predina JD, Newton AD, Xia L, Corbett C, Connolly C, Shin M, et al. An open label trial of folate receptor-targeted intraoperative molecular imaging to localize pulmonary squamous cell carcinomas. Oncotarget. 2018;9(17):13517.
[132] Fonnes T, Strand E, Fasmer KE, Berg HF, Espedal H, Sortland K, et al. Near-Infrared Fluorescent Imaging for Monitoring of Treatment Response in Endometrial Carcinoma Patient-Derived Xenograft Models. Cancers (Basel). 2020;12(2).
[133] Boogerd LSF, Boonstra MC, Prevoo HAJM, Handgraaf HJM, Kuppen PJK, van de Velde CJH, et al. Fluorescence-guided tumor detection with a novel anti-EpCAM targeted antibody fragment: Preclinical validation. Surg Oncol. 2019;28:1.
[134] van Leeuwen FWB, Cornelissen B, Caobelli F, Evangelista L, Rbah-Vidal L, Del Vecchio S, et al. Generation of fluorescently labeled tracers – which features influence the translational potential? EJNMMI Radiopharm Chem. 2017;2(1):15.
[135] Wang X, Huang SS, Heston WDW, Guo H, Wang B-C, Basilion JP. Development of Targeted Near-Infrared Imaging Agents for Prostate Cancer. Mol Cancer Ther. 2014;13(11):2595.
[136] Frigerio B, Bizzoni C, Jansen G, Leamon CP, Peters GJ, Low PS, et al. Folate receptors and transporters: biological role and diagnostic/therapeutic targets in cancer and other diseases. J Exp Clin Cancer Res. 2019;38(1):125.
[137] Vergote I, Armstrong D, Scambia G, Teneriello M, Sehouli J, Schweizer C, et al. A Randomized, Double-Blind, Placebo-Controlled, Phase III Study to Assess Efficacy and Safety of Weekly Farletuzumab in Combination With Carboplatin and Taxane in Patients With Ovarian Cancer in First Platinum-Sensitive Relapse. J Clin Oncol. 2016;34(19):2271.
[138] Scaranti M, Cojocaru EA-O, Banerjee S, Banerji UA-O. Exploiting the folate receptor α in oncology. Nat Rev Clin Oncol. 2020(17):349.
[139] Kelemen LE. The role of folate receptor α in cancer development, progression and treatment: Cause, consequence or innocent bystander? Int J Cancer. 2006;119(2):243.
[140] Ledermann JA, Canevari S, Thigpen T. Targeting the folate receptor: diagnostic and therapeutic approaches to personalize cancer treatments. Ann Oncol. 2015;26(10):2034.
[141] Jackman AL, Theti DS, Gibbs DD. Antifolates targeted specifically to the folate receptor. Adv Drug Deliv Rev. 2004;56(8):1111.
[142] Lutz RJ. Targeting the folate receptor for the treatment of ovarian cancer. Transl Cancer Res. 2015;4(1).
[143] Cheung A, Bax HJ, Josephs DH, Ilieva KM, Pellizzari G, Opzoomer J, et al. Targeting folate receptor alpha for cancer treatment. Oncotarget. 2016;7(32):52553.
[144] Sega EI, Low PS. Tumor detection using folate receptor-targeted imaging agents. Cancer Metastasis Rev. 2008;27(4):655.
[145] Boss SD, Ametamey SM. Development of Folate Receptor-Targeted PET Radiopharmaceuticals for Tumor Imaging-A Bench-to-Bedside Journey. Cancers (Basel). 2020;12(6):1508.
[146] Lee H, Kim J, Kim H, Kim Y, Choi Y. A folate receptor-specific activatable probe for near-infrared fluorescence imaging of ovarian cancer. Chem Commun (Camb). 2014;50(56):7507.

[147] Whitley MJ, Cardona DM, Lazarides AL, Spasojevic I, Ferrer JM, Cahill J, et al. A mouse-human phase 1 co-clinical trial of a protease-activated fluorescent probe for imaging cancer. Sci Transl Med. 2016;8(320).
[148] Obaid G, Spring BQ, Bano S, Hasan T. Activatable clinical fluorophore-quencher antibody pairs as dual molecular probes for the enhanced specificity of image-guided surgery. J Biomed Opt. 2017;22(12).
[149] Mochida A, Ogata F, Nagaya T, Choyke PL, Kobayashi H. Activatable fluorescent probes in fluorescence-guided surgery: Practical considerations. Bioorg Med Chem. 2018;26(4):925.
[150] McCormack E, Silden E, West RM, Pavlin T, Micklem DR, Lorens JB, et al. Nitroreductase, a near-infrared reporter platform for in vivo time-domain optical imaging of metastatic cancer. Cancer Res. 2013;73(4):1276.
[151] Li H, Yao Q, Xu F, Xu N, Sun W, Long S, et al. Lighting-Up Tumor for Assisting Resection via Spraying NIR Fluorescent Probe of gamma-Glutamyltranspeptidas. Front Chem. 2018;6:485.
[152] Kitagawa Y, Tanaka S, Kuriki Y, Yamamoto K, Ogasawara A, Nejo T, et al. Spray Fluorescent Probes for Fluorescence-Guided Neurosurgery. Front Oncol. 2019;9:727.
[153] Zhang J, Kale V, Chen M. Gene-directed enzyme prodrug therapy. AAPS J. 2015;17(1):102.
[154] Mishra AP, Chandra S, Tiwari R, Srivastava A, Tiwari G. Therapeutic Potential of Prodrugs Towards Targeted Drug Delivery. Open Med Chem J. 2018;12:111.
[155] Djeha AH, Hulme A, Dexter MT, Mountain A, Young LS, Searle PF, et al. Expression of Escherichia coli B nitroreductase in established human tumor xenografts in mice results in potent antitumoral and bystander effects upon systemic administration of the prodrug CB1954. Cancer Gene Ther. 2000;7(5):721.
[156] Wilson WR, Hicks KO, Pullen SM, Ferry DM, Helsby NA, Patterson AV. Bystander effects of bioreductive drugs: potential for exploiting pathological tumor hypoxia with dinitrobenzamide mustards. Radiat Res. 2007;167(6):625.
[157] Bashraheel SS, Domling A, Goda SK. Update on targeted cancer therapies, single or in combination, and their fine tuning for precision medicine. Biomed Pharmacother. 2020;125:110009.
[158] Li N, Zhou J, Weng D, Zhang C, Li L, Wang B, et al. Adjuvant adenovirus-mediated delivery of herpes simplex virus thymidine kinase administration improves outcome of liver transplantation in patients with advanced hepatocellular carcinoma. Clin Cancer Res. 2007;13(19):5847.
[159] Patel P, Young JG, Mautner V, Ashdown D, Bonney S, Pineda RG, et al. A phase I/II clinical trial in localized prostate cancer of an adenovirus expressing nitroreductase with CB1954 [correction of CB1984]. Mol Ther. 2009;17(7):1292.
[160] Knox RJ, Boland MP, Friedlos F, Coles B, Southan C, Roberts JJ. The nitroreductase enzyme in Walker cells that activates 5-(aziridin-1-yl)-2,4-dinitrobenzamide (CB 1954) to 5-(aziridin-1-yl)-4-hydroxylamino-2-nitrobenzamide is a form of NAD(P)H dehydrogenase (quinone) (EC 1.6.99.2). Biochem Pharmacol. 1988;37(24):4671.

[161] Pitsawong W, Hoben JP, Miller A-F. Understanding the broad substrate repertoire of nitroreductase based on its kinetic mechanism. J Biol Chem. 2014;289(22):15203.
[162] Tjuvajev JG, Doubrovin M, Akhurst T, Cai S, Balatoni J, Alauddin MM, et al. Comparison of radiolabeled nucleoside probes (FIAU, FHBG, and FHPG) for PET imaging of HSV1-tk gene expression. J Nucl Med. 2002;43(8):1072.
[163] Deng W-P, Yang WK, Lai W-F, Liu R-S, Hwang J-J, Yang D-M, et al. Non-invasive in vivo imaging with radiolabelled FIAU for monitoring cancer gene therapy using herpes simplex virus type 1 thymidine kinase and ganciclovir. Eur J Nucl Med Mol Imaging. 2004;31(1):99.
[164] Penuelas I, Mazzolini G, Boan JF, Sangro B, Marti-Climent J, Ruiz M, et al. Positron emission tomography imaging of adenoviral-mediated transgene expression in liver cancer patients. Gastroenterology. 2005;128(7):1787.
[165] Yaghoubi SS, Gambhir SS. PET imaging of herpes simplex virus type 1 thymidine kinase (HSV1-tk) or mutant HSV1-sr39tk reporter gene expression in mice and humans using [18F]FHBG. Nat Protoc. 2006;1(6):3069.
[166] Vorobyeva AG, Stanton M, Godinat A, Lund KB, Karateev GG, Francis KP, et al. Development of a Bioluminescent Nitroreductase Probe for Preclinical Imaging. Plos One. 2015;10(6):e0131037.
[167] Mowday AM, Copp JN, Syddall SP, Dubois LJ, Wang J, Lieuwes NG, et al. E. coli nitroreductase NfsA is a reporter gene for non-invasive PET imaging in cancer gene therapy applications. Theranostics. 2020;10(23):10548.
[168] Stummer W, Pichlmeier U, Meinel T, Wiestler OD, Zanella F, Reulen H-J. Fluorescence-guided surgery with 5-aminolevulinic acid for resection of malignant glioma: a randomised controlled multicentre phase III trial. Lancet Oncol. 2006;7(5):392.
[169] Ishizawa T, Fukushima N, Shibahara J, Masuda K, Tamura S, Aoki T, et al. Real-time identification of liver cancers by using indocyanine green fluorescent imaging. Cancer. 2009;115(11):2491.
[170] van Dam GM, Themelis G, Crane LMA, Harlaar NJ, Pleijhuis RG, Kelder W, et al. Intraoperative tumor-specific fluorescence imaging in ovarian cancer by folate receptor-alpha targeting: first in-human results. Nat Med. 2011;17(10):1315.
[171] Alisha VD, Huiyun L, Eric RH, Kimberley SS, Brian WP. Review of fluorescence guided surgery systems: identification of key performance capabilities beyond indocyanine green imaging. J Biomed Opt. 2016;21(8):1.
[172] Tringale KR, Pang J, Nguyen QT. Image-guided surgery in cancer: A strategy to reduce incidence of positive surgical margins. Wiley Interdiscip Rev Syst Biol Med. 2018;10(3):e1412.
[173] Hu Z, Fang C, Li B, Zhang Z, Cao C, Cai M, et al. First-in-human liver-tumour surgery guided by multispectral fluorescence imaging in the visible and near-infrared-I/II windows. Nat Biomed Eng. 2020;4(3):259.
[174] Choi HS, Kim HK. Multispectral image-guided surgery in patients. Nat Biomed Eng. 2020;4(3):245.
[175] Lacivita E, Leopoldo M, Berardi F, Colabufo NA, Perrone R. Activatable fluorescent probes: a new concept in optical molecular imaging. Curr Med Chem. 2012;19(28):4731.

[176] Terpetschnig E, Lakowicz JR. Synthesis and characterization of unsymmetrical squaraines: a new class of cyanine dyes. Dyes Pigm. 1993;21(3):227.
[177] Terpetschnig EA, Patsenker LD, Tatarets A. (2004). Luminescent compounds. (Patent No. US20040166515A1).
[178] Terpetschnig EA, Tatarets A, Galkina O, Fedyunyaeva I, Patsenker L. (2005). Luminescent compounds based on squaric acid derivatives. (Patent No. US20050202565A1).
[179] Ferreira CB, Sumner RP, Rodriguez-Plata MT, Rasaiyaah J, Milne RS, Thrasher AJ, et al. Lentiviral Vector Production Titer Is Not Limited in HEK293T by Induced Intracellular Innate Immunity. Mol Ther Methods Clin Dev. 2020;17:209.
[180] Kepa JK, Ross D. DT-diaphorase activity in NSCLC and SCLC cell lines: a role for fos/jun regulation. Br J Cancer. 1999;79(11):1679.
[181] Ross D, Kepa JK, Winski SL, Beall HD, Anwar A, Siegel D. NAD(P)H:quinone oxidoreductase 1 (NQO1): chemoprotection, bioactivation, gene regulation and genetic polymorphisms. Chem Biol Interact. 2000;129(1-2):77.
[182] Siwowska K, Schmid RM, Cohrs S, Schibli R, Muller C. Folate Receptor-Positive Gynecological Cancer Cells: In Vitro and In Vivo Characterization. Pharmaceuticals (Basel). 2017;10(3).
[183] Xing L, Xu Y, Sun K, Wang H, Zhang F, Zhou Z, et al. Identification of a peptide for folate receptor alpha by phage display and its tumor targeting activity in ovary cancer xenograft. Sci Rep. 2018;8(1):8426.
[184] Xu X, Yan Y, Liu F, Wu L, Shao M, Wang K, et al. Folate receptor-targeted 19F MR molecular imaging and proliferation evaluation of lung cancer. J Magn Reson Imaging. 2018;48(6):1617.
[185] Brown M, Wittwer C. Flow Cytometry: Principles and Clinical Applications in Hematology. Clin Chem. 2000;46(8):1221.
[186] Sanderson MJ, Smith I, Parker I, Bootman MD. Fluorescence microscopy. Cold Spring Harb Protoc. 2014;2014(10):pdb top071795.
[187] Bhaumik S, Sekar TV, Depuy J, Klimash J, Paulmurugan R. Noninvasive optical imaging of nitroreductase gene-directed enzyme prodrug therapy system in living animals. Gene Ther. 2012;19(3):295.
[188] Zhu S, Tian R, Antaris AL, Chen X, Dai H. Near-Infrared-II Molecular Dyes for Cancer Imaging and Surgery. Adv Mater. 2019;31(24):e1900321.
[189] Wang S, Li B, Zhang F. Molecular Fluorophores for Deep-Tissue Bioimaging. ACS Cent Sci. 2020;6(8):1302.
[190] Zhu S, Yung BC, Chandra S, Niu G, Antaris AL, Chen X. Near-Infrared-II (NIR-II) Bioimaging via Off-Peak NIR-I Fluorescence Emission. Theranostics. 2018;8(15):4141.
[191] Englman R, Jortner J. The energy gap law for radiationless transitions in large molecules. Mol Phys. 1970;18(2):145.
[192] Stackova L, Muchova E, Russo M, Slavicek P, Stacko P, Klan P. Deciphering the Structure-Property Relations in Substituted Heptamethine Cyanines. J Org Chem. 2020;85(15):9776.
[193] Levitz A, Marmarchi F, Henary M. Synthesis and Optical Properties of Near-Infrared meso-Phenyl-Substituted Symmetric Heptamethine Cyanine Dyes. Molecules. 2018;23(2):226.

[194] Gayton J, Autry SA, Meador W, Parkin SR, Hill GA, Jr., Hammer NI, et al. Indolizine-Cyanine Dyes: Near Infrared Emissive Cyanine Dyes with Increased Stokes Shifts. J Org Chem. 2019;84(2):687.
[195] Meador WE, Autry SA, Bessetti RN, Gayton JN, Flynt AS, Hammer NI, et al. Water-Soluble NIR Absorbing and Emitting Indolizine Cyanine and Indolizine Squaraine Dyes for Biological Imaging. J Org Chem. 2020;85(6):4089.
[196] Li D-H, Schreiber CL, Smith BD. Sterically Shielded Heptamethine Cyanine Dyes for Bioconjugation and High Performance Near-Infrared Fluorescence Imaging. Angewandte Chemie (International ed in English). 2020;59(29):12154.
[197] Antaris AL, Chen H, Cheng K, Sun Y, Hong G, Qu C, et al. A small-molecule dye for NIR-II imaging. Nat Mater. 2016;15(2):235.
[198] Wycisk V, Achazi K, Hirsch O, Kuehne C, Dernedde J, Haag R, et al. Heterobifunctional Dyes: Highly Fluorescent Linkers Based on Cyanine Dyes. ChemistryOpen. 2017;6(3):437.
[199] Du BJ, Jiang XY, Huang YY, Li SQ, Lin JC, Yu MX, et al. Tailoring Kidney Transport of Organic Dyes with Low-Molecular-Weight PEGylation. Bioconjug Chem. 2020;31(2):241.
[200] Duong T, Li X, Yang B, Schumann C, Albarqi HA, Taratula O, et al. Phototheranostic nanoplatform based on a single cyanine dye for image-guided combinatorial phototherapy. Nanomedicine. 2017;13(3):955.
[201] Botz B, Bolcskei K, Kemeny A, Sandor Z, Tekus V, Setalo G, Jr., et al. Hydrophobic cyanine dye-doped micelles for optical in vivo imaging of plasma leakage and vascular disruption. J Biomed Opt. 2015;20(1):016022.
[202] Kalyane D, Raval N, Maheshwari R, Tambe V, Kalia K, Tekade RK. Employment of enhanced permeability and retention effect (EPR): Nanoparticle-based precision tools for targeting of therapeutic and diagnostic agent in cancer. Mater Sci Eng C Mater Biol Appl. 2019;98:1252.
[203] van der Wal S, Kuil J, Valentijn ARPM, van Leeuwen FWB. Synthesis and systematic evaluation of symmetric sulfonated centrally C-C bonded cyanine near-infrared dyes for protein labelling. Dyes Pigm. 2016;132:7.
[204] Wu Z, Shao P, Zhang S, Bai M. Targeted zwitterionic near infrared fluorescent probe for improved imaging of type 2 cannabinoid receptors. J Biomed Opt. 2014;19(3):36006.
[205] Su D, Teoh CL, Samanta A, Kang NY, Park SJ, Chang YT. The development of a highly photostable and chemically stable zwitterionic near-infrared dye for imaging applications. Chem Commun (Camb). 2015;51(19):3989.
[206] Ji Y, Wang Y, Zhang N, Xu S, Zhang L, Wang Q, et al. Cell-Permeable Fluorogenic Probes for Identification and Imaging Nitroreductases in Live Bacterial Cells. J Org Chem. 2019;84(3):1299.
[207] Zhang C, Zhao Y, Zhao N, Tan D, Zhang H, Chen X, et al. NIRF Optical/PET Dual-Modal Imaging of Hepatocellular Carcinoma Using Heptamethine Carbocyanine Dye. Contrast Media Mol Imaging. 2018;2018:4979746.
[208] Smits AM, van den Hengel LG, van den Brink S, Metz CH, Doevendans PA, Goumans M-J. A new in vitro model for stem cell differentiation and interaction. Stem Cell Res. 2009;2(2):108.

[209] Stanton M, Cronin M, Lehouritis P, Tangney M. In Vivo Bacterial Imaging without Engineering; A Novel Probe-Based Strategy Facilitated by Endogenous Nitroreductase Enzymes. Curr Gene Ther. 2015;15(3):277.
[210] Markova LI, Terpetschnig EA, Patsenker LD. Comparison of a series of hydrophilic squaraine and cyanine dyes for use as biological labels. Dyes Pigm. 2013;99(3):561.
[211] Saikiran M, Sato D, Pandey SS, Kato T. Photophysical investigations of squaraine and cyanine dyes and their interaction with bovine serum albumin. J Phys Conf Ser. 2016;704:012012.
[212] Bae JG, McNamara LE, Nael MA, Mahdi F, Doerksen RJ, Bidwell GL, et al. Nitroreductase-triggered activation of a novel caged fluorescent probe obtained from methylene blue. Chem Commun. 2015;51(64):12787.
[213] Yang QZ, Wen YJ, Zhong AG, Xu J, Shao SJ. An HBT-based fluorescent probe for nitroreductase determination and its application inEscherichia colicell imaging. New J Chem. 2020;44(38):16265.
[214] Fukuda S, Okuda K, Kishino G, Hoshi S, Kawano I, Fukuda M, et al. In vivo retinal and choroidal hypoxia imaging using a novel activatable hypoxia-selective near-infrared fluorescent probe. Graefe's Arch Clin Exp Ophthalmol. 2016;254(12):2373.
[215] Feng L, Ning J, Tian XG, Wang C, Zhang LY, Ma XC, et al. Fluorescent probes for bioactive detection and imaging of phase II metabolic enzymes. Coordin Chem Rev. 2019;399.
[216] Lee JH, Park G, Hong GH, Choi J, Choi HS. Design considerations for targeted optical contrast agents. Quant Imaging Med Surg. 2012;2(4):266.
[217] Hernot S, van Manen L, Debie P, Mieog JSD, Vahrmeijer AL. Latest developments in molecular tracers for fluorescence image-guided cancer surgery. Lancet Oncol. 2019;20(7):e354.
[218] Cilliers C, Nessler I, Christodolu N, Thurber GM. Tracking Antibody Distribution with Near-Infrared Fluorescent Dyes: Impact of Dye Structure and Degree of Labeling on Plasma Clearance. Mol Pharm. 2017;14(5):1623.
[219] Debie P, Declerck NB, van Willigen D, Huygen CM, De Sloovere B, Mateusiak L, et al. The Design and Preclinical Evaluation of a Single-Label Bimodal Nanobody Tracer for Image-Guided Surgery. Biomolecules. 2021;11(3):360.
[220] De Jesus E, Keating JJ, Kularatne SA, Jiang J, Judy R, Predina J, et al. Comparison of Folate Receptor Targeted Optical Contrast Agents for Intraoperative Molecular Imaging. Int J Mol Imaging. 2015;2015:469047.
[221] Cal PM, Frade RF, Chudasama V, Cordeiro C, Caddick S, Gois PM. Targeting cancer cells with folic acid-iminoboronate fluorescent conjugates. Chem Commun (Camb). 2014;50(40):5261.
[222] Liu J, Li Z, Yang X, Liu W, Wang B, Zhu Y, et al. A high-performance imaging probe with NIR luminescence and synergistically enhanced T1-T2 relaxivity for in vivo hepatic tumor targeting and multimodal imaging. Chem Commun (Camb). 2015;51(69):13369.
[223] Zhao X, Jia X, Liu L, Zeng J, Tian K, Zhou T, et al. Double-Cross-Linked Hyaluronic Acid Nanoparticles with pH/Reduction Dual-Responsive Triggered

Release and pH-Modulated Fluorescence for Folate-Receptor-Mediated Targeting Visualized Chemotherapy. Biomacromolecules. 2016;17(4):1496.
[224] Figliola C, Marchal E, Groves BR, Thompson A. A step-wise synthetic approach is necessary to access gamma-conjugates of folate: folate-conjugated prodigiosenes. Rsc Adv. 2019;9(25):14078.
[225] Bettio A, Honer M, Muller C, Bruhlmeier M, Muller U, Schibli R, et al. Synthesis and preclinical evaluation of a folic acid derivative labeled with 18F for PET imaging of folate receptor-positive tumors. J Nucl Med. 2006;47(7):1153.
[226] Muller C. Folate-based radiotracers for PET imaging--update and perspectives. Molecules. 2013;18(5):5005.
[227] Ke C-Y, Mathias CJ, Green MA. Targeting the tumor-associated folate receptor with an 111In-DTPA conjugate of pteroic acid. J Am Chem Soc. 2005;127(20):7421.
[228] Mahalingam SM, Kularatne SA, Myers CH, Gagare P, Norshi M, Liu X, et al. Evaluation of Novel Tumor-Targeted Near-Infrared Probe for Fluorescence-Guided Surgery of Cancer. J Med Chem. 2018;61(21):9637.
[229] Usama SM, Park GK, Nomura S, Baek Y, Choi HS, Burgess K. Role of Albumin in Accumulation and Persistence of Tumor-Seeking Cyanine Dyes. Bioconjug Chem. 2020;31(2):248.
[230] Dunbar CE, High KA, Joung JK, Kohn DB, Ozawa K, Sadelain M. Gene therapy comes of age. Science. 2018;359(6372):175.
[231] Doudna JA, Charpentier E. Genome editing. The new frontier of genome engineering with CRISPR-Cas9. Science. 2014;346(6213):1258096.
[232] Xing H, Meng LH. CRISPR-cas9: a powerful tool towards precision medicine in cancer treatment. Acta Pharmacol Sin. 2020;41(5):583.
[233] Sukumar UK, Rajendran JCB, Gambhir SS, Massoud TF, Paulmurugan R. SP94-Targeted Triblock Copolymer Nanoparticle Delivers Thymidine Kinase–p53–Nitroreductase Triple Therapeutic Gene and Restores Anticancer Function against Hepatocellular Carcinoma in Vivo. Acs Appl Mater Inter. 2020;12(10):11307.
[234] Hossain JA, Marchini A, Fehse B, Bjerkvig R, Miletic H. Suicide gene therapy for the treatment of high-grade glioma: past lessons, present trends, and future prospects. Neurooncol Adv. 2020;2(1):vdaa013.
[235] Mowday AM, Dubois LJ, Kubiak AM, Chan-Hyams JVE, Guise CP, Ashoorzadeh A, et al. Use of an optimised enzyme/prodrug combination for Clostridia directed enzyme prodrug therapy induces a significant growth delay in necrotic tumours. Cancer Gene Ther. 2021;DOI: 10.1038/s41417-021-00296-7.
[236] Karjoo Z, Chen X, Hatefi A. Progress and problems with the use of suicide genes for targeted cancer therapy. Adv Drug Deliv Rev. 2016;99:113.
[237] Hill AB, Chen M, Chen CK, Pfeifer BA, Jones CH. Overcoming Gene-Delivery Hurdles: Physiological Considerations for Nonviral Vectors. Trends Biotechnol. 2016;34(2):91.
[238] Penet M-F, Chen Z, Li C, Winnard PT, Bhujwalla ZM. Prodrug enzymes and their applications in image-guided therapy of cancer: tracking prodrug enzymes to minimize collateral damage. Drug Deliv Transl Res. 2012;2(1):22.
[239] Sanduleanu S, Wiel A, Lieverse RIY, Marcus D, Ibrahim A, Primakov S, et al. Hypoxia PET Imaging with [18F]-HX4-A Promising Next-Generation Tracer. Cancers (Basel). 2020;12(5):1322.

[240] Park GT, Kim SU, Choi KC. Anti-proliferative Effect of Engineered Neural Stem Cells Expressing Cytosine Deaminase and Interferon-beta against Lymph Node-Derived Metastatic Colorectal Adenocarcinoma in Cellular and Xenograft Mouse Models. Cancer Res Treat. 2017;49(1):79.
[241] Abbaspour A, Esmaeilzadeh A, Sharafi A. Suicide gene therapy-mediated purine nucleoside phosphorylase/fludarabine system for in vitro breast cancer model with emphasis on evaluation of vascular endothelial growth factor promoter efficacy. 3 Biotech. 2021;11(3):140.
[242] Metz MZ, Gutova M, Lacey SF, Abramyants Y, Vo T, Gilchrist M, et al. Neural Stem Cell-Mediated Delivery of Irinotecan-Activating Carboxylesterases to Glioma: Implications for Clinical Use. Stem Cells Transl Med. 2013;2(12):983.
[243] Keu KV, Witney TH, Yaghoubi S, Rosenberg J, Kurien A, Magnusson R, et al. Reporter gene imaging of targeted T cell immunotherapy in recurrent glioma. Sci Transl Med. 2017;9(373):eaag2196.
[244] Iafrate M, Fruhwirth GO. How Non-invasive in vivo Cell Tracking Supports the Development and Translation of Cancer Immunotherapies. Front Physiol. 2020;11:154.
[245] Majzner RG, Mackall CL. Clinical lessons learned from the first leg of the CAR T cell journey. Nat Med. 2019;25(9):1341.
[246] Yu S, Yi M, Qin S, Wu K. Next generation chimeric antigen receptor T cells: safety strategies to overcome toxicity. Mol Cancer. 2019;18(1):125.
[247] Sellmyer MA, Richman SA, Lohith K, Hou C, Weng CC, Mach RH, et al. Imaging CAR T Cell Trafficking with eDHFR as a PET Reporter Gene. Mol Ther. 2020;28(1):42.
[248] Simonetta F, Alam IS, Lohmeyer JK, Sahaf B, Good Z, Chen W, et al. Molecular Imaging of Chimeric Antigen Receptor T Cells by ICOS-ImmunoPET. Clin Cancer Res. 2021;27(4):1058.
[249] Casucci M, Falcone L, Camisa B, Norelli M, Porcellini S, Stornaiuolo A, et al. Extracellular NGFR Spacers Allow Efficient Tracking and Enrichment of Fully Functional CAR-T Cells Co-Expressing a Suicide Gene. Front Immunol. 2018;9:507.
[250] Diaconu I, Ballard B, Zhang M, Chen Y, West J, Dotti G, et al. Inducible Caspase-9 Selectively Modulates the Toxicities of CD19-Specific Chimeric Antigen Receptor-Modified T Cells. Mol Ther. 2017;25(3):580.
[251] Iwasawa C, Tamura R, Sugiura Y, Suzuki S, Kuzumaki N, Narita M, et al. Increased Cytotoxicity of Herpes Simplex Virus Thymidine Kinase Expression in Human Induced Pluripotent Stem Cells. Int J Mol Sci. 2019;20(4):810.
[252] Klebanoff CA, Rosenberg SA, Restifo NP. Prospects for gene-engineered T cell immunotherapy for solid cancers. Nat Med. 2016;22(1):26.

App. I

8. Appendix I:

1. Introduction

To further increase signal specificity, targeted strategies employing activatable fluorescent dyes may be implemented. The advantage of these dyes over "always-on" fluorophores is that they exhibit reduced off-target fluorescence signals and provide increased TBR [1, 2]. The fluorescence of such dyes is quenched until activation by tumour-specific enzymes [3] or by chemical reactions following cellular accumulation [4, 5]. CytoCy5S is a NIR activatable fluorophore whose fluorescence is quenched by the presence of the 3,5-dinitrobenzyl moiety. The enzyme nitroreductase NfsB (NTR) from *E. coli* is able to reduce the nitro groups ($-NO_2$) to hydroxylamines (-NHOH) restoring its fluorescence. This bioreductive mechanism has previously been exploited to follow-up the dissemination of NTR-expressing cancer cells using CytoCy5S-FLI, providing higher sensitivity than bioluminescence or GFP-FLI, and to evaluate the therapeutic efficacy of a prodrug in a preclinical metastatic model [6].

The NTR-activatable fluorescent dye CytoCy5S (substrate **1** in **paper I**) was conjugated to EDAF to obtain a fluorescent conjugate (**2**) that is expected to bind to the membrane-bound FRα. Endolysosomal internalisation of the conjugate and release of the fluorophore, with subsequent fluorescence enhancement after the activating reduction by NTR, will allow the localisation of engineered NTR-expressing cancer cells. Furthermore, compared to the free dye, a reduction of the fluorescence signal in healthy tissues is expected. To test all this, the *in vitro* behaviour of this conjugate was compared with that of a conjugate (**1**) formed by an "always-on" fluorophore with the same squaraine scaffold (Cy5 active).

2. Results and discussion

The specificity of **1** and **2** (Figure 1) towards FRα was investigated *in vitro* by fluorescence microscopy using three different cells lines, Skov-3, OV-90 and A549, with intermediate (Skov-3 and OV-90) and low (A549) levels of expression of the molecular target. First, calcein AM (green fluorescence) stained Skov-3^{NTR+} and A549 cells were incubated with **1** or **2** for 2.5 h and up to 36 h and imaged (Figure 1). A weak NIR fluorescence signal was observed 2.5 hours after incubation with **1**, which increased with longer incubation times, particularly at 24 and 36 hours in Skov-3^{NTR+} (Figure 1a). A weaker NIR fluorescence signal is also observed in the negative control cell line A549 at 36 hours. No fluorescence signal in cells incubated with **2** was obtained at any of the given incubation times (Figure 1b). We next used the GFP^+ OC cell line OV-90, which allowed us to follow the fate of **1** over time, starting 8 hours after conjugate removal. These results confirmed the data obtained previously (Figure 1a), demonstrating that the contrast agent is not able to reach the cytoplasm, but is retained in vesicles for up to 24 hours after removal of the conjugate from the medium.

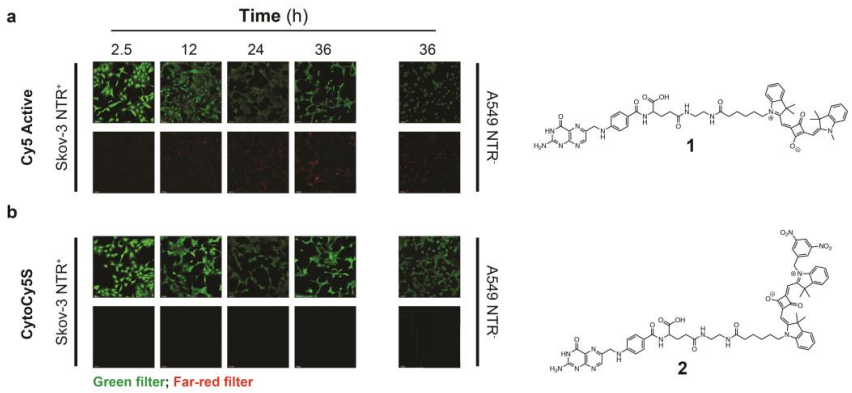

Figure 1: Live cell fluorescence confocal microscopy imaging. Images of the representative times for the green channel and for the far-red channel are presented with their corresponding chemical structures for a) **1**, "always-on" dye and b) **2**, activatable dye.

The selected activatable Cy5-derivative **2** and its control **1** served as proof of principle prior to working with more clinically relevant fluorophores e.g. Cy7. Retention in vesicles was observed after internalisation of **1** in the two different experiments, thus preventing the passage of the dye to the cytoplasm. This observation has a major impact for the use of **2** as the release of the dye into the cytoplasm is imperative for the activating reduction by NTR to occur and therefore no fluorescence signal can be observed at any given time with this conjugate. This finding deterred us from further experiments with these conjugates and prompted us to study new linkers to ensure cytoplasmic release of the CytoCy5S fluorophore to ultimately reduce the off-target signal in optical FLI (ongoing work in our group).

3. Materials and methods

3.1 Synthetic overview of conjugates 1 and 2

γ-Ethylenediamine folate was conjugated to the NHS esters of Cy5 active (**1**, in house synthesised) and CytoCy5S (**2**, in house synthesised). As shown in Scheme 1, activation of the carboxylic acid of the dyes **3** and **4** was performed by reacting them with NHS and DIC in dry DMSO at rt overnight. **5** and **6** were purified by RP-HPLC and further reacted with EDAF and DIPEA in dry DMSO at rt for 6 h to give conjugates **1** and **2** in modest yields. Conjugates **1** and **2** were purified by RP-HPLC prior to *in vitro* and *in vivo* testing.

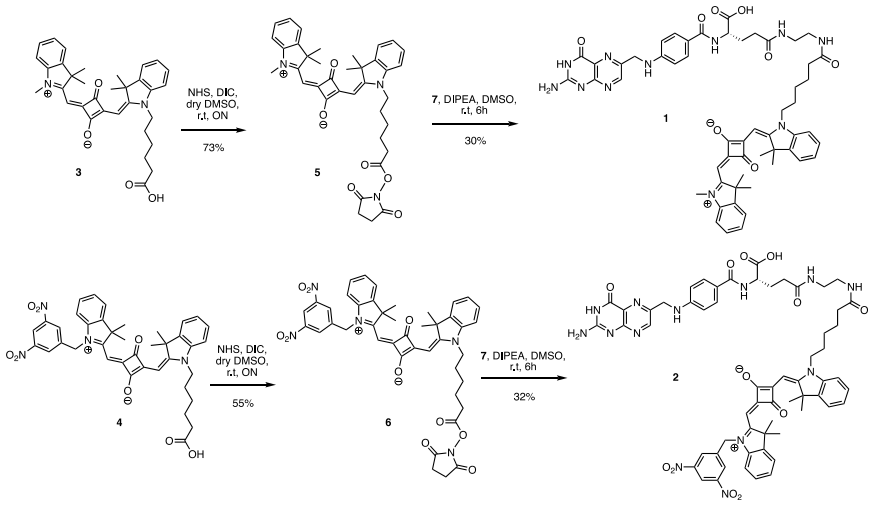

Scheme 1. Synthesis of EDAF-Cy5 conjugates.

3.2 Cell lines and cell culture

Human ovarian carcinoma, Skov-3 and OV-90^{GFP+} and lung carcinoma A549 cell lines were employed to study the suitability of conjugates **1** and **2** in a targeted approach. Cells were cultured in DMEM (Sigma-Aldrich, St. Louis, USA) with exception of OV-90 cultured in RPMI 1640, supplemented with 10% FBS and 1% L-glutamine (Sigma-Aldrich), and kept at 37 °C and 5% CO_2. Skov-3 and OV-90^{GFP+} cell lines were transduced *in vitro* to express *E. coli* NfsB nitroreductase (NTR) using lentiviral particles [7]. NTR expression was assessed using an established flow cytometric method [6].

3.3 Confocal fluorescence microscopy

1 x 10^5 Skov-3^{NTR+} cells were seeded in 35 mm µ-dishes with high glass bottom (Ibidi, Martinsried, Germany) and incubated with 4 µM of **1** or **2** for 2.5, 12, 24 and 36 hours at 75% confluency. 1 x 10^5 of A549^{NTR-} cells incubated for 36 hours with 4 µM of the aforementioned conjugates were employed as negative control. 30 minutes before fluorescence imaging, cells were washed with PBS and fresh medium containing calcein AM (1 µM) was added.

OV-90$^{GFP+NTR+}$ cells (1 x 10^5) were incubated with **1** for 14 hours. After this time, the cells were thoroughly washed with PBS and fresh medium was added. 8 hours post-removal of the conjugate, fluorescence images were acquired at 10 min intervals for up to 16 hours (24 hours post-removal). Cells were maintained at 37 °C and 5% CO_2.

Live cell imaging fluorescence was acquired using a confocal Andor Dragonfly microscope (Oxford Instruments America, Inc., Concord MA, USA) with a 40X magnification. 488 nm excitation filter and green emission filter (500 to 550 nm) for calcein AM internalisation and GFP expression and 637 nm excitation filter and far-red emission filter (663 to 738 nm) for Cy5-derivatives interrogation were employed. All data collected were analysed with Imaris 9.6 (Oxford Instruments, USA).

3.4 Synthesis of (*Z*)-4-((1-(5-carboxypentyl)-3,3-dimethyl-3*H*-indol-1-ium-2-yl)methylene)-3-oxo-2-(((*E*)-1,3,3-trimethylindolin-2-ylidene)methyl)cyclobut-1-en-1-olate (3): [8]

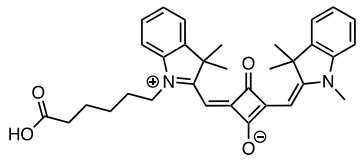

1,2,3,3-Tetramethyl-3*H*-indolium iodide (303 mg, 1.01 mmol), 1-(5-carboxypentyl)-2,3,3-trimethyl-3*H*- indolium iodide (417 mg, 1.04 mmol) and 3,4-dihydroxycyclobutane-1,2-dione (128 mg, 1.10 mmol) were mixed with pyridine (4.5 mL), acetic acid (4.5 mL) and acetic anhydride (1 mL) and the mixture was heated at 110 °C for 3 h. The reaction mixture was partitioned between dichloromethane (10 mL) and water (10 mL) and the organic layer was dried over $MgSO_4$, filtered and the solvent was evaporated to yield an iridescent blue sticky residue. This material was purified using semi-preparative RP-HPLC

(50 - 90% acetonitrile in water, both solvents containing 0.1% formic acid) to give the title compound.

Blue solid; 29 mg (21% yield). ^{1}H-NMR (850 MHz, $(CD_3)_2SO$): δ = 12.10 (bs, 1H), 7.52 (m, 2H), 7.34 (m, 4H), 7.16 (m, 2H), 5.79 (s, 1H), 5.76 (s, 1H), 4.07 (s, 2H), 3.57 (s, 3H), 2.20 (t, *J* = 7.2 Hz, 2H), 1.71 (m, 2H), 1.68 (s, 12H), 1.56 (m, 2H), 1.40 (m, 2H); ^{13}C-NMR (MHz, $(CD_3)_2SO$): δ = 180.5 (2C), 178.8 (2C), 174.3, 169.7, 168.9, 142.8 , 142.2, 141.4 (2C), 127.6 (2C), 123.3 (2C), 121.9 (2C), 109.9 (2C), 85.9, 85.7, 48.4 (2C), 42.5, 33.2, 30.1, 26.1 (5C), 25.6, 23.9; ESI-MS: Calcd. *m/z* for $C_{33}H_{37}N_2O_4^+$ $[M + H]^+$: 525.3; found: 525.3 and 547.3.

3.5 Synthesis of (*Z*)-2-(((*E*)-1-(5-carboxypentyl)-3,3-dimethylindolin-2-ylidene)methyl)-4-((1-(3,5-dinitrobenzyl)-3,3-dimethyl-3*H*-indol-1-ium-2-yl)methylene)-3-oxocyclobut-1-en-1-olate (4): [8]

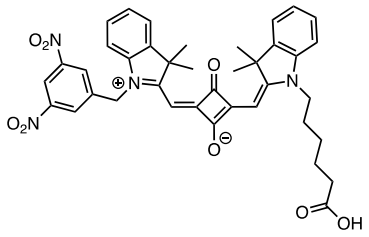

1-(5-Carboxypentyl)-2,3,3-trimethyl-3*H*-indolium iodide (765 mg, 1.9 mmol), 1-(3,5-dinitrobenzyl)-2,3,3-trimethyl-3*H*-indolium iodide (999 mg, 2.1 mmol) and 3,4-dihydroxy-3-cyclobuten-1,2-dione (238 mg, 2.1 mmol) were dissolved in pyridine (9.7 mL), acetic acid (9.7 mL) and acetic anhydride (2.2 mL) and the resulting mixture was heated at 110 °C for 3 h. The reaction mixture was partitioned between dichloromethane (10 mL) and water (10 mL). The combined organic phases were dried over $MgSO_4$, filtered and evaporated under reduced pressure to give an iridescent blue sticky residue (1.261 g), which was purified using semi-preparative RP-HPLC (50 - 90% acetonitrile in water, both solvents containing 0.1% TFA).

Iridiscent blue solid; 109 mg (9% yield). ^{1}H-NMR (850 MHz, $(CD_3)_2SO$) δ = 11.99 (s, 1H), 8.73 (d, *J* = 2.6 Hz, 1H), 8.40 (d, *J* = 2.1 Hz, 2H), 7.58 (d, *J* = 7.3 Hz, 1H), 7.55 (dd, *J* = 7.4, 1.1 Hz, 1H), 7.42 (d, *J* = 8.0 Hz, 1H), 7.38 (td, *J* = 7.7, 1.2 Hz, 1H), 7.29 (td, *J* = 7.6, 1.2 Hz, 1H), 7.23 (q, *J* = 7.2 Hz, 2H), 7.16 (t, *J* = 7.4 Hz, 1H), 5.88 (s, 1H), 5.75 (s, 1H), 5.66 (s, 2H), 4.14 (t, *J* = 7.6 Hz, 2H), 2.20 (t, *J* = 7.3 Hz, 2H), 1.79 (s, 6H), 1.72 (m, 2H), 1.65 (s, 6H), 1.55 (p, *J* = 7.4 Hz, 2H), 1.39 (p, *J* = 7.7 Hz, 2H); HR-ESI-MS: Calcd. *m/z* for $C_{39}H_{39}N_4O_8^+$ $[M+H]^+$: 691.27624; found: 691.27721.

Analytical data are in accordance with those reported previously [8]

3.6 Synthesis of (*Z*)-4-((1-(6-((2,5-dioxopyrrolidin-1-yl)oxy)-6-oxohexyl)-3,3-dimethyl-3*H*-indol-1-ium-2-yl)methylene)-3-oxo-2-(((*E*)-1,3,3-trimethylindolin-2-ylidene)methyl)cyclobut-1-en-1-olate (5):

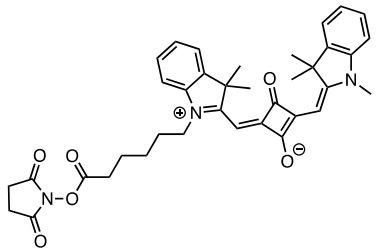

3 (22.4 mg, 0.04 mmol), *N*-hydrosuccinimide (13. 6 mg, 0.11 mmol) and DIC (0.01 mL, 0.06 mmol) were dissolved in 1.5 mL of anhydrous DMSO and the reaction mixture was stirred at rt overnight protected from the light. The excess of solvent was removed by rotary evaporation to give a bright blue sticky solid residue, which was purified using semi-preparative RP-HPLC (50 - 90% acetonitrile in water, both solvents containing 0.1% TFA) to give the title compound.

Iridiscent blue solid; 18.1 mg (73% yield).

3.7 Synthesis of (*Z*)-4-((1-(3,5-dinitrobenzyl)-3,3-dimethyl-3*H*-indol-1-ium-2-yl)methylene)-2-(((*E*)-1-(6-((2,5-dioxopyrrolidin-1-yl)oxy)-6-oxohexyl)-3,3-dimethylindolin-2-ylidene)methyl)-3-oxocyclobut-1-en-1-olate (6):

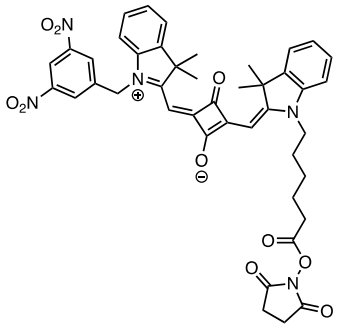

4 (18.5 mg, 0.04 mmol), *N*-hydrosuccinimide (13. 6 mg, 0.11 mmol) and DIC (0.01 mL, 0.06 mmol) were dissolved in 1.5 mL of anhydrous DMSO and the reaction mixture was stirred at rt overnight protected from the light. The excess of solvent was removed by rotary evaporation to give a blue sticky solid residue, which was purified using semi-preparative RP-HPLC (50 - 90% acetonitrile in water, both solvents containing 0.1% TFA) to give the title compound.

Iridiscent blue solid; 17.2 mg (55% yield).

3.8 Synthesis of (*Z*)-4-((1-(6-((2-(4-(4-(((2-amino-4-oxo-3,4-dihydropteridin-6-yl)methyl)amino)benzamido)-4-carboxybutanamido)ethyl)amino)-6-oxohexyl)-3,3-dimethyl-3*H*-indol-1-ium-2-yl)methylene)-3-oxo-2-(((*E*)-1,3,3-trimethylindolin-2-ylidene)methyl)cyclobut-1-en-1-olate (1):

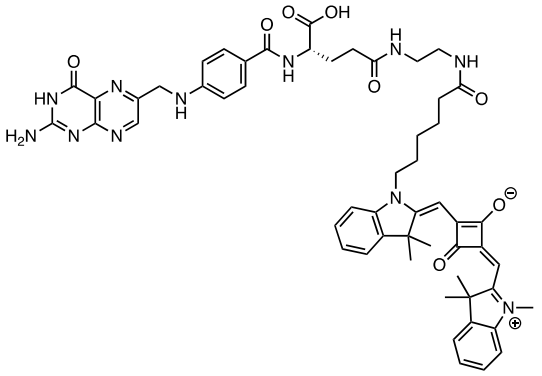

Folate derivative **7** (13 mg, 0.027 mmol), **5** (18.1 mg, 0.03 mmol) and DIPEA (200 µL) were dissolved in DMSO (1.1 mL) and the mixture was stirred for 6 h at rt. The reaction mixture was then purified using semi-preparative RP-HPLC (30 - 90% acetonitrile in water, both solvents containing 0.1% TFA) to give the title compound.

Blue solid; 7.67 mg (30% yield). ESI-MS: Calcd m/z for $C_{54}H_{60}N_{11}O_8^+$ $[M + H]^+$: 990.4621; found: 990.4622.

3.9 Synthesis of (*Z*)-2-(((*E*)-1-(6-((2-(4-(4-(((2-amino-4-oxo-3,4-dihydropteridin-6-yl)methyl)amino)benzamido)-4-carboxybutanamido)ethyl)amino)-6-oxohexyl)-3,3-dimethylindolin-2-ylidene)methyl)-4-((1-(3,5-dinitrobenzyl)-3,3-dimethyl-3*H*-indol-1-ium-2-yl)methylene)-3-oxocyclobut-1-en-1-olate (2):

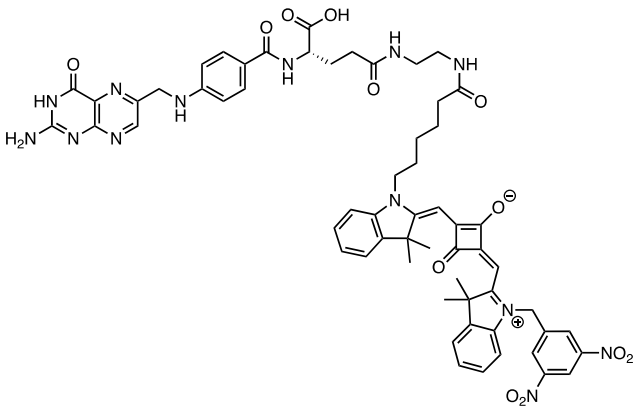

Folic acid derivative **7** (11 mg, 0.022 mmol), **6** (17.2 mg, 0.02 mmol) and DIPEA (200 µL) in DMSO (1 mL) were reacted for 6 h at rt. The reaction mixture was then purified using semi-preparative RP-HPLC (30 - 90% acetonitrile in water, both solvents containing 0.1% TFA) to give the title compound.

Blue solid; 7.99 mg (32% yield). ESI-MS: Calcd m/z for $C_{60}H_{62}N_{13}O_{12}^{+}$ [M + H]$^{+}$: 1156.4635; found: 1156.4638.

Figure 2: ^{1}H-NMR spectrum of **3** in DMSO

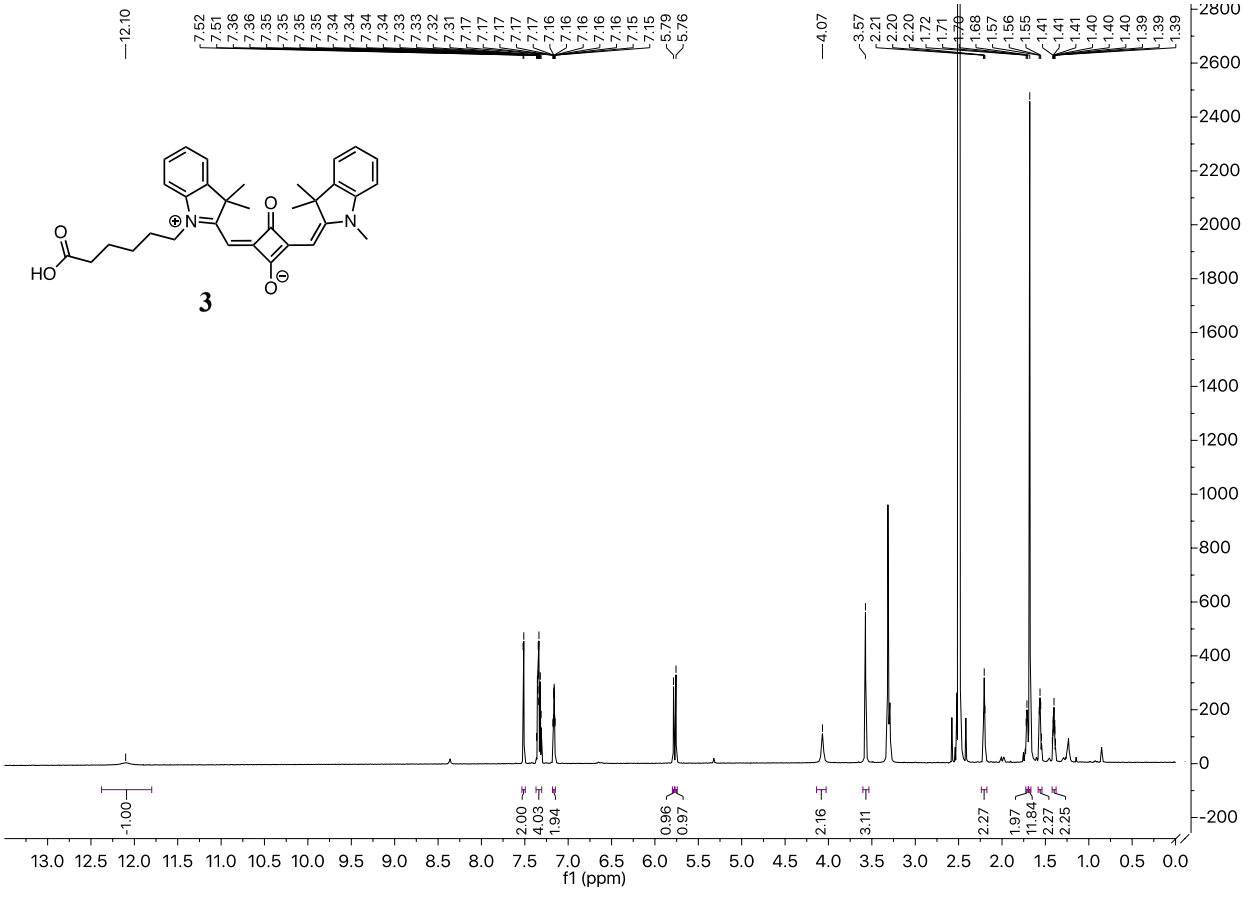

Figure 3: ^{1}H-NMR spectrum of **4** in DMSO

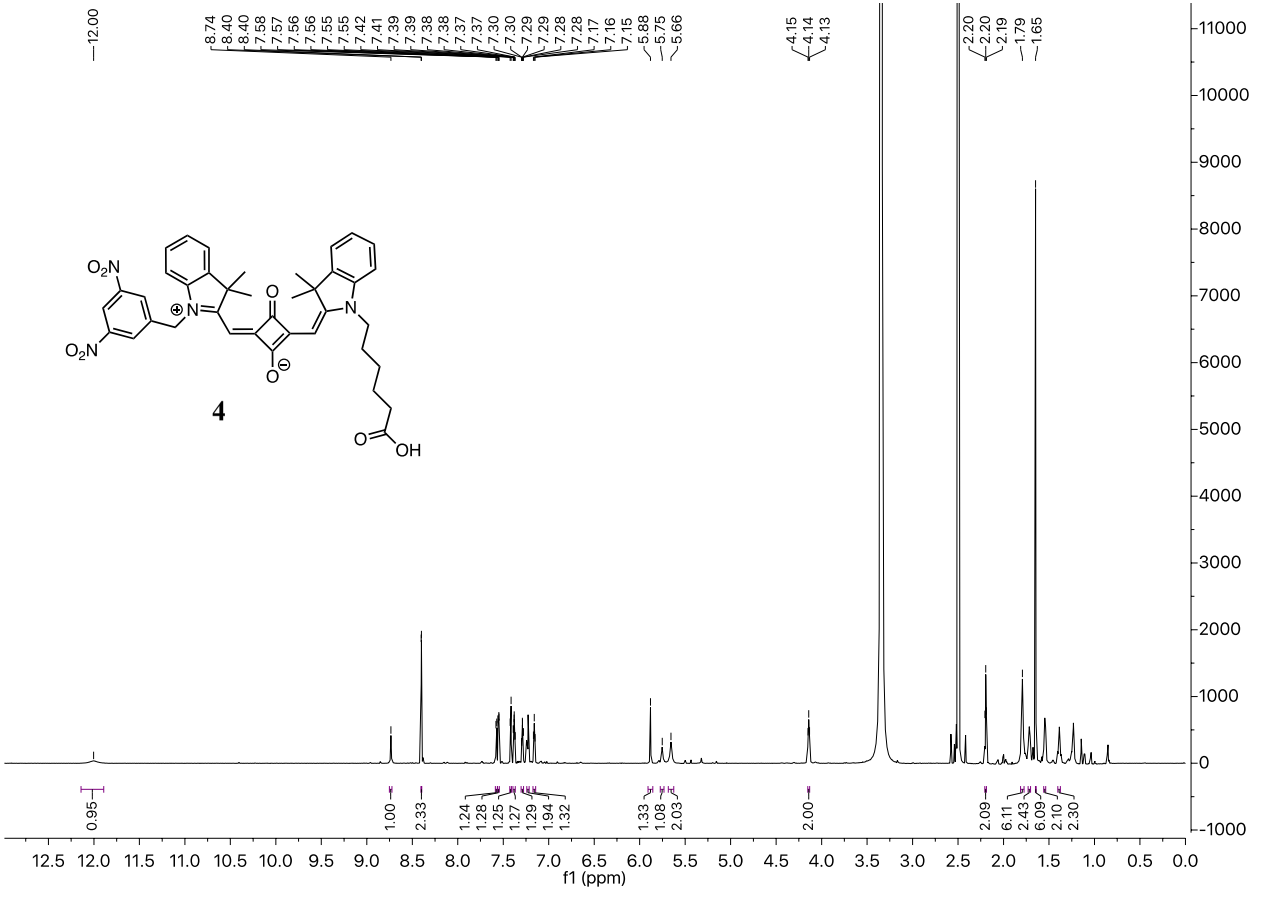

Figure 4: HRMS spectrum of **1**

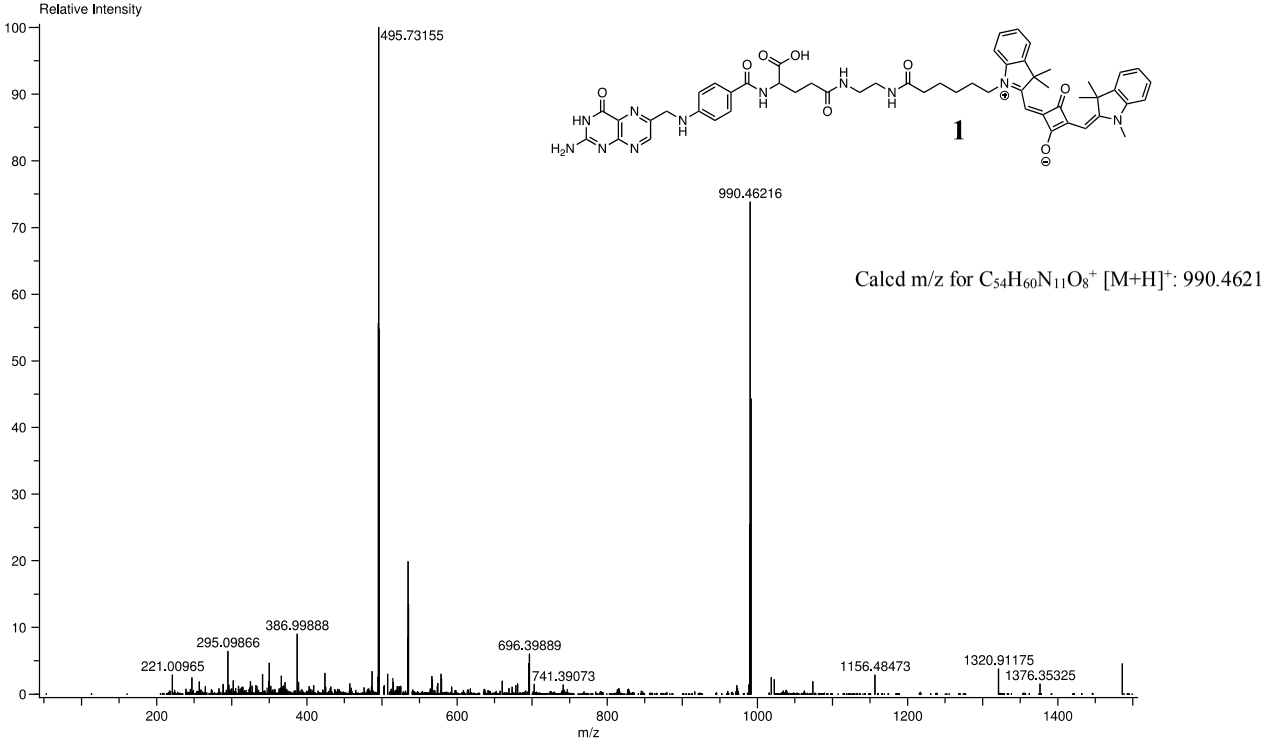

Figure 5: HRMS spectrum of **2**

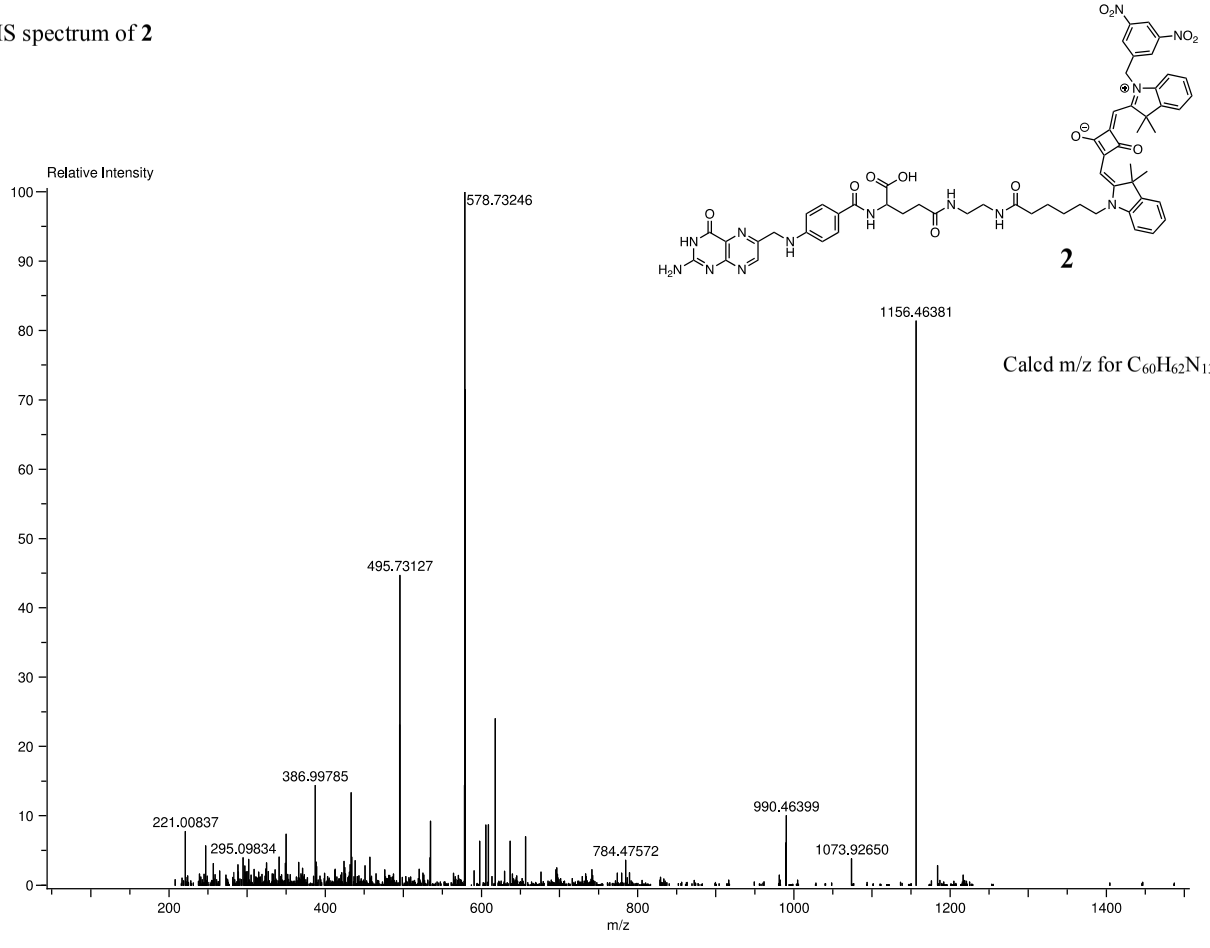

4. References

[1] Lee H, Kim J, Kim H, Kim Y, Choi Y. A folate receptor-specific activatable probe for near-infrared fluorescence imaging of ovarian cancer. Chem Commun (Camb). 2014;50(56):7507-10.
[2] Kim H, Cho MH, Choi HS, Lee BI, Choi Y. Zwitterionic near-infrared fluorophore-conjugated epidermal growth factor for fast, real-time, and target-cell-specific cancer imaging. Theranostics. 2019;9(4):1085-95.
[3] Whitley MJ, Cardona DM, Lazarides AL, Spasojevic I, Ferrer JM, Cahill J, et al. A mouse-human phase 1 co-clinical trial of a protease-activated fluorescent probe for imaging cancer. Sci Transl Med. 2016;8(320).
[4] Obaid G, Spring BQ, Bano S, Hasan T. Activatable clinical fluorophore-quencher antibody pairs as dual molecular probes for the enhanced specificity of image-guided surgery. J Biomed Opt. 2017;22(12).
[5] Mochida A, Ogata F, Nagaya T, Choyke PL, Kobayashi H. Activatable fluorescent probes in fluorescence-guided surgery: Practical considerations. Bioorg Med Chem. 2018;26(4):925-30.
[6] McCormack E, Silden E, West RM, Pavlin T, Micklem DR, Lorens JB, et al. Nitroreductase, a near-infrared reporter platform for in vivo time-domain optical imaging of metastatic cancer. Cancer Res. 2013;73(4):1276-86.
[7] Ruiz de Garibay G, García de Jalón E, Stigen E, Lund KB, Popa M, Davidson B, et al. Repurposing ¹⁸F-FMISO as a PET tracer for translational imaging of nitroreductase-based gene directed enzyme prodrug therapy. Theranostics. 2021;11(12):6044-57.
[8] West RM, Ismail R. (2005). Nitro-substituted squaraine reporter dyes as reagent for measuring nitroreductase enzyme activity. (Patent No. WO2005118839A1). https://worldwide.espacenet.com/patent/search/family/032671256/publication/WO2005118839A1?q=WO2005118839A1

I

CytoCy5S™, a compound of many structures. *In vitro* and *in vivo* evaluation of four near-infrared fluorescent substrates of nitroreductase (NTR)

Elvira García de Jalón[1,2], Gorka Ruiz de Garibay[1], Bengt Erik Haug[2*], Emmet McCormack[1,3,4*]

[1]Centre for Cancer Biomarkers CCBIO, Department of Clinical Science, The University of Bergen, Jonas Lies vei 65, Bergen 5021, Norway; [2]Department of Chemistry and Centre for Pharmacy, University of Bergen, Allégaten 41, N-5007, Bergen, Norway; [3]Centre for Pharmacy, Department of Clinical Science, The University of Bergen, Jonas Lies vei 65, Bergen 5021, Norway; [4]Vivarium, Department of Clinical Medicine, The University of Bergen, Jonas Lies vei 65, 5021 Bergen, Norway.

Corresponding Authors:
Professor Emmet Mc Cormack
Tel: +47 55 97 3097
Email: emmet.mc.cormack@uib.no

Professor Bengt Erik Haug
Tel: +47 55 58 34 68
Email: Bengt-Erik.Haug@uib.no

First Author:
Elvira García de Jalón, M.S.
Tel: + 47 94434599
Email: elvira.vioegra@uib.no

Abstract:

CytoCy5S™, a quenched, red-shifted fluorescent probe, has been used to exploit the imaging potential of the nitroreductase (NTR) reporter gene platform. Its use has been reported in a number of publications, however there are discrepancies in both the reported structure and its physicochemical properties. Herein, we aim to highlight these discrepancies and to define the best candidate of the four substrates under study for preclinical work in NTR reporting by optical applications.

We report the synthesis, purification and characterisation of four NTR substrates, including alternately described structures currently referred by the name CytoCy5S. A comparative NTR enzymatic assay was performed to assess the spectroscopic characteristics of the different reductively activated probes. The NTR expressing triple-negative breast carcinoma cell line, MDA-MB-231 NTR^{+}, was employed to compare, both *in vitro* and *in vivo*, the suitability of these fluorescent probes as reporters of NTR activity. Comparison of the reporting properties was achieved by flow cytometry, fluorescence microscopy and optical imaging, both *in vivo* and *ex vivo*.

This study evaluated the different spectroscopic and biological characteristics of the four substrates and concluded that substrate **1** presents the best features for oncological *in vivo* preclinical optical imaging.

Keywords:

CytoCy5S, Cyanine, Squaraine, Nitroreductase, *NfsB*, Near-Infrared Fluorescence Imaging

1. Introduction

Fluorescence imaging (FLI) is a non-invasive, easy to perform and cheap imaging modality permitting real-time visualisation, which has become fundamentally important in preclinical studies of oncological malignancies [1]. This technique relies on the detection of the light emitted directly by an exogenous fluorescent probe, endogenous reporter gene or indirectly by the combination of a reporter gene and its corresponding fluorescent substrate. By employing an appropriate selection of reporter genes, FLI can be used to assess anatomical location of tumour cells and ongoing biological processes [2, 3].

Of particular relevance in biological applications is the exploitation of the near-infrared (NIR) region of the electromagnetic spectrum (650 - 950 nm) [4, 5]. This privileged region is characterised by reduced tissue absorption caused by haemoglobin or melanin and deeper tissue penetration compared to the visible region [6, 7]. Non-invasive FLI using NIR dyes has proven to be a very useful tool in preclinical oncology models for detection of metastasis and treatment response monitoring in orthotopic models [8] and has been widely explored in both preclinical and clinical settings for fluorescence image-guided surgery [9-12]. A number of fluorescent probes that emit light in the NIR region such as phthalocyanines [13], porphyrins [14] or BODIPY dyes [15] (Figure 1A I - III) have been employed as contrast agents or theranostics. However, so far cyanines and their squaraine analogues (Figure 1A IV - V) have been the preferred NIR dyes for the study of oncological conditions [4, 16].

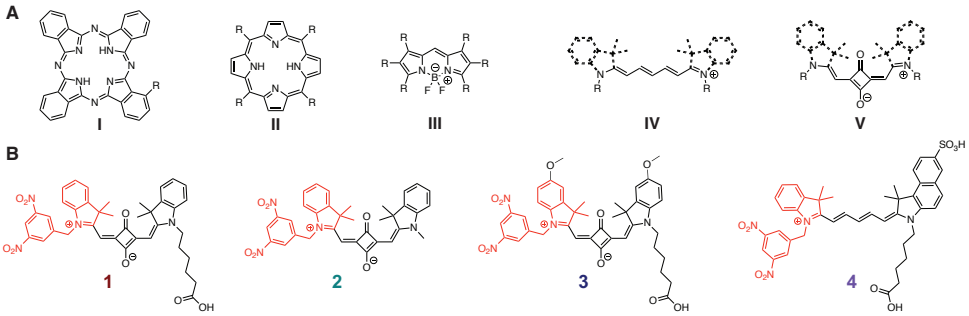

Figure 1: Common scaffolds employed for molecular interrogation in biological applications. **A)** Phthalocyanine (I), porphyrin (II), BODIPY (III), cyanine structure (IV), squaraine structure (V). **B)** Different substrates evaluated in this study. Structures **1** and **4** referred as CytoCy5S in the literature. (Structures are represented in their cis conformation although this is not the most stable one [17]).

One limitation of these "always-on" probes is the accumulation of background fluorescence in off-target tissues that limits the detection of the pathology under study. To overcome this challenge, activatable probes that are specifically activated at the pathology of interest are employed, providing better contrast that allows non-invasive FLI of different biological processes associated with tumour growth [18-21].

Several examples can be found where reductive properties of nitroreductases have been exploited for non-invasive FLI of tumorigenesis and hypoxia in tumour cells [22, 23] but also of bacterial infections and response to antibiotics [24-26], among others [27]. Furthermore, the NTR reporter gene can be exploited as a suicide gene, in a gene directed enzyme prodrug therapy setting (GDEPT), with high potential as a theranostic agent, affording therapy and therapy efficacy visualisation simultaneously [8, 28]. NTR-activatable probes, including CytoCy5S[29] or 6-chloro-9-nitro-5-oxo-5*H*-benzo[a]phenoxazine (CNOB)[30], are non-fluorescent prior to enzymatic metabolism and become highly fluorescent after the catalytic reaction. These NTR-activatable probes contain aromatic nitro groups that render them non-fluorescent. However, reduction of the nitro groups to the

corresponding hydroxylamines and/or amines by nitroreductases in the presence of FMN and NADH and NADPH restores fluorescence (Figure 2) [31, 32].

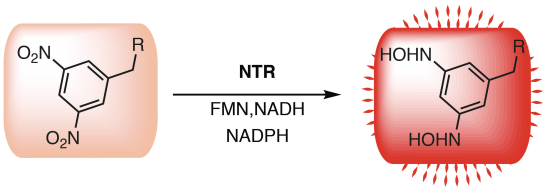

Figure 2: NTR-mediated reduction of aromatic nitro groups

NTR-mediated reduction of substrates **1** - **4** in the presence of FMN (bound to NTR) and NADH and NADPH to give the proposed product and restore fluorescence.

CytoCy5S is the most extensively utilised NTR-activatable fluorescent probe. This compound has been widely exploited for different purposes [8, 24, 33-36] and despite its promising performance, there is a discrepancy in the literature with respect to its structure, as both **1** and **4** (Fig. 1B) have been referred to as CytoCy5S [37-39]. Both structures contain a 3,5-dinitrobenzyl moiety, but while **1** is a squaraine derivative, **4** is a cyanine derivative. Consequently, there is also a lack of consensus in the literature regarding the spectroscopic properties and its behaviour in biological systems, which might hamper its use. The manufacturer describes CytoCy5S as a hydrophobic molecule, with limited availability in aqueous buffers, and with improved cell permeability [40], however Parker *et al.* [41] describe CytoCy5S as a photo-stable and water soluble compound. Furthermore, the reduced version of CytoCy5S is described by the manufacturer as a red-shifted substrate with excitation at 628 nm and emission at 638 nm [40], while Inglese *et al.* [42] reports the excitation and emission maxima for the reduced version to be 647 nm and 667 nm, respectively. No information on the structure was included [40, 42]. In our previous work, the final reduction product of **1** revealed excitation and emission maxima of 631 and 688 nm, respectively [8]. Finally, in a recent review [43], compound **4** is proposed as CytoCy5S and

the version we employed in the aforementioned work [8], **1**, is described as a squaraine analogue of **4**.

Based on these discrepancies in the literature [8, 24, 33, 37, 40, 41, 43], we decided to compare four different NTR-activatable probes, two of them the alternative versions of CytoCy5S found in the literature. In addition, we included compound **2** (squaraine) as we believe that this compound might also have been used as CytoCy5S, however, also in order to investigate how the carboxylic acid tail that is present in both compounds **1** and **4** affects its behaviour in a biological system. Finally, we included compound **3** (squaraine) [37] since this NTR substrate was found to have superior spectroscopic properties to that of compound **1** in an *in vitro* screening of different contrast agents (unpublished data). The four probes (Figure 1B) were synthesised and analysed *in vitro* and *in vivo* in order to shed light on their performance and properties with the intention of identifying the most suitable NIR dye for biological imaging of NTR.

2. Materials and methods

2.1. Synthesis and characterization of dyes 1 - 4

Detailed protocols for the synthesis of **1** - **4** and investigations into increasing the yield for the synthesis of **1** are provided in the electronic supplementary material.

2.2. NTR enzymatic assays

A mixture containing 4.5% DMSO, 60 μM **β**-NADH in 10 mM Tris-HCl and 0.98 mM **β**-NADPH in 10 mM Tris-HCl was prepared and the reaction mixture completed as follows: For the blank, Tris-HCl 10 mM quantum satis (q.s.) and 0.2 μM NTR were added. For the references, 4 μM of either of **1** - **4** (in 90% DMSO and 10% Tris-HCl 100

mM) q.s. was added. And for the study sample, 4 µM of either of **1** - **4** (in 90% DMSO and 10% Tris-HCl 100 mM) q.s. and 0.2 µM NTR were added (all reagents added in the stated order). After a two-hour reaction, the excitation and emission spectra of the different dyes reductively activated by NTR were acquired. Excitation and absorbance scans were performed from 500 to 700 nm and emission scans from 600 to 800 nm in 2 nm steps and a 20 nm bandwidth in both cases.

The optimal settings for excitation and emission were then used to measure the fluorescence intensity during the course of the enzymatic reactions (up to 24 h). The optimal settings for the different substrates were defined as follows: substrates **1** and **2**: $\lambda_{ex}/\lambda_{em}$ 630/645 nm; substrate **3**: $\lambda_{ex}/\lambda_{em}$ 650/670 nm; substrate **4**: $\lambda_{ex}/\lambda_{em}$ 660/690 nm; 5 nm bandwidth in all cases. Fluorescence intensity was analysed using a Tecan Spark® multimode microplate reader (Tecan Group Ltd., Männedorf, Switzerland) and data was plotted as the average ± SD.

2.3. Cell lines and cell culture

The human mammary carcinoma cell line MDA-MB-231 was employed for *in vitro* and *in vivo* assays. MDA-MB-231^{Luc+} (NTR^-) cells were kindly provided by Prof. James Lorens (University of Bergen) and MDA-MB-231$^{Luc+GFP+NTR+}$ (NTR^+) cells have been generated in our lab as previously reported by McCormack *et al.* [8]. All cell types were cultured in DMEM (Sigma-Aldrich, Merck KGaA, Darmstadt, Germany) supplemented with 10% FBS and 1% L-glutamine (Sigma-Aldrich) in a humidified atmosphere at 37 °C and 5% CO_2.

2.4. Flow Cytometry

Comparative quantification of the fluorescence intensities obtained with the different substrates was performed by incubating 1 x 10^5 of the NTR^+ and NTR^- cells (negative

control) with each of them. First, different substrate concentrations (1 μM, 3 μM, 12 μM, 25 μM) were tested, by incubating the cells for one hour. Once the best concentration was identified, different incubation times were assessed in triplicate (0.25 h, 0.5 h, 1 h, 2 h, 4 h and 8 h). In all cases, after the incubation time the cells were rinsed with PBS, trypsinised and washed twice before resuspension in PBS supplemented with 2% BSA. Acquisition was performed in a BD LSR Fortessa flow cytometer (BD Biosciences, Franklin Lakes, NJ, USA) with a 640 nm excitation laser and a 670 ± 14 nm emission filter. The voltage of the detector was optimised for the brightest signal and kept at the optimal setting for all the different experiments.

2.5. Fluorescence microscopy

1 x 10^5 NTR^+ cells were seeded in 35 mm μ-dishes with high glass bottom (Ibidi, Martinsried, Germany) and were incubated with 3 μM of each individual substrate for 10 min. Uptake, fluorescence release and the fate of the reduced substrates in the cell was followed at 10 min intervals for up to 4 h. Cells were maintained at 37 °C and 5% CO_2. Live cell imaging fluorescence was acquired using a confocal Andor Dragonfly microscope (Oxford Instruments America, Inc., Concord MA, USA) with a 40X magnification, with the 488 nm excitation filter and green emission filter (500 to 550 nm) for GFP expression and the 637 nm excitation filter and the far red emission filter (663 to 738 nm) for NTR interrogation. All data collected were analysed with Imaris 9.6 (Oxford Instruments, USA).

2.6. General animal care

All applicable institutional and/or national guidelines for the care and use of animals were followed. All experiments were approved by The Norwegian Animal Research Authority (Application ID 14128) and conducted according to The European Convention

for the Protection of Vertebrates Used for Scientific Purposes. NOD-*scid* IL2Rg^{null} mice (referred to as NSG) were bred at Vivarium (University of Bergen) from breeding pairs purchased from Charles River. Mice were housed in groups of ≤ 5 in individually ventilated cages (Techniplast S.p.A., Buguggiate, Italy). Observations for general condition and body weights were recorded twice a week. Mice were fed with low-autofluorescence rodent imaging food (Rodent imaging diet D1001 from Research diets Inc., Brunswick, USA) from, at least, two weeks prior to experiments. Mice were depilated prior to image acquisition. When required, mice were anesthetised under 1.5% isoflurane (Abbot Laboratories Ltd., North Chicago, USA) and they were euthanised according to institutional guidelines.

2.7. MDA-MB-231 subcutaneous xenografts

NTR$^-$ and NTR$^+$ MDA-MB-231 subcutaneous xenografts were implanted in the left flank of the scapular area by injection of 5 x 10^6 cells suspended in 100 µL DMEM with 25% Matrigel (Corning Inc., Waltham, USA). Tumour volumes were measured weekly with a digital calliper and calculated using the ellipsoid volume formula: Volume = π (length x width x height)/6.

2.8. *in vivo* fluorescence imaging

2.8.1. *in vivo* biodistribution

For biodistribution and pharmacokinetic assessment of the four different substrates, when mean tumour volumes reached 120 ± 16 mm^3, mice were intravenously injected with 100 µL of a 1 mM substrate solution. Optical imaging was performed at established time points (0 h, 0.75 h, 2 h, 4 h, 8 h, 12 h and 24 h) using an IVIS Spectrum imaging system (PerkinElmer Inc., Waltham, USA) with the following filter pairs ($\lambda_{ex}/\lambda_{em}$) 640/680 and 640/700 nm. To assess the background fluorescence, all mice were imaged

prior to injection. Analysis of the collected data was performed with the Living Imaging® software v4.5 (PerkinElmer Inc.). Regions of interest (ROI) in the lateral view were manually drawn around the tumours and fluorescence was expressed as radiance (p/s/cm^2/sr). The radiance values reported were normalised by the mean of the NTR$^-$ radiance values.

2.8.2. Longitudinal tumour imaging

Tumours were longitudinally imaged three times over the course of the tumour progression. Imaging acquisitions were performed when the mean tumour volumes reached 222 ± 44 mm^3, 300 ± 71 mm^3 and 451 ± 115 mm^3. 100 µL of a 1 mM substrate solution were injected intravenously and images were acquired after 0.75 hours for **1** and **3** and after two hours for **2** using an IVIS Spectrum imaging system with λ_{ex} = 640 nm and λ_{em} = 680 nm. To assess the background fluorescence, all mice were imaged prior to injection. Analysis of the collected data was performed as explained before. The radiance values reported were normalised by the mean of the NTR$^-$ radiance values.

2.8.3. *Ex vivo* biodistribution

Mice were euthanised 0.75 hours after i.v. administration of **1** and **3** and two hours after i.v **2** injection (100 µl, 1 mM) and tumours and organs were harvested. Organ biodistribution was assessed for each substrate in the NTR$^-$ and the NTR$^+$ groups. Fluorescence intensities were measured and analysed as explained above. The reported values were normalised by the sum of the radiance values for all organs and they were presented as the percentage of biodistributed substrate in the organs of interest.

2.9. Statistics

Results are given as mean ± standard deviation (SD). All statistical tests were performed using GraphPad Prism v 6.0h (GraphPad Software Inc) and $p < 0.05$ was considered

significant. After randomisation, a one-way ANOVA was applied to ensure unbiased assignment of tumour volumes among the experimental groups. Comparison of means was performed using Student t-tests and one-way ANOVA.

3. Results and discussion

3.1. Synthesis of 1 - 4

Detailed discussion of the different synthetic approaches for **1** – **4**, purification strategies and characterisation by ^{1}H-NMR and high-resolution mass spectrometry (HRMS) are provided in the electronic supplementary material (Figures S1 to S22).

3.2. Spectroscopic properties and performance of the four NTR substrates in an enzymatic assay

After two hours incubation with NTR, absorbance, excitation and emission spectra (Figure S24C and Figure 3A) revealed overlapping excitation and emission maxima for **1** and **2** and higher, red-shifted properties for **3** and **4**, which presented the highest bathochromic shift and the largest Stokes shift (Table 1). For **3**, this far-red shift is a result of the introduction of the methoxy groups, while for **4**, this can be attributed to both the sulfonate group and the lower planarity of cyanines compared to the squaraine derivatives, which renders substrate **4** less conformationally restricted [17]. It was also observed that **1** and **2** exhibit an emission intensity in the same range as their corresponding excitation, although **2** exhibits a markedly lower absolute fluorescence intensity. **3** and **4**, however, exhibit high excitation intensities but very low emission intensities (Table 1). The UV-vis-NIR absorbance spectra of the quenched substrates and the vis-NIR absorbance spectra of the reduced substrates can be found in the electronic supplementary material (Figure S24).

240 **Table 1:** General spectroscopic properties from the substrates under study.

Substrate	Excitation max. (nm)	Emission max. (nm)	Stokes Shift (nm)	Excitation intensity (RFU)	Emission intensity (RFU)
1	628	646	18	18500	18800
2	628	646	18	3000	4300
3	650	670	20	25000	4300
4	666	692	26	205000	28000

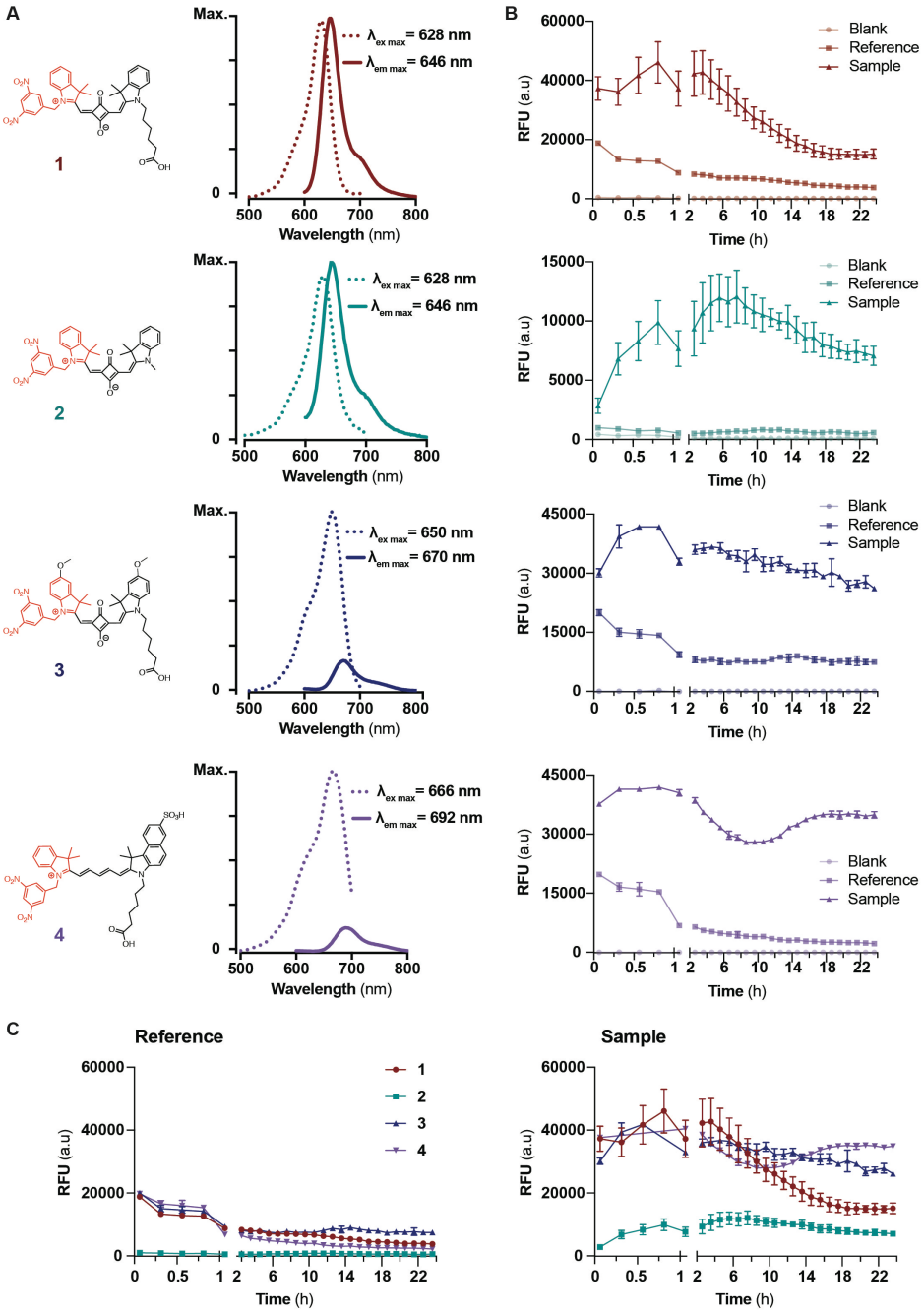

Figure 3: Spectral characterisation of substrates **1 - 4**

A) Chemical structures of substrates **1** – **4** and their respective excitation and emission spectra after two hours incubation of 4 μM of substrate and 0.2 μM NTR enzyme. The Y axis represents both the excitation and

emission fluorescence intensity maxima expressed in Relative Fluorescence Units (RFU) for each substrate. For each dye the maximum of the scale is adjusted to the highest excitation RFU as follows: **1** (Max: 19000 RFU), **2** (Max: 4500 RFU), **3** (Max: 25000 RFU) and **4** (Max: 210000 RFU). **B)** Kinetic assessment of NTR reduction of the four different substrates, starting 3 minutes after NTR addition and over 24 hours, expressed in Relative Fluorescence Units (RFU) as arbitrary units (a.u.). Blank consists of DMSO, β-NADH and β-NADPH in Tris-HCl buffer and NTR (0.2 μM). Reference contains DMSO, β-NADH and β-NADPH in Tris-HCl buffer and substrate under study (4 μM). Sample is composed of DMSO, β-NADH and β-NADPH in Tris-HCl buffer, substrate under study (4 μM) and NTR (0.2 μM). **C)** Overlay of the four different reduction kinetic curves for the reference and the sample, for easier visual comparison of the fluorescence intensity of the different substrates before and after reduction. From 3 minutes after enzyme addition and up to 24 hours.

From the excitation and emission spectra, the optimal fluorescence settings for each substrate were selected to perform a kinetic assay in which the fluorescence intensity was monitored for 24 hours. As shown in Figure 3B, **1**, **3** and **4** displayed a similar kinetic profile reaching the maximum fluorescence emission intensity at around 0.75 hours, while maximum fluorescence for **2** was reached after seven hours. Of note, **1** exhibits the steepest reduction in fluorescence intensity of all the examined substrates (Figure 3C). Interestingly, despite the low absolute fluorescence intensity of **2**, this is the substrate with the highest ratio of emission intensity at any given time between the reference and the sample, mainly due to the low fluorescence background it exhibits in the presence of NADH and NADPH (Figure 3C). The three other substrates showed higher non-specific activation by the NADH and NADPH present in the mixture. All the data suggest that the four fluorescent probes are suitable substrates of NTR and worthy of biological evaluation in cell cultures.

3.3. *in vitro* performance of the four NTR substrates

The suitability of the four substrates for intracellular interrogation of NTR expression was assessed by incubation of NTR^- and NTR^+ MDA-MB-231 cells with different substrate concentrations (1 – 25 μM), followed by flow cytometry analysis (Figure 4A). The mean fluorescence intensity (MFI) of the NTR^+ cells increased with increasing

concentrations of the substrates, plateauing at 12 µM for **1** and **2**. In contrast, a plateau was not observed for **3**, demonstrating a high dependence of this substrate on the concentration. Indeed, MFI values of around 12 x 10^3 were obtained with 1 µM of **2** and 3 µM of **1**, while 12 µM of **3** were required to obtain MFI in the same range. The MFI of NTR^- cells was notably lower but also increased with increasing concentrations of the substrates, except for **2** where a maximum was reached at 12 µM. **4** performed poorly at any given concentrations in both cell types. For **2**, NTR^+/NTR^- ratios were very similar at all concentrations whereas for **1** and **3** the highest ratios were achieved at 12 µM, due to a higher MFI of the NTR^+ cells for **1** and a reduced MFI of the NTR^- cells for **3**, at this concentration. Substrate **3** shows the highest NTR^+/NTR^- ratios followed by **1** and **2** with comparable ratios.

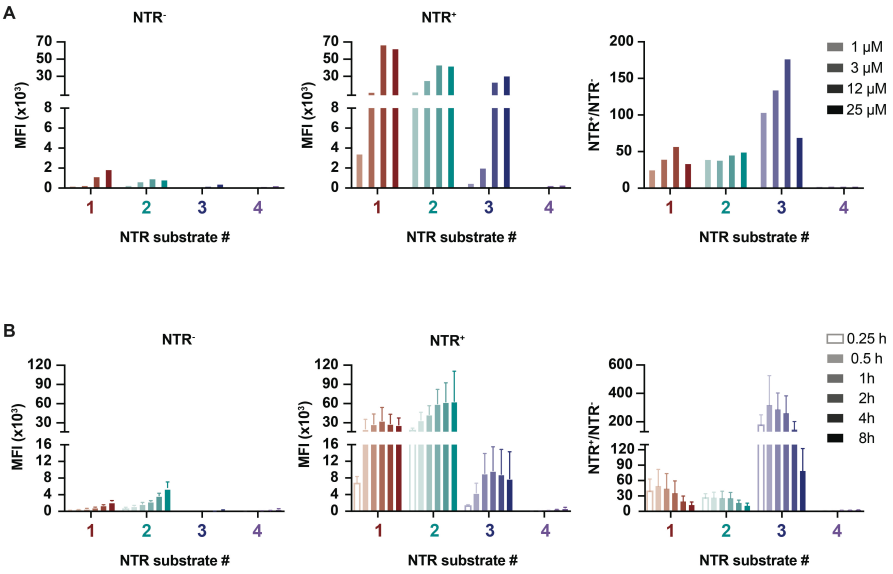

Figure 4: Flow cytometry analysis

A) Dose-dependent fluorescence intensity was assessed by incubation of NTR^- and NTR^+ cells for one hour with increasing concentrations of the four substrates. Values are reported as Mean Fluorescence Intensity (MFI). NTR^+/NTR^- ratios represented for each substrate at the different studied concentrations. **B)** With 3 µM,

time-dependent fluorescence intensity was determined at different incubation times with NTR^- and NTR^+ cells (0.25 h, 0.5 h, 1 h, 2 h, 4 h and 8 h). NTR^+/NTR^- ratios represented for each substrate at the different studied time points.

In order to examine the dependency of MFI on incubation times, the suboptimal concentration of 3 μM was chosen and different incubation times (0.25 h to 8 h) were assessed (Figure 4B). For the NTR^- cells, the MFI showed a similar trend for the four different substrates with the highest values observed at the longest incubation times. Non-specific activation of the substrates was observed, however not significantly higher compared to the unstained cells (Figure S25). For the NTR^+ cells, the fluorescence intensity of **1** and **3** plateaued at two hours, in accordance with the observations in the kinetic enzymatic assay where the fluorescence intensity started to decrease after three hours. The results for **2** are also in accordance with the delayed reduction reaction observed during the kinetic assay (Figure 3B), with MFI values reaching the maximum at eight hours, although in the same range for two, four and eight hours. Interestingly, the NTR^+/NTR^- ratios for all substrates did not increase with increasing incubation times, reaching their maximum after 0.5 h.

Based on the spectroscopic data, similar fluorescence behaviour was expected for **3** and **4**, however, as can be seen in Figures 4A and 4B, the sulfonated **4** exhibited almost no fluorescence enhancement at any of the given conditions. In contrast, substrate **3** resulted in modest MFI values when incubated in NTR^- cells and a high fluorescence enhancement in NTR^+ cells, rendering this substrate around 200 times brighter after reduction (Figure 4B). **1** and **2** showed comparable results, both under concentration- and time-dependent conditions, with NTR^+/NTR^- ratios in the same range.

The flow cytometry results suggest different substrate-cell interactions and confocal fluorescence microscopy was performed to investigate the intracellular behaviour of the

substrates. Qualitative analysis of the fluorescence live imaging of NTR^+ cells incubated with the different substrates (3 μM) corroborated the previous observations, yielding **1** and **2** as the brightest substrates and highlighting the low emission intensity from **3** and **4** (Figure S23). As can be seen in Figure 5, substrate **4** required longer incubation times for the signal to be observed. From the images obtained, cellular accumulation of this substrate occurred in discrete vesicle-like structures, in contrast to the more homogeneous staining observed for the other substrates. **1**, **2** and **3** displayed homogeneous perinuclear staining. While the localisation of these three substrates was the same, the kinetics of accumulation of **3** differed from the others. The first two substrates appear to sustain comparable fluorescence intensity during four hours of incubation, while the fluorescence intensity of **3** starts decaying after 90 minutes of incubation, in line with the steeper decrease in MFI observed in flow cytometry (see video S1 - S4 for full time lapse for each substrate). To get a clearer idea of the biological behaviour of these substrates, in particular regarding tumour biodistribution, they were further investigated in murine xenograft models.

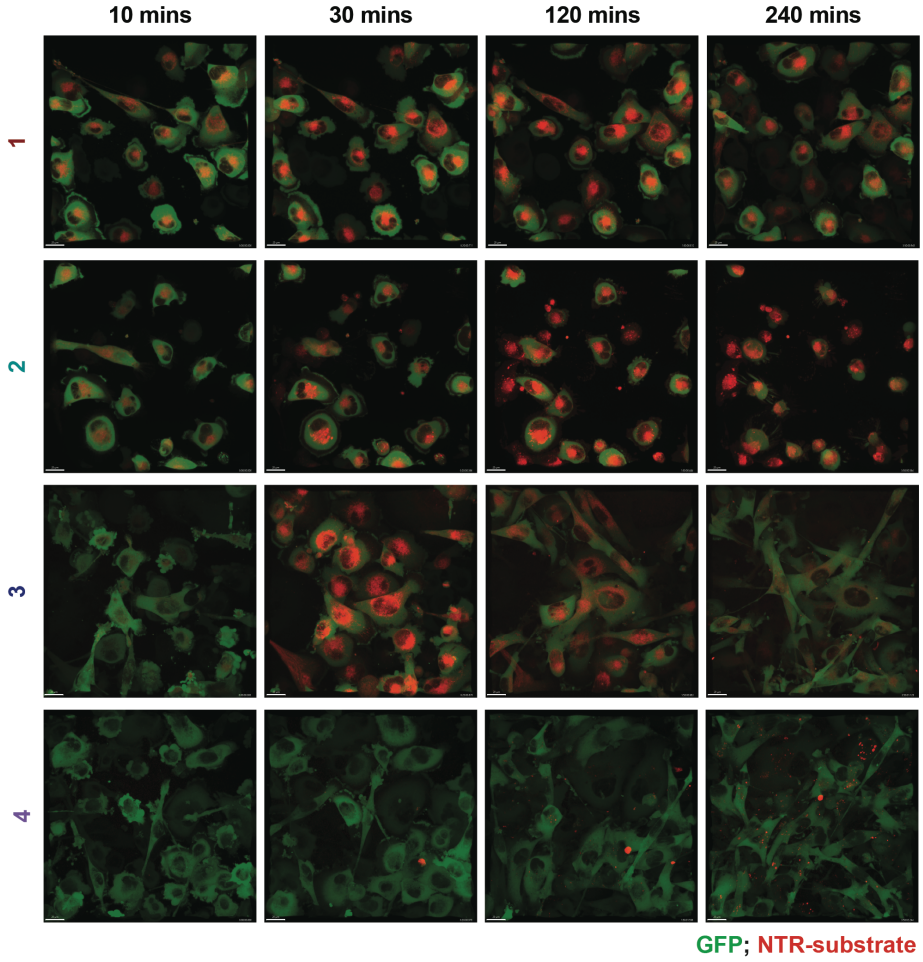

329

330 **Figure 5:** Live cell fluorescence confocal microscopy imaging

331 Uptake, fluorescence enhancement and localisation of the NTR-reduced metabolites were assessed over time
332 and up to four hours. Cells were incubated with 3 µM of each substrate for ten minutes and sequential images
333 were acquired every ten minutes for 240 minutes. Images of the most representative time points are presented
334 as the merged images of the green channel (GFP; excitation: 488 nm and emission: 500 - 550 nm) and far-red
335 channel (NTR-substrate; excitation: 637 nm and emission: 663 – 738 nm) obtained at 40X magnification. GFP
336 is included to allow localisation of the cells in the field of view. Images are displayed in the optimal far-red
337 channel intensity for each of the substrates. A video with the complete time-lapse for each substrate is included
338 in the electronic supplementary material (Video S1 – S4).

339

340 **3.4. *in vivo* biodistribution**

341 To understand the pharmacokinetic properties of these substrates, *in vivo* biodistribution
342 studies over a course of 24 hours were performed and compared in a subcutaneous
343 xenograft model. Mice bearing NTR^- or NTR^+ subcutaneous tumours in the scapular
344 region (indicated by the pink sphere in Figure 6A) were intravenously injected with 100
345 µL of a 1 mM substrate solution and imaging was performed at the optimal excitation
346 and emission wavelengths for each substrate (n = 3 per substrate and cell type). As
347 shown in Figure 6A, fluorescence from the NTR^+ tumours was observed 0.75 hours post-
348 intravenous administration with the exception of **2**, whose signal became obvious two
349 hours post-injection.

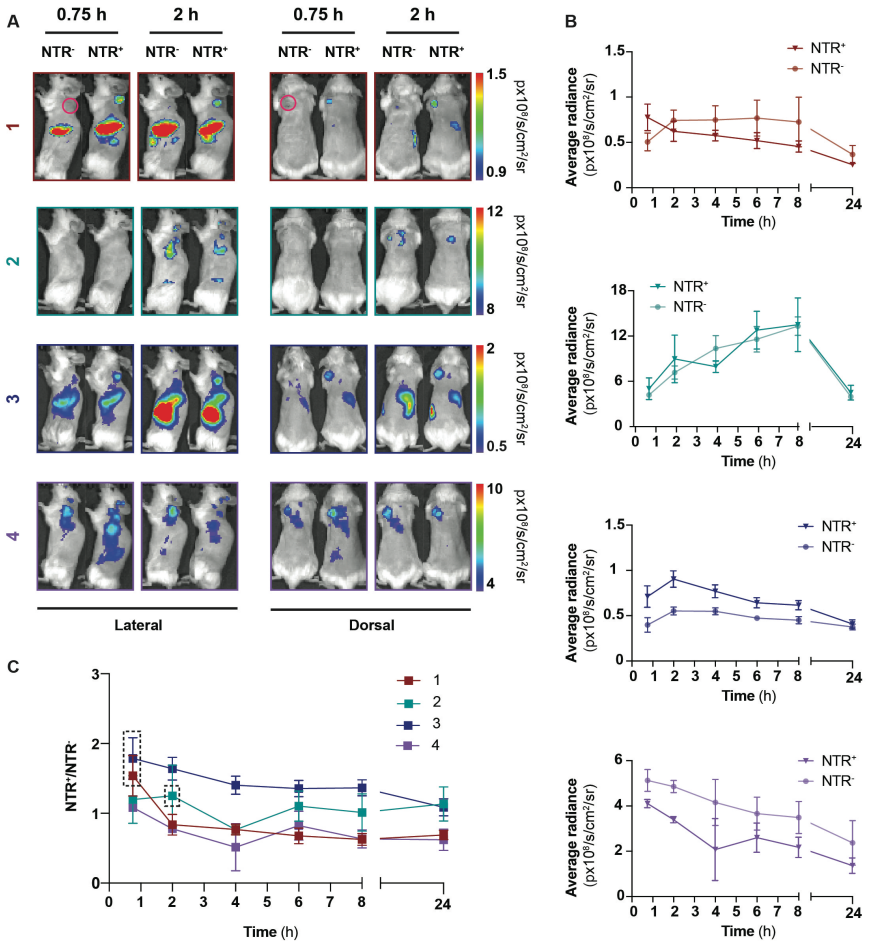

Figure 6: *in vivo* pharmacokinetic assessment

A) NIR FLI of NTR$^-$ and NTR$^+$ xenografts (n = 3 per group per substrate) at the two most representative time points acquired, one and two hours, after i.v. injection of 100 µL of a 1 mM substrate solution. Accumulation in the NTR$^+$ tumours is observed after one-hour injection of **1** and **3** and after two hours for **2**. Substrate **4** accumulates indistinctly in NTR$^-$ and NTR$^+$ tumours at both time points. **B)** Fluorescence intensity of NTR$^-$ and NTR$^+$ tumours over time and up to 24 hours for each substrate. Data expressed as radiance in px10^8/s/cm^2/sr. For substrate **4**, fluorescence intensity is consistently higher in NTR$^-$ than in NTR$^+$ xenografts. **C)** NTR$^+$/NTR$^-$ ratios calculated to determine the time point with the best contrast for each substrate. One hour for **1** and **3** and two hours for **2** (dashed black box) were found optimal.

Radiance decreased with time for substrates **1**, **3** and **4** after 0.75 h, 2 h and 0.75 h respectively, and increased with time for substrate **2** reaching the maximum at 8 h (Figure 6B). As seen in Figure 6C, the best contrast (dashed black box in Figure 6C) for **1** and **3** was observed 0.75 h post-injection, with NTR^+/NTR^- ratios of 1.5 and 1.8 respectively, and after two hours for **2** with an NTR^+/NTR^- ratio of 1.3. These time points were employed for longitudinal imaging. The fluorescence intensity of **4** was consistently higher in NTR^- compared to NTR^+ tumours at all time points studied (Figure 6B), thus it was excluded from further *in vivo* experiments. Interestingly, strong fluorescence intensity decay was observed for **1** after 0.75 h, in accordance with the observations *in vitro*. Also, the decrease in fluorescence emission of **3** after two hours is in line with the fluorescence decay observed by confocal microscopy (Figure 5).

3.5. Longitudinal tumour imaging

Further longitudinal FLI studies were performed at different mean tumour volumes, with the selected incubation times for each substrate. Mice bearing NTR^- and NTR^+ tumours (n = 6 per substrate and cell type) were injected with the three different substrates under study (**1 - 3**) and imaged 0.75 hours or two hours after injection (Figure 7A).

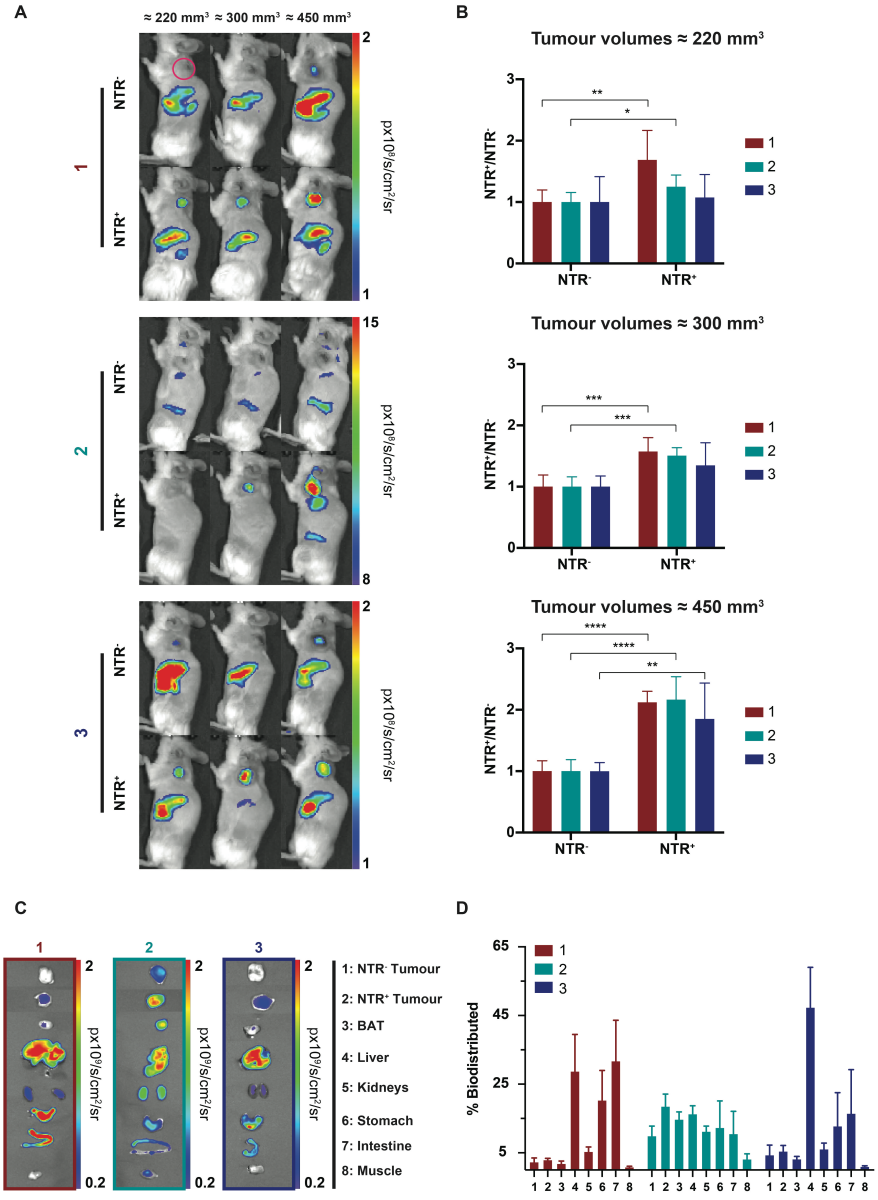

Figure 7: Longitudinal *in vivo* optical imaging of MDA-MB-231 NTR⁻ and NTR⁺ subcutaneous xenografts and *ex vivo* biodistribution

A) Representative NIR fluorescence images of NTR⁻ and NTR⁺ xenografts (n = 6 per group and substrate) at different mean tumour volumes. **B)** NTR⁺/NTR⁻ ratios calculated for the different mean tumour volumes. For **1** and **2**, average radiance was significantly higher in the NTR⁺ group at any mean tumour volume (with *p*-values: **, $p < 0.01$ and *, $p < 0.05$ respectively at 220 mm³; ***, $p < 0.001$ for both at 300 mm³ and ****, $p < 0.0001$

for both at 450). The NTR^- and NTR^+ groups imaged with **3** showed no significant differences in average radiance until mean tumour volumes reached 450 mm^3 (**, $p < 0.01$). **C)** *ex vivo* biodistribution assessment after i.v. injection of 100 µL of a 1 mM substrate solution. Values expressed as radiance in $px10^9/s/cm^2/sr$. 1: NTR^- tumour; 2: NTR^+ tumour 3: Interscapular brown adipose tissue (BAT); 4: Liver; 5: Kidneys; 6: Stomach; 7: Intestine; 8: Muscle. **D)** *ex vivo* biodistribution of the different substrates represented as % of sum average radiance in all organs. It shows hepatobiliary clearance of **1** and **3** and high biodistribution of the former in the gastrointestinal tract. **2** biodistributes, to all organs studied, in a more homogenous manner than the other two substrates. Higher biodistribution in NTR^+ tumours than in NTR^- was observed in all instances.

For **1** and **2** average radiance was significantly higher in the NTR^+ group at any mean tumour volumes. NTR^+/NTR^- ratios through the longitudinal image range for **1** from 1.7 ± 0.5 to 2.1 ± 0.2 (*p*-values from 0.01 to 0.0001) and for **2** from 1.3 ± 0.2 to 2.2 ± 0.4 (*p*-values from 0.05 to 0.0001). In the case of **3**, no significant differences in average radiance were observed until mean tumour volumes reached 450 mm^3 when NTR^+/NTR^- ratio was 1.9 ± 0.6 ($p < 0.01$) (Figure 7B). As observed in Figure 4A, substrate **3** requires higher concentrations (12 µM) to achieve fluorescence intensities in the range of those obtained with 3 µM of **1** or 1 µM of **2**. It was also observed that, due to the low brightness of substrate **3**, fluorescence intensities after 0.75 h were closer to background fluorescence than those from the other two substrates. NTR^+/background ratios for substrates **1**, **2** and **3** were 3.8 ± 2.1, 14.0 ± 5.9 and 2.9 ± 1.3, respectively. From these results it can be concluded that tumour contrast increased with the increase of the mean tumour volumes for all substrates. The quantitative comparison of fluorescence intensity as a function of time in NTR^+ vs. NTR^- xenografts over the progression of the tumours allowed us to conclude that **1** is the best substrate for *in vivo* NTR interrogation even at small tumour volumes, with the highest significance between groups.

3.6. *ex vivo* biodistribution

To acquire a deeper understanding of the substrates' biodistribution, 0.75 hours post-injection of 100 µL of a 1 mM solution of **1** and **3** and two hours post-injection of **2**,

NTR$^-$ and NTR$^+$ tumour-bearing mice were euthanised, their organs excised and imaged (Figure 7C). The percentage of biodistributed substrate was calculated and plotted in Figure 7D. Consistent with the *in vivo* observations (Figure 6A) high hepatobiliary uptake is observed for **1** and particularly for **3**, compatible with their highly lipophilic character. **1** also exhibits high fluorescence signal in the gastrointestinal tract with uptake in the stomach and with high uptake in the large intestine, due to activation by bacterial nitroreductases present in the GI tract [8, 33]. **2** exhibits a homogeneous accumulation pattern in all organs, without clear hepatobiliary or renal excretion pathway evidence, and with a slightly higher accumulation in NTR$^+$ tumours compared to other organs. Residual signal is also observed for substrate **2** in control organs such as muscle and in mitochondria-enriched tissues, with known nitroreductase activity [44], such as the interscapular brown adipose tissue.

4. Conclusions

We have previously demonstrated that CytoCy5S is useful for non-invasive preclinical NIR NTR reporter gene imaging in cancers *in vivo* [8]. In the present study, we set out to clarify an ongoing discrepancy regarding the structure and physicochemical properties of CytoCy5S in order to establish which of the structures denoted CytoCy5S is best suited for preclinical studies in oncology models.

The introduction of the methoxy group in **3** and the sulfonate and cyanine scaffold in **4** resulted in a modest bathochromic shift compared to **1** and **2**. All compounds were confirmed as NTR substrates with delayed kinetics observed for **2** and low emission intensities for **3** and **4**. *In vitro,* **3** was found to display the highest NTR$^+$/NTR$^-$ ratio, followed by **1**. **4** performed poorly *in vitro* and *in vivo*. These results are in line with

previous studies which reported that due to the contribution of the sulfonate group to increased fluorescent probe polarity these compounds exhibit limited lipid bilayer penetrance [45, 46]. Despite its promising performance *in vitro*, **3** did not prove useful for discerning between NTR^- and NTR^+ until tumours reached 450 mm^3 due to the limited brightness of this substrate *in vivo*. This substrate might benefit from an increase in concentration for *in vivo* applications, and although this may yield better imaging results, the cost may make *in vivo* use of this probe impracticable. **1** and **2** provided similar suitability for NTR interrogation, being **1** slightly more sensitive at smaller tumour volumes and presenting faster kinetics.

In conclusion, the spectral and biological properties of substrates **1 – 4** have been discerned and compared. NIR dye **1** was found to be best suited for imaging of NTR, both *in vitro* and *in vivo*, with superior kinetics and lower background fluorescence from surrounding tissues allowing a better delineation of tumours in our model than **2**. The latter result could potentially be explained by **2** having a methyl group and thus is expected to more easily permeate across cell membranes. Another key advantage of **1** over **2** is the presence of the carboxylic functionality, which can be exploited for further derivatisation or conjugation to biomolecules of interest for biomarker interrogation, making substrate **1** the ideal candidate for further studies. Although the substrates have been investigated in an oncology model we believe that these results can be extrapolated to other uses as already shown elsewhere [24].

Declaration of competing interest

The authors declare that they have no known competing financial interests or personal relationships that could have appeared to influence the work reported in this paper.

Acknowledgements

The authors would like to thank Constance de Villardi de Montlaur for technical assistance with the animal work. Flow cytometry analysis was performed at the Flow Cytometry Core Facility, fluorescence microscopy was carried out at the Molecular Imaging Center (MIC) and all the *in vivo* work was performed at the animal facility in Vivarium, Department of Clinical Medicine, University of Bergen. The authors thank Brith Bergum for excellent flow cytometry technical support. Bjarte Holmelid is thanked for the technical support with the HRMS spectra acquisition and for the insightful discussions regarding optimal MS conditions. Jarl Underhaug is thanked for technical assistance with NMR. This work was partly supported by the Research Council of Norway through the Norwegian NMR Platform, NNP (226244/F50). Funding sources are acknowledged for making this work possible, University of Bergen (815900), The Norwegian Cancer Society (182735), The Research Council of Norway through its Centres of Excellence funding scheme (223250, 262652 and SonoCURE grant no. 250317), Helse Vest RHF and Helse Bergen HF (911809, 911852, 912171, 240222, 911974, HV1269). Elvira García de Jalón was the recipient of a MedIm bridging grant from the Norwegian Research School in Medical Imaging.

References

[1] Martelli C, Lo Dico A, Diceglie C, Lucignani G, Ottobrini L. Optical imaging probes in oncology. Oncotarget. 2016;7(30):48753.

[2] Li M, Wang Y, Liu M, Lan X. Multimodality reporter gene imaging: Construction strategies and application. Theranostics. 2018;8(11):2954-73.

[3] Shaikh FA, Kurtys E, Kubassova O, Roettger D. Reporter gene imaging and its role in imaging-based drug development. Drug Discov Today. 2020;25(3):582-92.

[4] Luo SL, Zhang EL, Su YP, Cheng TM, Shi CM. A review of NIR dyes in cancer targeting and imaging. Biomaterials. 2011;32(29):7127-38.

[5] Owens EA, Lee S, Choi J, Henary M, Choi HS. NIR fluorescent small molecules for intraoperative imaging. Wiley Interdiscip Rev Nanomed Nanobiotechnol. 2015;7(6):828-38.

[6] Jacques SL. Optical properties of biological tissues: a review. Phys Med Biol. 2013;58(11):R37-61.

[7] Owens EA, Henary M, El Fakhri G, Choi HS. Tissue-Specific Near-Infrared Fluorescence Imaging. Accounts Chem Res. 2016;49(9):1731-40.

[8] McCormack E, Silden E, West RM, Pavlin T, Micklem DR, Lorens JB, et al. Nitroreductase, a near-infrared reporter platform for in vivo time-domain optical imaging of metastatic cancer. Cancer Res. 2013;73(4):1276-86.

[9] van Dam GM, Themelis G, Crane LMA, Harlaar NJ, Pleijhuis RG, Kelder W, et al. Intraoperative tumor-specific fluorescence imaging in ovarian cancer by folate receptor-alpha targeting: first in-human results. Nat Med. 2011;17(10):1315-9.

[10] Zhu B, Wu G, Robinson H, Wilganowski N, Hall MA, Ghosh SC, et al. Tumor margin detection using quantitative NIRF molecular imaging targeting EpCAM validated by far red gene reporter iRFP. Mol Imaging Biol. 2013;15(5):560-8.

[11] Hoogstins CES, Tummers QRJG, Gaarenstroom KN, de Kroon CD, Trimbos JBMZ, Bosse T, et al. A Novel Tumor-Specific Agent for Intraoperative Near-Infrared Fluorescence Imaging: A Translational Study in Healthy Volunteers and Patients with Ovarian Cancer. Clin Cancer Res. 2016;22(12):2929-38.

[12] Kleinmanns K, Fosse V, Davidson B, de Jalon EG, Tenstad O, Bjorge L, et al. CD24-targeted intraoperative fluorescence image-guided surgery leads to improved cytoreduction of ovarian cancer in a preclinical orthotopic surgical model. EBioMedicine. 2020;56:102783.

[13] Li X, Yu S, Lee Y, Guo T, Kwon N, Lee D, et al. In Vivo Albumin Traps Photosensitizer Monomers from Self-Assembled Phthalocyanine Nanovesicles: A Facile and Switchable Theranostic Approach. J Am Chem Soc. 2019;141(3):1366-72.

[14] Tsolekile N, Nahle S, Zikalala N, Parani S, Sakho EHM, Joubert O, et al. Cytotoxicity, fluorescence tagging and gene-expression study of CuInS/ZnS QDS - meso (hydroxyphenyl) porphyrin conjugate against human monocytic leukemia cells. Sci Rep. 2020;10(1):4936.

[15] Gawale Y, Adarsh N, Kalva SK, Joseph J, Pramanik M, Ramaiah D, et al. Carbazole-Linked Near-Infrared Aza-BODIPY Dyes as Triplet Sensitizers and Photoacoustic Contrast Agents for Deep-Tissue Imaging. Chemistry. 2017;23(27):6570-8.

[16] Zhu S, Tian R, Antaris AL, Chen X, Dai H. Near-Infrared-II Molecular Dyes for Cancer Imaging and Surgery. Adv Mater. 2019;31(24):e1900321.

[17] Tong L, Bi-Xian P, Fenglian B. The structure and 13C-NMR of an indolenium squaraine dye. Dyes Pigm. 1999;43(2):67-71.

[18] Zhu H, Fan J, Mu H, Zhu T, Zhang Z, Du J, et al. d-PET-controlled "off-on" Polarity-sensitive Probes for Reporting Local Hydrophilicity within Lysosomes. Sci Rep. 2016;6(1):35627.

[19] Murata O, Shindo Y, Ikeda Y, Iwasawa N, Citterio D, Oka K, et al. Near-Infrared Fluorescent Probes for Imaging of Intracellular Mg2+ and Application to Multi-Color Imaging of Mg2+, ATP, and Mitochondrial Membrane Potential. Anal Chem. 2020;92(1):966-74.

[20] Lee H, Akers W, Bhushan K, Bloch S, Sudlow G, Tang R, et al. Near-Infrared pH-Activatable Fluorescent Probes for Imaging Primary and Metastatic Breast Tumors. Bioconjug Chem. 2011;22(4):777-84.

[21] Lacivita E, Leopoldo M, Berardi F, Colabufo NA, Perrone R. Activatable fluorescent probes: a new concept in optical molecular imaging. Curr Med Chem. 2012;19(28):4731-41.

[22] Klockow JL, Hettie KS, LaGory EL, Moon EJ, Giaccia AJ, Graves EE, et al. An activatable NIR fluorescent rosol for selectively imaging nitroreductase activity. Sensor Actuat B-Chem. 2020;306:127446.

[23] Wei C, Shen Y, Xu Z, Peng S, Yuan Z, He Y, et al. A novel off-on fluorescent probe for imaging of hypoxia in tumor cell. J Photoch Photobio A. 2018;353:292-8.

[24] Stanton M, Cronin M, Lehouritis P, Tangney M. In Vivo Bacterial Imaging without Engineering; A Novel Probe-Based Strategy Facilitated by Endogenous Nitroreductase Enzymes. Curr Gene Ther. 2015;15(3):277-88.

[25] Welling MM, Hensbergen AW, Bunschoten A, Velders AH, Scheper H, Smits WK, et al. Fluorescent imaging of bacterial infections and recent advances made with multimodal radiopharmaceuticals. Clin Transl Imaging. 2019;7(2):125-38.

[26] Zhang L, Guo L, Shan X, Lin X, Gu T, Zhang J, et al. An elegant nitroreductase responsive fluorescent probe for selective detection of pathogenic Listeria in vitro and in vivo. Talanta. 2019;198:472-9.

[27] Huang B, Chen W, Kuang Y-Q, Liu W, Liu X-J, Tang L-J, et al. A novel off–on fluorescent probe for sensitive imaging of mitochondria-specific nitroreductase activity in living tumor cells. Org Biomol Chem. 2017;15(20):4383-9.

[28] Djeha AH, Hulme A, Dexter MT, Mountain A, Young LS, Searle PF, et al. Expression of Escherichia coli B nitroreductase in established human tumor xenografts in mice results in potent antitumoral and bystander effects upon systemic administration of the prodrug CB1954. Cancer Gene Ther. 2000;7(5):721-31.

[29] Smits AM, van den Hengel LG, van den Brink S, Metz CH, Doevendans PA, Goumans M-J. A new in vitro model for stem cell differentiation and interaction. Stem Cell Res. 2009;2(2):108-12.

[30] Thorne SH, Barak Y, Liang W, Bachmann MH, Rao J, Contag CH, et al. CNOB/ChrR6, a new prodrug enzyme cancer chemotherapy. Mol Cancer Ther. 2009;8(2):333.

[31] Parkinson GN, Skelly JV, Neidle S. Crystal Structure of FMN-Dependent Nitroreductase from Escherichia coli B: A Prodrug-Activating Enzyme. J Med Chem. 2000;43(20):3624-31.

[32] Johansson E, Parkinson GN, Denny WA, Neidle S. Studies on the Nitroreductase Prodrug-Activating System. Crystal Structures of Complexes with the Inhibitor Dicoumarol and Dinitrobenzamide Prodrugs and of the Enzyme Active Form. J Med Chem. 2003;46(19):4009-20.

[33] Bhaumik S, Sekar TV, Depuy J, Klimash J, Paulmurugan R. Noninvasive optical imaging of nitroreductase gene-directed enzyme prodrug therapy system in living animals. Gene Ther. 2012;19(3):295-302.

[34] Sekar TV, Foygel K, Ilovich O, Paulmurugan R. Noninvasive Theranostic Imaging of HSV1-sr39TK-NTR/GCV-CB1954 Dual-Prodrug Therapy in Metastatic Lung Lesions of MDA-MB-231 Triple Negative Breast Cancer in Mice. Theranostics. 2014;4(5):460-74.

[35] Devulapally R, Lee T, Barghava-Shah A, Sekar TV, Foygel K, Bachawal SV, et al. Ultrasound-guided delivery of thymidine kinase–nitroreductase dual therapeutic genes by PEGylated-PLGA/PEI nanoparticles for enhanced triple negative breast cancer therapy. Nanomedicine. 2018;13(9):1051-66.

[36] Kanada M, Kim BD, Hardy JW, Ronald JA-OX, Bachmann MA-O, Bernard MP, et al. Microvesicle-Mediated Delivery of Minicircle DNA Results in Effective Gene-Directed Enzyme Prodrug Cancer Therapy. Mol Cancer Ther. 2019;18(12):2331-42.

[37] West RM, Ismail R. (2005). Nitro-substituted squaraine reporter dyes as reagent for measuring nitroreductase enzyme activity. (Patent No. WO2005118839A1). https://worldwide.espacenet.com/patent/search/family/032671256/publication/WO2005118839A1?q=WO2005118839A1

[38] Thomas N, Michael NP, Millar V, Davies B, Briggs MSJ. (2001). Methods for increased fluorescence of Cyanine dye reagents with nitroreductase. (Patent No. WO2001057237A2). https://worldwide.espacenet.com/patent/search/family/009884728/publication/WO0157237A2?q=WO2001057237A2

[39] Bhaumik S, Agdeppa ED, Klimash J, Depuy JC. (2009). In vivo optical imaging. (Patent No. US20090004116A1). https://worldwide.espacenet.com/patent/search/family/040160790/publication/US2009004116A1?q=US20090004116A1

[40] Cytiva. (2020, 25th August). Nitroreductase Gene Reporter System. https://cdn.cytivalifesciences.com/dmm3bwsv3/AssetStream.aspx?mediaformatid=10061&destinationid=10016&assetid=13959.

[41] Parker CN, Ottl J, Gabriel D, Zhang J-H. Chapter 8 Advances in Biological Screening for Lead Discovery. Natural Product Chemistry for Drug Discovery: The Royal Society of Chemistry; 2009. p. 243-71.

[42] Inglese J. Measuring Biological Responses with Automated Microscopy, Volume 414. 2006.

[43] Elmes RB. Bioreductive fluorescent imaging agents: applications to tumour hypoxia. Chem Commun (Camb). 2016;52(58):8935-56.

[44] Chevalier A, Zhang Y, Khdour OM, Kaye JB, Hecht SM. Mitochondrial Nitroreductase Activity Enables Selective Imaging and Therapeutic Targeting. J Am Chem Soc. 2016;138(37):12009-12.

[45] Loew LM, Cohen LB, Salzberg BM, Obaid AL, Bezanilla F. Charge-Shift Probes of Membrane-Potential - Characterization of Aminostyrylpyridinium Dyes on the Squid Giant-Axon. Biophys J. 1985;47(1):71-7.

[46] Yan Q, Schmidt BF, Perkins LA, Naganbabu M, Saurabh S, Andreko SK, et al. Near-instant surface-selective fluorogenic protein quantification using sulfonated triarylmethane dyes and fluorogen activating proteins. Org Biomol Chem. 2015;13(7):2078-86.

602

603 **Electronic Supplementary Material**

604

605 CytoCy5S™, a compound of many structures. *In vitro* 606 and *in vivo* evaluation of four near-infrared fluorescent 607 substrates of nitroreductase (NTR)

608

609

610 Elvira García de Jalón[1,2], Gorka Ruiz de Garibay[1], Bengt Erik Haug[2*] and Emmet
611 McCormack[1,3,4*]

612 *[1]Centre for Cancer Biomarkers CCBIO, Department of Clinical Science, The University of Bergen,*
613 *Jonas Lies vei 65, Bergen 5021, Norway;[2]Department of Chemistry and Centre for Pharmacy,*
614 *University of Bergen, Allégaten 41, N-5007, Bergen, Norway [3]Centre for Pharmacy, Department of*
615 *Clinical Science, The University of Bergen, Jonas Lies vei 65, Bergen 5021, Norway;*
616 *[4]Vivarium, Department of Clinical Science, The University of Bergen, Jonas Lies vei 65, 5021 Bergen,*
617 *Norway.*

618

**Corresponding Authors:*

Professor Emmet Mc Cormack

Tel: +47 55 97 3097

Email: emmet.mc.cormack@uib.no

First Author:

Elvira García de Jalón, M.S.

Tel: + 47 94434599

Email: elvira.vioegra@uib.no

619

Professor Bengt Erik Haug

Tel: +47 55 58 34 68

Email: Bengt-Erik.Haug@uib.no

Content overview Supporting information:

Synthesis of dyes: 4

Materials and instruments 9

Methods: 10

3,5-Dinitrobenzyl iodide (**5**): 10

5-Methoxy-2,3,3-trimethyl-3H-indole (**6**): 10

1,1,2-Trimethyl-1H-benzo[e]indol-3-ium-7-sulfonate (**7**): [3] 11

1-(3,5-Dinitrobenzyl)-2,3,3-trimethyl-3H-indol-1-ium iodide (**8**): [2] 156

1-(5-Carboxypentyl)-2,3,3-trimethyl-3H-indol-1-ium iodide (**9**): 156

1,2,3,3-Tetramethyl-3H-indol-1-ium iodide (**10**): 157

1-(3,5-Dinitrobenzyl)-5-methoxy-2,3,3-trimethyl-3H-indol-1-ium iodide (**11**): 158

1-(5-Carboxypentyl)-5-methoxy-2,3,3-trimethyl-3H-indol-1-ium bromide (**12**): 14

3-(5-Carboxypentyl)-1,1,2-trimethyl-1H-benzo[e]indol-3-ium-7-sulfonate (**13**): [3] 15

(E)-3-hydroxy-4-((1,3,3-trimethylindolin-2-ylidene)methyl)cyclobut-3-ene-1,2-dione (**14**): 16

(Z)-2-(((E)-1-(5-carboxypentyl)-3,3-dimethylindolin-2-ylidene)methyl)-4-((1-(3,5-dinitrobenzyl)-3,3-dimethyl-3H-indol-1-ium-2-yl)methylene)-3-oxocyclobut-1-en-1-olate (**1**): 17

(Z)-4-((1-(3,5-dinitrobenzyl)-3,3-dimethyl-3H-indol-1-ium-2-yl)methylene)-3-oxo-2-(((E)-1,3,3-trimethylindolin-2-ylidene)methyl)cyclobut-1-en-1-olate (**2**): 18

(Z)-2-(((E)-1-(5-carboxypentyl)-5-methoxy-3,3-dimethylindolin-2-ylidene)methyl)-4-((1-(3,5-dinitrobenzyl)-5-methoxy-3,3-dimethyl-3H-indol-1-ium-2-yl)methylene)-3-oxocyclobut-1-en-1-olate (**3**): 19

6-((E)-2-((2E,4E)-5-(1-(3,5-dinitrobenzyl)-3,3-dimethyl-3H-indol-1-ium-2-yl)penta-2,4-dien-1-ylidene)-1,1-dimethyl-7-sulfonato-1,2-dihydro-3H-benzo[e]indol-3-yl)hexanoate (**4**): 20

(E)-6-(2-((2-ethoxy-3,4-dioxocyclobut-1-en-1-yl)methylene)-3,3-dimethylindolin-1-yl)hexanoic acid (**15**): 21

(E)-3-((1-(3,5-dinitrobenzyl)-3,3-dimethylindolin-2-ylidene)methyl)-4-ethoxycyclobut-3-ene-1,2-dione (**16**): 22

(E)-3-((1-(3,5-dinitrobenzyl)-3,3-dimethylindolin-2-ylidene)methyl)-4-methoxycyclobut-3-ene-1,2-dione (**17**): 22

(E)-3-((1-(3,5-dinitrobenzyl)-3,3-dimethylindolin-2-ylidene)methyl)-4-hydroxycyclobut-3-ene-1,2-dione (**18**): 23

Synthesis of **1** using immobilized **9**: 24

Analytical data: 25

Figure S1: ^{1}H-NMR spectrum of **5** in DMSO 25

Figure S2: ^{1}H-NMR spectrum of **6** in DMSO 26

Figure S3: ^{1}H-NMR spectrum of **7** in DMSO 27

Figure S4: ^{1}H-NMR spectrum of **8** in MeOD **28**

Figure S5: ^{1}H-NMR spectrum of **9** in DMSO **29**

Figure S6: ^{1}H-NMR spectrum of **10** in DMSO **30**

Figure S7: ^{1}H-NMR spectrum of **11** in DMSO **31**

Figure S8: ^{1}H-NMR spectrum of **12** in DMSO **32**

Figure S9: ^{1}H-NMR spectrum of **13** in DMSO **33**

Figure S10: ^{1}H-NMR spectrum of **14** in DMSO **34**

Figure S11: ^{1}H-NMR spectrum of Substrate **1** in DMSO **35**

Figure S12: A: Analytical RP-HPLC chromatogram and UV trace of Substrate **1**; B: HRMS spectrum of Substrate **1** **36**

Figure S13: ^{1}H-NMR spectrum of Substrate **2** in DMSO **37**

Figure S14: A: Analytical RP-HPLC chromatogram and UV trace of Substrate **2**; B: HRMS spectrum of Substrate **2** **38**

Figure S15: ^{1}H-NMR spectrum of Substrate **3** in DMSO **39**

Figure S16: A: Analytical RP-HPLC chromatogram and UV trace of Substrate **3**; B: HRMS spectrum of Substrate **3** **40**

Figure S17: ^{1}H-NMR spectrum of Substrate **4** in DMSO **41**

Figure S18: A: Analytical RP-HPLC chromatogram and UV trace of Substrate **4**; B: HRMS spectrum of Substrate **4** **42**

Figure S19: ^{1}H-NMR spectrum of **15** in DMSO **43**

Figure S20: ^{1}H-NMR spectrum of **16** in DMSO **44**

Figure S21: ^{1}H-NMR spectrum of **17** in DMSO **45**

Figure S22: ^{1}H-NMR spectrum of **18** in DMSO **46**

Figure S23: Confocal fluorescence microscopy with substrates **1** – **4** with the same scale for "NTR substrate" channel **47**

Figure S24: Absorbance spectrum **48**

Figure S25: Flow cytometry analysis **49**

Video S1: Full time lapse for substrate **1** **49**

Video S2: Full time lapse for substrate **2** **49**

Video S3: Full time lapse for substrate **3** **49**

Video S4: Full time lapse for substrate **4** **49**

References: **50**

Synthesis of dyes:

The Fischer bases that were required for the synthesis of the asymmetric substrates **1** - **4** were obtained through N-alkylation of 2,3,3-trimethyl-3*H*-indole, its 5-methoxy analogue or 1,1,2-trimethyl-1*H*-benzo[*e*]indole (Scheme S1). The crude yields ranged from 24% to 94% and the intermediates, with the exception of the sulfonated **7**, were employed in further steps without purification, as we found that except for **7**, purification of the intermediates did not give any increase in the yields for the next steps. The introduction of the sulfonate functionality that was required for substrate **4** proved as a challenge, as several isomers of **7** were formed during sulphonation of the benzoindole. The sulfonated Fischer base **13** and its precursor **7** were purified by C18 flash chromatography to give the target compounds in modest yields of 14% and 32%, respectively).

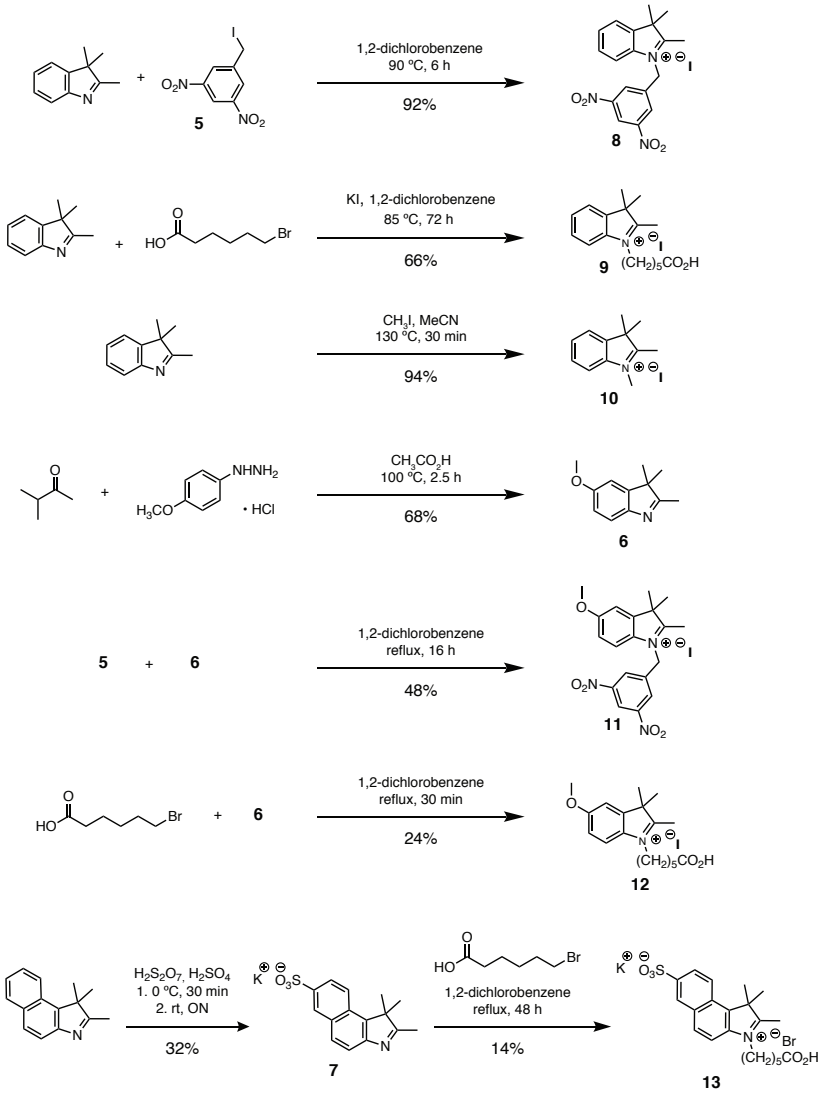

Scheme S1. Synthesis of Fischer bases **8** - **13** that have been employed in the synthesis of NIR dyes **1** – **4**.

As shown in Scheme S2, one-pot condensation of the various Fischer bases with either squaric acid or malonaldehyde bis(phenylimine) successfully gave substrates **1, 3** and **4**. In all cases, the reactions also gave the undesired symmetric side products, which resulted in overall low yields (1% to 16%) for the target dyes. The particularly low yield for substrate **4** is due to the co-elution with the symmetric dinitrobenzyl side product, which made the separation by conventional purification methods

unsuccessful. In the end, this material was purified by attaching it to a 2-chlorotrityl chloride resin, which was washed thoroughly prior to release and purification of **4** (see experimental section below). The product was isolated with acceptable purity but signals from a minor isomer can still be observed in the ^{1}H-NMR spectrum of substrate **4**.

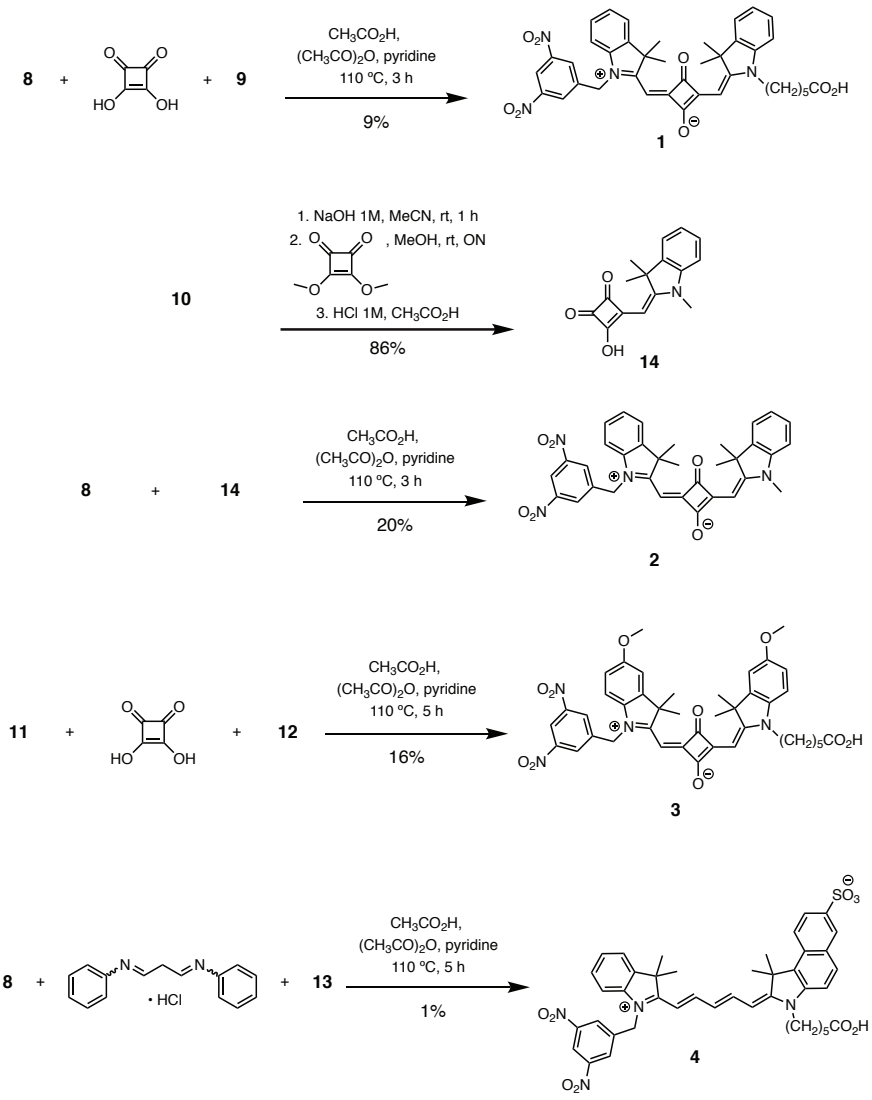

Scheme S2. Synthesis of NIR dyes **1** – **4**.

For substrate **2**, the one-pot approach proved to be unsuccessful as only the symmetric side product containing *N*-methylated side chains could be isolated from the reaction mixture. Substrate **2** was ultimately obtained through first synthesis of the mono-substituted methyl squaraine intermediate (Scheme S2), which after conversion to **14** under acidic conditions followed by condensation with **8** gave substrate **2** in a modestly higher yield than what was obtained for the other three substrates.

Based on the results for the synthesis of substrate **2** and in order to reduce the formation of the symmetric side products, a stepwise introduction of methylene bases was attempted also for substrate **1** (see Scheme S3) using either methyl or ethyl squarate as starting material.

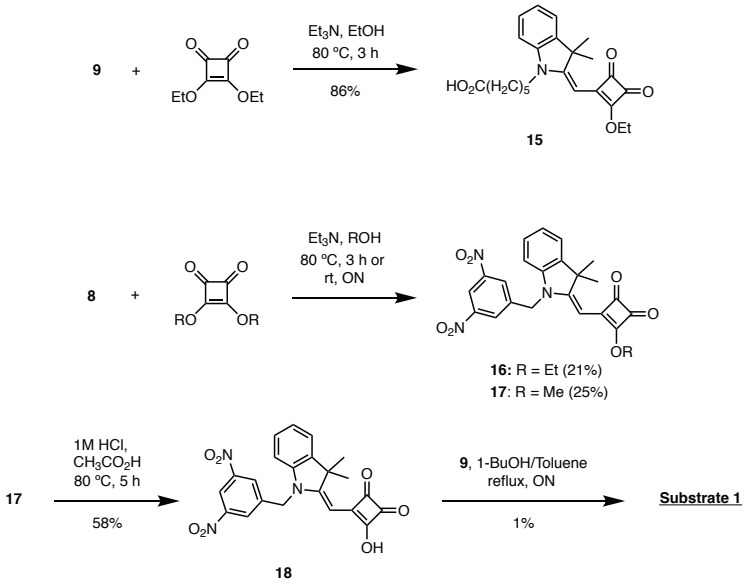

Scheme S3. Stepwise introduction of methylene bases [1-3].

To our dismay, these reactions produced complex mixtures, which translated into tedious purification procedures for each intermediate. Interestingly, the 3,5-dinitrobenzyl containing **8** gave particularly low conversion, both at room temperature and at reflux. On the other hand, both **16** and **17** proved amenable to further conversion to **18** under either basic or acidic conditions. The use of the same reaction

conditions with **15** were largely unsuccessful. In the end, the stepwise approach only resulted in an increase time requirement while the overall yield was not improved.

In a final attempt to improve the synthetic route to **1**, a solid supported approach was investigated (Scheme S4) [4]. Toward this end, **9** was immobilized on a 2-chlorotrityl chloride resin followed by reaction with squaric acid at rt and at 80 °C. Unfortunately, test-cleavage of a small amount of the resulting resin bound material did not provide the desired product. On the other hand, reaction of **18** with immobilised **9** (Scheme S4) in the presence of a carbodiimide (DIC) proved successful for the synthesis of **1** [4]. Overall, the solid supported approach reduced the number of side products formed, which alleviated the purification. Nevertheless, the overall yield of substrate **1** was not increased and together with the cost and the extra time required this approach did not prove to be advantageous.

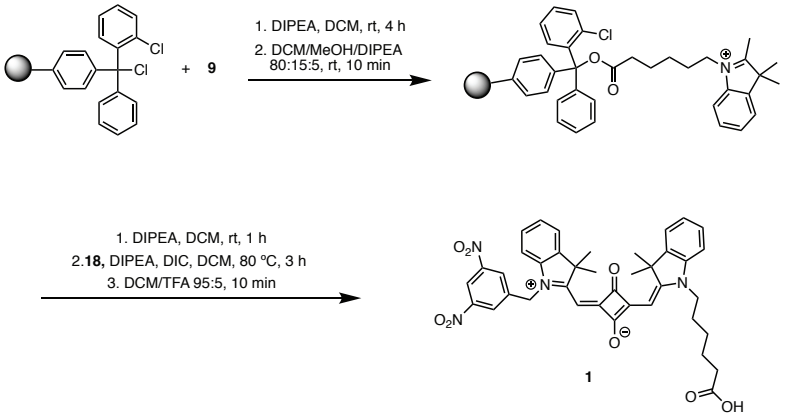

Scheme S4: Synthesis of substrate **1** using a solid supported approach

Materials and instruments

The reactants and reagents employed in the synthetic work were obtained from Sigma-Aldrich and were used as received. Reactions were generally carried out under argon atmosphere using overnight oven-dried equipment (130 °C) that was cooled down under reduced pressure and purged with argon prior to use. Solid phase syntheses were performed using a 2-chlorotrityl chloride polystyrene (1% DVB) resin (100 – 200 mesh, 1.14 mmol/g loading) provided by Novabiochem using 10 mL reactor vials (Biotage). Dry DCM was obtained from an anhydrous solvent delivery system (SPS-800 system from M. Braun GmbH, Garching, Germany) and kept in a Schlenk flask. Acetone, ethanol and methanol were dried over 3Å molecular sieves (10% w/v) overnight and stored under argon.

Flash chromatography was performed using silica (Silica gel 60, 0.040 – 0.063 mm, Merck) using manually packed glass columns or on a Puriflash XS 420 system (Interchim, Montlucon Cedex, France) using Grace™ Reveleris™ SRC C18 cartridges (40 µm, 40g, Grace Discovery Sciences, Maryland, USA). Preparative high-performance liquid chromatography (HPLC) was performed on a Gilson 321 multisolvent pump with a Dionex Ultimate 3000 variable wavelength detector using an Ascentis C18 (250 x 21.2 mm, 100 Å, 5 µm) column with mixtures of acetonitrile and water (both containing 0.1% TFA) as eluent.

Analytical HPLC was performed on a 1290 Infinity II Flexible pump with a 1260 Infinity II DAD WR detector using a ZORBAX RRHD Eclipse plus 300-SB C18 (50 x 2.1 mm, 300 Å, 1.8 µm) column with mixtures of acetonitrile and water (both containing 0.1% TFA) as eluent. High-resolution mass spectra were recorded with an AccuTOF™ mass spectrometer operated with an orthogonal electrospray ionization (ESI) source, an orthogonal accelerated time of flight (TOF), single stage reflectron mass analyzer and a dual micro channel plate (MCP) detector. NMR spectra were recorded using either a Bruker BioSpin AV500 and/or a Bruker BioSpin Ascend spectrometer operating at 850 MHz with an inverse-detected triple resonance (TCI) cryoprobe for ^{1}H NMR and 2D NMR spectra of the final compounds.

Methods:

3,5-Dinitrobenzyl iodide (5):

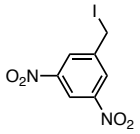

3,5-Dinitrobenzyl chloride (5.00 g, 23 mmol) and KI (8.87 g, 53 mmol) were dissolved in dry acetone (50 mL) under an argon stream. The resulting orange mixture was stirred for 20 h at rt. Thereafter, the orange solution was filtered and washed with cold acetone (3 x 20 mL). The solvent was removed under reduced pressure to afford the title compound, which was used in the next step without further purification.

Yellow-orange solid; 7.84 g (quantitative crude yield). ^{1}H-NMR (500 MHz, $(CD_3)_2SO$) δ = 8.73 (d, J = 2.1, 2H), 8.68 (t, J = 2.1, 1H), 4.88 (s, 2H).

Analytical data are in accordance with those reported previously [5]

5-Methoxy-2,3,3-trimethyl-3*H*-indole (6):

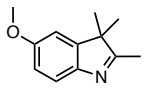

3-Methyl-2-butanone (3.7 mL, 34.6 mmol) and 4-methoxyphenylhydrazine (3.00 g, 17.2 mmol) were dissolved in acetic acid (30 mL) and the resulting pale pink mixture was heated at 100 °C (oil bath) for 2.5 h. The mixture was allowed to cool to rt and the solvent was evaporated under reduced pressure. The resulting dark brown residue was separated between ethyl acetate (30 mL) and a saturated solution of $NaHCO_3$ (60 mL). The organic phase was dried over $MgSO_4$, filtered and the solvent was removed using a rotary evaporator to give the title compound. This material was used in the next step without further purification.

Brown oil; 2.22 g, (68% yield). ^{1}H-NMR (500 MHz, $(CD_3)_2SO$): δ = 7.30 (d, *J* = 8.3, 1H), 7.03 (d, *J* = 2.6, 1H), 6.80 (dd, *J* = 8.3, 2.6, 1H), 3.76 (s, 3H), 2.15 (s, 3H), 1.22 (s, 6H).

Analytical data are in accordance with those reported previously [6]

1,1,2-Trimethyl-1*H*-benzo[*e*]indol-3-ium-7-sulfonate (7): [7]

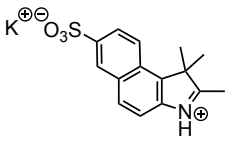

1,1,2-Trimethyl-1*H*-benz(e)indole (530 mg, 2.5 mmol) was cooled in an ice/water bath and partially dissolved in sulphuric acid (1 mL). To his mixture, fuming sulfuric acid (2.5 mL) was added dropwise and the mixture was stirred for 30 min after which the cooling bath was removed and stirring continued at rt overnight. The resulting mixture was poured into ice/water (50 mL) and the mixture was stirred for 30 min. Concentrated KOH was then added until basic pH (pH = 12). The mixture was placed in an ice/water bath to induce precipitation and the pearly yellow solid obtained was extracted with hot methanol. The solid material was isolated by filtration and dried under reduced pressure. The dried residue was then triturated with ethyl acetate, filtered and collected after drying by vacuum suction and it was further dried under vacuum. The crude product was purified using RP flash chromatography (1 - 50% acetonitrile in water, both solvents containing 10 mM of NH_4OAc) to give the title compound.

Yellow solid; 228 mg (32% yield). ^{1}H-NMR (500 MHz, $(CD_3)_2SO$): δ 8.21 (d, *J* = 1.8, 1H), 8.07 (d, *J* = 8.7, 1H), 7.95 (d, *J* = 8.5, 1H), 7.78 (dd, *J* = 8.7, 1.8, 1H), 7.69 (d, *J* = 8.5, 1H), 2.31 (s, 3H), 1.47 (s, 6H). The spectrum shows presence of a minor isomer.

Analytical data are in accordance with those reported previously [8]

1-(3,5-Dinitrobenzyl)-2,3,3-trimethyl-3*H*-indol-1-ium iodide (8): [6]

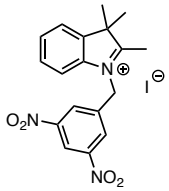

Iodide **7** (15.92 g, 51.7 mmol) was dissolved in 1,2-dichlorobenzene (65 mL) under argon and 2,3,3-trimethylindolenine (8.4 mL, 52.3 mmol) was added and the resulting brown mixture was stirred for 6 h at 90 °C (oil bath). The mixture was allowed to cool to rt, upon which a precipitate was formed. The red solid was isolated by filtration and washed with dichlorobenzene (2 x 25 mL) and diethyl ether (3 x 30 mL). The resulting yellow solid material was dried under vacuum to give the title compound, which was used in the next step without any further purification.

Yellow solid; 22.24 g (92% crude yield). ^{1}H-NMR (500 MHz, CD_3OD): δ = 9.04 – 9.00 (m, 1H), 8.60 – 8.55 (m, 2H), 7.90 – 7.81 (m, 2H), 7.69 (t, *J* = 7.7, 1H), 7.62 (t, *J* = 7.7, 1H), 6.15 (s, 2H) 1.73 (s, 6H). One CH_3 signal assumed to be hidden by solvent signal. LR-ESI-MS: Calcd. *m/z* for $C_{18}H_{18}N_3O_4^+$ $[M]^+$: 340.1; found: 340.2.

Analytical data are not reported previously

1-(5-Carboxypentyl)-2,3,3-trimethyl-3*H*-indol-1-ium iodide (9):

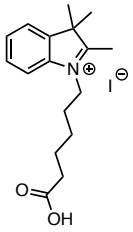

2,3,3-Trimethyl-3*H*-indolenine (3.2 mL, 20.0 mmol), 6-bromohexanoic acid (4.826 g, 24.7 mmol) and KI (4.168 g, 25.1 mmol) were dissolved in acetonitrile (140 mL) and the resulting mixture was stirred at 85 °C (oil bath) for 72 h under

855 argon atmosphere. After cooling to rt, the resulting red solution was filtered to
856 remove the beige solid (KBr) and the filtrate was concentrated using rotary
857 evaporation. The brown oily residue was mixed with warm (65 °C) ethyl acetate
858 (500 mL) and was slowly cooled (kept in the fridge overnight). The excess of
859 solvent was removed by rotary evaporation to give the title compound, which was
860 used in the next step without any further purification.

861 Grey solid; 5.275 g (66% crude yield). ^{1}H-NMR (500 MHz, $(CD_3)_2SO$): δ = 12.00
862 (bs, 1H), 8.00 – 7.95 (m, 1H), 7.87 – 7.82 (m, 1H), 7.65 – 7.60 (m, 2H), 4.45 (t, *J*
863 = 7.8, 2H), 2.84 (s, 3H), 2.23 (t, *J* = 7.3, 2H), 1.89 – 1.80 (m, 2H), 1.60 - 1.51 (m,
864 2H), 1.54 (s, 6H), 1.47 – 1.38 (m, 2H). LR-ESI-MS: Calcd. *m/z* for $C_{17}H_{24}NO_2^+$
865 $[M]^+$: 274.2; found: 274.2.

866 Analytical data are in accordance with those reported previously [9]
867

868 **1,2,3,3-Tetramethyl-3*H*-indol-1-ium iodide (10):**

869 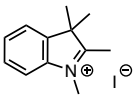

870 In three separate 10 mL microwave vials, 2,3,3-trimethylindolenine (0.96 mL x 3,
871 17.9 mmol in total) and iodomethane (0.56 mL x 3, 27.0 mmol in total) were
872 dissolved in acetonitrile (2.0 mL x 3). The vials were sealed, and the reaction
873 mixtures were heated at 130 °C in an oil bath for 30 min. The mixtures were
874 allowed to cool to rt and then further cooled in an ice/water bath. The solvent was
875 decanted, and the pink needle-shaped crystals from each vial were pooled and
876 isolated by filtration, washed with cold ethanol and dried under vacuum. The
877 crude product was used in the next step without further purification.

878 Pink crystalline solid; 5.099 g (94% crude yield). ^{1}H-NMR (500 MHz, $(CD_3)_2SO$):
879 δ = 7.92 – 7.89 (m, 1H), 7.84 – 7.81 (m, 1H), 7.65 – 7.59 (m, 2H), 3.97 (s, 3H),
880 2.76 (s, 3H), 1.52 (s, 6H); LR-ESI-MS: Calcd. *m/z* for $C_{12}H_{16}N$ $[M]^+$: 174.1;
881 found: 174.2.

882 Analytical data are in accordance with those reported previously [10]

1-(3,5-Dinitrobenzyl)-5-methoxy-2,3,3-trimethyl-3*H*-indol-1-ium iodide (11):

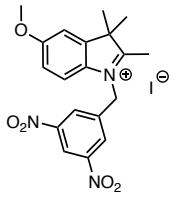

To a solution of **6** (1.11 g, 5.9 mmol) in 1,2-dichlorobenzene (6 mL), **5** (2.72 g, 8.8 mmol) was added. The reaction mixture was heated to reflux for 30 min and it was then allowed to cool to rt before it was cooled further in an ice/water bath. Once crystallization started, the mixture was heated to reflux for another 2 h and cooled to rt before the precipitate that formed was isolated by filtration and washed with 1,2-dichlorobenzene and diethyl ether and dried under vacuum to give the title compound.

Pale orange powder; 1.36 g (48% crude yield). ^{1}H-NMR (500 MHz, $(CD_3)_2SO$): δ = 8.82 (t, *J* = 2.0, 1H), 8.62 (d, *J* = 2.0, 2H), 7.77 (d, *J* = 8.9, 2.5, 1H), 7.53 (d, *J* = 2.5, 1H), 7.11 (dd, *J* = 8.9, 2.5, 1H), 6.04 (s, 2H), 3.85 (s, 3H), 2.91 (s, 3H), 1.60 (s, 6H). The spectrum contains additional peaks. LR-ESI-MS: Calcd. *m/z* for $C_{19}H_{20}N_3O_5^+$ $[M]^+$: 370.1; found: 370.2.

Analytical data are in accordance with those reported previously [6]

1-(5-Carboxypentyl)-5-methoxy-2,3,3-trimethyl-3*H*-indol-1-ium bromide (12):

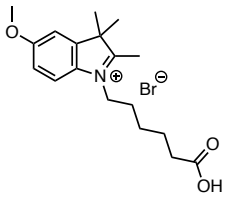

To a solution of **6** (1.11 g, 5.9 mmol) in 1,2-dichlorobenzene (6 mL) 6-bromohexanoic acid (1.73 g, 8.8 mmol) was added. The reaction mixture was heated to reflux for 16 h under an argon stream, cooled to rt and then diluted with

diethyl ether (10 mL) upon which a black precipitate formed. The solvents were removed by decantation and the residue was triturated with dichloromethane. The residue was suspended in diethyl ether and the solid material was isolated by filtration and dried under high vacuum.

Purple powder; 530 mg (24% crude yield). ^{1}H-NMR (500 MHz, $(CD_3)_2SO$): δ = 12.00 (bs, 1H), 7.87 (d, *J* = 8.9, 1H), 7.48 (d, *J* = 2.5, 1H), 7.14 (dd, *J* = 8.9, 2.5, 1H), 4.41 (t, *J* = 7.7, 2H), 3.86 (s, 3H), 2.76 (s, 3H), 2.22 (t, *J* = 7.3, 2H), 1.86 - 1.78 (m, 2H), 1.58 – 1.53 (m, 2H), 1.51 (s, 6H), 1.44 - 1.36 (m, 2H). LR-ESI-MS: Calcd. *m/z* for $C_{18}H_{26}NO_3^+$ $[M]^+$: 304.2; found: 304.2.

Analytical data are in accordance with those reported previously [6]

3-(5-Carboxypentyl)-1,1,2-trimethyl-1*H*-benzo[*e*]indol-3-ium-7-sulfonate (13): [7]

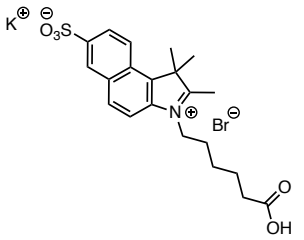

A mixture of potassium **7** (228 mg, 0.8 mmol) and 6-bromohexanoic acid (195 mg, 1.0 mmol) in 1,2-dichlorobenzene (3 mL) was heated to reflux for 48 h. The solvent was decanted off and the solid residue was triturated with ethyl acetate. The product was then dissolved in distilled water and methanol and the solvents were evaporated under reduced pressure. The crude product was purified using RP flash chromatography (1 - 50% acetonitrile in water, both solvents containing 10 mM of $NH_4CO_2CH_3$) to give the title compound.

Brown/orangish solid; 46 mg (14% yield). ^{1}H NMR (500 MHz, $(CD_3)_2SO$): δ = 7.99 (d, *J* = 1.9, 1H), 7.88 (d, *J* = 8.8, 1H), 7.77 (d, *J* = 8.7, 1H), 7.57 (dd, *J* = 8.8, 1.9, 1H), 7.15 (d, *J* = 8.7, 1H), 3.61 (t, *J* = 7.3, 2H), 2.19 (t, *J* = 7.3, 2H), 1.90 (s, 3H, overlaps with impurity), 1.56 (s, 6H), 1.54 – 1.49 (m, 2H), 1.38 – 1.31 (m,

930 2H), 1.24 (s, 2H). The spectrum contains additional peaks. LR-ESI-MS: Calcd.
931 *m/z* for $C_{21}H_{26}NO_5S^+$ $[M + H]^+$: 404.2; found: 404.2.

932 Analytical data are in accordance with those reported previously [8]

933

934 **(*E*)-3-hydroxy-4-((1,3,3-trimethylindolin-2-ylidene)methyl)cyclobut-3-ene-**
935 **1,2-dione (14):**

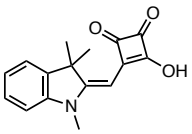

936

937 **10** (1.72 g, 5.7 mmol) was dissolved in acetonitrile (40 mL) and reacted with a
938 1M solution of NaOH (70 mL) for 1 h at rt. The final product was extracted by
939 means of CH_2Cl_2 (3 x 30 mL), dried over $MgSO_4$ and the excess of solvent was
940 removed by rotary evaporation to give the activated Fischer base (989 mg, 5.7
941 mmol). The dried activated Fischer base and 3,4-dimethoxy-3-cyclobutene-1,2-
942 dione (817 mg, 5.7 mmol) were dissolved in dry methanol (2.5 mL) and the
943 resulting mixture was stirred at rt for 18 h and then cooled in the fridge for 2 h.
944 The red solid was isolated by filtration and washed with cold methanol and cold
945 diethyl ether and dried under high vacuum to give (*E*)-3-methoxy-4-((1,3,3-
946 trimethylindolin-2-ylidene)methyl)cyclobut-3-ene-1,2-dione as a yellow solid.
947 The crude product (872 mg) was dissolved in acetic acid (9.5 mL) and a 1M
948 solution of HCl (1.55 mL) was added. The yellow-orangish mixture was heated at
949 80 °C for 5 h and the resulting mixture was evaporated under reduced pressure to
950 give a dark green iridescent residue. This residue was triturated with diethyl ether,
951 and the solid material was isolated by filtration and washed with diethyl ether and
952 dried under high vacuum to give the title compound, which was used in the next
953 step without further purification.

954 Dark green solid; 783 mg (86% crude yield). ^{1}H-NMR (500 MHz, $(CD_3)_2SO$): δ =
955 7.43 – 7.36 (m, 1H), 7.29 – 7.22 (m, 1H), 7.14 – 7.08 (m, 1H), 7.04 – 6.97 (m,
956 1H), 5.45 (s, 1H), 3.34 (s, 3H), 1.55 (s, 6H). The spectrum shows presence of
957 acetic acid.

Analytical data are in accordance with those reported previously [10]

(*Z*)-2-(((*E*)-1-(5-carboxypentyl)-3,3-dimethylindolin-2-ylidene)methyl)-4-((1-(3,5-dinitrobenzyl)-3,3-dimethyl-3*H*-indol-1-ium-2-yl)methylene)-3-oxocyclobut-1-en-1-olate (1):

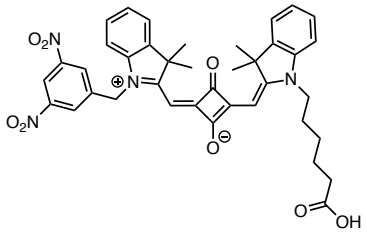

Compound **8** (999 mg, 2.1 mmol), **9** (765 mg, 1.9 mmol) and 3,4-dihydroxy-3-cyclobuten-1,2-dione (238 mg, 2.1 mmol) were dissolved in pyridine (9.7 mL), acetic acid (9.7 mL) and acetic anhydride (2.2 mL) and the resulting mixture was heated at 110 °C for 3 h. The reaction mixture was partitioned between dichloromethane (10 mL) and water (10 mL). The combined organic phases were dried over $MgSO_4$, filtered and evaporated under reduced pressure to give an iridescent blue sticky residue (1.261 g), which was purified using semi-preparative RP-HPLC (50 - 90% acetonitrile in water, both solvents containing 0.1% TFA) to give the title compound.

Iridiscent blue solid; 109 mg (9% yield). ^{1}H-NMR (850 MHz, $(CD_3)_2SO$): δ = 12.00 (bs, 1H), 8.74 (d, *J* = 2.4, 1H), 8.40 (d, *J* = 2.4, 2H), 7.58 (d, *J* = 7.4, 1H), 7.55 (dd, *J* = 7.4, 1.2, 1H), 7.42 (d, *J* = 8.0, 1H), 7.38 (td, *J* = 7.7, 1.2, 1H), 7.29 (td, *J* = 7.7, 1.2, 1H), 7.24 – 7.22 (m, 2H), 7.16 (t, *J* = 7.4, 1H), 5.88 (s, 1H), 5.75 (s, 1H), 5.66 (s, 2H), 4.14 (t, *J* = 7.6, 2H), 2.20 (t, *J* = 7.3, 2H), 1.79 (bs, 6H), 1.72 (m, 2H), 1.65 (s, 6H), 1.55 (m, 2H), 1.39 (m, 2H); HR-ESI-MS: Calcd. *m/z* for $C_{39}H_{39}N_4O_8^+$ $[M+H]^+$: 691.2762; found: 691.2772.

Analytical data are in accordance with those reported previously [11]

(*Z*)-4-((1-(3,5-dinitrobenzyl)-3,3-dimethyl-3*H*-indol-1-ium-2-yl)methylene)-3-oxo-2-(((*E*)-1,3,3-trimethylindolin-2-ylidene)methyl)cyclobut-1-en-1-olate (2):

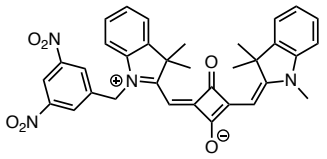

Squaric acid derivative **14** (398 mg, 1.5 mmol) and **8** (695 mg, 1.5 mmol) were dissolved in pyridine (7 mL), acetic acid (7 mL) and acetic anhydride (1.5 mL) and the resulting mixture was heated at 110 °C for 6 h. The reaction mixture was partitioned between dichloromethane (10 mL) and water (10 mL). The combined organic phases were dried over $MgSO_4$, filtered and evaporated under reduced pressure to give an iridescent blue sticky residue (1.099 g). The crude residue was purified by flash chromatography (CH_2Cl_2/MeOH, 95:5) to give a green/bluish material (307 mg). This material was further purified using semi-preparative RP-HPLC (50 - 90% acetonitrile in water, both solvents containing 0.1% TFA) to give the title compound.

Dark blue solid; 171 mg (20% yield). ^{1}H-NMR (850 MHz, $(CD_3)_2SO$): δ = 8.73 (s, 1H), 8.40 (d, *J* = 2.1, 2H), 7.57 (d, *J* = 7.4, 1H), 7.55 (dd, *J* = 7.4, 1.2, 1H), 7.43 (d, *J* = 7.7, 1H), 7.38 (td, *J* = 7.7, 1.2, 1H), 7.28 (td, *J* = 7.7, 1.2, 1H), 7.25 – 7.21 (m, 2H), 7.15 (m, 1H), 5.85 (s, 1H), 5.75 (s, 1H), 5.65 (s, 2H), 3.64 (s, 3H), 1.80 (s, 6H), 1.65 (s, 6H); HR-ESI-MS: Calcd. *m/z* for $C_{34}H_{31}N_4O_6^+$ $[M+H]^+$: 591.2238; found: 591.2247.

MS data are in accordance with those reported previously [6]

(Z)-2-(((E)-1-(5-carboxypentyl)-5-methoxy-3,3-dimethylindolin-2-ylidene)methyl)-4-((1-(3,5-dinitrobenzyl)-5-methoxy-3,3-dimethyl-3H-indol-1-ium-2-yl)methylene)-3-oxocyclobut-1-en-1-olate (3):

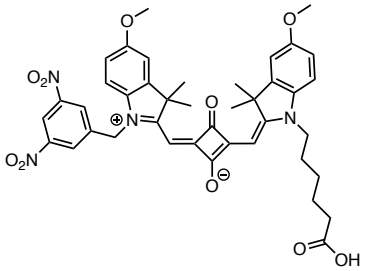

5-Methoxy indolenine **11** (264 mg, 0.5 mmol), 5-methoxy indolenine **12** (200 mg, 0.5 mmol) and 3,4-dihydroxy-3-cyclobutene-1,2-dione (66 mg, 0.6 mmol) were dissolved in pyridine (2.25 mL), acetic acid (2.25 mL) and acetic anhydride (0.5 mL) and the resulting mixture was stirred at 110 °C for 5 h. The resulting mixture was evaporated under reduced pressure to give a green/bluish iridescent residue (673 mg). This residue was purified by flash chromatography (CH_2Cl_2/MeOH, 90:10) to give a green/bluish material (96 mg). This material was further purified using semi-preparative HPLC (50-90% acetonitrile in water, both solvents containing 0.1% formic acid) to give the title compound.

Iridiscent blue solid; 62 mg (16% yield) ^{1}H-NMR (850 MHz, $(CD_3)_2SO$): δ = 12.00 (s, 1H), 8.73 (bs, 1H), 8.38 (bs, 2H), 7.33 (d, *J* = 8.6, 1H), 7.23 (d, *J* = 2.5, 1H), 7.21 (d, *J* = 2.5, 1H), 7.16 – 7.11 (m, 1H), 6.93 (dd, *J* = 8.6, 2.5, 1H), 6.84 (dd, *J* = 8.6, 2.5, 1H), 5.78 (s, 1H), 5.65 (s, 1H), 5.61 (s, 2H), 4.14 – 4.07 (m, 2H), 3.79 (s, 3H), 3.78 (s, 3H), 2.19 (t, *J* = 7.2, 2H), 1.79 (bs, 6H), 1.71 – 1.69 (m, , 2H), 1.64 (s, 6H), 1.55 – 1.53 (m, 2H), 1.37 – 1.36 (m, 2H); HR-ESI-MS: Calcd. *m/z* for $C_{41}H_{43}N_4O_{10}^+$ $[M+H]^+$: 751.2974; found: 751.2982.

MS data are in accordance with those reported previously [6]

6-((*E*)-2-((2*E*,4*E*)-5-(1-(3,5-dinitrobenzyl)-3,3-dimethyl-3*H*-indol-1-ium-2-yl)penta-2,4-dien-1-ylidene)-1,1-dimethyl-7-sulfonato-1,2-dihydro-3*H*-benzo[*e*]indol-3-yl)hexanoate (4):

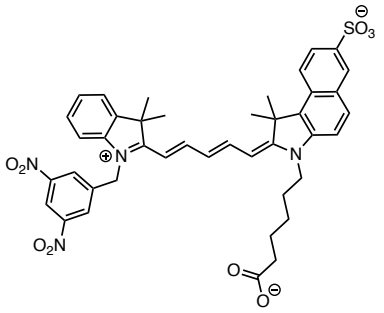

Benzo(e)indolenine **13** (146 mg, 0.33 mmol), dinitrobenzyl indolenine **8** (169 mg, 0.36 mmol) and malonaldehyde bis(phenylimine) monohydrochloride (91 mg, 0.35 mmol) were dissolved in pyridine (4.5 mL), acetic acid (4.5 mL) and acetic anhydride (1 mL) and the resulting mixture was heated at 110 °C for 5 h under an argon stream. The resulting mixture was cooled to rt and evaporated under reduced pressure to give a green/bluish iridescent oil (656 mg). A portion of the crude product (242 mg) was purified by means of solid support resin using 2-chlorotrityl chloride (281 mg). Briefly, a mixture of **4** and DIPEA (4 equiv) in dry DCM was loaded in the resin by agitation at rt for 3 h. The resin was then washed with DCM (6 x 2 mL) until solvent was colourless. Cleavage from the resin was facilitated by treatment with TFA, triisopropylsilane (TIS) and water (95:2.5:2.5, 2 mL) for 2 h. The mixture of sulfonate isomers obtained from the cleavage of the resin was further purified by semi-preparative RP-HPLC (50 - 70% acetonitrile in water, both solvents containing ammonium acetate 10 mM) to give the title compound.

Dark greenish solid; 3.61 mg (1% yield). ^{1}H-NMR (850 MHz, $(CD_3)_2SO$): δ = 8.75 (s, 1H), 8.53 – 8.46 (m, 1H), 8.44 (s, 2H), 8.32 (t, *J* = 13.0, 1H), 8.30 (s, 1H), 8.25 (d, *J* = 8.8, 1H), 8.20 (d, *J* = 8.8, 1H), 7.89 (dd, *J* = 8.8, 1.7, 1H), 7.83 (d, *J* = 9.0, 1H), 7.64 (d, *J* = 7.1, 1H), 7.33 (t, *J* = 7.6, 1H), 7.29 (d, *J* = 7.9, 1H), 7.19 (t, *J* = 7.6, 1H), 6.54 (m, 2H), 6.19 (m, 1H), 5.62 (s, 2H), 4.30 (m, 2H), 2.08 (bs, 2H), 1.94 (s, 6H), 1.79 (s, 6H), 1.75 – 1.72 (m, 2H), 1.52 – 1.44 (m, 2H), 1.40 – 1.37

(m, 2H) The spectrum contains additional peaks. HR-ESI-MS: Calcd. *m/z* for $C_{42}H_{43}N_4O_9S^+$ $[M+H]^+$: 779.2745; found: 779.2754.

Analytical data not reported previously

(*E*)-6-(2-((2-ethoxy-3,4-dioxocyclobut-1-en-1-yl)methylene)-3,3-dimethylindolin-1-yl)hexanoic acid (15):

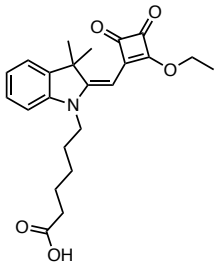

To a solution of **9** (306 mg, 0.76 mmol) in dry ethanol (3 mL), 3,4-diethoxy-3-cyclobutene-1,2-dione (110 μL, 0.74 mmol) was added and the resulting mixture was treated with triethylamine (300 μL, 2.15 mmol) and heated to reflux for 3 h. After cooling to rt, the solvent was removed under reduced pressure to give a dark brown viscous residue that was further evaporated under vacuum. The residue was purified using flash chromatography (ethyl acetate to 10% methanol in ethyl acetate) to give the title compound as a dark yellow solid.

Dark yellow solid; 251 mg (86 % yield). ^{1}H-NMR (500 MHz, $(CD_3)_2SO$): δ = 11.99 (s, 1H), 7.43 (dd, *J* = 7.4, 1.2, 1H), 7.29 (td, *J* = 7.7, 1.2, 1H), 7.17 (d, *J* = 7.7, 1H), 7.07 (td, *J* = 7.4, 1.2, 1H), 5.35 (s, 1H), 4.81 (q, *J* = 7.1, 2H), 3.90 (t, *J* = 7.3, 2H), 2.19 (t, *J* = 7.3, 2H), 1.65 (p, *J* = 7.3, 2H), 1.59 – 1.49 (s and m, 6H and 2H), 1.44 (t, *J* = 7.1, 3H), 1.39 – 1.32 (m, 2H). LR-ESI-MS: Calcd. *m/z* for $C_{23}H_{26}NO_5^-$ $[M+H]^-$: 396.2; found: 396.1.

Analytical data not reported previously

(*E*)-3-((1-(3,5-dinitrobenzyl)-3,3-dimethylindolin-2-ylidene)methyl)-4-ethoxycyclobut-3-ene-1,2-dione (16):

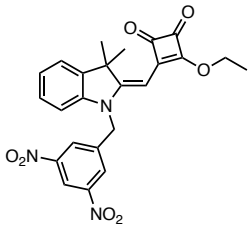

To a solution of **8** (133 mg, 0.39 mmol) in dry ethanol (4 mL), 3,4-diethoxy-3-cyclobutene-1,2-dione (60 μL, 0.39 mmol) was added and the resulting mixture was treated with triethylamine (150 μL, 1.08 mmol) and it was heated to reflux for 3 h. The crude product was concentrated under reduced pressure to give a dark purple residue that was further evaporated under vacuum.

Purple solid; 305 mg (21% yield). ^{1}H-NMRz (500 MHz, $(CD_3)_2SO$): δ = 8.59 (d, *J* = 2.4, 1H), 8.14 – 8.11 (m, 1H), 7.45 (dt, *J* = 7.6, 1.0, 1H), 7.34 (td, *J* = 7.6, 1.0, 1H), 7.08 (td, *J* = 7.6, 1.0, 1H), 7.01 (d, *J* = 7.6, 1H), 6.23 (bs, 1H), 5.37 (bs, 2H), 4.47 (q, *J* = 7.1, 2H), 3.20 (q, *J* = 7.1, 2H), 1.42 (s, 6H), 1.28 (t, *J* = 7.1, 3H). The rest of the signals correspond to 79% of unreacted starting material.

Analytical data not reported previously.

(*E*)-3-((1-(3,5-dinitrobenzyl)-3,3-dimethylindolin-2-ylidene)methyl)-4-methoxycyclobut-3-ene-1,2-dione (17):

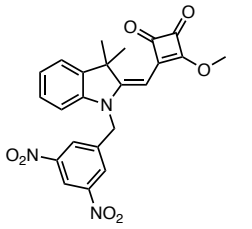

To a solution of **8** (328 mg, 0.97 mmol) in dry methanol (7 mL), 3,4-dimethoxy-3-cyclobutene-1,2-dione (153 mg, 1.1 mmol) was added and the resulting mixture was stirred at rt for 20 h. The reaction mixture was filtered and the filtrate was

evaporated under reduced pressure to give the crude product (855 mg), which was purified using flash chromatography (hexanes/ethyl acetate, 6:4) to give the title compound. Unreacted **8** (71 mg) was also isolated.

Orange powder; 106 mg (25% yield). ^{1}H-NMR (500 MHz, $(CD_3)_2SO$): δ = 8.73 (t, *J* = 2.1, 1H), 8.38 (d, *J* = 2.1, 2H), 7.54 - 7.50 (m, 1H), 7.30 - 7.24 (m, 1H), 7.19 – 7.16 (m, 1H), 7.14 - 7.08 (m, 1H), 5.55 (s, 2H), 5.42 (s, 1H), 4.36 (s, 3H), 1.65 (s, 6H). LR-ESI-MS: Calcd. *m/z* for $C_{23}H_{20}N_3O_7^+$ $[M+H]^+$: 436.1; found: 436.1. The mass spectrum contains additional peaks and the product peak is of very low intensity.

Analytical data not reported previously.

(*E*)-3-((1-(3,5-dinitrobenzyl)-3,3-dimethylindolin-2-ylidene)methyl)-4-hydroxycyclobut-3-ene-1,2-dione (18):

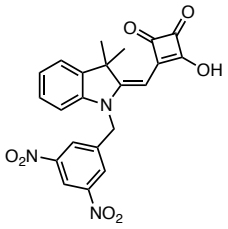

17 (280 mg, 0.62 mmol) was dissolved in acetic acid (6 mL) and a 1M solution of HCl (0.45 mL) was added. The dark orange mixture was heated at 80 °C for 5 h and the resulting mixture was evaporated under reduced pressure to give a brown viscous residue. This residue was triturated with diethyl ether, and the solid material was isolated by filtration and washed with diethyl ether and dried under high vacuum to give the title compound, which was used in the next step without further purification.

Olive green solid; 156 mg (58% yield). ^{1}H-NMR (500 MHz, $(CD_3)_2SO$): δ = 8.73 (t, *J* = 2.1, 1H), 8.40 (d, *J* = 2.1, 2H), 7.47 (dd, *J* = 7.6, 1.2, 1H), 7.22 (td, *J* = 7.6, 1.2, 1H), 7.10 – 7.01 (m, 2H), 5.50 (s, 1H), 5.45 (s, 2H), 1.66 (s, 7H). The material contains residual acetic acid and diethyl ether. LR-ESI-MS: Calcd. *m/z* for $C_{22}H_{18}N_3O_7^+$ $[M+H]^+$: 436.1; found: 436.1.

Analytical data not reported previously.

Synthesis of 1 using immobilized 9:

2-Chlorotrityl chloride resin (71 mg, 0.15 mmol) was swelled in dry CH_2Cl_2 for 1 h at rt in a 10 mL reactor vial (Biotage) and the solvent was drained off by vacuum suction. A mixture of **9** (45 mg, 0.1 mmol) and DIPEA (25 µL, 0.2 mmol) in dry CH_2Cl_2 (2 mL) was added to the swelled resin and the reaction mixture was agitated for 4 h at rt. The resin was then rinsed four times with DCM (2 mL) and the resin was agitated with a capping solution consisting of DCM/MeOH/DIPEA (8:1.5:0.5, 2 mL) rt for 10 min (step repeated twice). After a DCM (2 mL) wash, DIPEA (0.2 mL, 10 mmol) in DCM (2 mL) was added and reacted for 1 h at rt. After washing with DCM (3 x 2 mL), a mixture of **18** (45.1 mg, 0.1 mmol), DIPEA (25 µL, 0.2 mmol) and DIC (15 µL, 0.1 mmol) in DCM (2 mL) was added to the resin. The reaction mixture was transferred to a sealed vial and heated at 80 °C for 3 h. The resin was washed thoroughly with DCM (6 x 2 mL). The final compound was then cleaved from the resin with a mixture consisting of DCM/TFA (9.5:0.5, 2 mL) with agitation for 10 min at rt (step repeated twice). The TFA fraction was concentrated under reduced pressure and cold diethyl ether was added to the residual TFA. The title compound was isolated from diethyl ether by extraction with acetonitrile/water + 0.1%TFA (50:50) and was purified by semi-prep RP-HPLC (50 - 90% acetonitrile in water, both solvents containing 0.1% TFA) to give **1** as an iridiscent blue solid (0.5 mg, 1% yield).

Analytical data:

Figure S1: ^{1}H-NMR spectrum of **5** in DMSO

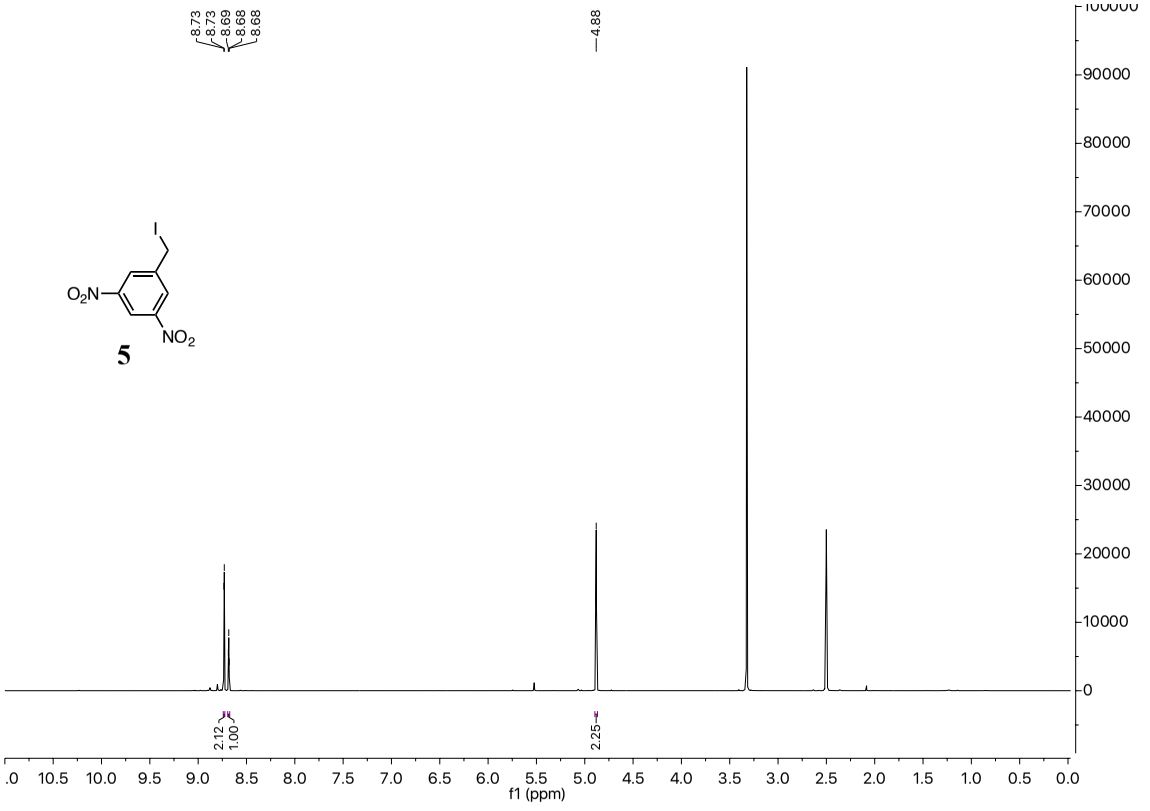

Figure S2: [1]H-NMR spectrum of **6** in DMSO

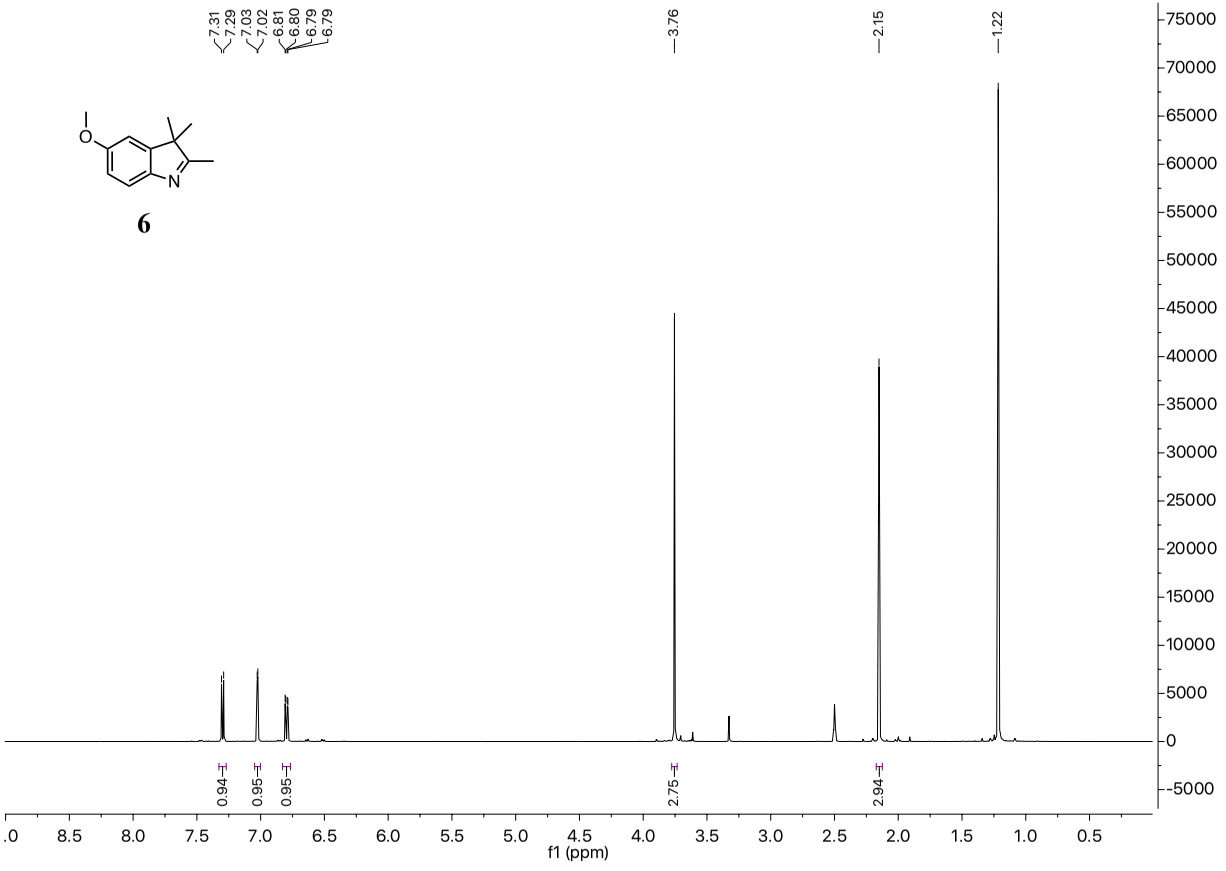

Figure S3: ^{1}H-NMR spectrum of **7** in DMSO

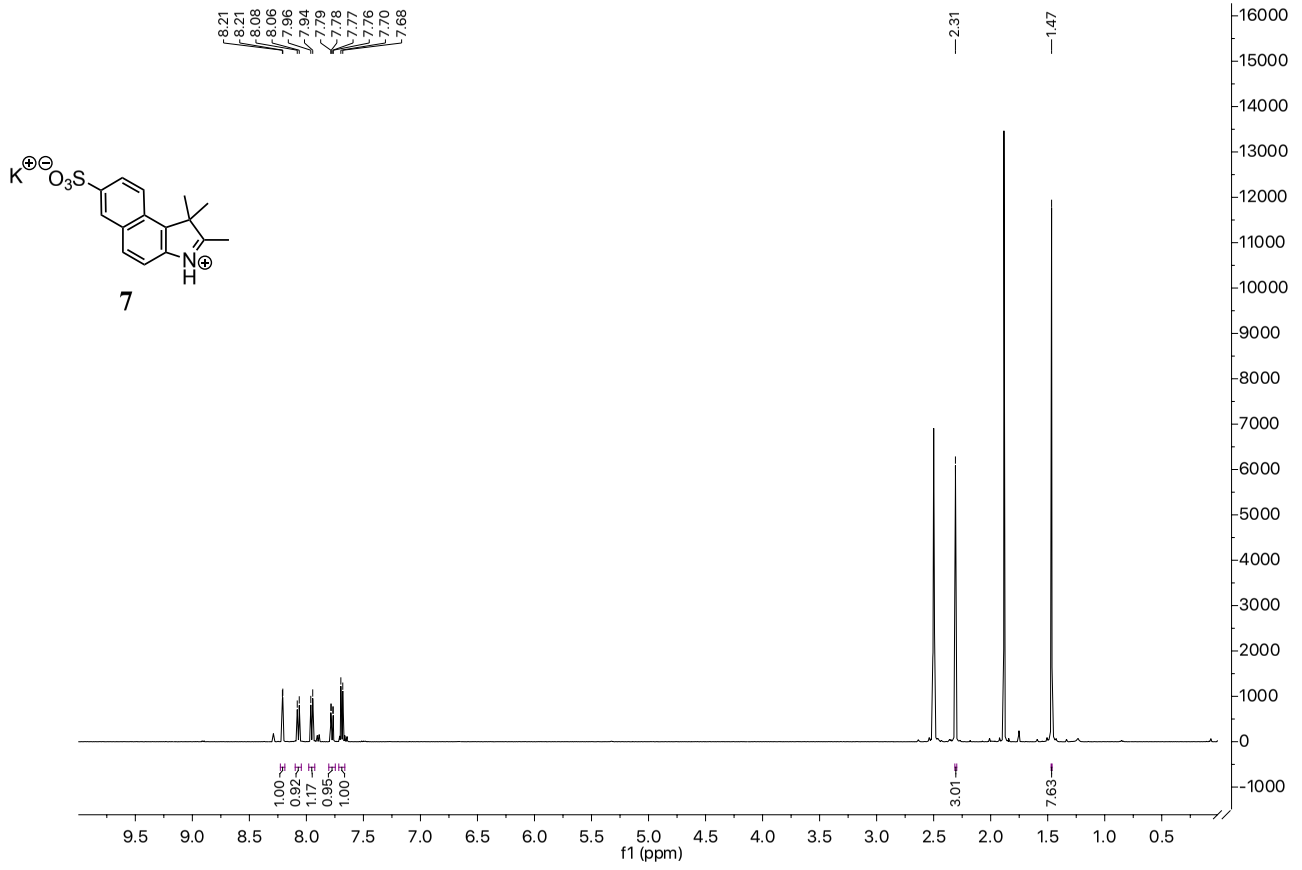

Figure S4: [1]H-NMR spectrum of **8** in MeOD

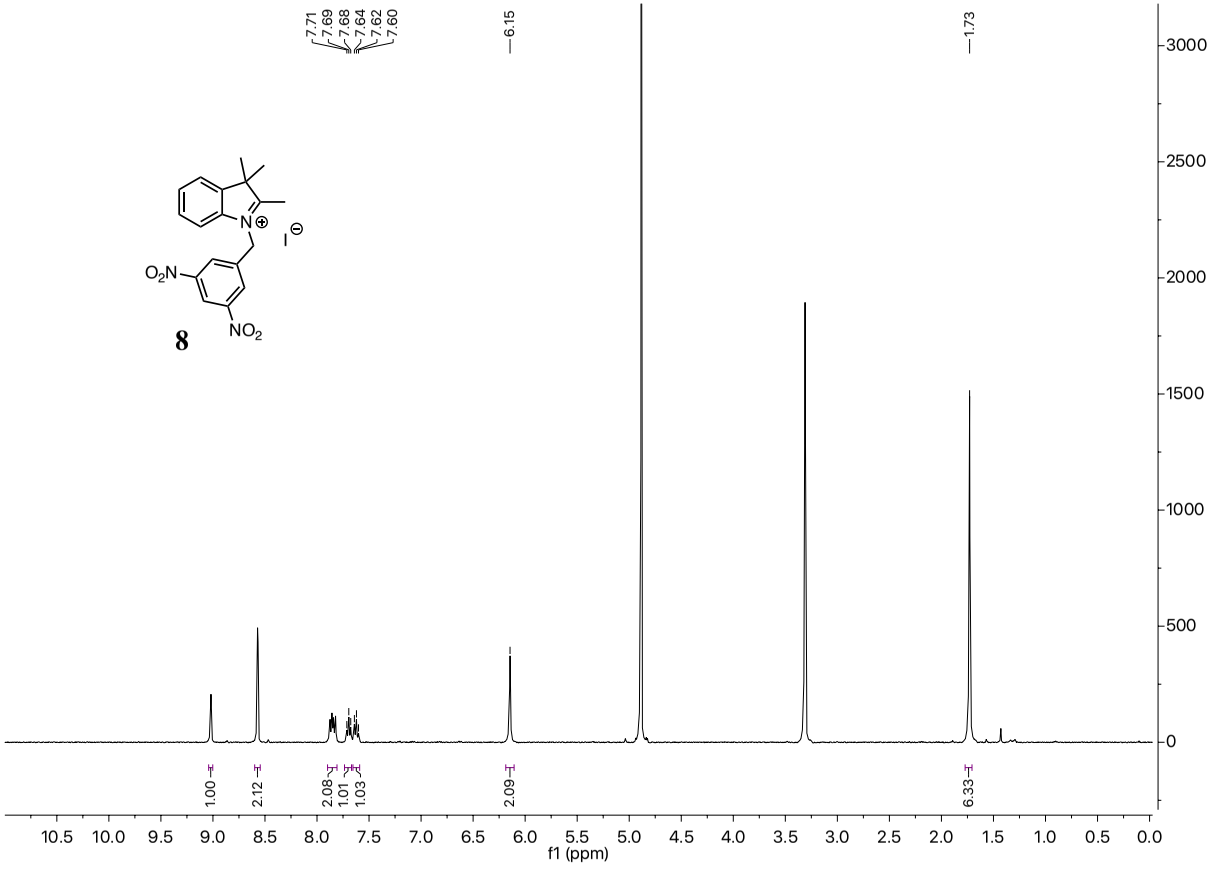

Figure S5: ^{1}H-NMR spectrum of **9** in DMSO

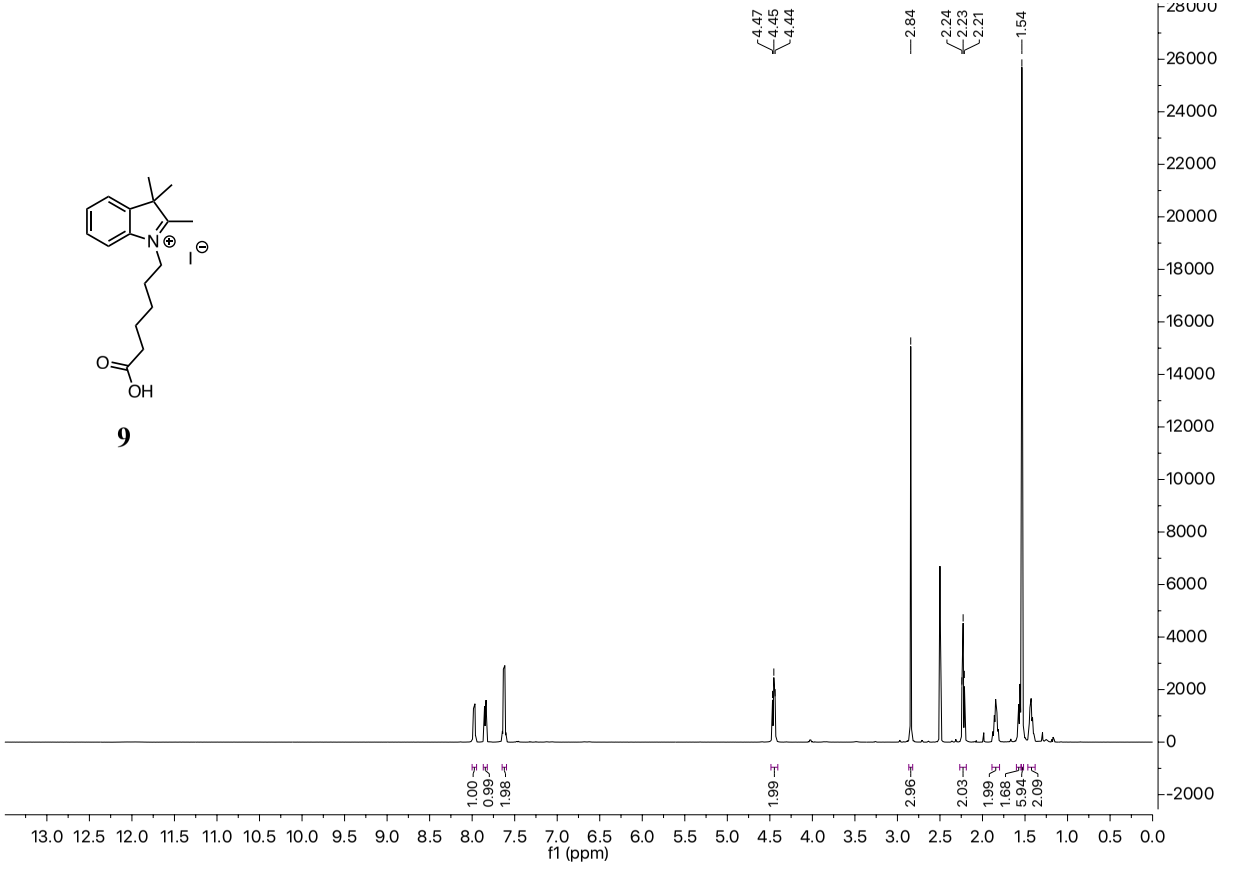

9

Figure S6: ^{1}H-NMR spectrum of **10** in DMSO

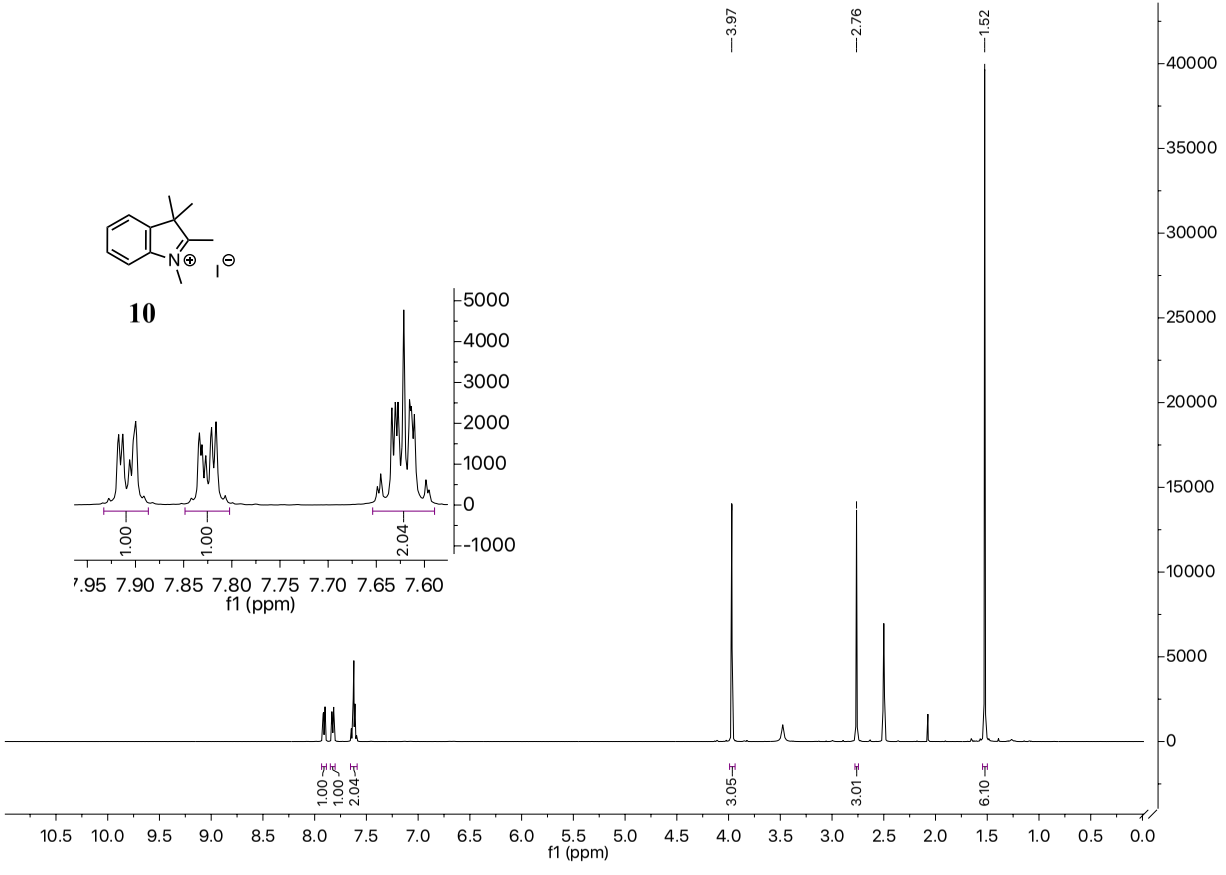

Figure S7: ^{1}H-NMR spectrum of **11** in DMSO

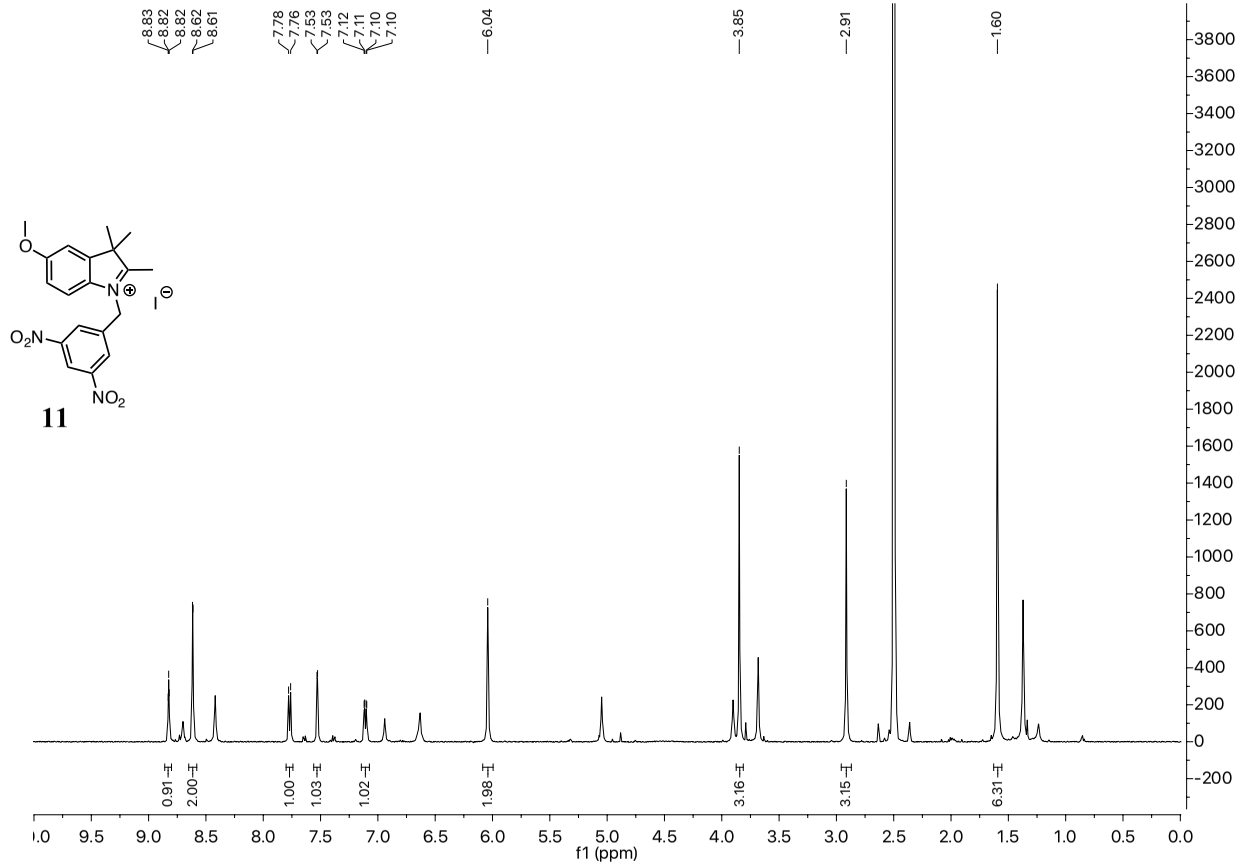

Figure S8: [1]H-NMR spectrum of **12** in DMSO

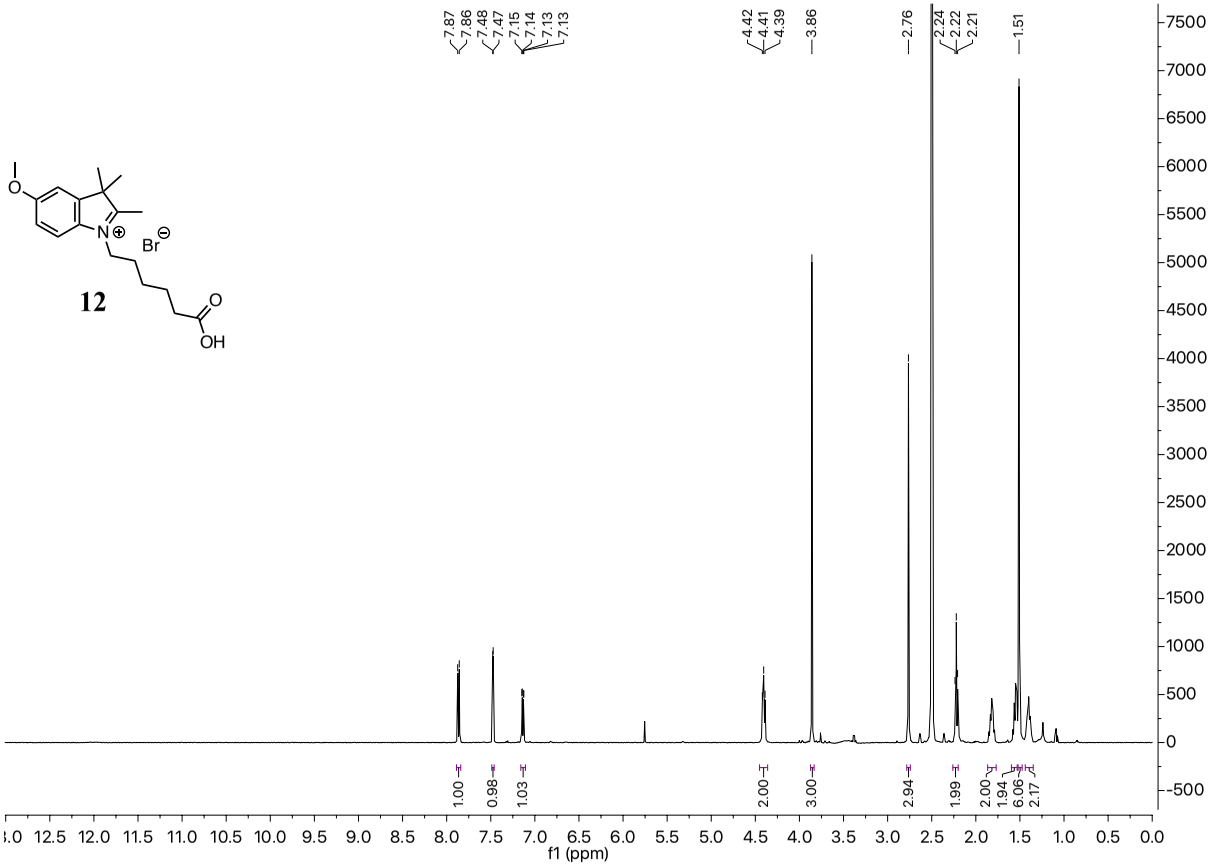

Figure S9: ^{1}H-NMR spectrum of **13** in DMSO

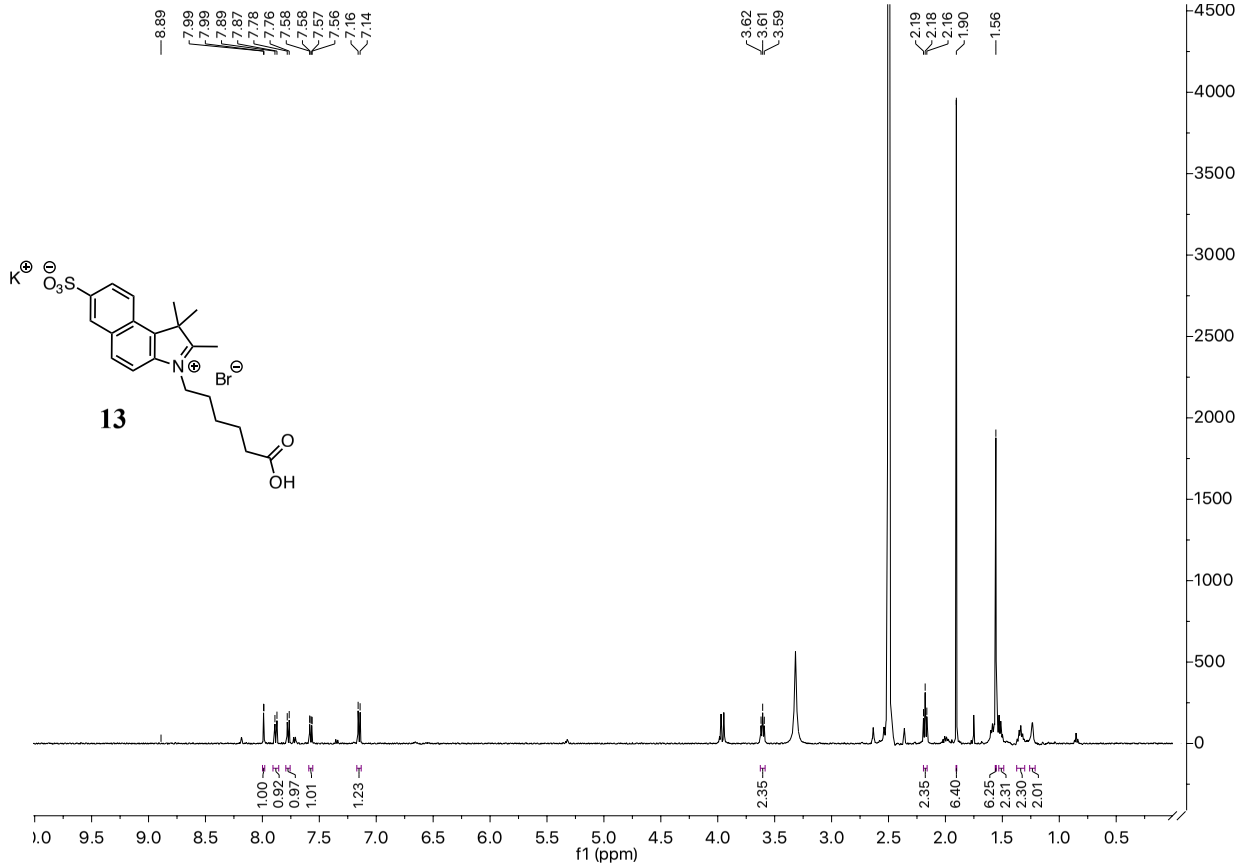

Figure S10: [1]H-NMR spectrum of **14** in DMSO

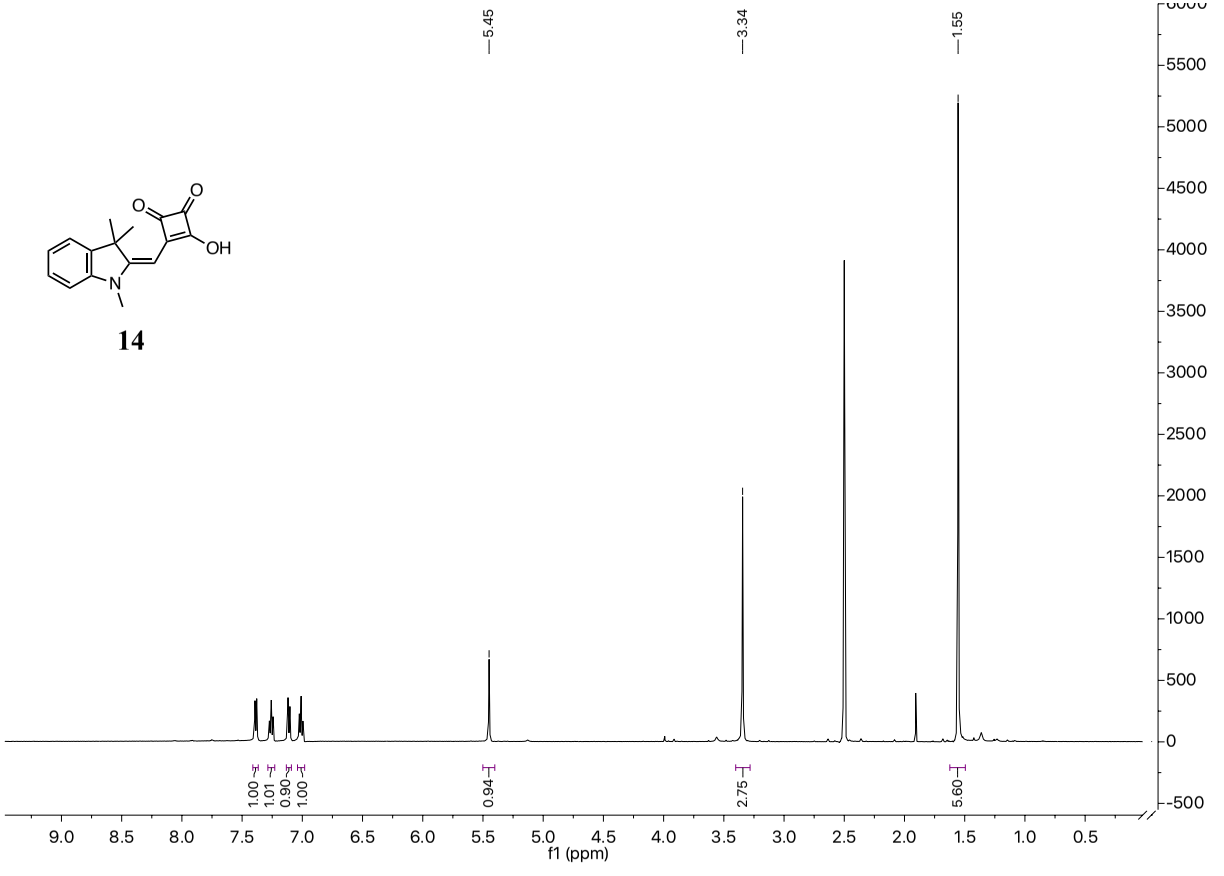

Figure S11: ^{1}H-NMR spectrum of Substrate **1** in DMSO

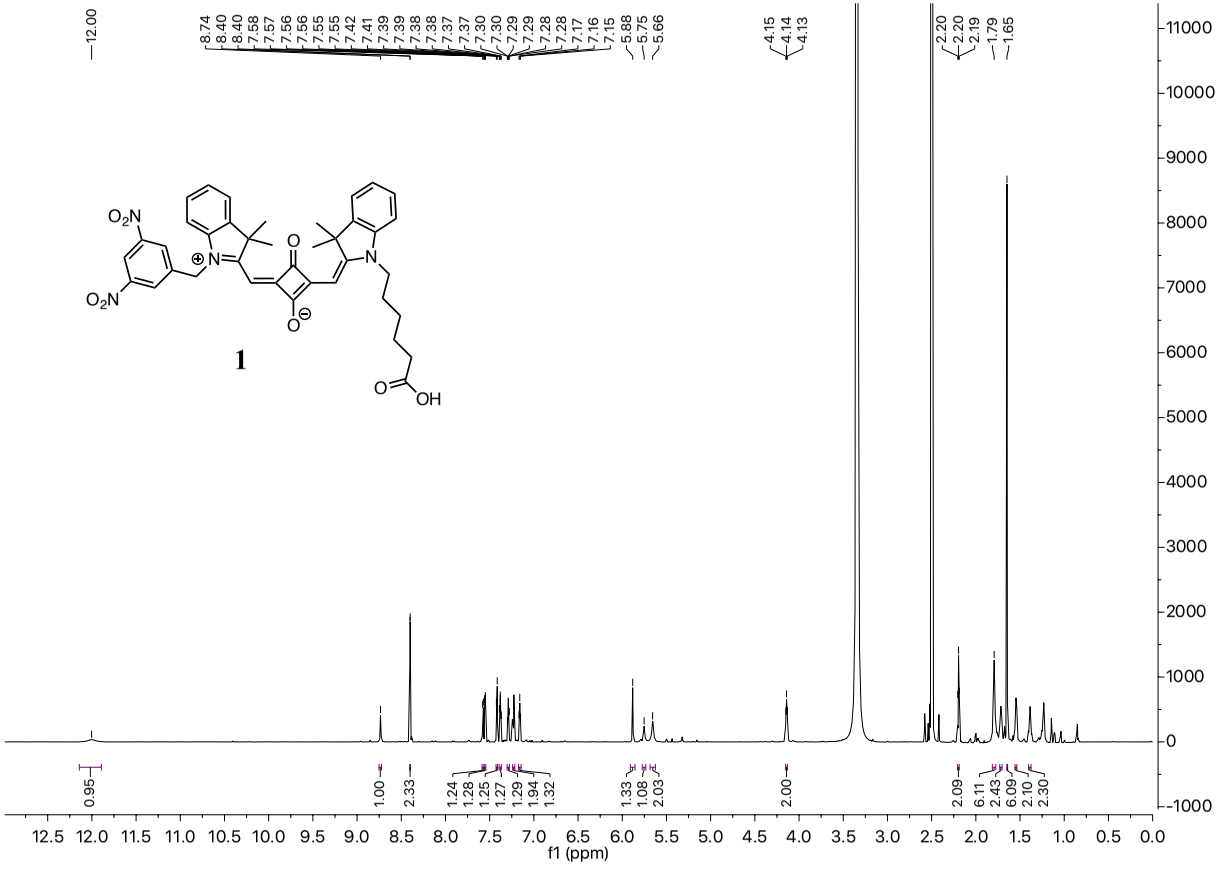

Figure S12: A: Analytical RP-HPLC chromatogram and UV trace of Substrate **1**; B: HRMS spectrum of Substrate **1**

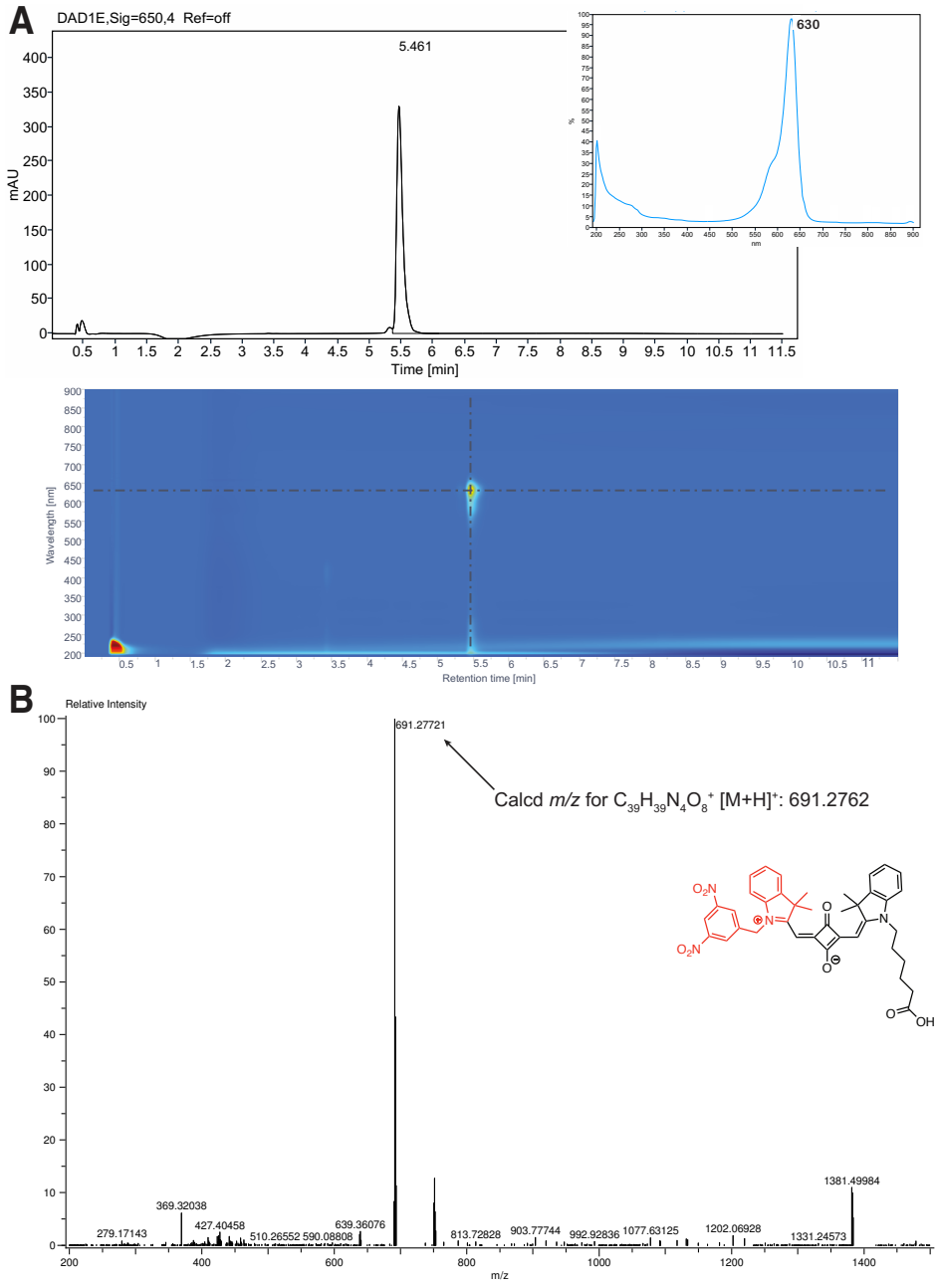

Figure S13: ^{1}H-NMR spectrum of Substrate **2** in DMSO

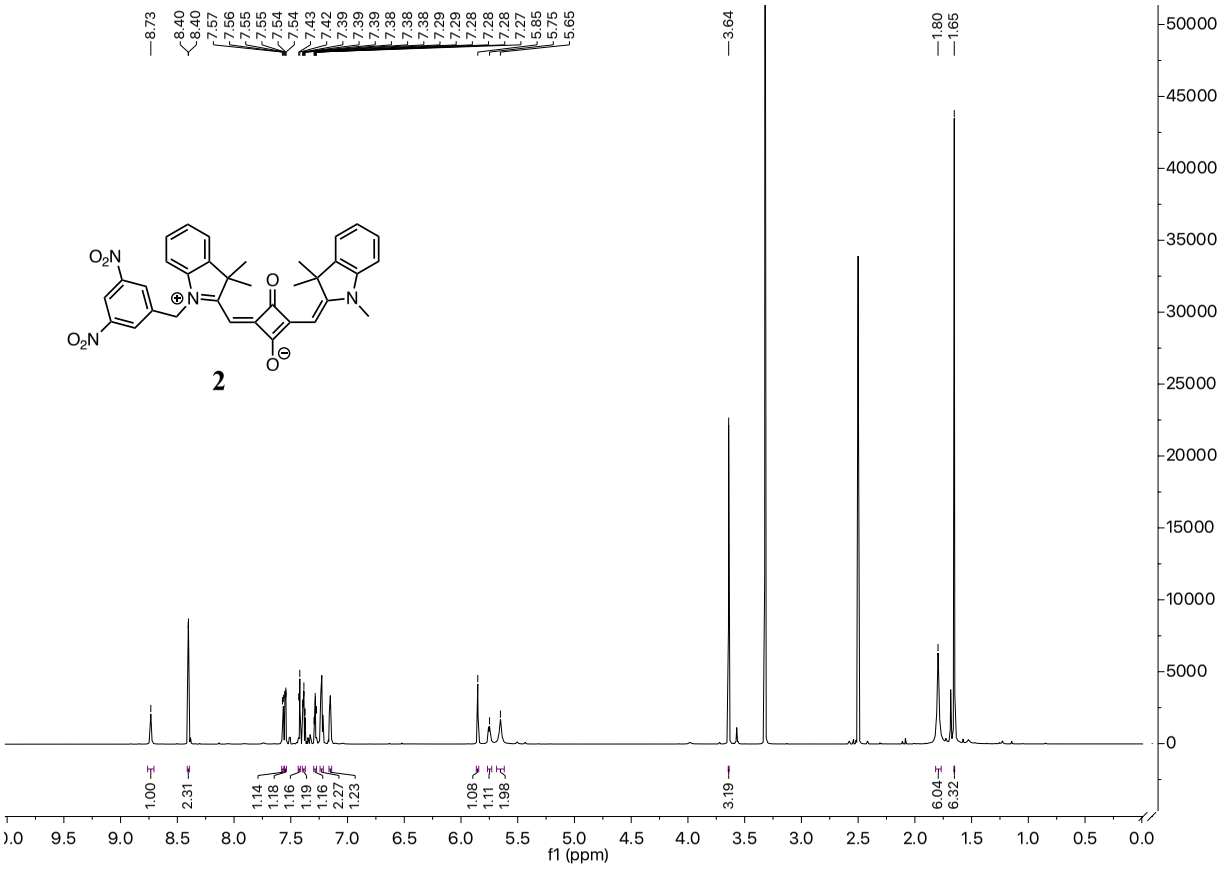

Figure S14: A: Analytical RP-HPLC chromatogram and UV trace of Substrate **2**; B: HRMS spectrum of Substrate **2**

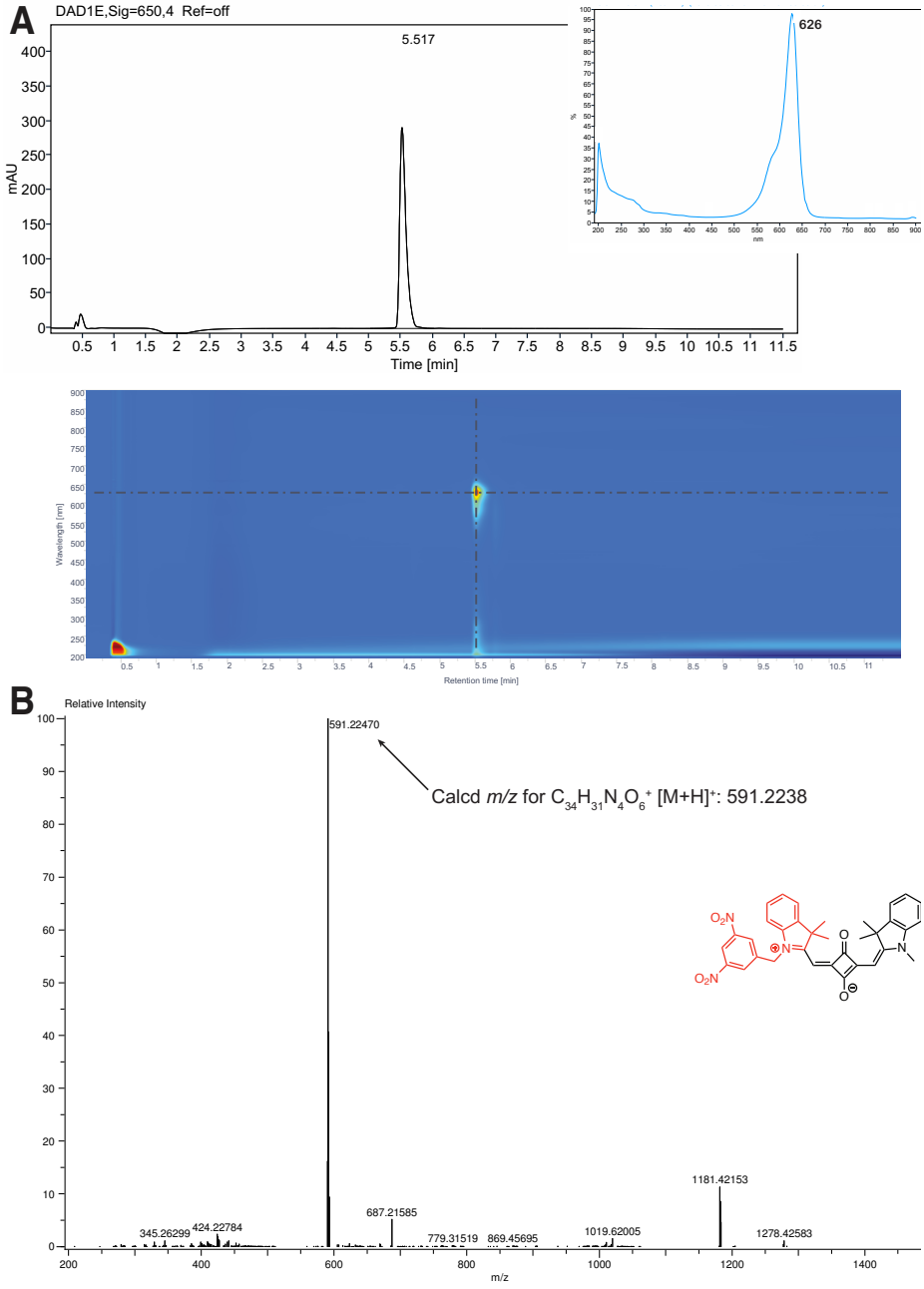

Figure S15: [1]H-NMR spectrum of Substrate **3** in DMSO

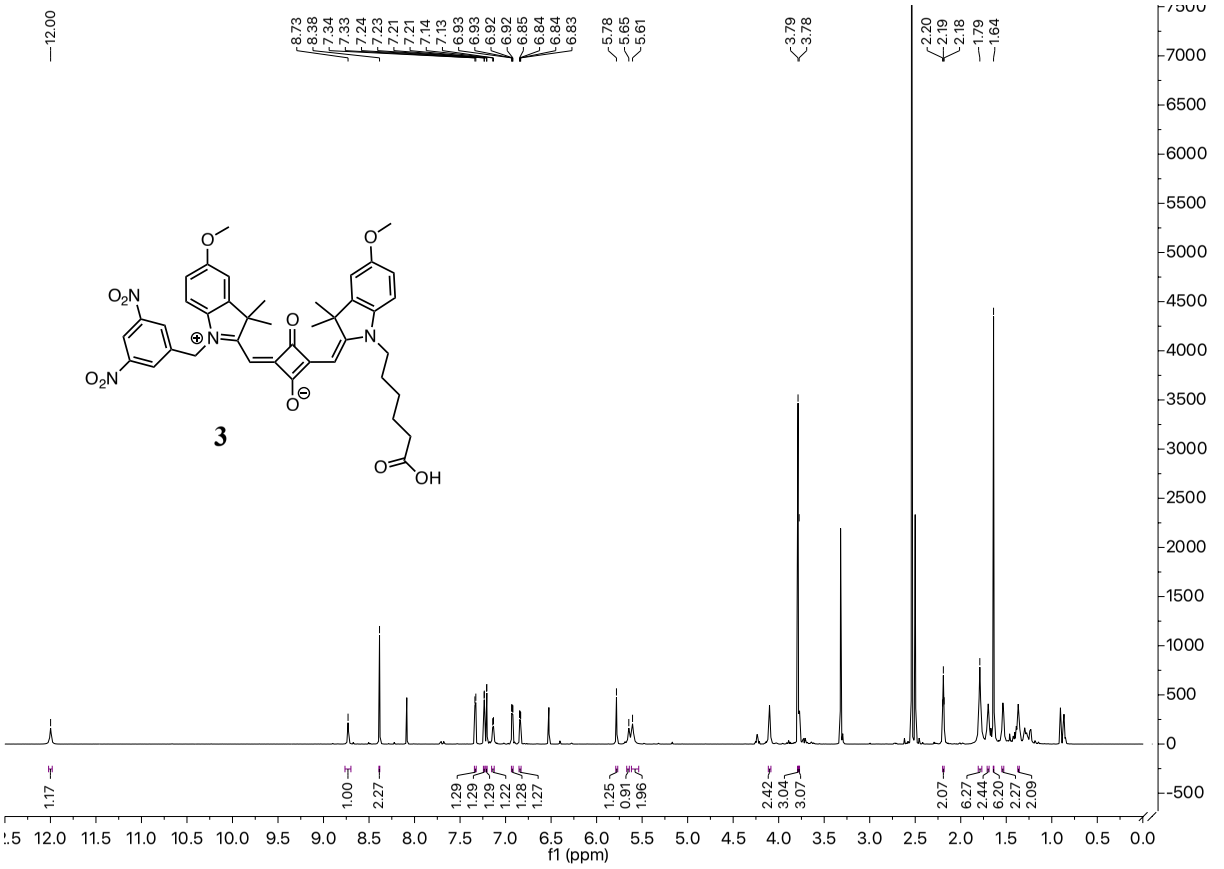

Figure S16: A: Analytical RP-HPLC chromatogram and UV trace of Substrate **3**; B: HRMS spectrum of Substrate **3**

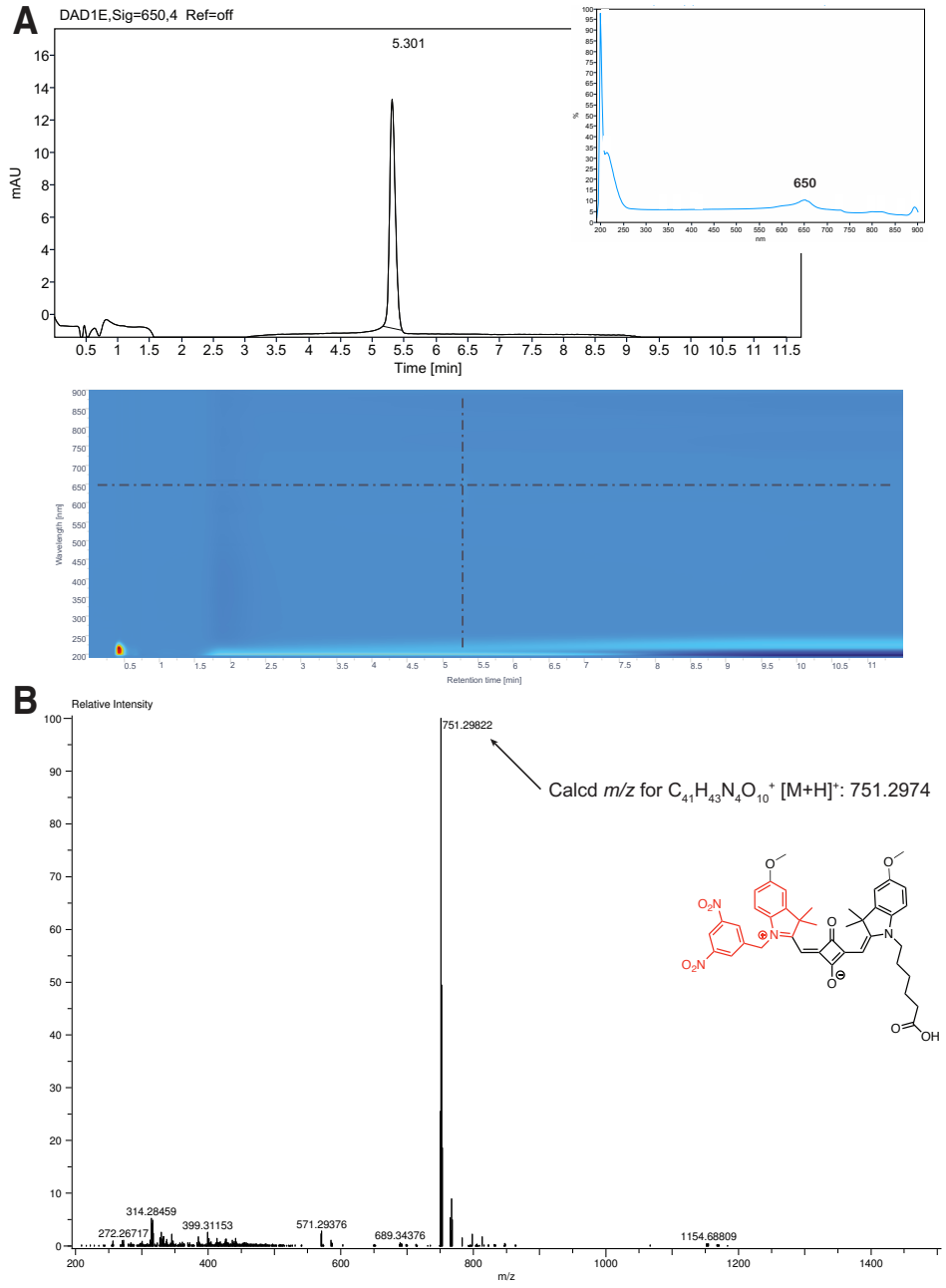

Figure S17: ^{1}H-NMR spectrum of Substrate **4** in DMSO

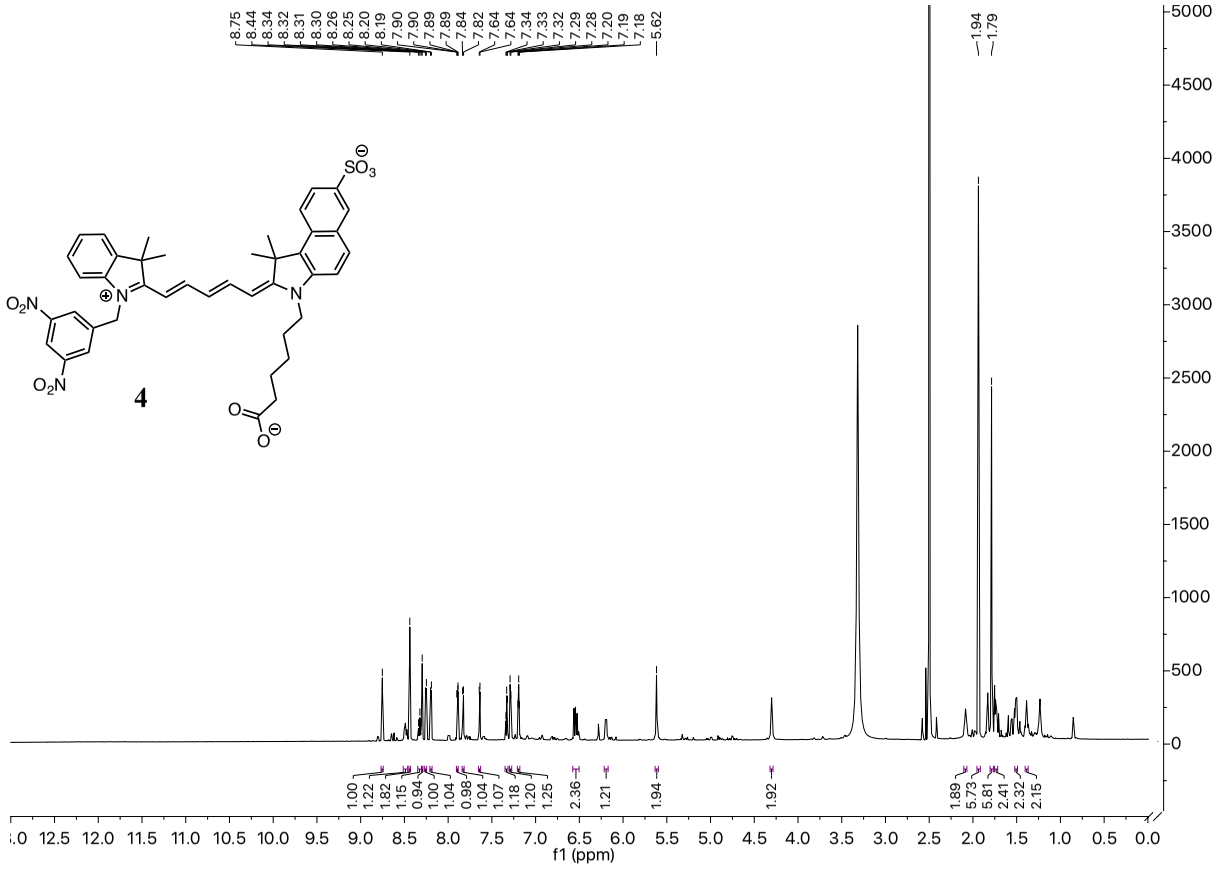

Figure S18: A: Analytical RP-HPLC chromatogram and UV trace of Substrate **4**; B: HRMS spectrum of Substrate **4**

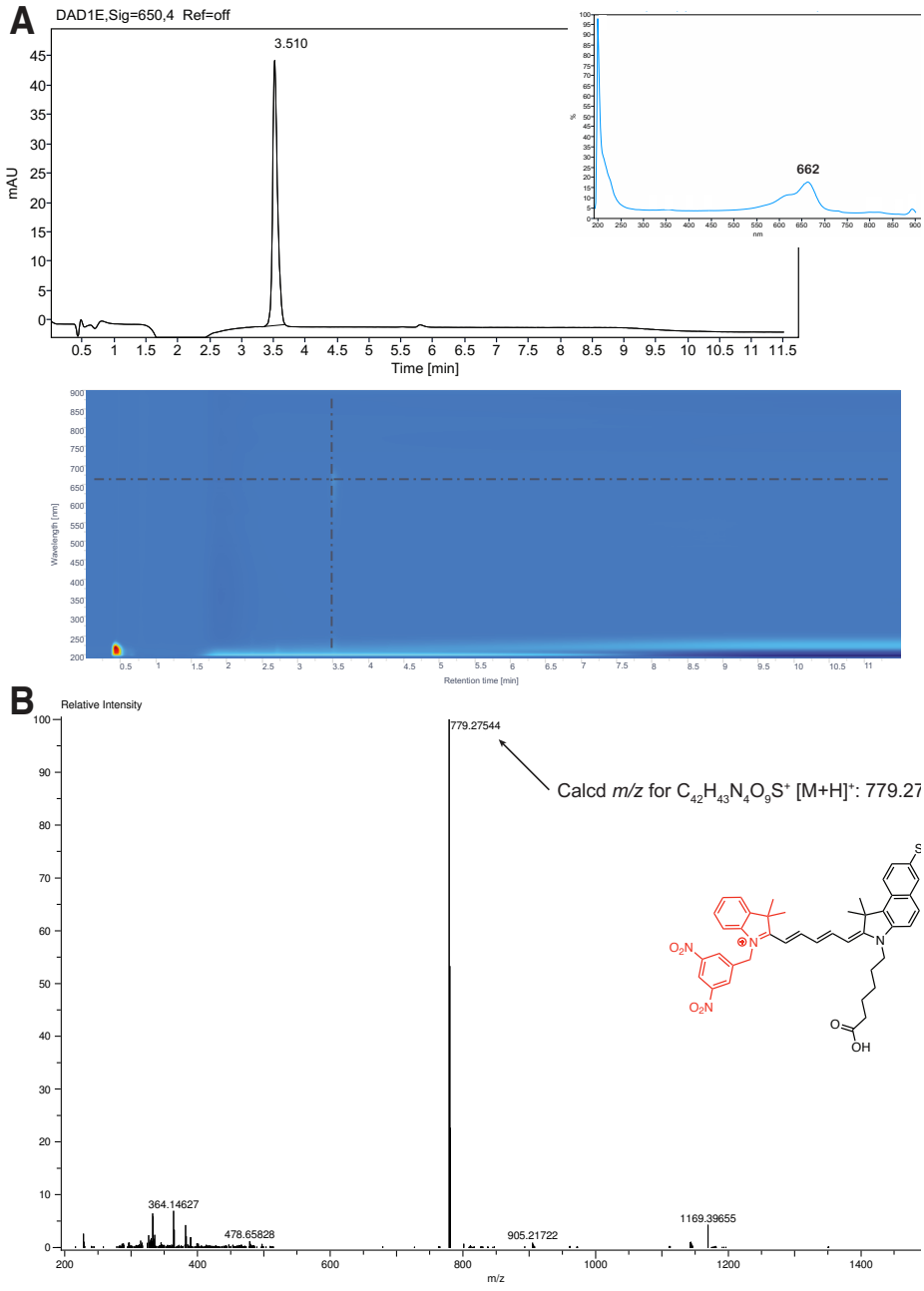

Figure S19: ^{1}H-NMR spectrum of **15** in DMSO

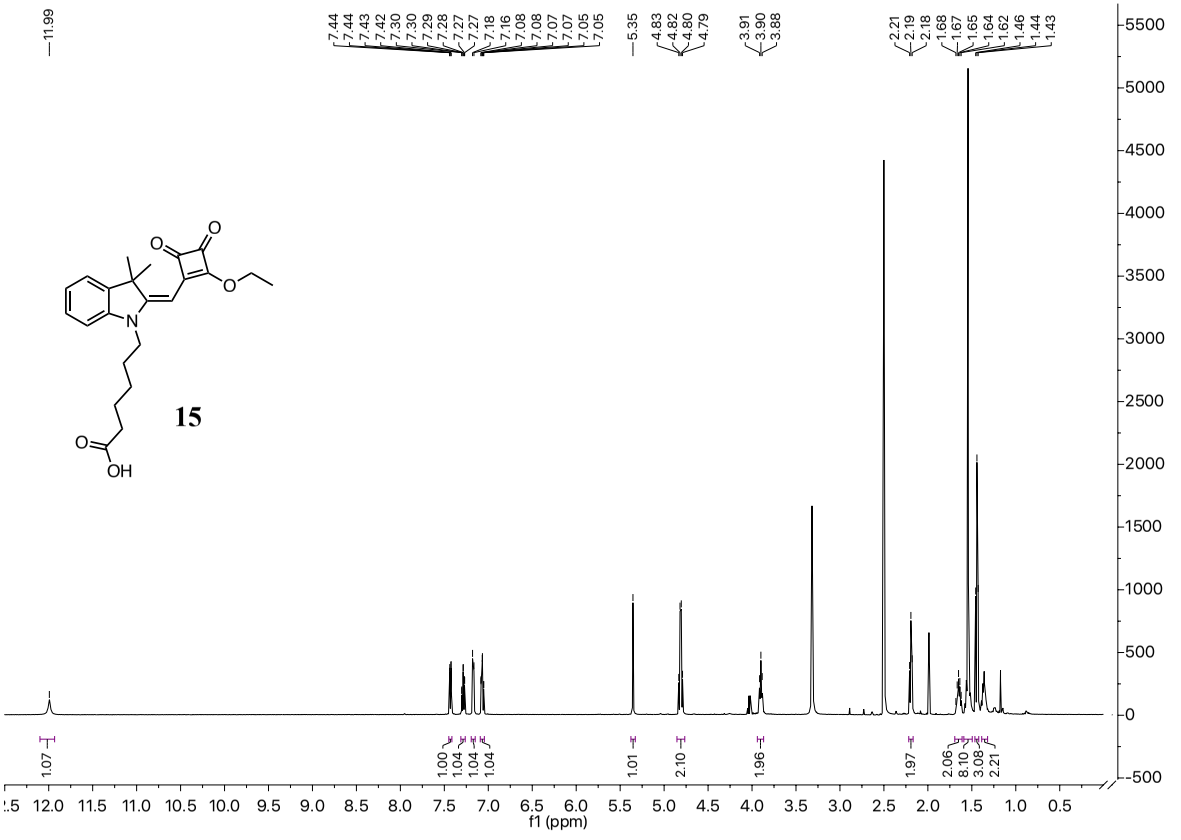

Figure S20: ^{1}H-NMR spectrum of **16** in DMSO

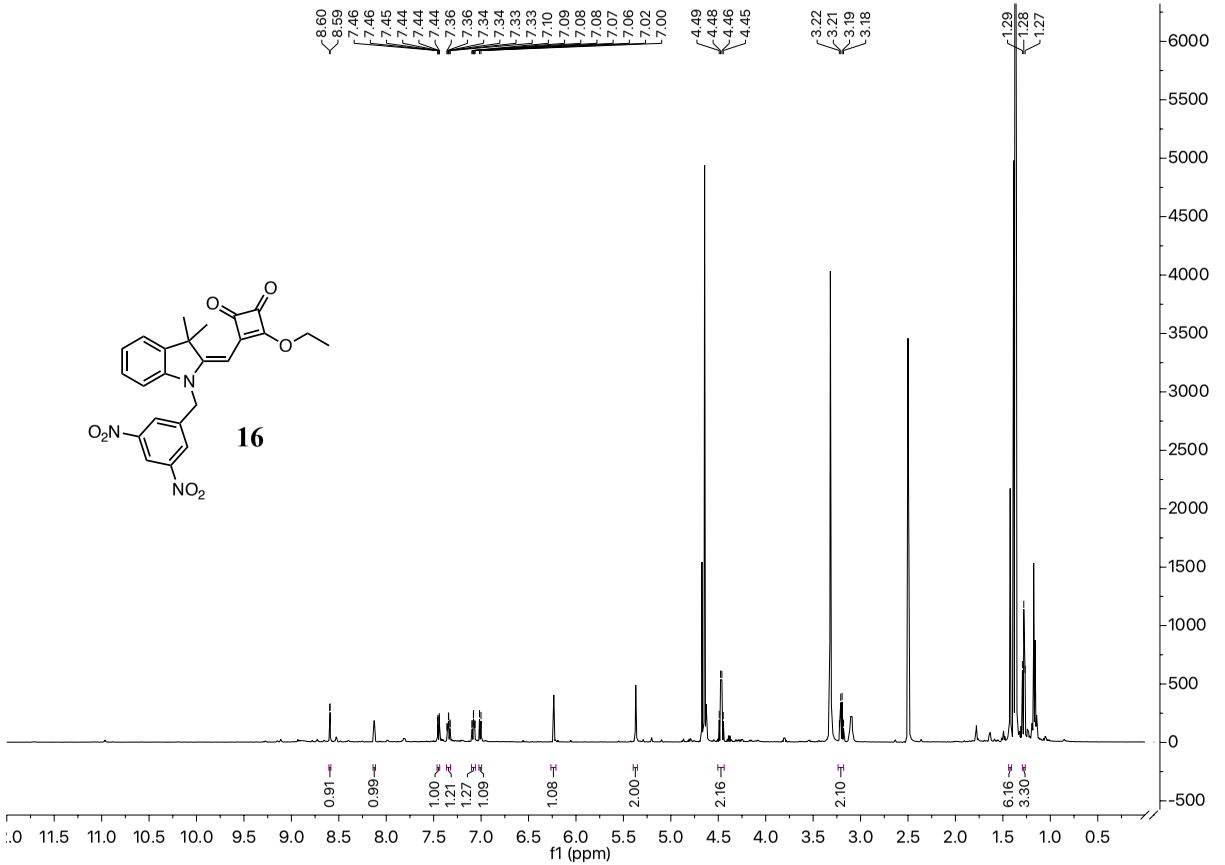

Figure S21: ^{1}H-NMR spectrum of **17** in DMSO

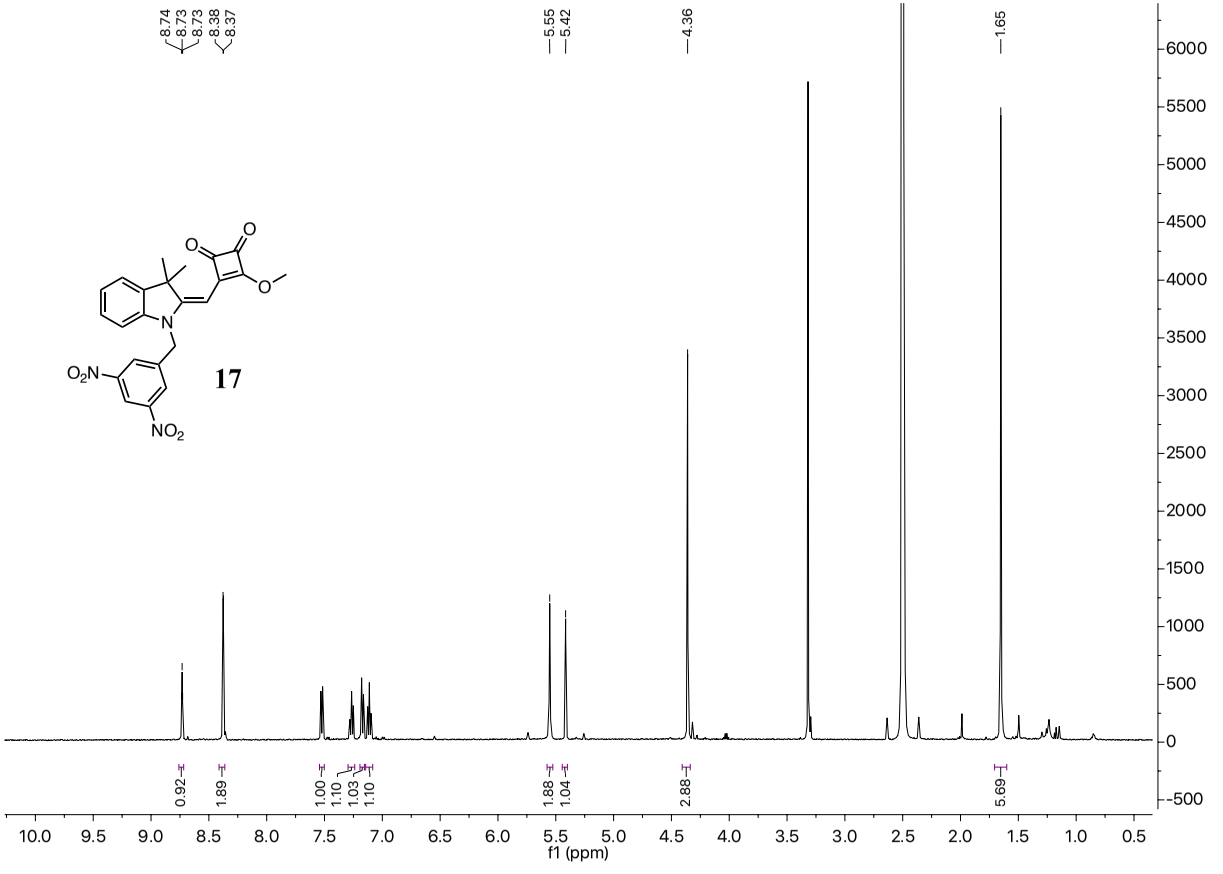

Figure S22: ^{1}H-NMR spectrum of **18** in DMSO

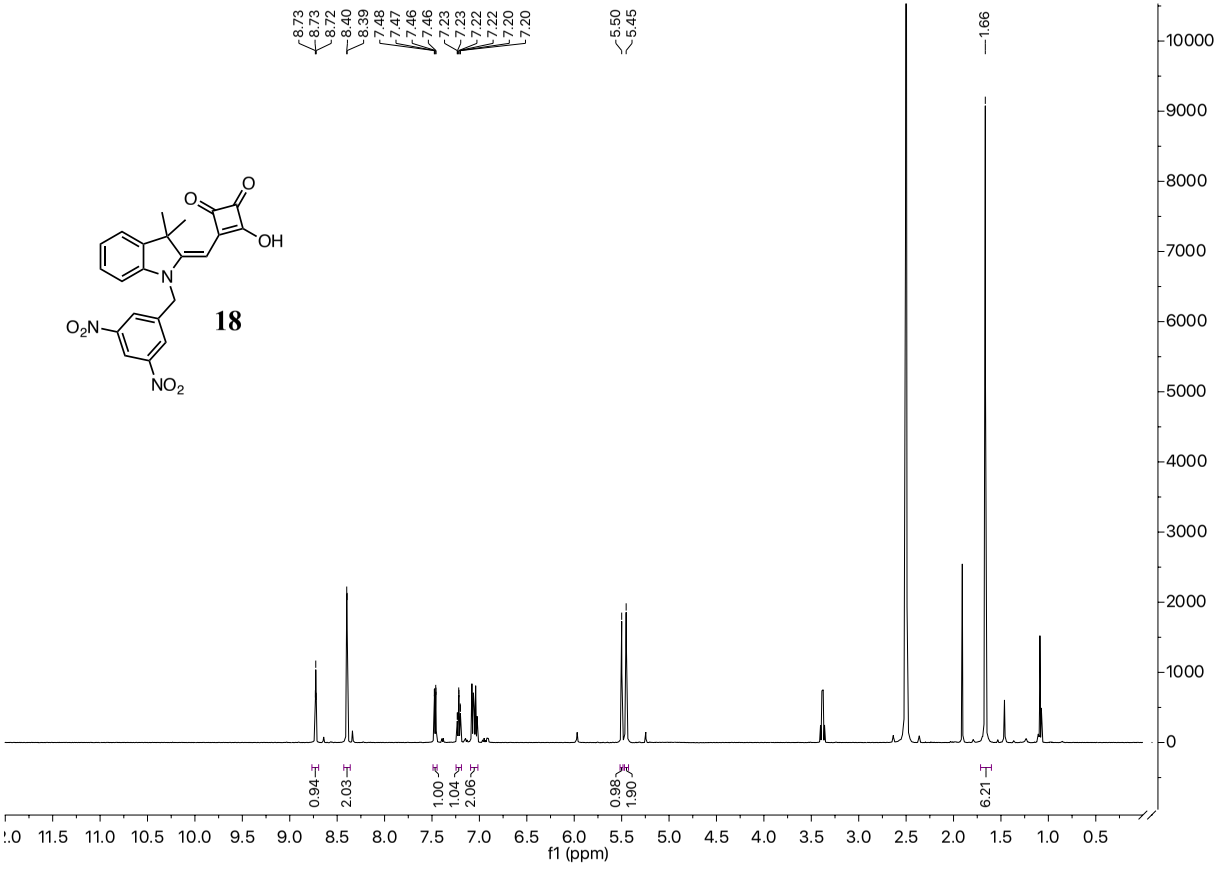

Figure S23: Confocal fluorescence microscopy with substrates **1** – **4** with the same scale for "NTR substrate" channel

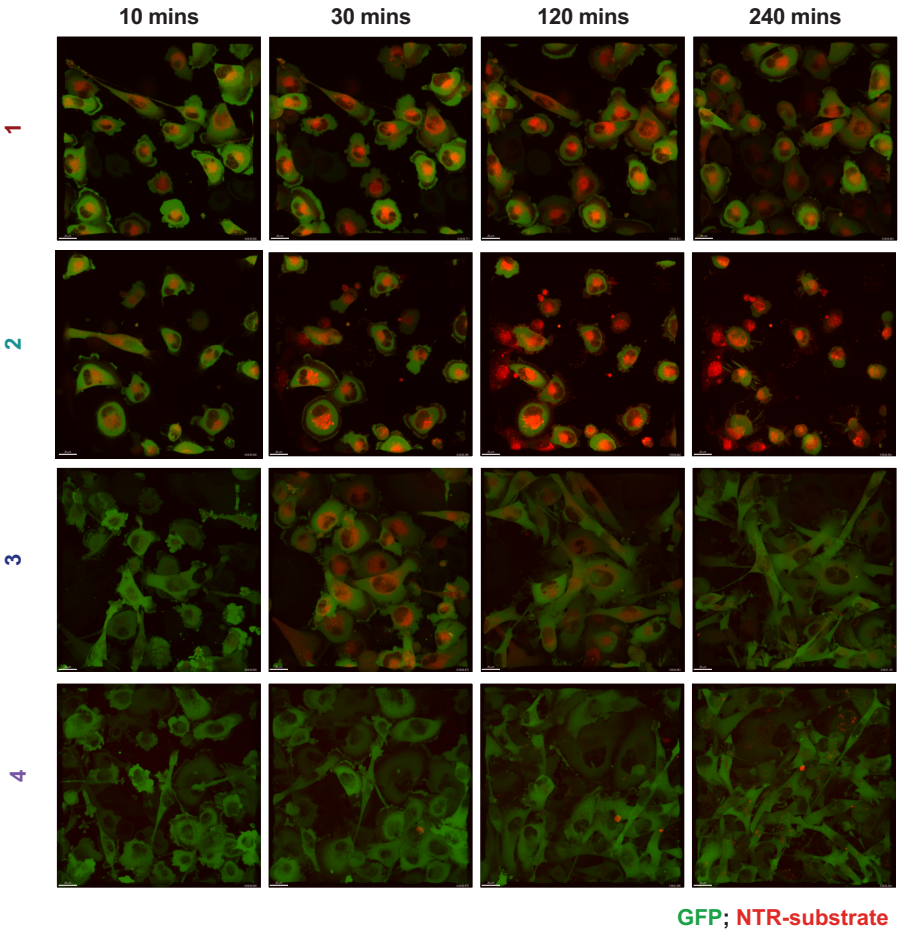

Figure S24: A) Chemical structures of substrates 1 – 4, their respective B) absorbance spectra (200 – 900 nm) from the HPLC UV trace showing the absorbance of the acetonitrile used as the buffer and the absorbance of each substrate at the given wavelength and C) Vis-NIR absorbance spectra (500 – 700 nm) after two hours incubation of 4 µM of substrate with 0.2 µM NTR enzyme.

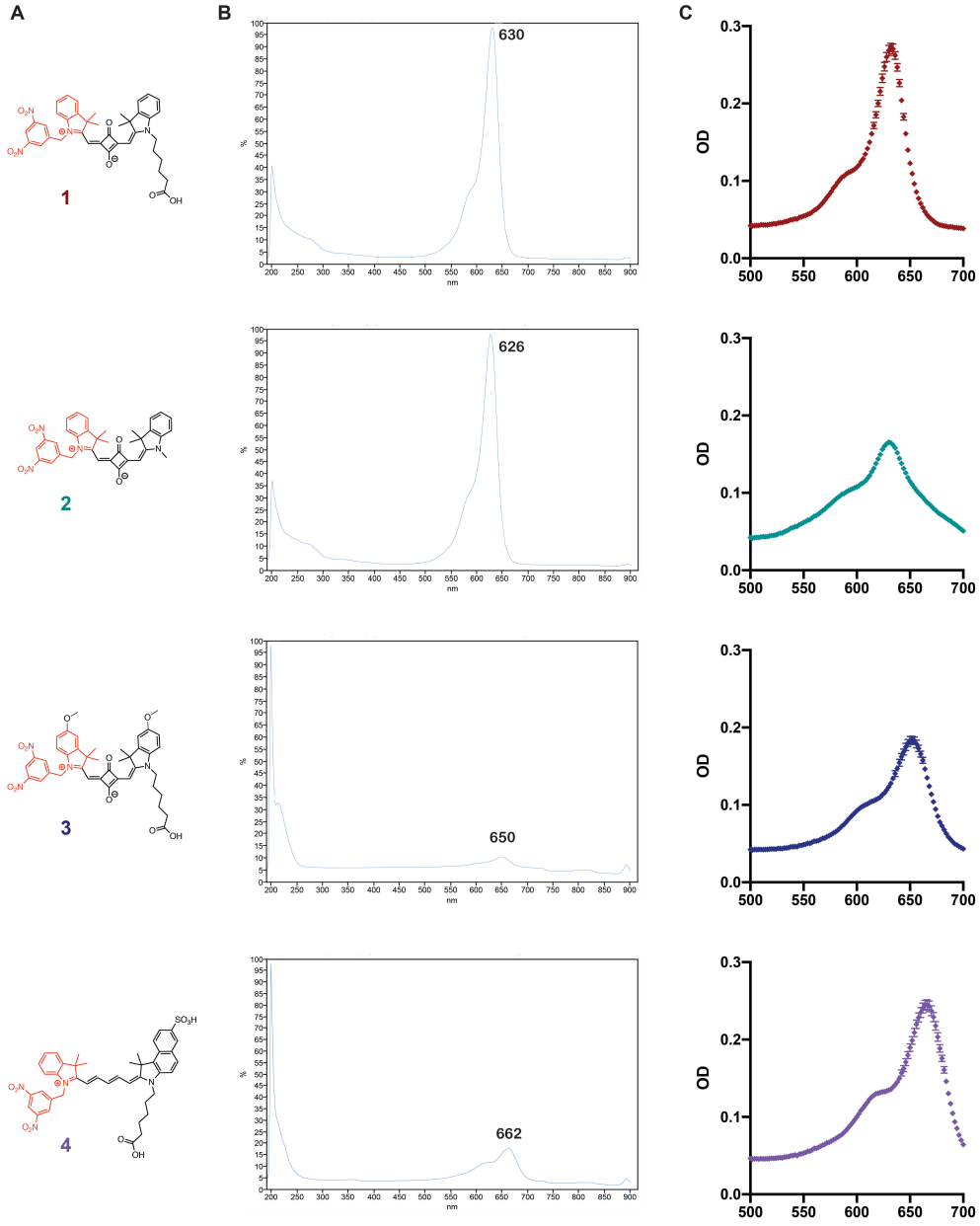

Figure S25: Flow cytometry analysis of unstained NTR^- and NTR^- and NTR^+ stained with 3 µM of substrates 1 - 4 for four hours. Values are reported as Mean Fluorescence Intensity (MFI) with the corresponding statistically significant differences between groups (One-way ANOVA. *p*-values: *, $p < 0.05$ ** and $p < 0.01$).

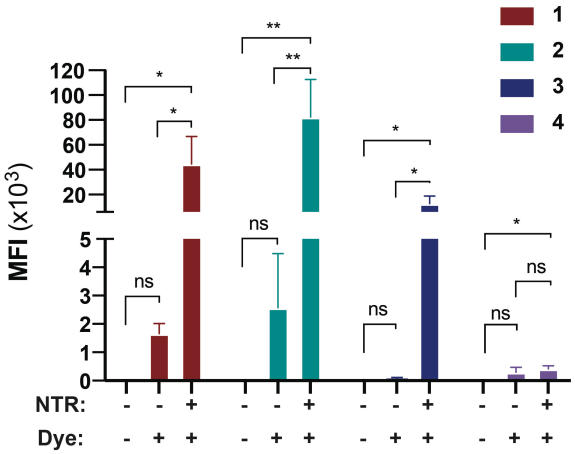

Video S1: Full time lapse for substrate 1

Video S2: Full time lapse for substrate 2

Video S3: Full time lapse for substrate 3

Video S4: Full time lapse for substrate 4

References:

[1] E. Terpetschnig, J.R. Lakowicz, Synthesis and characterization of unsymmetrical squaraines: a new class of cyanine dyes, Dyes Pigments 21(3) (1993) 227-234.

[2] E.A. Terpetschnig, L.D. Patsenker, A. Tatarets, Luminescent compounds, USA . 2004, pp. 37 pp., Cont.-in-part of Appl. No. PCT/US03/10995.

[3] E.A. Terpetschnig, A. Tatarets, O. Galkina, I. Fedyunyaeva, L. Patsenker, Luminescent compounds based on squaric acid derivatives, USA . 2005, pp. 34 pp., Cont.-in-part of U.S. Ser. No. 724,580.

[4] M.H. Sleiman, S. Ladame, Synthesis of squaraine dyes under mild conditions: applications for labelling and sensing of biomolecules, Chem Commun (Camb) (1364-548X (Electronic)) (2014).

[5] M. Alajarin, R.A. Orenes, J.A.K. Howard, E.C. Spencer, J.W. Steed, A. Pastor, Novel Capsular Aggregates from Flexible Tripodal Triureas with Cs Symmetry, Chem-Eur J 18(8) (2012) 2389-2397.

[6] R.M. West, R. Ismail, Nitro-substituted squaraine reporter dyes as reagent for measuring nitroreductase enzyme activity, Amersham Biosciences UK Limited, UK . 2005, p. 52 pp.

[7] G.G.Y. Shen, T.S. Dobashi, Preparation of cyanine dye activating group with improved coupling selectivity to label chain terminators in nucleotide sequencing, Beckman Instruments, Inc., USA . 1999, p. 19 pp.

[8] H.-J. Chen, C.Y. Chew, E.-H. Chang, Y.-W. Tu, L.-Y. Wei, B.-H. Wu, C.-H. Chen, Y.-T. Yang, S.-C. Huang, J.-K. Chen, I.C. Chen, K.-T. Tan, S-Cis Diene Conformation: A New Bathochromic Shift Strategy for Near-Infrared Fluorescence Switchable Dye and the Imaging Applications, J Am Chem Soc 140(15) (2018) 5224-5234.

[9] R.L. Simmons, R.T. Yu, A.G. Myers, Storable Arylpalladium(II) Reagents for Alkene Labeling in Aqueous Media, J Am Chem Soc 133(40) (2011) 15870-15873.

[10] A. Connell, P.J. Holliman, M.L. Davies, C.D. Gwenin, S. Weiss, M.B. Pitak, P.N. Horton, S.J. Coles, G. Cooke, A study of dye anchoring points in half-squarylium dyes for dye-sensitized solar cells, J Mater Chem A 2(11) (2014) 4055-4066.

[11] E. McCormack, E. Silden, R.M. West, T. Pavlin, D.R. Micklem, J.B. Lorens, B.E. Haug, M.E. Cooper, B.T. Gjertsen, Nitroreductase, a near-infrared reporter platform for in vivo time-domain optical imaging of metastatic cancer, Cancer Res 73(4) (2013) 1276-86.

III

IVYSPRING INTERNATIONAL PUBLISHER

Theranostics

2021; 11(12): 6044-6057. doi: 10.7150/thno.55092

Research Paper

Repurposing ^{18}F-FMISO as a PET tracer for translational imaging of nitroreductase-based gene directed enzyme prodrug therapy

Gorka Ruiz de Garibay[1,2*], Elvira García de Jalón[1,3*], Endre Stigen[1], Kjetil B Lund[1], Mihaela Popa[1,4], Ben Davidson[5], Mireia Mayoral Safont[4], Cecilie B. Rygh[6,7], Heidi Espedal[6], Torill M Barrett[8], Bengt Erik Haug[3] and Emmet McCormack[1,9,10]✉

1. Centre for Cancer Biomarkers CCBIO, Department of Clinical Science, University of Bergen, Jonas Lies vei 65, N-5021, Bergen, Norway.
2. University Hospital 12 de Octubre, Madrid, Spain; Lung Cancer Unit H12O-CNIO, Spain.
3. Department of Chemistry and Centre for Pharmacy, University of Bergen, Allégaten 41, N-5007, Bergen, Norway.
4. KinN Therapeutics AS, Jonas Lies vei 65, 5021 Bergen, Norway.
5. Department of Pathology, Oslo University Hospital, Norwegian Radium Hospital, and Faculty of Medicine, Institute of Clinical Medicine, University of Oslo, Oslo, Norway.
6. Molecular imaging Center, Department of Biomedicine, University of Bergen, Jonas Lies vei 91, N-5009, Bergen, Norway.
7. Western Norway University College, Inndalsveien 28, N-5063, Bergen, Norway.
8. Department of Pathology, Haukeland University Hospital, Jonas Lies vei 65, N-5021, Bergen, Norway.
9. Centre for Pharmacy, Department of Clinical Science, University of Bergen, Jonas Lies vei 65, Bergen 5021, Norway.
10. Vivarium, Department of Clinical Medicine, University of Bergen, Jonas Lies vei 65, 5021 Bergen, Norway.

*These authors contributed equally to this work.

✉ Corresponding authors: Professor Emmet Mc Cormack, Tel: +47 55 97 3097; Fax: +47 55 97 29 50; E-mail: emmet.mc.cormack@uib.no.

Received: 2020.10.27; Accepted: 2021.02.25; Published: 2021.04.07

Abstract

Nitroreductases (NTR) are a family of bacterial enzymes used in gene directed enzyme prodrug therapy (GDEPT) that selectively activate prodrugs containing aromatic nitro groups to exert cytotoxic effects following gene transduction in tumours. The clinical development of NTR-based GDEPT has, in part, been hampered by the lack of translational imaging modalities to assess gene transduction and drug cytotoxicity, non-invasively. This study presents translational preclinical PET imaging to validate and report NTR activity using the clinically approved radiotracer, ^{18}F-FMISO, as substrate for the NTR enzyme.

Methods: The efficacy with which ^{18}F-FMISO could be used to report NfsB NTR activity *in vivo* was investigated using the MDA-MB-231 mammary carcinoma xenograft model. For validation, subcutaneous xenografts of cells constitutively expressing NTR were imaged using ^{18}F-FMISO PET/CT and fluorescence imaging with CytoCy5S, a validated fluorescent NTR substrate. Further, examination of the non-invasive functionality of ^{18}F-FMISO PET/CT in reporting NfsB NTR activity *in vivo* was assessed in metastatic orthotopic NfsB NTR expressing xenografts and metastasis confirmed by bioluminescence imaging. ^{18}F-FMISO biodistribution was acquired *ex vivo* by an automatic gamma counter measuring radiotracer retention to confirm *in vivo* results. To assess the functional imaging of NTR-based GDEPT with ^{18}F-FMISO, PET/CT was performed to assess both gene transduction and cytotoxicity effects of prodrug therapy (CB1954) in subcutaneous models.

Results: ^{18}F-FMISO retention was detected in NTR$^+$ subcutaneous xenografts, displaying significantly higher PET contrast than NTR$^-$ xenografts ($p < 0.0001$). Substantial ^{18}F-FMISO retention was evident in metastases of orthotopic xenografts ($p < 0.05$). Accordingly, higher ^{18}F-FMISO biodistribution was prevalent *ex vivo* in NTR$^+$ xenografts. ^{18}F-FMISO NfsB NTR PET/CT imaging proved useful for monitoring *in vivo* NTR transduction and the cytotoxic effect of prodrug therapy.

Conclusions: ^{18}F-FMISO NfsB NTR PET/CT imaging offered significant contrast between NTR$^+$ and NTR$^-$ tumours and effective resolution of metastatic progression. Furthermore, ^{18}F-FMISO NfsB NTR

PET/CT imaging proved efficient in monitoring the two steps of GDEPT, *in vivo* NfsB NTR transduction and response to CB1954 prodrug therapy. These results support the repurposing of ^{18}F-FMISO as a readily implementable PET imaging probe to be employed as companion diagnostic test for NTR-based GDEPT systems.

Key words: ^{18}F-FMISO, Gene-directed enzymatic prodrug therapy, GDEPT, nitroreductase, NTR, cancer, xenograft, preclinical, mouse, PET/CT, imaging

Introduction

Gene directed enzyme prodrug therapy (GDEPT) is a promising anti-cancer strategy that aims to reduce off-target toxicity and limit severe side-effects by the combination of a prodrug and its activating enzyme [1]. In a first step, tumours are transduced to express a gene encoding for the prodrug-activating enzyme. In a second step, a non-toxic prodrug is delivered systemically and subsequently converted *in situ* to a cytotoxic derivative by the expressed enzyme [2]. In this way, GDEPT achieves high concentration of cytotoxic compounds locally, minimising systemic side effects associated with conventional cancer chemotherapy [3].

The most extensively studied prodrug/enzyme pairs for GDEPT are ganciclovir (GCV)/herpes simplex virus-thymidine kinase (HSV-TK) [4] and 5-(aziridin-1-yl)-2,4-dinitrobenzamide (CB1954, Figure 1B)/*E. Coli* nitroreductase NfsB (onwards referred as NTR) [5]. HSV-TK phosphorylates GCV, allowing its incorporation into DNA, resulting in toxicity due to interference with the DNA synthesis [6]. NTR reduces the nitro groups ($R\text{-}NO_2$) present in CB1954, into hydroxylamines (R-NHOH), resulting in the formation of an alkylating agent with cytotoxic activity [7, 8]. Moreover, the diffusion of the activated compound into neighbouring non-targeted cells amplifies this cytotoxic effect (bystander effect) [9, 10]. Several trials have evaluated the clinical application of HSV-TK and NTR-based GDEPT strategies with contrasting results [5, 11, 12]. The largest clinical trial, including 124 patients receiving HSV-TK-based GDEPT, reported no difference in comparison to standard therapy. Modest HSV-TK expression was suggested as a potential limiting factor [11]. Indeed, a phase II HSV-TK-based GDEPT trial using a more efficient gene transduction strategy reported a significant increase in survival [12]. These studies illustrate the need for monitoring the gene transduction efficiency. One of the NTR-based GDEPT clinical trials assessed the transduction efficiency using immunohistochemistry in tumour biopsies [5]. However, immunohistochemistry is time consuming and may be affected by inadequate sampling of representative tumoral areas. For large clinical trials, non-invasive techniques such as imaging, which allows for easier clinical implementation, are required. In this respect, positron emission tomography (PET), which is routinely employed in clinical settings, enables detection of the activity for some of the enzymes used in the GDEPT strategies and may be suitable for interrogation of transduction efficiency in clinical trials [13, 14].

The activity of HSV-TK can be evaluated using radiolabeled probes, such as ^{18}F-FIAU (1-(2-deoxy-2-[^{18}F]-fluoro-1-D-arabinofuranoside)-5-iodour acil), ^{18}F-FHBG (9-[4-[^{18}F]fluoro-3-(hydroxymethyl) butyl]guanine) and GCV analogues [15, 16]. HSV-TK PET/CT imaging has indeed been successfully applied for monitoring transduction efficiency, tissue specificity and therapeutic effect preclinically [15, 17]. Subsequently, HSV-TK PET/CT imaging was incorporated into phase I clinical trials to monitor transduction efficiency in healthy individuals and in cancer patients [18, 19]. In an ongoing phase I clinical trial investigating the use of HSV-TK-based GDEPT in combination with immunotherapy (NCT04313868), HSV-TK PET/CT imaging with ^{18}F-FHBG has been implemented to explore the effect of viral administration routes in transduction efficacy.

NTR activity has been effectively imaged in a preclinical context using the near-infrared fluorescent probe CytoCy5S [20] and a caged bioluminescent substrate "NTR caged luciferin" (NCL) [21]. However, the non-invasive clinical application of optical imaging approaches is challenging due to limited tissue penetrance of light and associated autofluorescence. This could potentially be overcome by employing PET as the imaging modality, provided that an appropriate NTR specific tracer is available. For this purpose, we have focused on radiolabelled 2-nitroimidazoles (2-NI) that have been extensively utilised as hypoxia imaging agents (e.g. FMISO or FETNIM) [22, 23]. Hypoxia induces expression of oxygen-sensitive nitroreductases, able to convert 2-NI (e.g. FMISO, Figure 1A) into the corresponding hydroxylamines, which covalently bind to macromolecules in the tumour, allowing PET contrast [24]. The mechanistic similarity between oxygen-sensitive and *E.coli* nitroreductases, oxygen-insensitive, (Figure 1B) and their ability to convert aromatic nitro groups of various substrates (Figure

1A) into aromatic hydroxylamines, render 2-NI as plausible probes for clinical imaging of NTR activity [25].

Recently, Mowday and co-workers [26] have demonstrated effective NTR PET imaging employing *NfsA* from *E. Coli* in combination with the 2-NI PET tracer ^{18}F-HX4. Similarly, in this work we have investigated whether ^{18}F-FMISO, a PET tracer approved by FDA as an investigational new drug for human use, could be repurposed as a PET probe for non-invasive imaging of NTR for application in the context of GDEPT. ^{18}F-FMISO was validated as an NTR specific PET imaging tracer using mammary carcinoma xenograft models. Further, the applicability of ^{18}F-FMISO imaging was demonstrated in the two steps of GDEPT i.e. gene transduction and cytotoxicity effects of prodrug therapy. These results support ^{18}F-FMISO as a readily implementable NTR specific PET imaging probe to be employed as a companion diagnostic test for NTR-based GDEPT.

Materials and methods

In vitro experiments

Cell culture

Cells were maintained in a humidified atmosphere at 37 °C in 5% CO_2 in complete medium, consisting of DMEM (Sigma-Aldrich, MO, USA) or RPMI-1640 supplemented with 10% FBS, 1% penicillin/streptomycin (Sigma-Aldrich), and 1% L-glutamine (Sigma-Aldrich). 293T cells were purchased from DSMZ (Braunschweig, Germany). MDA-MB-231^{Luc+} and NCI-H460 $^{Luc+}$ cells, stably expressing luciferase, (onwards referred to as NTR$^-$)

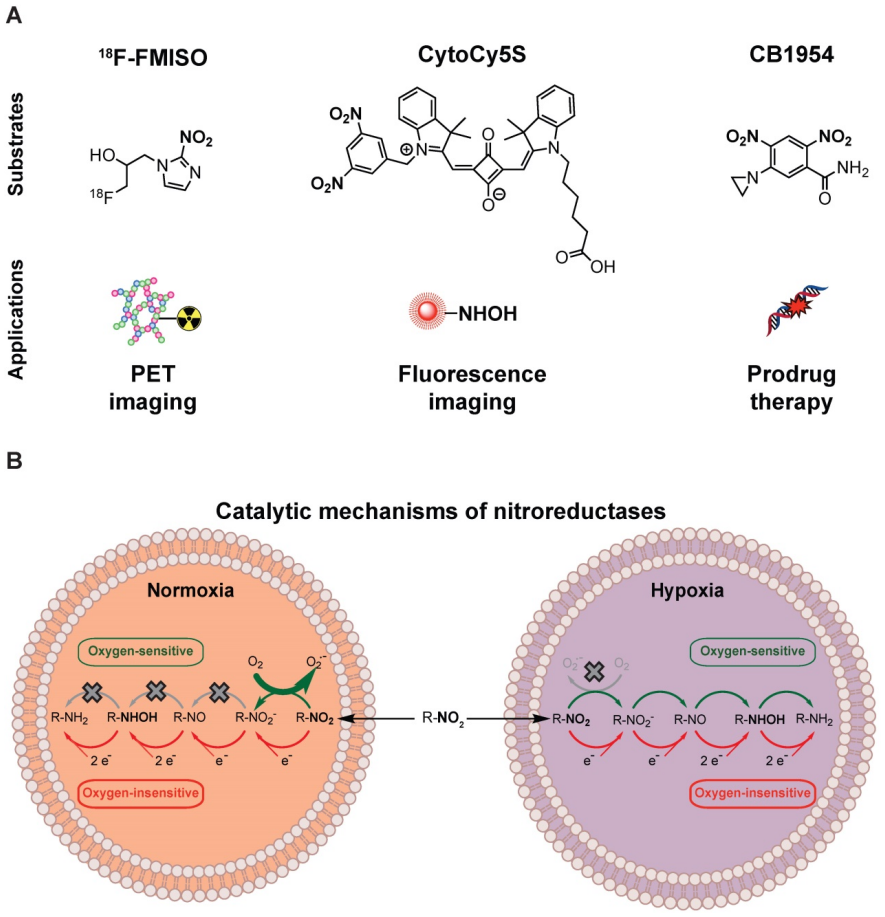

Figure 1. Nitroreductases and nitroaromatic substrates for multiple applications. (A) Nitroreductase subtrates employed in imaging or GDEPT. (B) Comparison of the catalytic mechanisms of oxygen-sensitive and oxygen-insensitive nitroreductases in normoxic and hypoxic conditions.

were kindly provided by Prof. James Lorens (University of Bergen). Generation of MDA-MB-231$^{Luc+GFP+NTR+}$ and NCI-H460$^{Luc+GFP+NTR+}$ cells, stably expressing luciferase, GFP and NfsB (onwards referred to as NTR$^+$) has been previously described by McCormack et al. [20]. Characterisation of the cell lines by flow cytometry can be found in Figures S1 and S3. To avoid possible expression drift due to cell culturing, NTR$^+$ cells were sorted prior to the experiments employing the flow cytometric methods described previously.

NTR lentivirus production

A custom-made lentiviral expression vector, pCDH-EF1α-NTR, containing the coding sequence of *E. coli NfsB* gene under the control of the EF1α promoter was produced by System Bioscience (CA, USA). Packaging into VSV-G pseudotyped viral particles was performed by co-transfection of pCDH-EF1α-NTR, pMD2.G and psPAX2 (Figure S1) into 293T cells. Viral titers were reported as transforming units (TU) per mL. TU were measured by transduction of 293T cells with serial dilutions of conditioned medium from virus packaging cells and analysis of NTR expression using a flow cytometric method described previously by McCormack et al. [20]. For validation purposes, it was confirmed that NTR expression levels in MDA-MB-231 cells transduced with pCDH-EF1α-NTR and in the NTR$^+$ cell line were within the same range (Figure S1).

Flow cytometry

For the analysis of NTR expression 0.1 x 10^6 cells were incubated at 37 °C with DMEM supplemented with 1 µM of CytoCy5S for 1 hour. All samples were washed twice with PBS + 2% BSA before acquisition with the BD Accuri C6 flow cytometer (BD Biosciences, NJ, USA) with a laser excitation at 640 nm and emission filter at 675 ± 12.5 nm.

In vivo experiments

General animal care

All experiments were approved by The Norwegian Animal Research Authority (FOTS approval ID 9059) and conducted according to The European Convention for the Protection of Vertebrates Used for Scientific Purposes. NOD-*scid* IL2Rg^{null} mice (referred to as NSG) were bred at Vivarium (University of Bergen). Mice were housed in groups of ≤ 5 in individually ventilated cages (Techniplast, Italy). General condition and body weight were recorded twice per week.

MDA-MB-231 and NCI-H460 subcutaneous xenografts

Tumours were engrafted subcutaneously mono- or bi-laterally in the scapular area. 5 × 10^6 cells were prepared in 50 µL DMEM with 25% BD Matrigel™ (BD Science, CA, USA) and injected at each site to form a single tumour. Tumour volumes were measured weekly with a digital calliper and calculated using the ellipsoid volume formula: Volume = π (length × width × height)/6.

MDA-MB-231 orthotopic xenografts

1 × 10^6 cells were prepared in 50 µL of DMEM with 25% BD Matrigel™ (BD Science) and engrafted in the right inguinal mammary fat pad, as previously described [20, 27]. Prior to cell implantation, mice were injected with 0.1 mg/kg buprenorphine (Temgesic, Indivior, UK) for analgesia.

CB1954 treatment

CB1954 (Sigma-Aldrich) was resuspended in DMSO at 26.6 mg/mL. CB1954 treatment was initiated when mean tumour volumes reached 172 ± 65 mm^3 in NTR$^+$ and NTR$^-$ xenografts or four weeks after *in vivo* transduction in NTR transduced xenografts. Animals received two intraperitoneal (i.p.) treatments in a six-day interval with a dose of 40 mg/kg diluted in saline.

In vivo NTR transduction with lentiviral particles

NTR lentiviral particles were concentrated using Lenti-Pac Lentivirus Concentration solution (Genecopoeia, MD, USA). Subcutaneous xenografts were transduced *in vivo* by intratumoral injection of 8 × 10^7 TU resuspended in 75 µL of the complete medium supplemented with 5 µg/mL Polybrene (Sigma-Aldrich) when mean tumour volume was 70 ± 25 mm^3. A single injection of viral particles per tumour was performed administering the viral suspension throughout the diameter of the tumour.

^{18}F-FMISO biodistribution

Tumours and organs were harvested from four mice, two hours post i.v. administration of ^{18}F-FMISO (150 µL, 8-12 MBq, 228-342 MBq/kg) and radiation was measured on a Wizard2® Automatic Gamma Counter (Perkin Elmer, MA, USA). The results are expressed as a percentage of the injected dose per gram of tissue (% ID/g).

Histopathology examinations

Following euthanasia, the tumour and the organs were fixed in neutral buffered formalin solution 10% (Sigma-Aldrich) at room temperature for 24 hours and later kept in PBS and stored in darkness at 4 °C. 5 µm thick sections were stained with

haematoxylin and eosin (HE) and were examined by a pathologist for verification of malignancy.

Immunohistochemical (IHC) staining was done on tumour tissue sectioned at 5 µm thickness. Deparaffinisation and antigen retrieval was performed with EnVision FLEX Target Retrieval Solution, Low pH (DAKO, Copenhagen, Denmark) on a Dako PT Link instrument (Dako). After antigen retrieval, tissues were incubated for 8 min with peroxidase blocker (Peroxidase Blocking Reagent, cat #S2001, Agilent Technologies) and thereafter for 10 min with protein blocker (Protein Block Serum-free, cat # X090930-2, DAKO) at room temperature. The blocking solution was then removed and the slide was wiped dry around the tissue section before application of the primary antibody. The sections were then incubated overnight at 4 °C degrees with the HIF1α primary antibody (ab51608, Abcam, Cambridge, UK) dilution 1:300. The staining was performed on a DAKO Autostainer using the EnVision+ System-HRP Labelled Polymer Anti-Rabbit K4002 as secondary antibody for 30 min (Agilent Technologies, Norway). 3,3`-Diaminobenzine (DAB+) Substrate-Chromogen was used as chromogen for 10 min. Sections were counterstained with haematoxylin (cat # S3301, Agilent Technologies) for 10 min, dehydrated, and mounted with a coverslip (Agilent Technologies) using Pertexx mounting medium (Histolab Products AB, Askim, Sweden). Human placenta with known reactivity to the selected marker was used as positive control.

Whole tissues were scanned employing an Olympus VS120 S6 Slide scanner (Olympus Corporation, Tokio, Japan). Quantification of the normalised HIF1α positive area was performed employing FIJI [28], following the protocol described by Crowe et al. [29].

PCR for monitoring *in vivo* NTR transduction

Following euthanasia, part of the tumour was snap-frozen on dry ice and stored at -80 °C. DNA was purified using QIAamp DNA Mini Kit (QIAGEN, Germany). A 348 bp fragment of the coding sequence of *E. coli NfsB* gene was PCR amplified in a thermocycler under standard conditions using *Taq* DNA Polymerase (Invitrogen, CA, USA) and the following primers: NTR-F 5′ GCGTCATTCCACTAA GGCAT 3′ and NTR-R 5′ GCGAAGAACTTGCGACC TTT 3′. DNA amplification was visualised by gel electrophoresis followed by imaging on a Gel Doc EZ system (Bio-Rad, CA, USA). Nancy-520 (Sigma-Aldrich) was used as an intercalating agent and 1 kb DNA Ladder (Sigma-Aldrich) to estimate DNA size.

Imaging techniques

During bioluminescence and fluorescence imaging mice were anaesthetised with 1.5% isoflurane (Abbot Labor Ltd, IL, USA), 3-4% sevoflurane (Abbot Labor Ltd) during PET/CT imaging.

Bioluminescence imaging

D-Luciferin (Biosynth, Switzerland) was administered i.p. at a dose of 150 mg/kg 10 minutes before imaging. Images were acquired using an In-Vivo FX Pro molecular imaging system (Carestream Health Inc., NY, USA). Analysis was performed with the Carestream molecular imaging software v5.0.6.20.

CytoCy5S-Fluorescence imaging

CytoCy5S was synthesised following a published method [20]. 100 µL of a 1 mM CytoCy5S solution were injected intravenously. Imaging was performed after a 1-hour washout using an IVIS Spectrum imaging system (PerkinElmer, MA, USA.). Analysis was performed with the Living Imaging® software v4.5 (PerkinElmer).

^{18}F-FMISO PET/CT imaging

^{18}F-FMISO synthesis

^{18}F-fluoride was produced by the ^{18}O(p,n)^{18}F-reaction in a niobium target on a GE PETtrace6 cyclotron (GE Healthcare,) with EOB-activities in the range of 80 - 100 GBq. The activity was delivered to the synthesis hot-cell by a Safe Transfer System (Skistad Elektroautomasjon AS, Norway). ^{18}F-FMISO was produced on a FASTlab2 (GE Healthcare, IL, USA) with the synthesis sequence provided by the supplier. The radiosynthesis has been described in detail previously [30, 31]. Reagents and synthesis cassette were purchased from GE Healthcare Norway AS (Norway). Purification of ^{18}F-FMISO was performed through a series of SPE-cartridges, and thus did not require any semi-preparative HPLC. The final ^{18}F-FMISO formulation contained approx. 7% ethanol. Total synthesis time was approximately 50 minutes and yields in the order of 20-30% (not decay corrected).

PET/CT imaging

PET/CT scans were acquired using the integrated nanoScan PC PET/CT (Mediso Ltd, Hungary) featuring spatial resolution of 800 µm and 300 µm of the PET and CT detector systems, respectively. The field of view (FOV) was 9.6 × 10 cm in axial direction and transaxial direction allowing whole-body imaging of the mice. The PET detectors consist of LYSO crystals, and acquisition was performed in a 1:5 coincidence and normal count

mode. Mice were scanned using a dual mouse bed with integrated heating (37 °C). Each PET scan was conducted over 30 minutes, 1.5 hours post i.v. administration of ^{18}F-FMISO (8-12 MBq, 228-342 MBq/kg). Prior to PET acquisition, a whole-body CT scan (helical projections with tube energy of 50kVp, exposure time 300 ms, 720 projections, max FOV, binning 1:4) was performed providing anatomical information, as well as attenuation correction PET image reconstruction.

PET/CT reconstruction and processing

PET images were reconstructed using the Nucline software by employing the Tera-Tomo 3D (OSEM) algorithm (four iterations and six subsets, 1-5 coincidence mode) and the following corrections: depth-of-interaction (DOI), randoms, crystal dead time, normalisation. Prior to PET, a whole-body CT (low energy) was acquired for anatomic reference and attenuation correction. CT images were reconstructed using a RamLak filter. The PET and CT images were co-registered automatically. Images were reconstructed with a voxel size of 0.25×0.25×0.25 mm^3 for CT, and 0.4×0.4×0.4 mm^3 for PET. Data analyses were performed using InterView Fusion version 3.03.078.0000 (Mediso Ldt.). Standard uptake value (SUV) was calculated using the equation: SUV = $C_{PET}(T)/(ID/BW)$, where $C_{PET}(T)$ was the measured activity in tissue, ID the injected dose measured in kBq, and BW the mouse's body weight in kg. For each scan a spherical volume of interest (VOI) with radius 2 mm was drawn manually over the muscle in the neck and SUV_{mean} was calculated to serve as reference. This value enabled segmentation of putative tumour tissue having SUV ratios of twice higher than reference for ^{18}F-FMISO. VOIs of primary tumours and of likely metastases were drawn semi-automatically in the PET images for estimation and calculation of SUV_{max} and SUV_{peak} values. SUV_{max} is the maximum SUV value of all voxels included in the VOI. For SUV_{peak} analysis a specific volume was set (5 mm^3 for SUV_{p5} and 10 mm^3 for SUV_{p10}) and all the possible spheres with that volume fitting inside the VOI were identified. The average SUV of all voxels within the spheres was calculated for all possible spheres and the highest average SUV values from this analysis were reported as SUV_{p5} and SUV_{p10}. The SUV_{peak} analyses were performed using PMOD software (Version 3.8).

Statistics

Results are given as mean ± standard deviation (SD). All statistical tests were performed using GraphPad Prism v 6.0h (GraphPad Software Inc, CA, USA) and $p < 0.05$ was considered significant. After randomisation, a one-way ANOVA was applied to ensure unbiased assignment of tumour volumes among the experimental groups. Comparison of means was performed using Student's t-tests. Test for equality of variances was performed using an F test. When variances were not equal Welch's correction was applied to Student's t-tests. Correlations were analysed by computing Pearson's correlation coefficients.

Results

^{18}F-FMISO permits imaging of NTR expression in subcutaneous xenograft models

Although fluorescent [20] and chemiluminescent [21] substrates have been successfully applied to report NTR expression in preclinical models of cancers, their clinical potential is limited. We hypothesised that ^{18}F-FMISO, a clinically approved PET tracer known to be sequestered and reduced in hypoxic cancer environments, may provide a PET-based imaging modality for the visualisation of NTR activity *in vivo*. To examine the potential of ^{18}F-FMISO as a PET tracer of NTR expression *in vivo*, ^{18}F-FMISO NTR PET/CT imaging and CytoCy5S-FLI were compared in a subcutaneous xenograft model.

Briefly, mice were xenografted bi-laterally in the scapular region with either NTR$^+$ or NTR$^-$ cells (n = 3 mice per group) in addition to one mouse implanted with both NTR$^+$ and NTR$^-$ on adjacent scapulae. Mice were imaged at three timepoints post-engraftment (weeks four, five and seven) and imaging results compared (Figure 2A). CytoCy5S-FLI confirmed significantly higher contrast between NTR$^+$ and NTR$^-$ xenografts from week five ($p < 0.05$, Figure 2A), when mean tumour volumes reached 243.6 ± 94.6 mm^3. ^{18}F-FMISO NTR PET/CT resulted in significantly higher contrast between NTR$^+$ and NTR$^-$ xenografts earlier, at week four, when mean tumour volumes were 154.0 ± 75.8 mm^3. At week four, NTR$^+$ and NTR$^-$ xenograft SUV_{max} values were 3.64 ± 0.36 g/mL and 1.24 ± 0.42 g/mL respectively ($p < 0.0001$). Contrast remained significantly higher at weeks five and seven (Figure 2A and 2B). To confirm these results, ^{18}F-FMISO tracer biodistribution was analysed *ex vivo*. The highest tracer retention was detected in the bladder, consistent with high renal clearance, and in the large intestine (Figure 2C), which is expected as a consequence of the expression of nitroreductases by the local microbiota. ^{18}F-FMISO retention was higher in NTR$^+$ compared to NTR$^-$ xenografts and remaining organs. Thus, our results suggest that ^{18}F-FMISO can act as an NTR PET tracer.

To confirm that the higher retention of ^{18}F-FMISO observed in NTR$^+$ is specific for NTR expression, we wanted to compare the hypoxic status

of the NTR$^-$ and NTR$^+$ xenografts. The hypoxic status of the subcutaneous MDA-MB-231 NTR$^-$ and NTR$^+$ xenografts was assessed employing IHC to detect HIF1α accumulation (Figure S2A). Quantification of the normalised area positive for HIF1α shows no statistical significance between MDA-MB-231 NTR$^-$ and NTR$^+$ xenografts (Figure S2B). This result suggests that ^{18}F-FMISO retention in NTR$^+$ xenografts is not related to increased levels of hypoxia, confirming ^{18}F-FMISO as an NTR PET tracer.

Next, we wanted to analyse the performance of ^{18}F-FMISO as an NTR PET tracer in the presence of other nitroreductases, both oxygen-insensitive and oxygen-sensitive. For this purpose we selected the non-small cell lung carcinoma NCI-H460 cell line, with high endogenous levels of the nitroreductase DT-diaphorase [32] and increased levels of hypoxia in comparison to MDA-MB-231 (hypoxic fractions of 13.6% and 4.7% respectively [33, 34]). First we confirmed *in vitro* that NTR$^+$/NTR$^-$ ratio was notably lower for NCI-H460 than for MDA-MB-231 cell line, being respectively 5.4 and 50 (Figure S3A). Then, mice were xenografted bi-laterally in the scapular region with either NTR$^+$ or NTR$^-$ NCI-H460 cells (n = 4 tumours per group). Mice were imaged two weeks after engraftment and imaging results compared (Figure S3B). ^{18}F-FMISO NTR PET/CT resulted in significantly higher contrast between NCI-H460 NTR$^+$ and NTR$^-$ xenografts with SUV_{max} values of 2.07 ± 0.36 g/mL and 1.51 ± 0.30 g/mL respectively ($p < 0.05$; Figure S3C). Interestingly, no significant differences were observed between SUV_{max} values from MDA-MB-231 NTR$^-$ xenografts (1.24 ± 0.42 g/mL) and from NCI-H460 NTR$^-$ xenografts. These results suggest that ^{18}F-FMISO can act as an NTR PET tracer, even in models with notable presence of oxygen-insensitive and oxygen-sensitive nitroreductases.

^{18}F-FMISO imaging of NTR$^+$ metastatic lesions in orthotopic xenograft models

Having demonstrated the ability of ^{18}F-FMISO to act as an NTR PET tracer in subcutaneous tumours, we next examined the suitability of the tracer for the detection of small metastatic lesions. We have previously visualised the axillary lymph node metastatic capacity of MDA-MB-231 cells when implanted orthotopically in immunodeficient mice *via* BLI [27]. Thus, 1 × 10^6 NTR$^+$ cells were xenografted orthotopically in the mammary fat pad (n = 3) and imaged weekly with BLI and, from the initiation of metastasis, also with ^{18}F-FMISO NTR PET/CT for five weeks (Figure 3A). Axillary lymph node metastases were clearly visible from week 8, with progressive increase in BLI up to week 12 (Figure 3A). Comparative ^{18}F-FMISO NTR PET/CT imaging of the same mice demonstrated contrast at the axillary lymph node metastatic site with SUV_{max} values of 2.37 ± 0.88 g/mL from week 9 (Figure 3B). Metastatic contrast increased in weeks 10, 11 and 12 with SUV_{max} values of

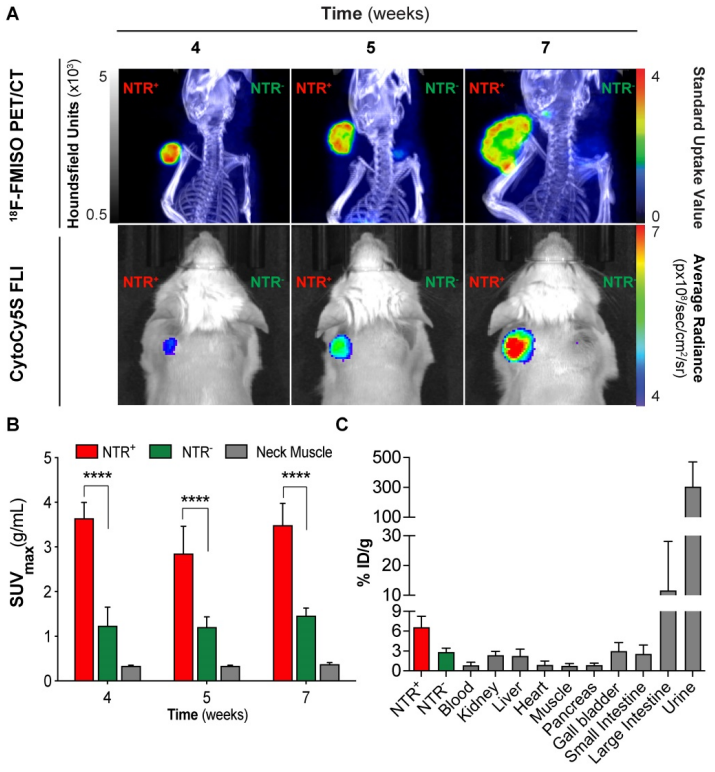

Figure 2. ^{18}F-FMISO permits imaging of NTR expression in subcutaneous xenograft models. (A) Representative ^{18}F-FMISO PET/CT MIP images and CytoCy5S-FLI 2D surface weighted images over four weeks. NTR$^-$ tumour (right flank) and NTR$^+$ tumour (left flank). (B) SUV_{max} values, were significantly higher in NTR$^+$ xenografts for all the time points (****, $p < 0.0001$, n=7). (C) *Ex vivo* biodistribution (n = 3) of ^{18}F-FMISO obtained at week seven. Biodistribution observed mainly in large intestines and bladder. Biodistribution was higher in NTR$^+$ tumours than in NTR$^-$ tumours and remaining organs. The p-values are represented as indicated: * $p < 0.05$, ** $p < 0.01$, *** $p < 0.001$ and **** $p < 0.0001$.

2.88 ± 1.41, 3.36 ± 1.37 and 4.25 ± 2.04 g/mL, which were significant from background (SUV_{max} of reference tissue range: 0.4-0.56 g/mL; $p < 0.05$). Further analysis of ^{18}F-FMISO NTR PET/CT images of NTR$^+$ xenografts revealed additional contrast in the thoracic and lumbar regions of metastatic mice suggestive of hepatic and pulmonary metastasis (Figure 3C, upper). Subsequently, mice were euthanised, and suspected metastatic organs excised. Histological examination of HE stained sections of the lungs, liver and axillary lymph node demonstrated the presence of metastases in organs where accumulation of ^{18}F-FMISO had been observed by ^{18}F-FMISO NTR PET/CT imaging (Figure 3C, lower).

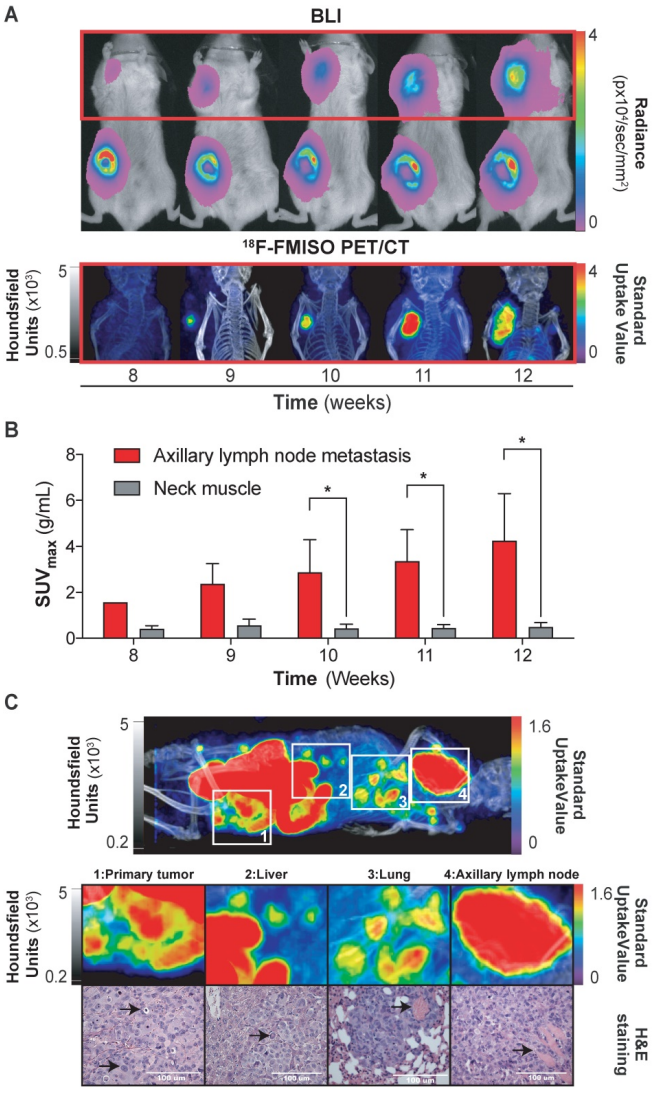

Figure 3. ^{18}F-FMISO imaging of NTR$^+$ metastatic lesions in orthotopic xenograft models. (A) Representative images from week eight to 12. Presence of primary tumour (inguinal area) and axillary metastases (red square) by BLI. ^{18}F-FMISO NTR PET/CT imaging in the axillary area. (B) Evolution of lymph node metastasis SUV_{max} compared to the reference tissue. Significant difference is observed at weeks ≥ 10 (*, $p < 0.05$), n = 3. (C) Whole body MIP images of ^{18}F-FMISO NTR PET/CT show contrast in the primary tumour, liver, lung and axillary lymph node. HE staining shows widespread metastatic neoplasia in all the analysed organs. The histological features associated with neoplasia (marked with black arrows) include atypical mitosis, pyknosis, hyperchromatism, desmoplasia, irregular shape and size. Excessive extranodal tumour extension invading the adjacent muscle tissue can be seen in the axillary lymph (marked with black arrow). The lungs show signs of scattered micrometastases and venous infiltration (marked with black arrow). The p-values are represented as indicated: * $p < 0.05$, ** $p < 0.01$, *** $p < 0.001$ and **** $p < 0.0001$.

^{18}F-FMISO allows assessment of NTR expression after *in vivo* transduction

While the aforementioned ^{18}F-FMISO imaging results demonstrate the useful application of ^{18}F-FMISO NTR PET/CT imaging for detection of constitutive NTR expression, the imaging demands of GDEPT are far greater. Initially, imaging of GDEPT should permit visual confirmation of *in vivo* viral transduction, which will occur in a discrete fraction of the tumoral cells [11, 12]. To examine the potential of ^{18}F-FMISO NTR PET/CT imaging to assess *in vivo* transduction of tumour cells by NTR, an NTR lentiviral construct was designed (Figure S1). Viral particles were collected, concentrated and 8 x 10^7 TU injected intratumorally into NTR$^-$ subcutaneous xenografts (Figure 4A).

NTR transduced xenografts (n = 10), in addition to NTR$^+$ and NTR$^-$ controls (n = 4 per group) were ^{18}F-FMISO NTR PET/CT imaged, two and four weeks post-transduction (Figure 4A). Clear contrast of NTR$^+$ controls could be demonstrated over NTR$^-$ controls both at week 2 and 4 (SUV_{max} of 3.97 ± 0.40 and 3.82 ± 0.57 g/mL respectively; p <0.001 Figure 4B & C). At week 2, minimal contrast was visualised in NTR transduced xenografts, albeit non-significant compared to NTR$^-$ controls (SUV_{max} of 1.94 ± 0.38 and 1.74 ± 0.32 g/mL respectively; Figure 4C). Imaging at week 4 demonstrated significant contrast compared with NTR$^-$ controls

(SUV_{max} of 4.12 ± 3.18 and 2.03 ± 0.20 g/mL respectively; $p < 0.05$). Similar results were obtained when SUV_{peak} was analysed (Figure S4). Interestingly, contrast in lentiviral transduced tumours was observed at discrete foci (Figure 4B).

At week 4, NTR transduced xenografts were randomised to receive CB1954 (two 40 mg/kg i.p. injections in a six-day interval) or vehicle (Figure 4A). Post-treatment ^{18}F-FMISO NTR PET/CT imaging, at week 6, showed a further increase in contrast in xenografts treated with vehicle, although non-significant (pre-treatment SUV_{max} of 3.5 ± 2.5 and post-treatment SUV_{max} of 4.4 ± 3.0 g/mL Figure 4D & E). On the other hand, a significant decrease in contrast was observed in xenografts treated with CB1954 (pre-treatment SUV_{max} of 5.57 ± 3.73 and post-treatment SUV_{max} of 2.02 ± 0.32 g/mL; $p < 0.05$; Figure 4D & E).

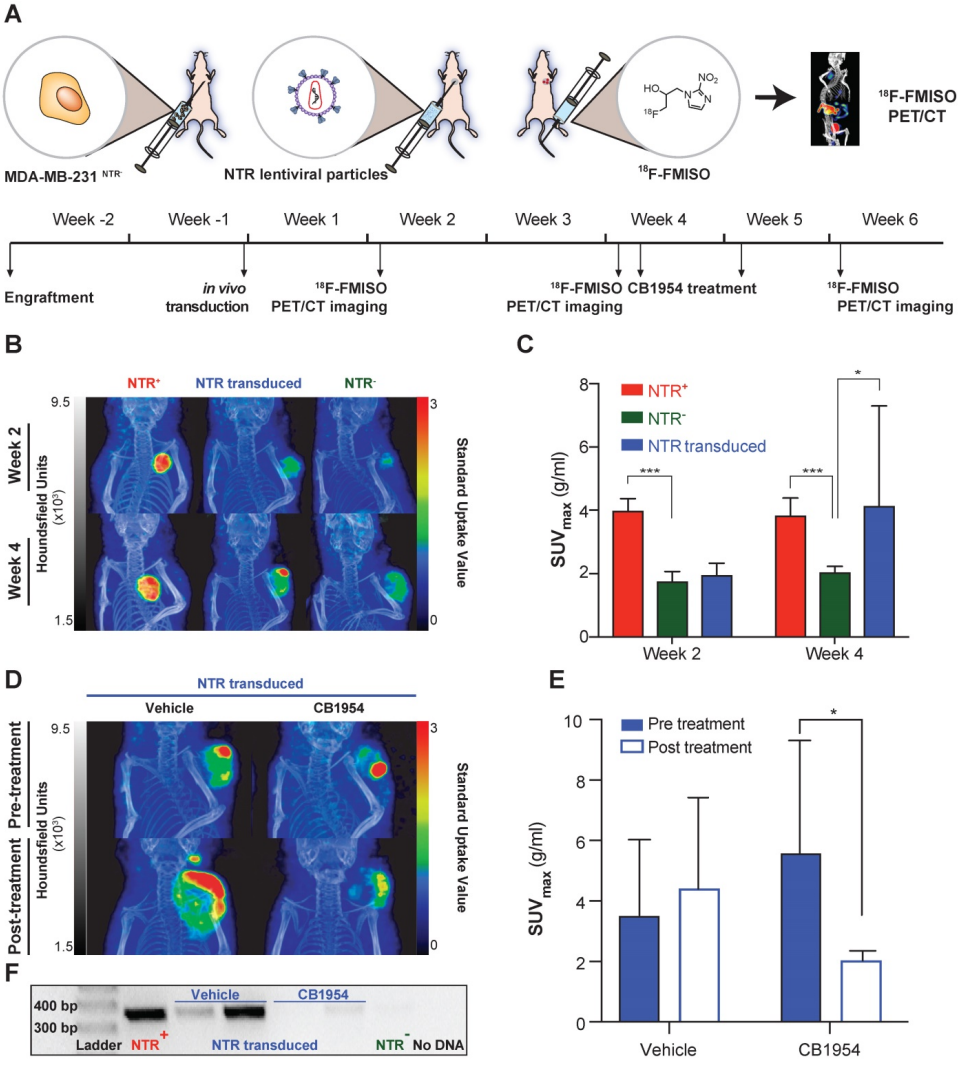

Figure 4. ^{18}F-FMISO allows assessment of NTR expression after *in vivo* transduction. (A) Experimental set-up for *in vivo* NTR lentiviral transduction, CB1954 treatment and ^{18}F-FMISO PET/CT imaging. (B) Representative ^{18}F-FMISO PET/CT MIP images suggesting the expression of NTR in the *in vivo* transduced tumours both at week two and four after transduction. (C) Four weeks after transduction, the SUV_{max} in the *in vivo* transduced tumours was significantly higher (*, $p < 0.05$ and ***, $p < 0.001$), n = 10). (D) Representative ^{18}F-FMISO PET/CT MIP images suggesting a decrease in ^{18}F-FMISO PET contrast in NTR transduced xenografts treated with CB1954 (E) SUV_{max} of the *in vivo* transduced tumours treated with vehicle showed a non-significant increase. SUV_{max} of the *in vivo* transduced tumours treated with CB1954 decreased significantly (*, $p < 0.05$ n = 6) (F) Confirmation of NTR transduction by PCR amplification of NTR coding sequences only in NTR+ xenografts and NTR transduced xenografts treated with vehicle. The p-values are represented as indicated: * $p < 0.05$, ** $p < 0.01$, *** $p < 0.001$ and **** $p < 0.0001$.

To confirm these imaging results, tumours were isolated post necropsy, DNA isolated and NTR transduction was corroborated by PCR amplification of an NTR coding sequence in the NTR transduced xenografts treated with vehicle and NTR$^+$ controls (Figure 4F). These results confirm the utility of ^{18}F-FMISO NTR PET/CT imaging for detecting NTR expression after *in vivo* viral transduction.

To exclude any possible confounding effect on ^{18}F-FMISO NTR PET/CT imaging arising from hypoxia induced by intratumoral injection, at the end of the experiment the accumulation of HIF1α was measured in NTR$^-$ transduced xenografts and compared with NTR$^-$ tumours not receiving an intratumoral injection. The spatial pattern of HIF1α accumulation was similar in both tumour groups (Figure S5A) and the mean normalised HIF1α positive area was indeed significantly lower in intratumorally injected tumours (Figure S5B). All the above-mentioned data confirms ^{18}F-FMISO NTR PET/CT imaging as a technique able to detect *in vivo* NTR viral transduction.

^{18}F-FMISO NTR PET/CT imaging reports CB1954 treatment efficacy in NTR expressing xenografts

Having demonstrated the potential of ^{18}F-FMISO NTR PET/CT imaging to successfully visualise *in vivo* NTR transduction, the capacity of ^{18}F-FMISO NTR PET/CT imaging to report on CB1954 prodrug treatment efficacy was examined. NTR$^-$ and NTR$^+$ subcutaneous xenografts (n = 7 per group) were treated with CB1954 (two 40 mg/kg i.p. injections in a six-day interval) (Figure 5). ^{18}F-FMISO NTR PET/CT imaging was performed pre-treatment (day -4), during treatment (day 3) and following completion of treatment (day 17), in addition to calliper measurements of tumour volumes (Figure 5A). As expected, pre-treatment ^{18}F-FMISO NTR PET/CT imaging of NTR$^+$ xenografts resulted in significant contrast in comparison to NTR$^-$ xenografts (SUV_{max} of 4.07 ± 0.23 and 1.22 ± 0.35 g/mL respectively; $p < 0.001$ (Figure 5B and C). At day 3, a significant decrease in NTR$^+$ tumour volumes was observed versus corresponding NTR$^-$ xenografts (normalised tumour volumes 2.53 ± 0.27 and 1.43 ± 0.41 mm^3; $p < 0.0001$). Similarly, significant decrease in NTR$^+$ tumour SUV_{max} values was also noted in ^{18}F-FMISO PET contrast performed at day 3 in comparison to pre-treatment SUV_{max} values (SUV_{max} 4.07 ± 0.23 and 3.19 ± 0.41 g/mL; $p < 0.001$). Progressive reductions in NTR$^+$ xenograft tumour volume continued following the completion of CB1954 treatment at days 7, 10 and 14 ($p < 0.001$), with normalised volumes of 0.1 ± 0.02 at termination of the experiment (Figure 5A). Final PET imaging of xenografts on day 17 (Figure 5B) confirmed calliper measurement results, with observed SUV_{max} values reduced to 0.72 ± 0.12 g/mL ($p < 0.0001$) (Figure 5C). These preclinical results validate translational development of ^{18}F-FMISO PET/CT for prodrug treatment efficacy monitoring in the context of NTR-based GDEPT.

Discussion

GDEPT has been suggested as an attractive novel therapeutic strategy aiming to address both drug resistance and off-target cytotoxicity [35], with promising preclinical results [36-39] and a number of HSV-TK-based GDEPT phase II/III clinical trials opened in the last five years (NCT02831933; NCT02768363; NCT03004183; NCT03541928; NCT03603405; NCT03596086; NCT02446093). Recent phase I studies (NCT03281382; NCT04313868) are evaluating the use of HSV-TK-based PET imaging as a companion diagnostic tool, facilitating the analysis of HSV-TK transduction efficacy and prodrug therapy response.

In the current study, we have investigated the repurposing of ^{18}F-FMISO, an FDA approved PET tracer as investigational new drug for human use, as a companion diagnostic tool for NTR-based GDEPT. Employing a mammary carcinoma xenograft model constitutively expressing NTR, we demonstrated that ^{18}F-FMISO PET/CT imaging is sensitive for detection of NTR, even in small metastases. ^{18}F-FMISO NTR PET/CT imaging was found to be effective for detection of *in vivo* NTR transduction and for monitoring response to CB1954 treatment, demonstrating the feasibility of ^{18}F-FMISO NTR PET/CT imaging in the context of GDEPT.

Whilst this work has utilised breast and lung cancer models, ^{18}F-FMISO NTR PET/CT imaging is expected to be applicable to any solid tumour type. As suggested by our results, the interaction between ^{18}F-FMISO NTR and ^{18}F-FMISO hypoxia PET/CT imaging does not appear to compromise this NTR imaging strategy. Indeed, preclinical ^{18}F-FMISO hypoxia PET/CT imaging in many different tumour types reported SUV_{max} values in the range of 0.19-0.70 mg/mL [40-45], notably lower than the SUV_{max} values values for ^{18}F-FMISO NTR PET/CT imaging reported in this study (1.5-9.95 mg/mL).

The general applicability of ^{18}F-FMISO NTR PET/CT imaging might be limited by the distribution of the tracer to the bladder and large intestine [46], which might interfere with the imaging of tumours in the abdominal cavity. One strategy to reduce PET signal in the abdominal cavity is to increase the bowel motility using laxatives prior to imaging, this has been explored in preclinical models [47]. Another possible

solution would be to employ *NfsA*, which is an NTR orthologue with higher affinity towards ^{18}F-FMISO [26]. *NfsA* may permit the use of lower ^{18}F-FMISO doses, resulting in a decrease in the retention in the abdominal cavity.

We acknowledge the limitations and sub-optimal PK properties of ^{18}F-FMISO. However, the extensive clinical use of this tracer for PET

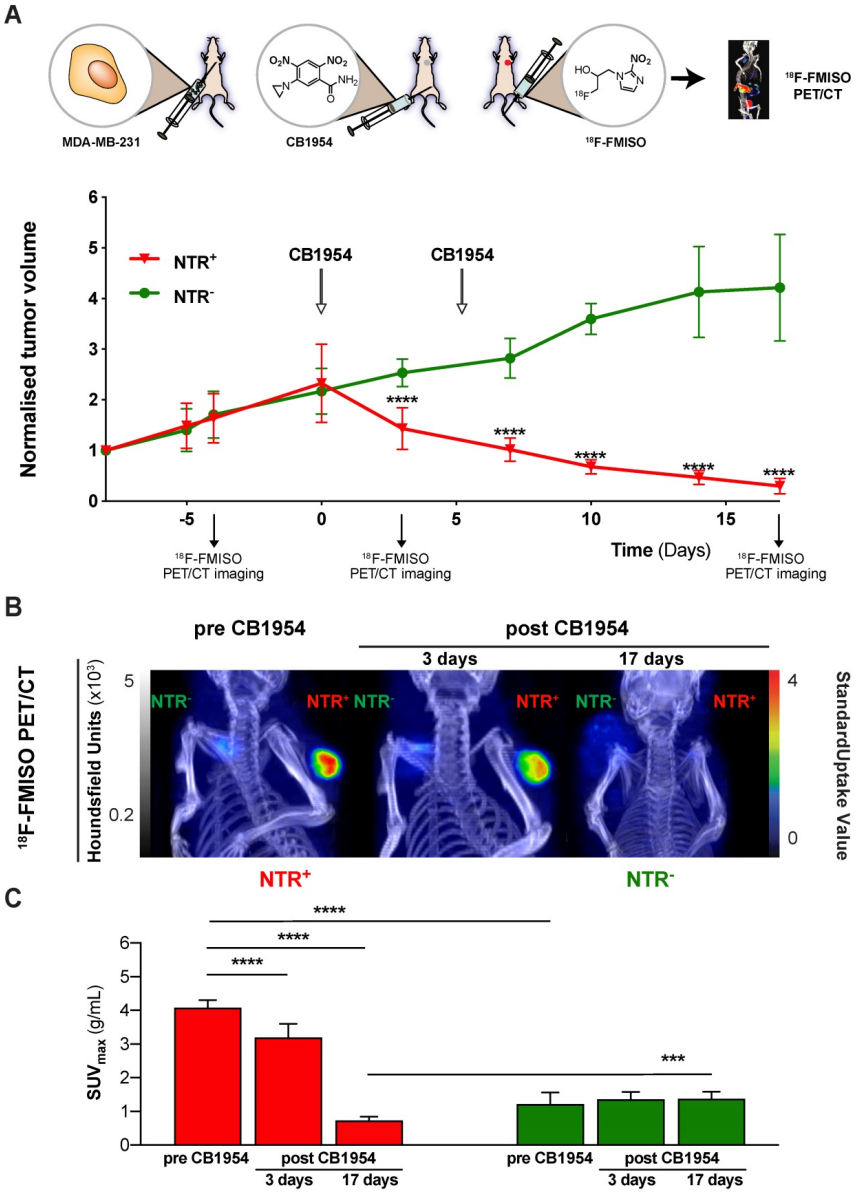

Figure 5. ^{18}F-FMISO NTR PET/CT imaging reports CB1954 treatment efficacy in NTR expressing xenografts. (A) CB1954 treatment response and experimental set-up for treatment monitoring employing ^{18}F-FMISO PET/CT imaging (B) Representative ^{18}F-FMISO PET/CT MIP images from NTR$^-$ tumour (left flank) and NTR$^+$ tumour (right flank) before treatment and three and 17 days after CB1954 dosing. (C) Before treatment, the SUV_{max} values were significantly higher in NTR$^+$ than in NTR$^-$ tumours (****, $p < 0.0001$, n = 7). Three and 17 days after, the SUV_{max} became significantly lower in NTR$^+$ xenografts in comparison to before treatment (****, $p < 0.0001$, n = 7). After 17 days, SUV_{max} of NTR$^+$ xenografts became significantly lower than the corresponding SUV_{max} of NTR$^-$ xenografts (***, $p < 0.0001$, n = 7). The p-values are represented as indicated: * $p < 0.05$, ** $p < 0.01$, *** $p < 0.001$ and **** $p < 0.0001$.

imaging of hypoxia makes the process of approval for a repurposed application easier. In parallel, novel tracers with optimised pharmacokinetic properties, in order to achieve high tumour accumulation and rapid healthy tissue clearance, are under development. A second generation 2-NI, ^{18}F-DiFA, has displayed slightly improved hypoxia sensitivity in clinical studies, accompanied by minimal distribution into the gastrointestinal tract [46, 48] and is an interesting candidate for further studies in the context of NTR imaging.

In comparison to HSV-TK-based GDEPT, NTR-based GDEPT possesses higher therapeutic potential, as NTR-based GDEPT targets cells independently of the cell cycle phase or proliferation status [49] and it results in a notable bystander effect caused by the diffusion of activated derivatives through the cell membrane [9, 10]. Despite the superior therapeutic potential of NTR-based GDEPT, clinical development is still in the early phases, as several of the steps for the NTR-based GDEPT strategy still need optimisation.

Efforts for optimisation of NTR-based GDEPT have in recent years focused on the key aspects of the technology, namely the delivery system, the NTR-enzyme and the prodrug. In an NTR GDEPT clinical trial, immune responses to the viral particles were detected [5]. Although it is not known if immune mediated responses will compromise the therapeutic efficacy, new gene delivery systems amenable for clinical translation, such as extracellular vesicles [50] and ultrasound and microbubble mediated sonoporation have been investigated [51]. While *NfsB* from *E. coli* has been the most commonly employed gene for NTR-based GDEPT, different NTR orthologs and homologs, with a much higher catalytic activity, such as *NfsA* from *E. coli* and *Nme* from *N. meningitidis* have been evaluated [26, 52, 53]. Finally, development of improved prodrug candidates is ongoing [54], since CB1954 has been associated with dose-limiting hepatotoxicity in humans [55]. Indeed, the last two aspects, NTR-enzyme and prodrug, have been optimised simultaneously through the engineering of a modified NTR enzyme that confers higher catalytic activity for an improved prodrug. Remarkable efforts by Gungor and co-workers employing an NTR from *S. saprophyticus, Ssap*-NtrB, and a library of different nitro-containing scaffolds has led to promising *in vitro* prodrug candidates, such as benzamide derivatives *N*-(2,4-dinitrophenyl)-4-nitrobenzamide, A5 or A20, and piperazine derivatives NHN12 or NHN14 [54, 56-58]. Other examples of such a strategy include *HChrR6* with CNOB [59, 60] and *NfsA* variant no. 22 with PR-104A [61]. Interestingly, *NfsA* variant no. 22 retained reductive activity towards the hypoxia PET tracers, ^{18}F-EF5 and ^{18}F-HX4, allowing the possibility of NTR PET/CT imaging as companion diagnostic tool, as shown in the recently published work of Mowday et al. [26, 61].

Increasing preclinical knowledge will contribute significantly to the successful clinical translation of NTR-based GDEPT. The combination of a clinically amenable gene delivery system, optimised NTR enzymes and improved prodrugs is expected to boost the clinical application of NTR-based GDEPT. ^{18}F-FMISO NTR PET/CT imaging should be integrated into the clinical testing of future NTR-based GDEPT strategies, providing a robust and sensitive technology to monitor forthcoming clinical trials. ^{18}F-FMISO NTR PET/CT is an FDA methodology readily available for clinical application. Our preclinical studies further establish this strategy as a strong candidate for companion diagnostic testing of NTR-based GEDPT.

Supplementary Material

Supplementary figures.
http://www.thno.org/v11p6044s1.pdf

Acknowledgements

The authors wish to thank Marianne Enger and André Sulen for cell sorting analysis performed in the Flow Cytometry Core Facility (Department of Clinical Science, UoB), Endy Spriet, Linda Sandven and Anne Karin Nyhaug (Molecular Imaging Center, Dept. of Biomedicine, UoB) for embedment and staining of histology samples, Molecular Imaging Center (MIC, Department of Biomedicine, UoB) for provision of optical imaging facility. Tom Christian Holm Adamsen and Anne Vaag Eikeland, from Center for Nuclear Medicine/PET, Haukeland University Hospital, are thanked for facilitating production of radiotracer and Hans Olav Rolfsnes (MIC, Department of Biomedicine, UoB) for assistance with the small animal PET/CT. All preclinical work was performed at the Vivarium, University of Bergen. This work was supported by The Research Council of Norway (SonoCURE grant no. 250317), the Norwegian Cancer Society (grant numbers 6833652, 421828 and 732200), the Western Norway Regional Health Authority (grant numbers 911779, 911182 and 912162), the University of Bergen and the Trond Mohn Foundation.

Funding

This work was supported by The Research Council of Norway (SonoCURE grant no. 250317), the Norwegian Cancer Society (grant numbers 6833652 and 182735), the Western Norway Regional Health Authority (grant numbers 911779, 911182, 912146 and

912035), Research Council of Norway through its Centers of excellence funding scheme, the University of Bergen and the Trond Mohn Foundation.

Author contributions

E.G.J. and G.R.G. contributed equally to this work. E.G.J., E.S., G.R.G. and K.B.L. participated in the *in vitro* and *in vivo* work. E.G.J., E.S., G.R.G., K.B.L. and E.M.C. conceived and designed the study. E.G.J provided optical probes for NTR verification supervised by B.E.H. M.P. and M.M.S assisted in animal handling and *in vivo* work. B.D. performed immunohistochemical analyses. C.B.R and H.E. ran the PET/CT acquisition and reconstructed the images. T.B. performed histopathology on obtained tissue. E.G.J. and G.R.G wrote the manuscript, E.M.C. and B.E.H. contributed to writing and editing the manuscript.

Competing Interests

The authors have declared that no competing interest exists.

References

1. Zhang J, Kale V, Chen M. Gene-directed enzyme prodrug therapy. AAPS J. 2015; 17: 102-10.
2. Mishra AP, Chandra S, Tiwari R, Srivastava A, Tiwari G. Therapeutic Potential of Prodrugs Towards Targeted Drug Delivery. Open Med Chem J. 2018; 12: 111-23.
3. Bashraheel SS, Domling A, Goda SK. Update on targeted cancer therapies, single or in combination, and their fine tuning for precision medicine. Biomed Pharmacother. 2020; 125: 110009.
4. Li N, Zhou J, Weng D, Zhang C, Li L, Wang B, et al. Adjuvant adenovirus-mediated delivery of herpes simplex virus thymidine kinase administration improves outcome of liver transplantation in patients with advanced hepatocellular carcinoma. Clin Cancer Res. 2007; 13: 5847-54.
5. Patel P, Young JG, Mautner V, Ashdown D, Bonney S, Pineda RG, et al. A phase I/II clinical trial in localized prostate cancer of an adenovirus expressing nitroreductase with CB1954 [correction of CB1984]. Mol Ther. 2009; 17: 1292-9.
6. Ladd B, O'Konek JJ, Ostruszka LJ, Shewach DS. Unrepairable DNA double-strand breaks initiate cytotoxicity with HSV-TK/ganciclovir. Cancer Gene Ther. 2011; 18: 751-9.
7. Knox RJ, Boland MP, Friedlos F, Coles B, Southan C, Roberts JJ. The nitroreductase enzyme in Walker cells that activates 5-(aziridin-1-yl)-2,4-dinitrobenzamide (CB 1954) to 5-(aziridin-1-yl)-4-hydroxylamino-2-nitrobenzamide is a form of NAD(P)H dehydrogenase (quinone) (EC 1.6.99.2). Biochem Pharmacol. 1988; 37: 4671-7.
8. Pitsawong W, Hoben JP, Miller A-F. Understanding the broad substrate repertoire of nitroreductase based on its kinetic mechanism. J Biol Chem. 2014; 289: 15203-14.
9. Denny WA, Wilson WR. Bioreducible mustards: a paradigm for hypoxia-selective prodrugs of diffusible cytotoxins (HPDCs). Cancer Metastasis Rev. 1993; 12: 135-51.
10. William RW, Kevin OH, Susan MP, Dianne MF, Nuala AH, Adam VP. Bystander Effects of Bioreductive Drugs: Potential for Exploiting Pathological Tumor Hypoxia with Dinitrobenzamide Mustards. Radiat Res. 2007; 167: 625-36.
11. Rainov NG. A phase III clinical evaluation of herpes simplex virus type 1 thymidine kinase and ganciclovir gene therapy as an adjuvant to surgical resection and radiation in adults with previously untreated glioblastoma multiforme. Hum Gene Ther. 2000; 11: 2389-401.
12. Immonen A, Vapalahti M, Tyynela K, Hurskainen H, Sandmair A, Vanninen R, et al. AdvHSV-tk gene therapy with intravenous ganciclovir improves survival in human malignant glioma: a randomised, controlled study. Mol Ther. 2004; 10: 967-72.
13. Shah K, Jacobs A, Breakefield XO, Weissleder R. Molecular imaging of gene therapy for cancer. Gene Ther. 2004; 11: 1175-87.
14. Sekar TV, Foygel K, Ilovich O, Paulmurugan R. Noninvasive theranostic imaging of HSV1-sr39TK-NTR/GCV-CB1954 dual-prodrug therapy in metastatic lung lesions of MDA-MB-231 triple negative breast cancer in mice. Theranostics. 2014; 4: 460-74.
15. Tjuvajev JG, Doubrovin M, Akhurst T, Cai S, Balatoni J, Alauddin MM, et al. Comparison of radiolabeled nucleoside probes (FIAU, FHBG, and FHPG) for PET imaging of HSV1-tk gene expression. J Nucl Med. 2002; 43: 1072-83.
16. Gambhir SS, Barrio JR, Wu L, Iyer M, Namavari M, Satyamurthy N, et al. Imaging of adenoviral-directed herpes simplex virus type 1 thymidine kinase reporter gene expression in mice with radiolabeled ganciclovir. J Nucl Med. 1998; 39: 2003-11.
17. Deng W-P, Yang WK, Lai W-F, Liu R-S, Hwang J-J, Yang D-M, et al. Non-invasive *in vivo* imaging with radiolabelled FIAU for monitoring cancer gene therapy using herpes simplex virus type 1 thymidine kinase and ganciclovir. Eur J Nucl Med Mol Imaging. 2004; 31: 99-109.
18. Yaghoubi SS, Gambhir SS. PET imaging of herpes simplex virus type 1 thymidine kinase (HSV1-tk) or mutant HSV1-sr39tk reporter gene expression in mice and humans using [18F]FHBG. Nat Protoc. 2006; 1: 3069-75.
19. Penuelas I, Mazzolini G, Boan JF, Sangro B, Marti-Climent J, Ruiz M, et al. Positron emission tomography imaging of adenoviral-mediated transgene expression in liver cancer patients. Gastroenterology. 2005; 128: 1787-95.
20. McCormack E, Silden E, West RM, Pavlin T, Micklem DR, Lorens JB, et al. Nitroreductase, a near-infrared reporter platform for *in vivo* time-domain optical imaging of metastatic cancer. Cancer Res. 2013; 73: 1276-86.
21. Vorobyeva AG, Stanton M, Godinat A, Lund KB, Karateev GG, Francis KP, et al. Development of a Bioluminescent Nitroreductase Probe for Preclinical Imaging. PLoS One. 2015; 10: e0131037.
22. Koch CJ, Evans SM. Optimizing hypoxia detection and treatment strategies. Semin Nucl Med. 2015; 45: 163-76.
23. Horsman MR, Mortensen LS, Petersen JB, Busk M, Overgaard J. Imaging hypoxia to improve radiotherapy outcome. Nat Rev Clin Oncol. 2012; 9: 674-87.
24. Shimizu Y, Zhao S, Yasui H, Nishijima KI, Matsumoto H, Shiga T, et al. A Novel PET Probe "[(18)F]DiFA" Accumulates in Hypoxic Region via Glutathione Conjugation Following Reductive Metabolism. Mol Imaging Biol. 2019; 21: 122-9.
25. Williams EM, Little RF, Mowday AM, Rich MH, Chan-Hyams JVE, Copp JN, et al. Nitroreductase gene-directed enzyme prodrug therapy: insights and advances toward clinical utility. Biochem J. 2015; 471: 131-53.
26. Mowday AM, Copp JN, Syddall SP, Dubois LJ, Wang J, Lieuwes NG, et al. E. coli nitroreductase NfsA is a reporter gene for non-invasive PET imaging in cancer gene therapy applications. Theranostics. 2020; 10: 10548-62.
27. Gjerdrum C, Tiron C, Høiby T, Stefansson I, Haugen H, Sandal T, et al. Axl is an essential epithelial-to-mesenchymal transition-induced regulator of breast cancer metastasis and patient survival. Proc Natl Acad Sci U S A. 2010; 107: 1124-9.
28. Schindelin J, Arganda-Carreras I, Frise E, Kaynig V, Longair M, Pietzsch T, et al. Fiji: an open-source platform for biological-image analysis. Nat Methods. 2012; 9: 676-82.
29. Crowe AR, Yue W. Semi-quantitative Determination of Protein Expression using Immunohistochemistry Staining and Analysis: An Integrated Protocol. Bio Protoc. 2019; 9: e3465.
30. Lim JL, Berridge MS. An efficient radiosynthesis of [18F]fluoromisonidazole. Appl Radiat Isot. 1993; 44: 1085-91.
31. Adamsen TCH, Grierson JR, Krohn KA. A new synthesis of the labeling precursor for [18F]-fluoromisonidazole. J Labelled Comp Radiopharm. 2005; 48: 923-7.
32. Fitzsimmons SA, Workman P, Grever M, Paull K, Camalier R, Lewis AD. Reductase enzyme expression across the National Cancer Institute Tumor cell line panel: correlation with sensitivity to mitomycin C and EO9. J Natl Cancer Inst. 1996; 88: 259-69.
33. Franco M, Man S, Chen L, Emmenegger U, Shaked Y, Cheung AM, et al. Targeted anti-vascular endothelial growth factor receptor-2 therapy leads to short-term and long-term impairment of vascular function and increase in tumor hypoxia. Cancer Res. 2006; 66: 3639-48.
34. Sun JD, Liu Q, Wang J, Ahluwalia D, Ferraro D, Wang Y, et al. Selective tumor hypoxia targeting by hypoxia-activated prodrug TH-302 inhibits tumor growth in preclinical models of cancer. Clin Cancer Res. 2012; 18: 758-70.
35. Moolten FL. Tumor chemosensitivity conferred by inserted herpes thymidine kinase genes: paradigm for a prospective cancer control strategy. Cancer Res. 1986; 46: 5276-81.
36. McNeish IA, Green NK, Gilligan MG, Ford MJ, Mautner V, Young LS, et al. Virus directed enzyme prodrug therapy for ovarian and pancreatic cancer using retrovirally delivered E. coli nitroreductase and CB1954. Gene Ther. 1998; 5: 1061-9.
37. Djeha AH, Hulme A, Dexter MT, Mountain A, Young LS, Searle PF, et al. Expression of Escherichia coli B nitroreductase in established human tumor xenografts in mice results in potent antitumoral and bystander effects upon systemic administration of the prodrug CB1954. Cancer Gene Ther. 2000; 7: 721-31.
38. Caruso M, Panis Y, Gagandeep S, Houssin D, Salzmann JL, Klatzmann D. Regression of established macroscopic liver metastases after *in situ* transduction of a suicide gene. Proc Natl Acad Sci U S A. 1993; 90: 7024-8.
39. Kuriyama S, Mitoro A, Yamazaki M, Tsujinoue H, Nakatani T, Akahane T, et al. Comparison of gene therapy with the herpes simplex virus thymidine kinase gene and the bacterial cytosine deaminase gene for the treatment of hepatocellular carcinoma. Scand J Gastroenterol. 1999; 34: 1033-41.
40. Wobb J, Krueger SA, Kane JL, Galoforo S, Grills IS, Wilson GD, et al. The Effects of Pulsed Radiation Therapy on Tumor Oxygenation in 2 Murine

Models of Head and Neck Squamous Cell Carcinoma. Int J Radiat Oncol Biol Phys. 2015; 92: 820-8.
41. Mena-Romano P, Cheng C, Glowa C, Peschke P, Pan L, Haberkorn U, et al. Measurement of hypoxia-related parameters in three sublines of a rat prostate carcinoma using dynamic (18)F-FMISO-Pet-Ct and quantitative histology. Am J Nucl Med Mol Imaging. 2015; 5: 348-62.
42. Arvold ND, Heidari P, Kunawudhi A, Sequist LV, Mahmood U. Tumor Hypoxia Response After Targeted Therapy in EGFR-Mutant Non-Small Cell Lung Cancer: Proof of Concept for FMISO-PET. Technol Cancer Res Treat. 2015; 15: 234-42.
43. Zhao SJ, Kuge YJ, Zhao Y, Takeuchi S, Murakami M, Li H, et al. FMISO PET can early evaluate antiangiogenic response to anti-EGFR molecular-targeting therapy (cetuximab) in human lung cancer xenograft. J Nucl Med. 2011; 52.
44. Sorace AG, Syed AK, Barnes SL, Quarles CC, Sanchez V, Kang H, et al. Quantitative [(18)F]FMISO PET Imaging Shows Reduction of Hypoxia Following Trastuzumab in a Murine Model of HER2+ Breast Cancer. Mol Imaging Biol. 2017; 19: 130-7.
45. Jiang H, Zhang R, Jiang H, Zhang M, Guo W, Feng G, et al. Evaluation of [18F]FDG/[18F]FLT/[18F]FMISO-based micro-positron emission tomography in detection of liver metastasis in human colorectal cancer. Nucl Med Biol. 2019; 72-73: 36-44.
46. Nakata N, Kiriu M, Okumura Y, Zhao S, Nishijima K-I, Shiga T, et al. Comparative evaluation of [18F]DiFA and its analogs as novel hypoxia positron emission tomography and [18F]FMISO as the standard. Nucl Med Biol. 2019; 70: 39-45.
47. Ruggiero A, Brader P, Serganova I, Zanzonico P, Cai S, Lipman NS, et al. Different strategies for reducing intestinal background radioactivity associated with imaging HSV1-tk expression using established radionucleoside probes. Mol Imaging. 2010; 9: 47-58.
48. Watanabe S, Shiga T, Hirata K, Magota K, Okamoto S, Toyonaga T, et al. Biodistribution and radiation dosimetry of the novel hypoxia PET probe [(18)F]DiFA and comparison with [(18)F]FMISO. EJNMMI research. 2019; 9: 60.
49. Denny WA. Nitroreductase-based GDEPT. Curr Pharm Des. 2002; 8: 1349-61.
50. Forterre AV, Wang JH, Delcayre A, Kim K, Green C, Pegram MD, et al. Extracellular Vesicle-Mediated *In vitro* Transcribed mRNA Delivery for Treatment of HER2(+) Breast Cancer Xenografts in Mice by Prodrug CB1954 without General Toxicity. Mol Cancer Ther. 2020.
51. Devulapally R, Lee T, Barghava-Shah A, Sekar TV, Foygel K, Bachawal SV, et al. Ultrasound-guided delivery of thymidine kinase-nitroreductase dual therapeutic genes by PEGylated-PLGA/PIE nanoparticles for enhanced triple negative breast cancer therapy. Nanomedicine (Lond). 2018; 13: 1051-66.
52. Heap JT, Theys J, Ehsaan M, Kubiak AM, Dubois L, Paesmans K, et al. Spores of Clostridium engineered for clinical efficacy and safety cause regression and cure of tumors *in vivo*. Oncotarget. 2014; 5: 1761-9.
53. Vass SO, Jarrom D, Wilson WR, Hyde EI, Searle PF. E. coli NfsA: an alternative nitroreductase for prodrug activation gene therapy in combination with CB1954. Br J Cancer. 2009; 100: 1903-11.
54. Gungor T, Onder FC, Tokay E, Gulhan UG, Hacioglu N, Tok TT, et al. PRODRUGS FOR NITROREDUCTASE BASED CANCER THERAPY- 2: Novel amide/Ntr combinations targeting PC3 cancer cells. Eur J Med Chem. 2019; 171: 383-400.
55. Chung-Faye G, Palmer D, Anderson D, Clark J, Downes M, Baddeley J, et al. Virus-directed, enzyme prodrug therapy with nitroimidazole reductase: a phase I and pharmacokinetic study of its prodrug, CB1954. Clin Cancer Res. 2001; 7: 2662-8.
56. Gungor T, Yetis G, Onder FC, Tokay E, Tok TT, Celik A, et al. Prodrugs for Nitroreductase Based Cancer Therapy- 1: Metabolite Profile, Cell Cytotoxicity and Molecular Modeling Interactions of Nitro Benzamides with Ssap-NtrB. Med Chem. 2018; 14: 495-507.
57. Tokay E, Güngör T, Hacıoğlu N, Önder FC, Gülhan ÜG, Tok TT, et al. Prodrugs for nitroreductase-based cancer therapy-3: Antitumor activity of the novel dinitroaniline prodrugs/Ssap-NtrB enzyme suicide gene system: Synthesis, *in vitro* and *in silico* evaluation in prostate cancer. Eur J Med Chem. 2020; 187: 111937.
58. Güngör T, Tokay E, Güven Gülhan Ü, Hacıoğlu N, Çelik A, Köçkar F, et al. Prodrugs for nitroreductase based cancer therapy-4: Towards prostate cancer targeting: Synthesis of N-heterocyclic nitro prodrugs, Ssap-NtrB enzymatic activation and anticancer evaluation. Bioorg Chem. 2020; 105: 104450.
59. Forterre AV, Wang J-H, Matin AC, Delcayre A, Kim K, Green C, et al. Extracellular Vesicle-Mediated *In vitro* Transcribed mRNA Delivery for Treatment of HER2(+) Breast Cancer Xenografts in Mice by Prodrug CB1954 without General Toxicity. Mol Cancer Ther. 2020; 19: 858-67.
60. Wang J-H, Forterre AV, Zhao J, Frimannsson DO, Matin AC, Delcayre A, et al. Anti-HER2 scFv-Directed Extracellular Vesicle-Mediated mRNA-Based Gene Delivery Inhibits Growth of HER2-Positive Human Breast Tumor Xenografts by Prodrug Activation. Mol Cancer Ther. 2018; 17: 1133-42.
61. Copp JN, Mowday AM, Williams EM, Guise CP, Ashoorzadeh A, Sharrock AV, et al. Engineering a Multifunctional Nitroreductase for Improved Activation of Prodrugs and PET Probes for Cancer Gene Therapy. Cell Chem Biol. 2017; 24: 391-403.

SUPPLEMENTARY FIGURES:

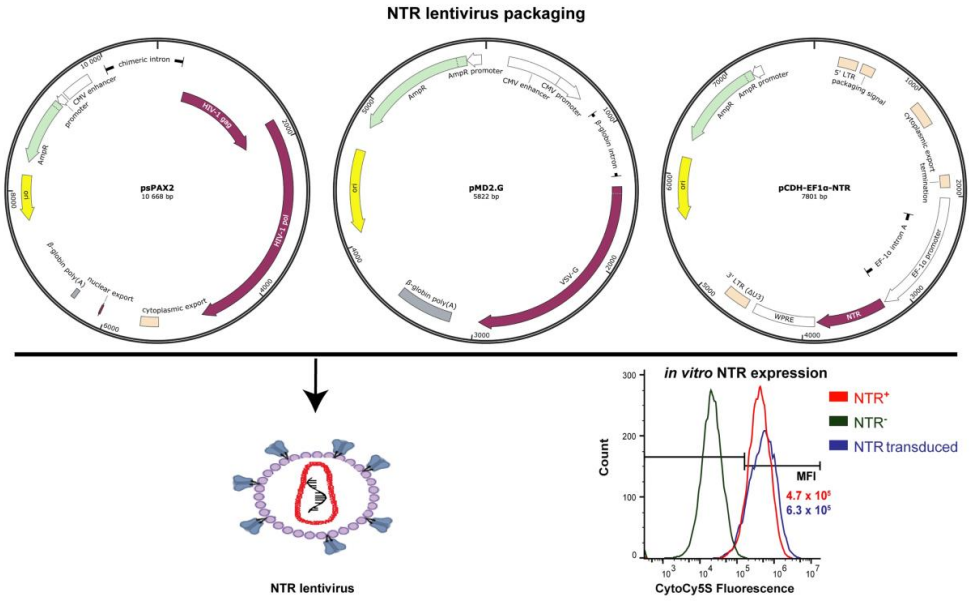

FIGURE S1

NTR lentiviral packaging plasmids. *In vitro* analysis of the levels of expression of NTR in the MDA-MB-231 NTR^{+} cell line and in the MDA-MB-231 after transduction and sorting with the lentiviral NTR particles. Similar levels of expression were observed in both cell lines.

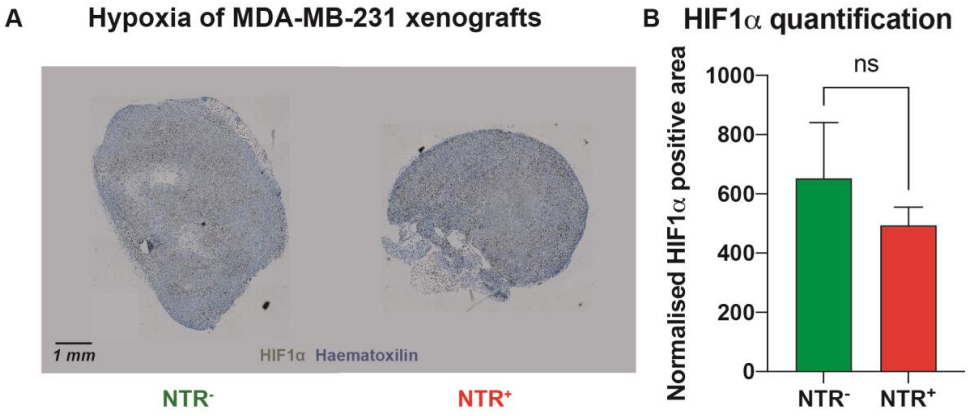

FIGURE S2

(A) Example of HIF1α IHC in NTR$^-$ and NTR$^+$ MDA-MB-231 xenografts. (B) No significant difference was observed in the normalised area positive for HIF1α between NTR$^-$ and NTR$^+$ MDA-MB-231 xenografts (n = 3, per group).

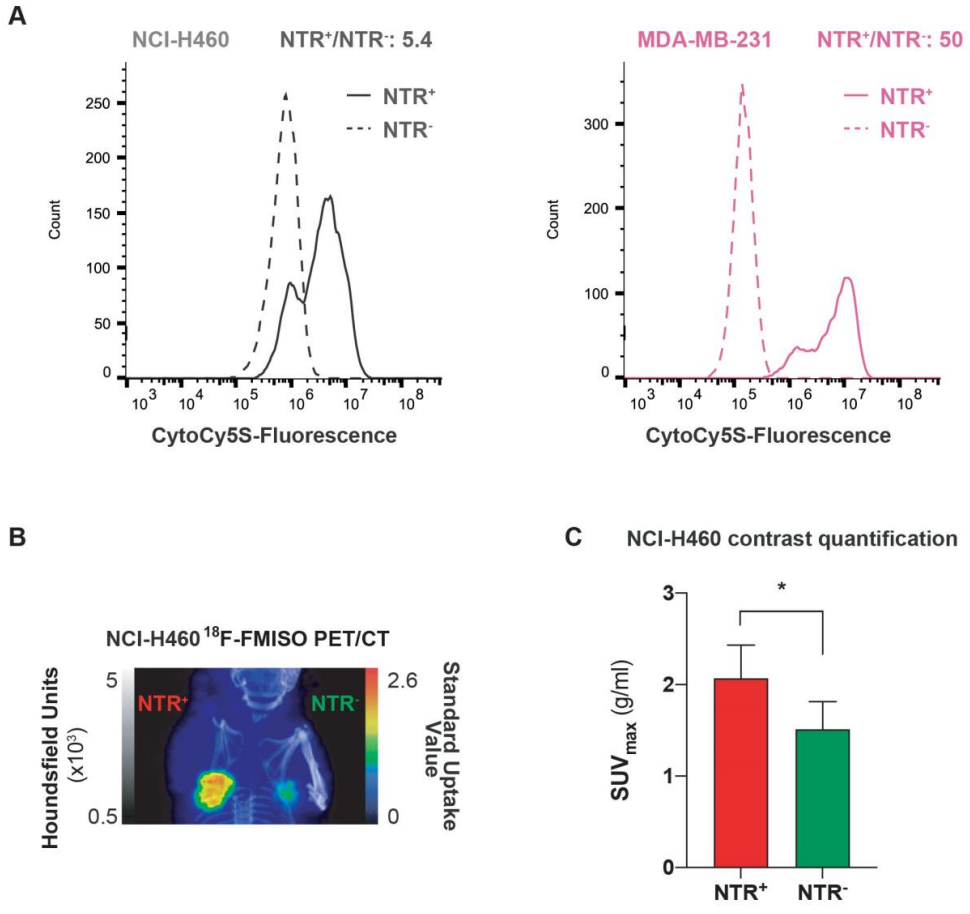

FIGURE S3

(A) NTR^+/NTR^- ratio was notably lower for NCI-H460 than for MDA-MB-231 cell line. (B) Representative ^{18}F-FMISO PET/CT MIP images of NCI-H460 xenografts. NTR^- tumour (right flank) and NTR^+ tumour (left flank). (C) SUV_{max} values were significantly higher in NTR^+ xenografts. (*, $p < 0.05$, n = 4).

The p-values are represented as indicated: * $p < 0.05$, ** $p < 0.01$, *** $p < 0.001$ and **** $p < 0.0001$.

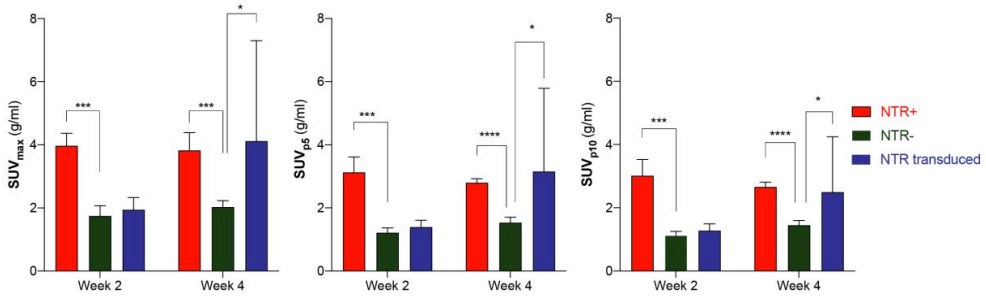

FIGURE S4

SUV_{max} , SUV_{p5} and SUV_{p10} analyses show similar results in the *in vivo* transduced tumours.
The p-values are represented as indicated: * $p < 0.05$, ** $p < 0.01$, *** $p < 0.001$ and **** $p < 0.0001$.

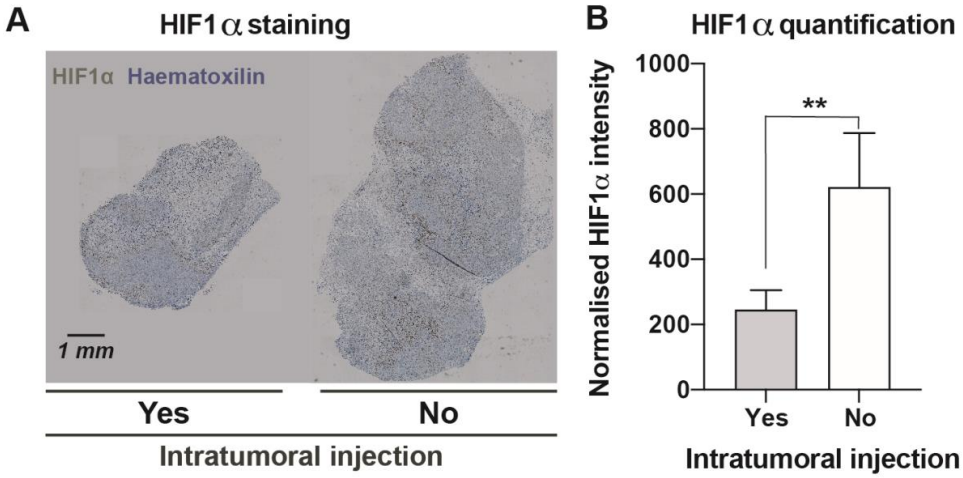

FIGURE S5

(A) The spatial pattern of HIF1α accumulation was similar in both intratumorally injected and non-injected tumours MDA-MB-231 NTR^- xenografts. (B) The normalised HIF1α positive area was significantly lower in intratumorally injected xenografts (n = 4 per group).

Errata for
Preclinical molecular imaging in oncology – From chemical synthesis to clinical translatable applications

Elvira García de Jalón Viñegra

Thesis for the degree philosophiae doctor (PhD)
at the University of Bergen

31st of May 2021,
Elvira García de Jalón Viñegra

(date and sign. of candidate)

31/5 21

(date and sign. of faculty)

Errata

Page 28 Mistake: "...ground state (S_1 à S_0)." – corrected to "...ground state (S_1 → S_0)."

Page 43 Mistake "...employing *NfsA* from *E. coli*..." – corrected to "...employing NfsA from *E. coli*..."

Page 60 Missing spaces: "...and A549 ($p<0.05$)." – corrected to "...and A549 ($p < 0.05$)."

Page 98 Mistake: "A weak NIR fluorescent signal was observed..." – corrected to "A weak NIR fluorescence signal was observed..."

Page 98 Mistake: "...which allows us to follow the fate of **1** over time..." – corrected to "...which allowed us to follow the fate of **1** over time..."

Page 99 Wrong numbering: "As shown in Scheme S1..." – corrected to "As shown in Scheme 1..."

Page 100 Wrong numbering: "**Scheme S1.** Synthesis of EDAF-Cy5 conjugates." – corrected to "**Scheme 1.** Synthesis of EDAF-Cy5 conjugates."

Page 100 Mistake: "...to express *E. coli NfsB* nitroreductase..." – corrected to "...to express *E. coli* NfsB nitroreductase..."

Page 101 Wrong numbering: "...were incubated with **7** for 14 hours." – corrected to "...were incubated with **1** for 14 hours."

Page 101 Missing italics: "1,2,3,3-Tetramethyl-3H-indolium iodide..." - corrected to "1,2,3,3-Tetramethyl-3*H*-indolium iodide..."

Page 102 Missing italics: "1-(5-Carboxypentyl)-2,3,3-trimethyl-3H-indolium iodide..." - corrected to "1-(5-Carboxypentyl)-2,3,3-trimethyl-3*H*-indolium iodide..."

Page 102 Missing italics: "1-(3,5-dinitrobenzyl)-2,3,3-trimethyl-3H-indolium iodide..." - corrected to "1-(3,5-dinitrobenzyl)-2,3,3-trimethyl-3*H*-indolium iodide..."

Page 106 Mistake: "Calcd m/z for $C_{60}H_{62}N_{13}O_{12}^+$ $[M + H]^+$: 1156.4635; found: 1156.46381." – corrected to "Calcd m/z for $C_{60}H_{62}N_{13}O_{12}^+$ $[M + H]^+$: 1156.4635; found: 1156.4638."

Page 153 Mistake: "...high-pressure liquid chromatography (HPLC)" – corrected to "...high-performance liquid chromatography (HPLC)"

Page 202 Wrong numbering: "one in-house synthesised dye (**6**)" – corrected to "one in-house synthesised dye (**5**)"

Page 209 Wrong numbering: "Summary of the spectroscopic properties of conjugates **1** - **6**" – corrected to "Summary of the spectroscopic properties of conjugates **1** - **5**"

Page 210, Line 248 Mistake: "…the HeLa cells for all six conjugates…" – corrected to "…the HeLa cells for all five conjugates…"

Page 210, Line 258 Mistake: "…specific binding of all six conjugates…" – corrected to "…specific binding of all five conjugates…"

Page 213 Mistake: "…was obtained for conjugate **2** ($p < 0.01$)…" – corrected to "…was obtained for conjugate **2** ($p < 0.05$)…"

Page 231 Misspelling: "bis-ethylendiamine" – corrected to "bis-ethylenediamine"

Page 246 Wrong figure numbering: "Figure S6" – corrected to "Figure S2"

Page 247 Wrong figure numbering: "Figure S7" – corrected to "Figure S3"

Page 248 Wrong figure numbering: "Figure S8 and Figure S9" – corrected to "Figure S4 and Figure S5"

Page 249 Wrong figure numbering: "Figure S10" – corrected to "Figure S6"

Page 250 Wrong figure numbering: "Figure S11" – corrected to "Figure S7"

Page 251 Wrong figure numbering: "Figure S12" – corrected to "Figure S8"

Page 252 Wrong figure numbering: "Figure S13" – corrected to "Figure S9"

Page 253 Wrong figure numbering: "Figure S14" – corrected to "Figure S10"

Page 254 Wrong figure numbering: "Figure S15" – corrected to "Figure S11"

Page 255 Wrong figure numbering: "Figure S16" – corrected to "Figure S12"

Page 256 Wrong figure numbering: "Figure S17" – corrected to "Figure S13"

Page 257 Wrong figure numbering: "Figure S18" – corrected to "Figure S14"

Page 258 Wrong figure numbering: "Figure S19" – corrected to "Figure S15"

Page 259 Wrong figure numbering: "Figure S20" – corrected to "Figure S16"

Page 260 Wrong figure numbering: "Figure S21" – corrected to "Figure S17"

Page 261 Wrong figure numbering: "Figure S22" – corrected to "Figure S18"

Page 278 Mistake: "EGJV-345 F15 (10-90% MeCN) Fraction containing the unreacted dye (Conjugate **5**). No HPLC trace for this fraction." – corrected to "EGJV-345 F15 (10-90% MeCN) Fraction containing the unreacted dye (in-house synthesised Cy7). No HPLC trace for this fraction."

Graphic design: Communication Division, UiB / Print: Skipnes Kommunikasjon AS

uib.no

ISBN: 9788230845608 (print)
9788230856352 (PDF)